

Geomechanical aspects of deepwater well planning around salt structures

Leš, Borna

Master's thesis / Diplomski rad

2022

Degree Grantor / Ustanova koja je dodijelila akademski / stručni stupanj: **University of Zagreb, Faculty of Mining, Geology and Petroleum Engineering / Sveučilište u Zagrebu, Rudarsko-geološko-naftni fakultet**

Permanent link / Trajna poveznica: <https://urn.nsk.hr/urn:nbn:hr:169:657411>

Rights / Prava: [In copyright](#)/[Zaštićeno autorskim pravom.](#)

Download date / Datum preuzimanja: **2025-01-23**



Repository / Repozitorij:

[Faculty of Mining, Geology and Petroleum Engineering Repository, University of Zagreb](#)



UNIVERSITY OF ZAGREB
FACULTY OF MINING, GEOLOGY AND PETROLEUM ENGINEERING
MASTER PROGRAMME IN PETROLEUM ENGINEERING

**GEOMECHANICAL ASPECTS OF DEEPWATER WELL PLANNING AROUND
SALT STRUCTURES**

Master's Thesis

Borna Leš

N343

Zagreb, 2022.

GEOMECHANICAL ASPECTS OF DEEPWATER WELL PLANNING AROUND SALT STRUCTURES

Borna Leš

Thesis completed at: The University of Zagreb
Faculty of Mining, Geology and Petroleum Engineering
Department of Petroleum and Gas Engineering and Energy
Pierottijeva 6, 10 000 Zagreb

Abstract

Exploration around the salt bodies has always been challenging for well planning and construction due to associated geological complexity and well-planning uncertainties. With the placement of wells in a deep and complex offshore salt environment, the wellbore stability becomes an all-important element for meeting well construction objectives. The well construction risks associated with instabilities encountered around salt structures can be high to the extent where they drastically influence the well design and delivery costs. To facilitate the planning and drilling of wells in such a challenging and expensive environment, the in-situ conditions around salt bodies must be accurately characterized. In turn, that will enable accurate quantification of formation pressure and fracture gradients, a crucial input for casing design. The standalone approach to well architecture design is often preferred during the planning stage due to its simplicity. However, such an approach may become inadequate once the influence of salt structures on the well design is properly understood. The salt-induced stress perturbations and local geomechanical instabilities found around salt bodies, if underestimated, may incur substantial well construction costs and consequently jeopardize the overall economics of a prospect. Hence, one shall adhere to a holistic approach toward the well architecture design by considering the multiple factors including, but not limited to, geomechanical instabilities, abnormal pore pressures, areas of accelerated creep, and other trajectory-specific drilling problems. In other words, leveraging a multidimensional approach to well architecture design, such that all specific risks peculiar to the offshore salt environment are well understood and evaluated, shall enable operators to capture additional value from the well construction while improving returns, decreasing risks, and enhancing operational safety in Deepwater salt plays.

Keywords: Offshore well architecture, wellbore stability, pre-salt, subsalt, well design, salt creep

Thesis contains: 158 pages, 81 figures, 3 tables, 2 Appendices and 138 references.

Language of the original: English

Thesis stored at: Library of Faculty of Mining, Geology and Petroleum Engineering
Pierottijeva 6, Zagreb

Supervisor: PhD Borivoje Pašić, Associate Professor
Co-mentor: PhD Petar Mijić, Postdoctoral Researcher

Reviewing Comitee: PhD Borivoje Pašić, Associate Professor
PhD Vladislav Brkić, Associate Professor
PhD Zdenko Krištafor, Full Professor

Date of defense: February 17, 2022., University of Zagreb Faculty of Mining, Geology and Petroleum Engineering

GEOMEHANIČKI ASPEKTI PROJEKTIRANJA ODOBALNIH BUŠOTINA U BLIZINI SOLNIH STRUKTURA

Borna Leš

Diplomski rad je izrađen: Sveučilište u Zagrebu
Rudarsko-geološko-naftni fakultet
Zavod za naftno-plinsko inženjerstvo i energetiku
Pierottijeva 6, 10000 Zagreb

Sažetak

Složenost geoloških struktura u podzemlju i nesigurnosti povezane s istraživanjem ležišta ugljikovodika u blizini solnih naslaga dodatno usložnjavaju proces projektiranja i izrade bušotina u odobalju. Pri projektiranju bušotina u dubljim i složenijim dijelovima odobalja, stabilnost kanala bušotine postaje vrlo važan element u postizanju ciljeva izrade istih. Stupanj nestabilnosti kanala odobalnih bušotina povezanih s bušenjem naslaga soli može utjecati na projektiranje i tehničku izvedbu tako da ugrožava ekonomičnost bušotine. Stoga je važno odrediti deformacije i stanje naprezanja unutar i u neposrednoj blizini naslaga soli, a s ciljem lakšeg planiranja i što efikasnije izrade bušotine. Precizna karakterizacija spomenutih veličina omogućuje točnu procjenu pornog tlaka i gradijenta loma, ključnih parametara za projektiranje zacjevljenja kanala bušotine. S ciljem pojednostavljenja projekta izrade bušotine, utjecaj perturbacija naprezanja i lokalnih geomehaničkih nestabilnosti uzrokovanih dugotrajnim puzanjem soli često je umanjen tijekom procesa planiranja. Posljedično, necjelovit pristup projektiranju može prouzročiti dodatne troškove izrade bušotine u odobalju te, u određenim slučajevima, dovesti u pitanje ekonomsku opravdanost investicije u razradu polja. Stoga je, zbog višestrukog utjecaja solnih struktura na tehničku izvedbu kanala bušotine, vrlo važno holistički pristupiti projektiranju putanje bušotine. Sveobuhvatnim pristupom moguće je konvencionalan pristup planiranju proširiti razmatranjem utjecaja geomehaničkih nestabilnosti, lokalnih perturbacija pornog tlaka, rizika vezanih uz puzanje soli i ostalih problema koji izravno utječu na projektiranje putanje kanala bušotine. Naime, sagledavanjem svih rizika svojstvenih naslagama soli u odobalju, naftno-plinskim kompanijama omogućeno je stvoriti dodanu vrijednost kroz ubrzani povrat ulaganja, smanjenje rizika te povećanje operativne sigurnosti.

Ključne riječi: konstrukcija odobalne bušotine, stabilnost kanala bušotine, bušenje kroz naslage soli, puzanje soli

Diplomski rad sadrži: 158 stranica, 81 sliku, 3 tablice i 138 referenci

Jezik izvornika: engleski

Diplomski rad pohranjen: Knjižnica Rudarsko-geološko-naftnog fakulteta
Pierottijeva 6, Zagreb

Mentor: Dr. sc. Borivoje Pašić, izvanredni profesor RGNF
Komentor: Dr. sc. Petar Mijić

Ocjenjivači: Dr. sc. Borivoje Pašić, izvanredni profesor RGNF
Dr. sc. Vladislav Brkić, izvanredni profesor RGNF
Dr. sc. Zdenko Krištafor, redoviti profesor RGNF

Datum obrane: 17. veljače 2022., Sveučilište u Zagrebu, Rudarsko-geološko-naftni fakultet

CONTENTS

I. LIST OF FIGURES	V
II. LIST OF TABLES	X
III. NOMENCLATURE	XI
IV. LIST OF ABBREVIATIONS	XV
1. INTRODUCTION	1
2. PROBLEM SELECTION AND HYPOTHESIS	7
3. SALT PROPERTIES	9
3.1. Basic salt properties	9
3.2. Salt strength	10
3.3. Salt solubility	10
3.4. Salt thermal properties	10
4. FLOWING NATURE OF SALT	12
4.1. Salt morphology	12
<i>4.1.1. Salt diapirs</i>	<i>15</i>
<i>4.1.2. Salt sheets</i>	<i>16</i>
4.2. Salt behavior	16
<i>4.2.1. Creep micromechanisms</i>	<i>18</i>
<i>4.2.2. Creep regimes</i>	<i>19</i>
4.3. Modeling salt behavior	21
<i>4.3.1. Maxwell's constitutive model</i>	<i>22</i>
5. BASIC CONCEPTS IN ROCK MECHANICS	25
5.1. Rock strength	25
5.2. Stress	26
<i>5.2.1. Principal stresses</i>	<i>27</i>
<i>5.2.2. Deviatoric stresses</i>	<i>29</i>

5.2.3. Octahedral stress theory.....	30
5.2.4. Von Mises equivalent stress.....	32
5.3. Laboratory tests.....	33
5.4. Failure criteria	34
5.4.1. Effective stress.....	35
5.4.2. Linear Mohr-Coulomb failure criterion.....	36
5.4.3. Alternative expression for Mohr-Coulomb failure criterion.....	37
5.4.4. Limitations of Mohr-Coulomb failure criterion	41
5.5. Rock Failure.....	41
5.5.1. Compressive failure.....	42
5.5.2. Tensile failure.....	43
5.5.3. Shear failure	43
6. PETROLEUM ROCK MECHANICS IN THE FUNCTION OF WELLBORE STABILITY	46
6.1. In-situ stress	46
6.1.1. Andersonian stress classification	47
6.2. Stress concentration around a vertical wellbore	51
6.2.1. Wellbore stability in vertical wells.....	54
6.3. Stress concentration around a deviated wellbore.....	58
6.3.1. Wellbore stability in deviated wells.....	62
6.4. General considerations for wellbore stability	64
7. PORE PRESSURE AND FRACTURE GRADIENT IN DEEPWATER SALT ENVIRONMENT	67
7.1. Pore-pressure regimes in Deepwater	70
7.2. Salt effects on the pore pressure:	74
7.3. Salt stringers	77
8. WELLBORE STABILITY IN DEEPWATER SUBSALT.....	80

8.1. Estimating in-situ conditions around salts	81
8.1.1. <i>Literature review on numerical modeling of salt-induced stress perturbations</i>	83
8.1.2. <i>General trends in stress disturbances around salt bodies.....</i>	85
8.1.3. <i>Stress perturbations around spherical salt bodies</i>	86
8.1.4. <i>Stress perturbations around salt sheets.....</i>	87
8.2. Drilling hazards around salt bodies	88
8.2.1. <i>Area of tectonic instability.....</i>	88
8.2.2. <i>Rubble (brecciated) zones</i>	89
8.2.3. <i>Salt welds with trapped pressure.....</i>	90
8.2.4. <i>Tar bands.....</i>	90
8.2.5. <i>Major subsalt pressure regression</i>	90
8.2.6. <i>Overtuned beds</i>	91
8.2.7. <i>Salt idiosyncrasies</i>	92
8.2.8. <i>Overpressured fluids trapped against salt.....</i>	92
8.2.9. <i>Fractured carapace zones</i>	92
8.2.10. <i>Salt shear zone.....</i>	93
8.3. Salt implications to wellpath optimization in Deepwater salt environment.....	95
8.3.1. <i>Salt entry and exit selection strategy.....</i>	96
8.3.2. <i>Wellbore stability implications to well architecture in Deepwater salt environment.....</i>	99
8.3.3. <i>Well trajectory design challenges in offshore salt play.....</i>	103
9. CREEP IMPLICATIONS TO WELLBORE STABILITY.....	107
9.1. Industry models for creep estimation	107
9.1.1. <i>The Munson and Dawson “Sandia” model.....</i>	107
9.1.2. <i>Double Mechanism creep law</i>	108
9.1.3. <i>Creep modeling applications.....</i>	108

9.2. Creep relation to octahedral stress	109
9.3. Creep-caused borehole closure.....	113
9.4. Overburden and temperature effects on creep.....	118
<i>9.4.1. Overburden implications to salt creep</i>	<i>119</i>
<i>9.4.2. Temperature implications to salt creep.....</i>	<i>121</i>
10. CASING SEAT SELECTION IN DEEPWATER SALT ENVIRONMENT	125
10.1. Mud weight window design	125
<i>10.1.1. Base pressure constraints.....</i>	<i>125</i>
<i>10.1.2. Uncertainty-related constraints.....</i>	<i>125</i>
<i>10.1.3. Wellbore pressure shocks</i>	<i>126</i>
<i>10.1.4. Differential sticking</i>	<i>127</i>
<i>10.1.5. Wellbore stability constraints.....</i>	<i>127</i>
<i>10.1.6. Riser margin</i>	<i>129</i>
<i>10.1.7. Constraints caused by salt creep.....</i>	<i>130</i>
<i>10.1.8. Regulatory requirements</i>	<i>130</i>
<i>10.1.9. Kick tolerance.....</i>	<i>130</i>
10.2. Deepwater casing sizing	131
10.3. Dubiousness in Deepwater casing shoe selection in subsalt and presalt.....	136
11. CONCLUSION	138
12. REFERENCES	140
13. APPENDICES.....	154
13.1. Appendix - 1	154
13.2. Appendix - 2	155

I. LIST OF FIGURES

Figure 1-1. Schematic representation of (a) Allochthonous and Autochthonous salt and (b) map of worldwide basins containing Allochthonous evaporites	3
Figure 1-2. Tabulated representation of the most notable discoveries in GoM.....	4
Figure 1-3. Global oil supply growth in the period from 2017-2030.....	5
Figure 3-1. Comparison of thermal gradient projections using numerical (thermal flow study) and linear regression from offset well data	11
Figure 4-1. Mechanisms of (a) creep strain and (b) stress relaxation.....	12
Figure 4-2. The strength profile of deeply buried salt, λ is the ratio of pore pressure to a lithostatic pressure	14
Figure 4-3. Evolution of salt structures in the subsurface	15
Figure 4-4. Differential stress required to initiate salt creep as a function of (a) confining pressure and strain rate and (b) temperature and salt wetness.....	17
Figure 4-5. Creep rates of different salts for varying p-T conditions	17
Figure 4-6. Deformation micromechanism map for salt in probable Deepwater GoM conditions	19
Figure 4-7. The (a) theoretical creep curve and (b) creep curve obtained through laboratory testing	21
Figure 4-8. Schematic representation of Maxwell's viscoelastic model	22
Figure 4-9. (a) Sensitivity plot of elastic stress relaxation time versus viscosity and (b) Elastic stress relaxation time for wellbore stresses as a function of salt viscosities in the range from 10^{16} to 10^{18} Pa s	24
Figure 5-1. Traction vector and stress tensor components	27
Figure 5-2. Schematic representation of principal stresses	29
Figure 5-3. Decomposition of total stress tensor to deviatoric and isotropic component ..	30
Figure 5-4. Schematic representation of octahedral stress	31

Figure 5-5. Different states of stress applied to laboratory specimens. Note: Uniaxial: $\sigma_1 \neq 0; \sigma_2 = \sigma_3 = 0$, Biaxial: $\sigma_1 \neq 0; \sigma_3 \neq 0; \sigma_2 = 0$, Triaxial: $\sigma_1 \neq 0; \sigma_2 \neq 0; \sigma_3 \neq 0$, Polyaxial: $\sigma_1 \neq \sigma_2 \neq \sigma_3$	34
Figure 5-6. The Mohr-Coulomb and the Drucker-Prager plastic yield criteria in the (a) principal stress space and (b) π - plane	35
Figure 5-7. Decomposition of total stress Tensor of a porous material	36
Figure 5-8. Representation of 2D Tensor components acting on the arbitrarily cut plane	38
Figure 5-9. (a) Running triaxial tests on different core specimens allows (b) fitting a non-linear M-C model or (c) constructing a linearized M-C model	40
Figure 5-10. The effect of the confining pressure on the (a) compressive rock strength and (b) compressive failure modes	43
Figure 5-11. Failure envelope in principal stress space	45
Figure 5-12. P-Q failure envelope	45
Figure 6-1. Representation of convergent (left) and divergent (right) margins	47
Figure 6-2. Schematic representation of in-situ stresses acting on the infinitesimal subsurface element	48
Figure 6-3. Andersonian classification of stress states.....	49
Figure 6-4. General stress-depth relation of principal stresses in different tectonic environments	50
Figure 6-5. (a) Rock formation with uniform stress state, (b) rock formation with a drilled hole that perturbs in-situ stresses, and (c) distribution of stresses around a wellbore.....	52
Figure 6-6. Hoop stress variation around the vertical wellbore as a function of normalized distance	54
Figure 6-7. Schematic representation of stress concentration at the wellbore wall.....	55
Figure 6-8. Schematic representation of stress bounds at the wellbore wall.....	56
Figure 6-9. The allowable MW window	57
Figure 6-10. Workflow for defining an MW window in a vertical wellbore	57
Figure 6-11. The thermal effects on the hoop stress variation	58

Figure 6-12. (a) The orientation of arbitrarily deviated wellbore relative to the principal stresses and (b) effective stresses obtained upon the transformation	61
Figure 6-13. Breakout and tensile fracture creation in deviated wells	63
Figure 6-14. Wellbore stability workflow to assess shear failure gradient	64
Figure 6-15. Schematic representation of a lower hemisphere diagram aka Schmidt plot	65
Figure 6-16. The effect of well`s azimuth on the wellbore stability	66
Figure 7-1. Data to estimate PPFG trends expressed in confidence ranking. “Equivalent depth” in this case refers to relative comparison of data	68
Figure 7-2. PPFG plot including both pre-drill and post-drill MW window.....	69
Figure 7-3. Generalized pore pressure profiles in Deepwater	70
Figure 7-4. Sedimentation rate at the DCM in the deltaic environment.....	71
Figure 7-5. Effect of the water depth on pore pressure gradient	72
Figure 7-6. Simulation of salt sheet emplacement and overpressure generation in the undrained environment.....	75
Figure 7-7. Scatter plot of pore pressure data from GoM represented as (a) pressure trend with depth BML and (b) normalized pore pressure versus normalized minimum principal stress	76
Figure 7-8. Simulation of salt relaxation against elastoplastic sediments; (a) horizontal displacement around the salt body in drained conditions and (b) stress-induced pressure change around the salt body	77
Figure 7-9. Evolution of abnormally pressured stringers	79
Figure 8-1. Plane-strain numerical model of a Mad Dog cross section with the representation of (a) deviatoric stress at the time of salt emplacement and after the relaxation (ca. after 0,4 million years) and (b) salt outward horizontal displacements loading the wall rocks	81
Figure 8-2. Seismic lines in the vicinity of two other salt bodies in the Gulf of Mexico ..	82
Figure 8-3. Representation of (a) displacement vectors around moving salt sheet and (b) horizontal strains resulting from these displacements (compressive strains have positive value)	85

Figure 8-4. Generalized stress gradient character for different positioned well trajectories around (a) large spherical salt body and (b) thick salt sheet	88
Figure 8-5. Summary of geomechanical instabilities around and within salt bodies	95
Figure 8-6. Typical indicators used to evaluate potential salt entry and exit	97
Figure 8-7. Wellbore shear limit expressed in EMW for (a) unperturbed stress state (b) perturbed stress state where no rotation of principal stresses occurs and (c) perturbed state of stress and corresponding stress rotation adjacent to the spherical salt body.....	98
Figure 8-8. Summary of procedure for creating 3D MEM and its applications.....	101
Figure 8-9. A MW window evaluated for different well architectures using Fast Wellbore Stability engine; yellow - shear limit; gray - pore pressure; bright blue - minimum horizontal stress; dark blue - tensile failure limit	102
Figure 8-10. Trajectory optimization workflow	103
Figure 9-1. The creep rate as a function of octahedral stress displayed together with threshold limits	111
Figure 9-2. Representation of (a) realistic GoM model containing a buried salt layer with appropriate porosity and density trends, and (b) the corresponding mud pressure P_1 and P_2 expressed as an EMW as expressed by Eq. (9.5) and (9.6) for (I) isotropic stress state and (II) anisotropic stress state ($\sigma_h = S_h = 0.8 \sigma_H$; $\sigma_H = S_H = 1.1 \sigma_v$; $\sigma_v = S_v$)	113
Figure 9-3. Typical well-construction problems encountered in thick salt sections	114
Figure 9-4. Sensitivity analysis of differential stress (left) and temperature (right) effects on creep closure for the given set of parameters	116
Figure 9-5. Projections on borehole closure of a well in GoM are shown for 10, 30, 60, and 90 days upon drilling activity	117
Figure 9-6. Creep rate of different salts as a function of MW	118
Figure 9-7. The effect of salt burial depth on the overburden gradient through salt	119
Figure 9-8. Effect of salt burial depth on MW/OBG ratio through salt	120
Figure 9-9. MW (12 ppg; 1440 kg/m ³) needed to retain Tachyhydrite layer below 5,08 cm (2 in) closure over the period of +500 hours for case a) 4502,5m TVD; ca. 60 °C and b) 5872,5m TVD; ca. 145 °C	121

Figure 9-10. The strain rate of the GoM salt sheet predicted from FEA.....	122
Figure 9-11. Temperature Profiles as a function of time and radial distance from the wellbore	124
Figure 10-1. Wellbore shock constraints on allowable wellbore pressure	126
Figure 10-2. Incorporating tolerance to breakout width into MW window construction.	128
Figure 10-3. Adjustment of acceptable MW range for RM	129
Figure 10-4. Example of MW window design in Deepwater GoM	131
Figure 10-5. Chart for typical Deepwater casing selection	132
Figure 10-6. Typical Deepwater production well with a dry tree configuration	134
Figure 10-7. Common casing designs for the Deepwater wells; (a) normal and (b) tight clearance	135
Figure 13-1. Wellbore trajectory optimization workflow.....	154
Figure 13-2. Possible salt-casing contacts	155
Figure 13-3. Proposed tubular solutions for varying creep rates.....	157

II. LIST OF TABLES

Table 5-1. Laboratory tests for determining rock`s strength and deformability properties	33
Table 7-1. General PPFG trends across the continental margin	73
Table 13-1. Advantages and drawbacks of different casing configurations to combat creep loading	158

III. NOMENCLATURE

$\dot{\epsilon}_D$ - dashpot strain rate; Maxwell`s Constitutive model [*dimensionless*]

$\dot{\epsilon}_s$ - spring strain rate; Maxwell`s Constitutive model [*dimensionless*]

$\dot{\epsilon}_0$ - reference strain rate; experimentally determined point [*dimensionless*]

C_0 - Cohesion [Pa]

σ_n - normal stress [Pa; psi]

$A\sigma_{\theta\theta}$ - amplitude of hoop stress variation around the wellbore wall [psi; Pa]

$\frac{D}{t}$ - External diameter to wall thickness ratio [*dimensionless*]

E_d - Dynamic Young`s modulus [psi; Pa]

I_i where $i=1, 2, 3$ - Stress invariants

J_i where $i=1, 2, 3$ - Deviatoric stress invariants

K_b - drained bulk modulus [psi; Pa]

K_g - rock`s solid grains bulk modulus [psi; Pa]

P_p - pore pressure [psi; Pa]

P_w - pressure exerted by mud [psi; Pa]

S_h - minimum horizontal far-field stress (also σ_h) [psi; Pa]

S_H - maximum horizontal far-field stress (also σ_H) [psi; Pa]

S_i where $i=1, 2, 3$ - Far-field principal stresses [Pa]

S_{ij} where $i, j=1, 2, 3$ - Far-field stress tensor [Pa]

S_o - unconfined compressive strength [Pa; psi]

S_v - total vertical (overburden) stress (also σ_v) [psi; Pa]

T_0 - experimental, reference temperature [$^{\circ}$ K]

T_b - formation temperature [$^{\circ}$ C]

T_m - Melting temperature [$^{\circ}$ k; $^{\circ}$ C]

T_w - mud temperature [$^{\circ}\text{C}$]

q_{ij} where $i, j=1, 2, 3$ (or x, y, z) - Deviatoric stress tensor [psi; Pa]

\mathbf{n}_j - unit normal vector

$\mathbf{t}_{(n)j}$ - traction vector

α_t - Thermal expansion coefficient [$^{\circ}\text{C}^{-1}$]

δ_{ij} - Kronecker delta symbol [*dimensionless*]

$\dot{\epsilon}$ - resultant strain from the (steady state) creep [*dimensionless*]

ϵ_{xx} - maximum (compressive) tectonic strain [*dimensionless*]

ϵ_{yy} - minimum (compressive) tectonic strain [*dimensionless*]

θ_c - azimuth of compressive failure [$^{\circ}$]

θ_t - azimuth of tensile failure [$^{\circ}$]

λ_i where $i=1, 2, 3$ - stress tensor eigenvalues [psi; Pa]

μ_i - coefficient of internal friction [*dimensionless*]

ν_d - Dynamic Poisson`s ratio [*dimensionless*]

$\bar{\sigma}$ - mean stress [psi; Pa]

σ_0 - reference effective stress experimentally determined point [psi; Pa]

σ_h - minimum horizontal effective stress [psi; Pa]

σ_H - maximum horizontal effective stress [psi; Pa]

σ_i where $i=1, 2, 3$ - principal effective stress [psi; Pa]

σ_{tmax} - maximum effective stresses acting in the plane tangential to the wellbore [psi; Pa]

σ_{tmin} - minimum effective stresses acting in the plane tangential to the wellbore [psi; Pa]

$\sigma_{\Delta T}$ - thermal stress [psi; Pa]

σ_{T0} - rock` tensile strength [psi; Pa]

σ_e - Equivalent multiaxial stress [psi; Pa]

$\sigma_{elastic}$ - elastic stress component; Maxwell's Constitutive model [psi; Pa]

σ_i where $i=1, 2, 3$ - principal stress [Pa; psi]

σ_{ij} where $i, j=1, 2, 3$ (or x, y, z) - Effective stress tensor [psi; Pa]

σ_{ij} where $i, j=1, 2, 3$ (or x, y, z) - Stress tensor [Pa]

σ_o - octahedral stress [psi; Pa]

σ_{rr} - stress in radial direction [psi; Pa]

$\sigma_{viscous}$ - viscous stress component; Maxwell's Constitutive model [psi; Pa]

σ_y - Yield strength [psi; Pa]

$\sigma_{\theta\theta}$ - Tangential (also hoop or circumferential) stress [psi; Pa]

τ_o - octahedral stress [psi; Pa]

τ_{oe} - octahedral shear stress limit for elastic behavior [psi; Pa]

τ_{omax} - maximum value of octahedral stress at the wellbore wall [psi; Pa]

τ_{op} - octahedral shear stress for indefinite plastic flow [psi; Pa]

ϵ_{ijk} - Levi-Civita symbol [*dimensionless*]

ΔT - Temperature difference [$^{\circ}\text{C}$]

λ - ratio of pore pressure to lithostatic stress [*dimensionless*]

E - Young's modulus (also Modulus of elasticity) [psi; Pa]

K - effective stress ratio [*dimensionless*]

Q - Activation energy [J/mol]

R - Universal gas constant; 8.31446 [J/(Kmol)]

R - wellbore radius [ft; m]

T - the rock (specimen) temperature [$^{\circ}\text{K}$]

n - experimental stress coefficient [*dimensionless*]

r - radial coordinate measured from the wellbore center [ft; m]

t - time [s]

ΔP - differential pressure across the wellbore wall [psi; Pa]

$\Delta\sigma$ - differential stress [psi; Pa]

α - Biot's coefficient [dimensionless]

β - angle between normal to the fracture plane and vertical; analogously the angle at which rock specimen fractures [°]

δ - wellbore azimuth [°]

η - Dynamic viscosity [Pa s]

θ - angle between the azimuth of S_H along the wellbore [°]

ν - Poisson's ratio [*dimensionless*]

τ - shear stress [psi; Pa]

φ - Internal friction angle [*dimensionless*]

ω - initial inclination of the fracture trace at the wall of deviated wellbore wall with respect to the wellbore centreline [°]

ϕ - wellbore inclination [°]

IV. LIST OF ABBREVIATIONS

AoA - Angle Of Attack

AP - Abnormal Pressure

H₂S - Hydrogen Sulfide

APB - Annulus Pressure Buildup

BHA - Bottomhole Assembly

BML - Below Mudline

BOE - Barrels of Oil Equivalent

BOP - Blow-Out Preventer

DCM - Deepwater Continental Margin

DoD - Depth of Damage

DLS - Dogleg Severity

DM creep model - Double-mechanism creep model

DwC- Drilling with Casing

ECD - Equivalent Circulating Density

EMW - Equivalent Mud Weight

FADC - Fluid Assisted Difussional Creep

FEM - Finite Element Method

FPSO - Floating Production Storage and Offloading

GoM - Gulf of Mexico

HCRC - High Collapse Resistant Casing

HPWHH - High Pressure Wellhead Housing

HWC - Heavy-walled Casing

KOP - Kick-Off Point

KT - Kick Tolerance

LOT - Leak-Off Test

LPWHH - Low Pressure Wellhead Housing

LWD - Logging While Drilling

M-C - Mohr-Coulomb

MD creep model - Munson and Dawson (also Multi-mechanism Deformation) creep model

MEM - Mechanical Earth Model

MPD - Managed Pressure Drilling

MSL - Mean Sea Level

MW - Mud Weight

MWD - Measurement While Drilling

NF - Normal Faulting

NPT - Non-Productive Time

O&G - Oil and Gas

OBG - Overburden Gradient

PPFG - Pore Pressure Fracture Gradient

PWD - Pressure While Drilling

RF - Reverse Faulting

RIH - Running In Hole

POOH - Pulling Out of Hole

ROP - Rate of Penetration

SCOW - Salt Creep Operational Window

SF - Shear Failure

SS - Strike-Slip

SSSV - Subsurface Safety Valve

ST - Sidetrack

T&D - Torque and Drag

TVD - True Vertical Depth

UCS - Unconfined Compressive Strength (also Uniaxial Compressive Strength)

UTS - Unconfined Tensile Strength (also Uniaxial Tensile Strength)

TOAP - Top Of Abnormal Pressure

VME Stress - Von Mises Equivalent Stress

WOW - Wait On Weather

XLOT - Extended Leak-Off Test

YP - Yield Point

1. INTRODUCTION

“From Spindletop to Ghawar, Tupi to Thunder Horse, oil and gas fields formed or sealed by evaporites include some of the most significant discoveries made in the history of the petroleum industry” (Jackson and Hudec, 2017). The massive salt formations have no porosity or permeability, properties pertinent to good cap rocks, and move rapidly in the subsurface on geologic time scales. Due to their properties, evaporites can trap large hydrocarbon volumes under very high pressures and temperatures while maintaining excellent sealing abilities¹. Due to the wide range of salt structures encountered underground and the range of deformational styles, practically all known types of hydrocarbon traps occur in conjunction with salt structures (van Oort, 2004; Jackson and Hudec, 2017). Yet, in 1979, Halbouty apud Barker and Meeks (2003) argued that 80% of proven US Gulf coast basin reserves are likely related to salt structures. As per Warren (2006), evaporites seal fourteen of the world's twenty-five largest oil fields and nine of the world's twenty-five largest gas fields.

Deepwater hydrocarbon-bearing formations underlying salt massive salt bodies have been established as commercial reserves in Brazil, Gulf of Mexico (GoM), North Sea, Gabon basin, North Africa, Gulf of Suez, Offshore Nova Scotia, and many more (Pratsch, 1995; Arbouille et al., 2013; Zhang et al., 2019). A typical Deepwater well can exceed depth of 9144 m (30 000 ft) below the mean sea level (MSL) in depths of approximately 1829 m (6 000 ft). Considering the 7315 m (24,000 ft) of total formation drilled, a typical salt section whose thickness easily exceeds 3048 m (10000 ft) can account for more than half of the length of the well drilled (Omojuwa et al., 2011). While from the exploration point of view, properties of salt may seem like appealing structures for hydrocarbon accumulation, it poses significant challenges for the operators in terms of seismic interpretation, well planning and construction, and well integrity (van Oort, 2004; Dusseault et al., 2004b; Wilson and Fredrich, 2005; Israel et al., 2008; Omojuwa et al., 2010, Castagnoli et al., 2016; Alfayyadh et al., 2020). Offshore wells drilled in salt formations can be divided into two groups, based on the formation they target: subsalt and presalt. Subsalt wells target formations deposited before the emplacement of the salt that remains at its original stratigraphic level

¹ First, as a crystalline solid, salt poses very low porosity and permeability. Second, intrinsically low permeability is difficult to modify by shear since salt tends to relax on a geologic timescale. Moreover, low permeabilities are difficult to modify by dilatational fractures as salt ductile flow is non-dilatant. Finally, salt tends to anneal after deformation, restoring the salt to its original sealing condition through creep (Jackson and Hudec, 2017).

(autochthonous or motherly salt). By contrast, subsalt wells are drilled into formations lying beneath mobile canopies of allochthonous salt. The term "allochthonous" stands for the salt masses, connected or disconnected from the original autochthonous layer, that rise through overlying layers and spread laterally (refer to figure 1-1a.) (Beasley et al., 2010). Allochthonous evaporites occur in more than thirty-five basins worldwide, with many of them found offshore (e.g., Offshore Brazil, GoM, North Sea, offshore Arabian Peninsula, offshore Nova Scotia (Jackson and Hudec, 2017) (refer to figure 1-1b.).

Although offshore salt plays were suspected in the 1960s (Beasley et al., 2010), the commercial development was not of interest since the industry preferred to explore elsewhere rather than establish the reserve potential in these challenging petroleum systems (Pratsch, 1995). However, amid the 1980s, operators, encouraged by exploration success in Brazil (Beasley et al., 2010), commenced exploring formations lying below salt in GoM. Then, with Exxon's Mica Prospect subsalt discovery in 1990, extensive exploration started in GoM subsalt environment. Soon afterward, the industry found its way to subsalt exploration, which resulted in numerous discoveries over 20 years (Cromb et al., 2000; Dribus et al., 2008). The list of notable subsalt discoveries in GoM (figure 1-2.) was compiled by Dribus et al. (2008). As seen from figure 1-2., the search for hydrocarbons around salt pushed the operators progressively to Ultradeep waters².

² The concept of Deepwater has evolved over the years. Deepwater was originally defined as areas with water depth exceeding 200 m (656 ft). This mark was later eclipsed by industry drilling trends, and now the Deepwater standard is set at 305 m (1000 ft). Water depths greater than 1,524 m(5000 ft) are deemed to be Ultradeep (Beasley et al., 2010)

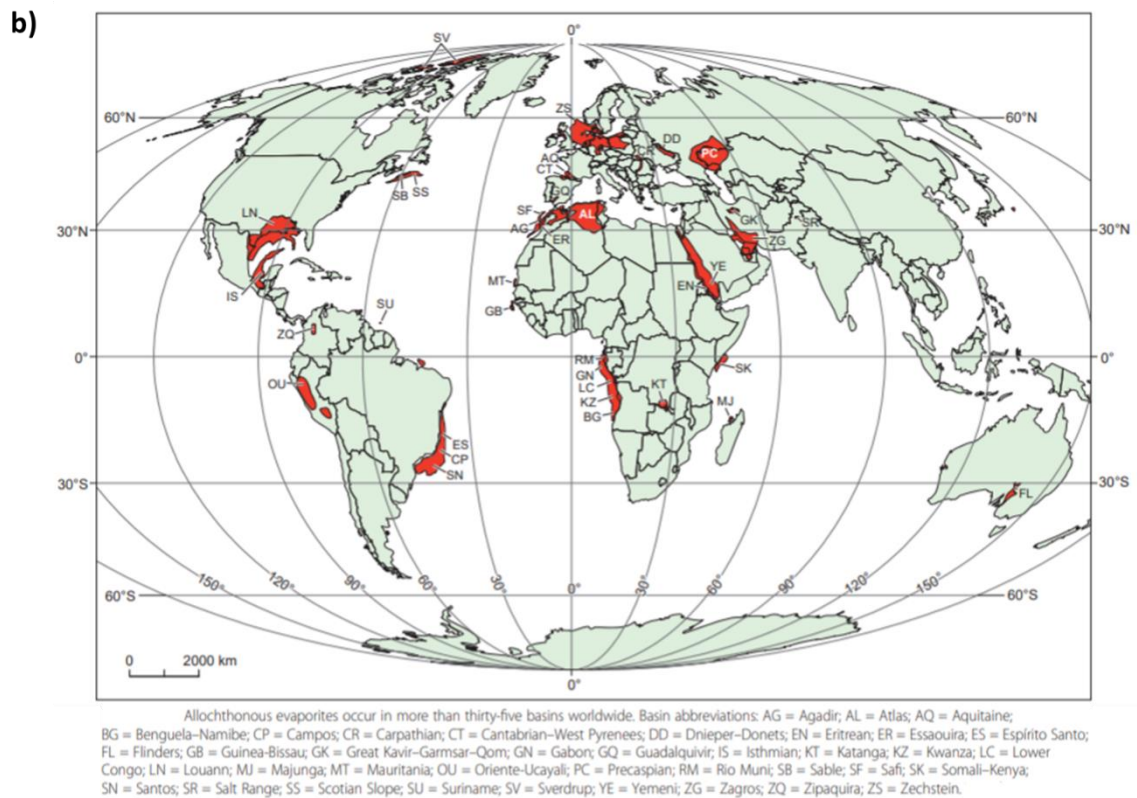
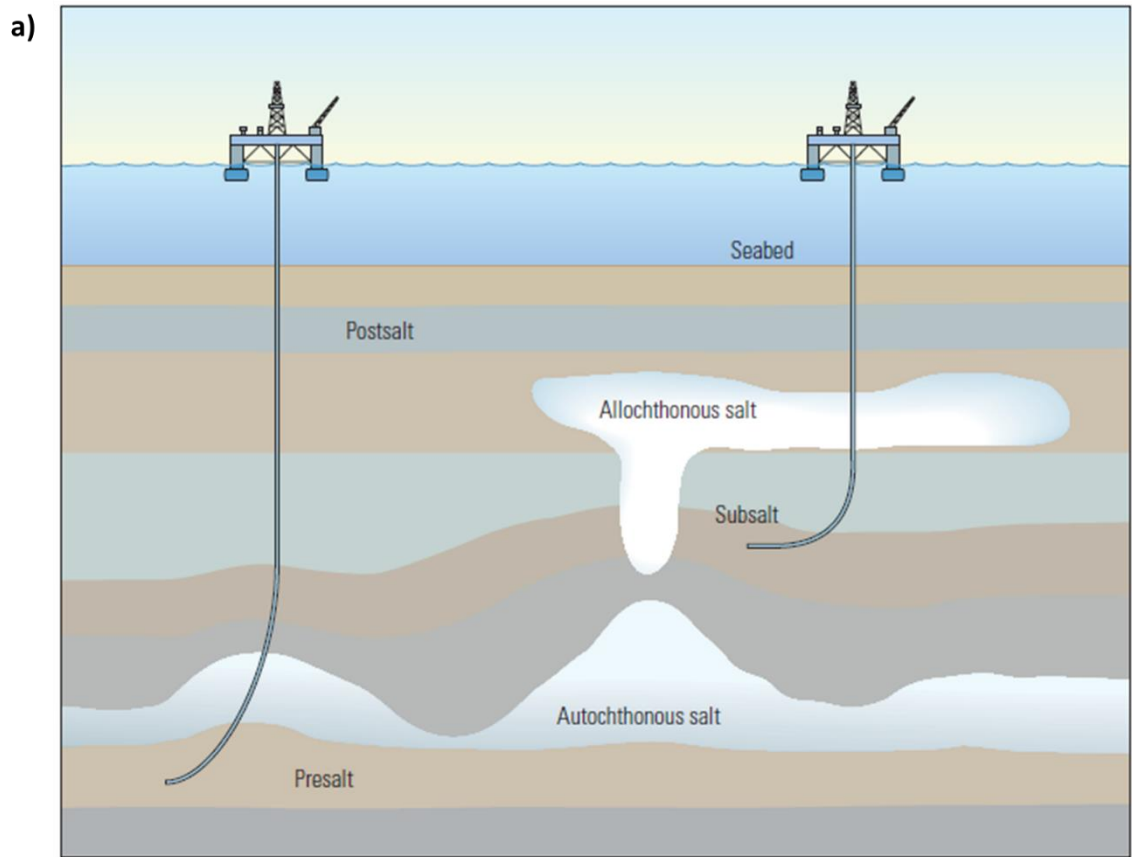


Figure 1-1. Schematic representation of (a) Allochthonous and Autochthonous salt (Beasley et al., 2010) and (b) map of worldwide basins containing Allochthonous evaporites (modified from Jackson and Hudec, 2017)

During the last 15 years, exploration focus started leaning towards Pre-salt as breakthroughs have been made in Tupi offshore Brazil and Kwanza Basin offshore central West Africa (Zhang et al., 2019). Even though the subsalt and presalt discoveries combined have resulted in significant reserves across different parts of the globe (see Dribus et al., 2008; Beasley et al., 2010; Arbouille et al., 2013), only a fraction of potential in Deepwater and Ultra-Deepwater has been tapped so far. According to Arbouille et al. (2013) yet to find reserves are approximated around 50 000 MM BOE.

Protraction Area	Block Number	Total Depth		Water Depth		Year Drilled	Field Name	Remarks
		feet	meters	feet	meters			
Ship Shoal	366	8,203	2,500	453	138	1983	—	Dry hole. Targeted a direct hydrocarbon indicator (DHI); drilled through salt.
South Marsh Island	200	13,500	4,115	475	145	1986	—	Dry hole. DHI target proved to be salt; however, 1,000 ft [305 m] of wet, reservoir-quality sand lay beneath it.
Mississippi Canyon	211	12,763	3,890	4,356	1,328	1990	Mica	First significant occurrence of hydrocarbons in five thin pay zones beneath salt.
Ship Shoal	349	16,563	5,048	372	113	1993	Mahogany	Put on line before Mica. Became the first commercial development in the Gulf of Mexico subsalt play.
Garden Banks	128	18,454	5,625	705	215	1994	Enchilada	Salt weld discovery.
Garden Banks	127	14,730	4,490	630	192	1995	Chimichanga	Second commercial subsalt discovery; drilled 1,300 ft [396 m] of salt, tested at 2,100 bbl/d [334 m ³ /d] of oil and 20 MMcf/d [566,337 m ³ /d] of gas.
Mississippi Canyon	292	17,976	5,479	3,405	1,038	1995	Gemini	Third commercial discovery of the play, in Pliocene-Miocene sands.
Green Canyon	699	19,525	5,951	6,133	1,869	1998	Atlantis	Deepest moored floating oil and gas production facility in the world and also one of the largest.
Grand Isle	116	21,600	6,584	323	98	1998	Hickory	Penetrated 8,000 ft [2,438 m] of salt.
Eugene Island	346	11,833	3,607	314	96	1998	Tanzanite	First well tested 1,917 bbl/d [305 m ³ /d] of oil and 29.7 MMcf/d [841,100 m ³ /d] of gas, one of the highest rates in the shallow-water Gulf of Mexico.
Mississippi Canyon	778	23,531	7,172	6,050	1,844	1999	Thunder Horse	Largest field in the Gulf of Mexico.
Garden Banks	783	16,867	5,141	4,668	1,423	1999	Magnolia	Tension leg platform (TLP) installed in record water depth for TLPs.
Green Canyon	562	25,624	7,810	3,979	1,213	1999	K2	Drilled through 10,000-ft [3,048-m] salt canopy of the Miocene fold trend.
Green Canyon	782	22,826	6,957	4,420	1,347	2001	Mad Dog	300 ft [91 m] of net pay discovered in Mississippi Fan fold belt.
Garden Banks	877	23,500	7,163	5,300	1,615	2001	Redhawk	Produced from the world's first truss spar facility.
Green Canyon	640	26,804	8,170	4,017	1,224	2002	Tahiti	Middle Miocene trap beneath 11,000-ft [3,353-m] salt canopy.
Walker Ridge	678	29,066	8,859	7,036	2,145	2003	St. Malo	First subsalt well of the Wilcox trend, drilled through 10,000 ft [3,048 m] of Sigsbee salt canopy, with 450 ft [137 m] of net pay.
Walker Ridge	759	28,175	8,588	6,850	2,088	2004	Jack	Wilcox test: deepest extended drillstem test in deepwater Gulf of Mexico history.
Keathley Canyon	292	32,500	9,906	5,860	1,786	2006	Kaskida	First Wilcox subsalt wildcat located significantly inboard of the Sigsbee Escarpment, northern frontier of Wilcox prospects. Found 800 ft [244 m] of net pay.
Green Canyon	726	25,680	7,827	4,700	1,433	2007	West Tonga	Discovered 350 ft [107 m] of net oil in three Miocene sands.

Figure 1-2. Tabulated representation of the most notable discoveries in GoM (Dribus et al., 2008)

Although upstream investment has declined sharply over the past years, aggravated by an unanticipated pandemic, ongoing demand for Oil and Gas (O&G) will necessitate an increase in the near future to prevent market disruptions at a time when demand is set to recover (see McMonigle et al., 2020; Khasawneh et al., 2021). According to McKinsey (Yanosek and Rogers, 2018), roughly 36 MBOE/day of new crude production from unsanctioned projects will be needed to meet the growing demand. Authors expect Deepwater prospects to play an essential part in the future O&G supply, accounting for more than a third of projected supply (see figure 1-3.). Here, Brazil and GoM are expected to contribute almost 50% to the new Deepwater production supply for 2030. Similarly, Zhang

et al. (2019) exemplify a pre-salt as one of the main exploration frontiers expected to see further interest in the upcoming decades. Given the challenged greenfield project economics in Deepwater and Ultra-Deepwater, operators are urged to increase competitiveness. Here, integral to successful economic development is a well service lifetime of 15-30 years, where costs of drilling such deepwater wells can be more than triple those of shallow-water wells (Fredrich et al., 2003). However, the ongoing global pandemic and the acceleration of the energy transition push operators to adjust to less favorable economic margins and prioritize investments with a high rate of returns over a shorter period. The reason for that is in the complex salt tectonics, which, when coupled with the deep waters and reservoirs, incurs substantially high development costs while requiring innovative technology to bring these fields on stream. At the same time, challenges with abnormal and uncertain formation pressures exist both in the overburden and the reservoir, thus requiring a better understanding of geomechanical properties, stress regimes, downhole pressures, and wellbore hazards (Schlumberger, 2014).

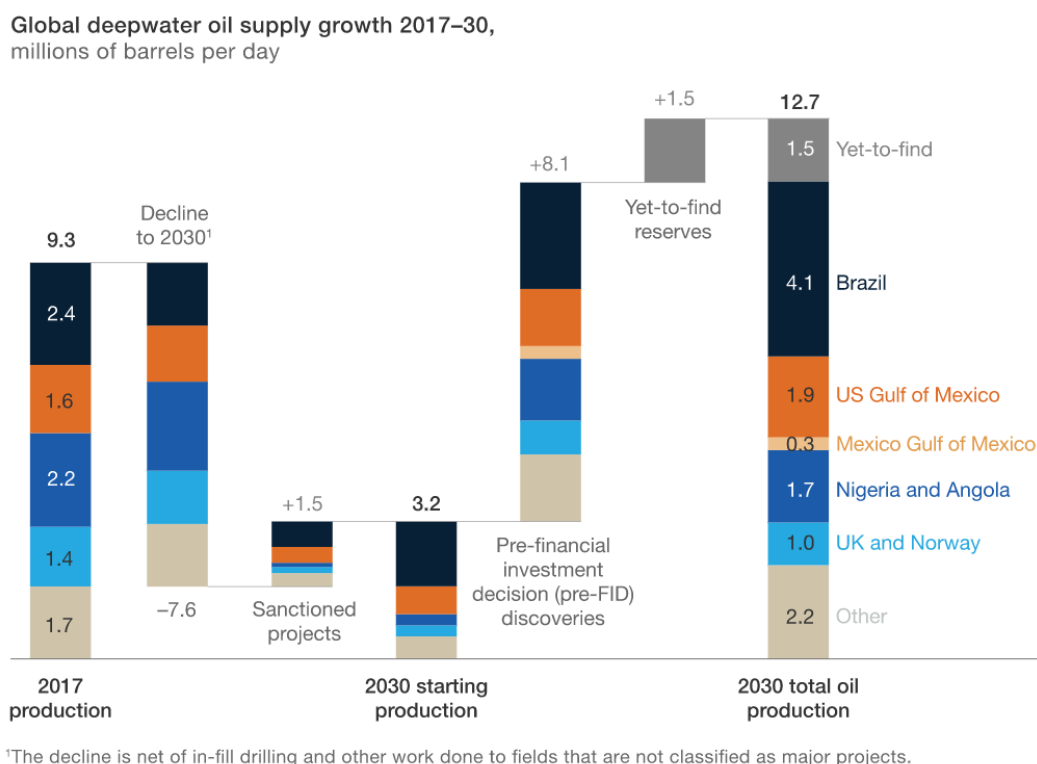


Figure 1-3. Global oil supply growth in the period from 2017-2030 (Yanosek and Rogers, 2018)

Nevertheless, given the success rate of Deepwater exploration wells ranging around 60% to 70%, the Deepwater environment remains more lucrative for further investments, especially

when compared to Ultra-Deepwater where this rate drops to rather 40 to 50%; not to mention more challenging and expensive operating conditions encountered in Ultra-Deepwater (Yanosek and Rogers, 2018).

In addition, the costs of Ultra-Deepwater wells often contribute to limiting the offset well information to constrain the subsurface interpretations adequately. However, massive salt bodies can be lucrative investment-wise, even in mature exploration areas. Namely, salt trapping mechanisms and a variety of traps found around salt bodies can provide means of improving returns in the mature subsalt fields. Furthermore, with a focus on developing existing but untapped reserves, already present infrastructure opens the possibility of tieback development around massive salt bodies. As a result, shorter development cycles and accelerated cash flows are obtained (Seymour et al., 1993; van Oort, 2004; Yanosek and Rogers, 2018). However, due to high drilling costs in Deepwater, even for development wells, infill drilling and exploration from existing facilities to access satellite reserves costs must be economically constrained. Otherwise, these smaller hydrocarbon accumulations may not be financially viable. Again, technical investment in the pre-planning and drilling phases of the development well is essential to maximize profitability (Wilson et al., 2003).

2. PROBLEM SELECTION AND HYPOTHESIS

Exploration around the salt bodies has always been challenging for well planning and construction due to their geological complexity, which, in turn, yields highly uncertain drilling windows. Undoubtedly, a large opportunity exists for the O&G industry in offshore salt plays. However, to navigate narrow economic margins, risks associated with the well construction challenges must be addressed proactively during the well design phase. With the placement of wells in a deep and complex offshore environment found around massive salts, the wellbore stability becomes an all-important element for meeting well construction objectives. To facilitate the planning and drilling of wells in such a difficult and potentially very expensive environment, in-situ conditions around salt bodies must be accurately estimated. Moreover, knowledge of pore pressure (PP) and fracture gradient (FG) is crucial for constructing an accurate drilling window and providing input data for casing design. Since the abnormal pressures (AP) and very tight drilling margins are likely to exist around salt bodies, precise determination of pressure gradients comes as imperative for the well design in and around salt bodies. A statement is made that a standalone approach to well design is inadequate and can easily result in well failures that can make field development economically inviable. As opting for standalone trajectory design may be counter-intuitive to overall well economics, one shall consider the presence of multiple factors affecting the overall well design:

- geomechanical instabilities and abnormal pore pressures around the salt bodies reduce drillability and increase overall well construction risks; Lost circulation (LC), Well Control Incidents (WCI), etc.
- unfavorable temperature and/or overburden distributions that aggravate salt creep,
- trajectory-specific drilling problems such as Torque and Drag (T&D), drilling vibrations, poor deviation control; all of which impact overall well construction economics.

Thus, a holistic, multidimensional approach to well placement is required, such that all the specific risks peculiar to the offshore salt environment are well understood and evaluated. Finding techno-economically the most appropriate solution shall enable operators to capture additional value from the well construction while improving returns, decreasing risks, and enhancing operational safety in offshore salt plays.

This Thesis will cover pore and fracture pressure trends pertinent to offshore salt plays. The reader will be familiarized with the rock mechanics principles necessary to assess favorable

drilling conditions and offshore well placement in salt plays. Furthermore, the implications of salt-induced stress state disturbances on well placement will be explained in detail. In conclusion, the Thesis shall provide a deep insight into offshore well design practices worldwide. Integrating lessons learned over the years of offshore sub/pre-salt development, the author will put emphasis on wellpath optimization and well planning guidelines that ensure the well long-term value creation in Deepwater.

3. SALT PROPERTIES

3.1. Basic salt properties

Salt deposits are formed from the gradual evaporation and ultimate desiccation of enclosed saline water bodies (Wilson and Fredrich, 2005; Jackson and Hudec, 2017). With the increased burial depth, the salt is subjected to stress and continues to compact, displacing brine until the porosity becomes entirely occluded. If the temperature and the stress conditions are high enough, the brine-filled porosity of 0,3 to 1,5% can be achieved. The remaining porosity consists of thin, dendritic voids at the grain boundaries (Dusseault et al., 2004b). Similarly, the permeability of intact salt is usually at the scale of 10^{-21} m². Hence, it may be expected that flow through salt only occurs in non-salt lithologies around the salt body or within the non-salt inclusions at the time scale relevant to well-engineering (Jackson and Hudec, 2017). The mineralogical composition of natural rock salts varies from very homogeneous (99% halite) to heterogeneous mineral associations. Based on their chemical composition, the most common salts and minerals associated with salt deposits are characterized as follows (van Oort, 2004):

- Sodium salts - halite (NaCl),
- Potassium salts - sylvite, carnallite, polyhalite,
- Sulphates - gypsum, anhydrite (and less known langbeinite, kieserite, epsomite, kainite),
- Chlorides - bischofite and tachyhydrite.

Urai et al. (2008) compiled the list of the main evaporite minerals and their associated wireline log properties. In drilling applications, halite is the most frequently encountered salt. However, pure halite commonly contains additional minerals, notably anhydrite, gypsum, and clay minerals (Fossen, 2010). For instance, in GoM, salt deposits are primarily constituted from a massive halite deposit with averaging purity of 96% with some occasionally trapped sediment inclusions (impurities). Depending on its purity, the in-situ salt density for a very pure salt is 2,16 g/cm³ (Barker et al.,1994). The salt density is a function of its composition and impurities, where the density of impure salt is slightly higher than pure salt (Fossen, 2010). Salts with a high proportion of clay impurities and where shale interbedding occurs are often referred to as "dirty salts" that may impose the risk of wellbore instability and tight hole conditions (Wilson and Fredrich, 2005).

3.2. Salt strength

Although there is little published information about sub/pre-salt formations' strength, the limited data indicates an unconfined compressive strength (UCS) to range from 20.68 to 24.13 MPa (3000 to 3500 psi) (Wilson and Fredrich, 2005). Likewise, the same group of authors reported that the tensile strength of approximately one-twelfth of the unconfined strength was observed. In the case of polymineralic salt (non-single salt component), its strength will fall in between the strengths of their weak and strong constituents, following nonlinear proportionality between the strength values of these minerals. Therefore, proper laboratory testing is required to characterize salt strength (Jackson and Hudec, 2017).

3.3. Salt solubility

Salt deposits are typically non-radioactive, electrically nonconductive, and soluble (Tixier and Alger, 1970). Their solubility is dependent on the constitutive minerals and the liquid that may dissolve these minerals. Different salt formations have relative differences in their water solubility due to their varying compositions. Van Oort (2004) provided an overview of the solubility of common salt minerals. In essence, the anhydrite and gypsum have low solubility, decreasing with increasing temperature. On the contrary, the squeezing salts show high solubility that increases with temperature. This behavior has a detrimental impact on wellbore quality during drilling long, open intervals. The wellbore diameter can be enlarged due to the salt dissolution and mud flushing if the rheological properties of mud and wellbore hydraulics are not managed adequately.

3.4. Salt thermal properties

The salt poses high thermal conductivity due to which temperature distributions around the salt body will be perturbed from the far-field conditions (Dusseault et al., 2004a, b; Poiate et al., 2006; Meier et al., 2015; Jackson and Hudec, 2017). In the case of a simple, horizontal lying sheet, formations above the salt body will be heated due to heat flux across the salt sheet, whereas underlying formations are correspondingly cooled. Likewise, the thicker the salt layer is, the more pronounced the temperature change. Situations become more complex around the piercing and bulbous structures where temperature perturbation strongly depends on the diapir shape, dimensions, and connectivity to the source layer (Mello et al., 1995; Jackson and Hudec, 2017). The diapir-related temperature disturbances are much more spatially restricted than changes across continuous horizontal salt layers (Mello et al., 1995; Meier et al., 2015; Pardo, 2016). This topic is well beyond the Thesis` scope; however, the

author found it important to mention because the presence of thick salt sheets or rising diapirs will perturb the surrounding temperature, making a linear extrapolation of a temperature gradient from offset well data invalid (Poiate et al., 2006; Pardo, 2016). The representation is given in figure 3-1. Due to implications to salt creep, temperature distribution around the salt body shall be considered.

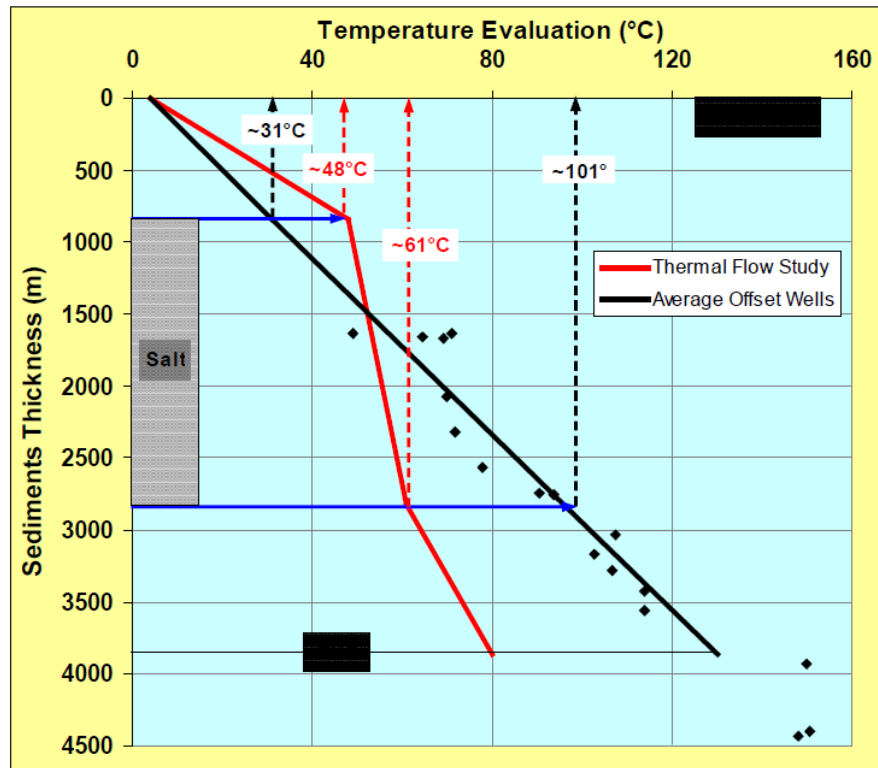


Figure 3-1. Comparison of thermal gradient projections using numerical (thermal flow study) and linear regression from offset well data (Poiate et al., 2006)

4. FLOWING NATURE OF SALT

Most rocks for petroleum engineering applications can be characterized as elastoplastic solids. However, materials with uncemented grains, like loose sands, immature shales, and salt do not behave elastically. These materials exhibit rheological behavior and undergo time-dependent processes such as creep (increasing strain under constant stress) and relaxation (decreasing stress under constant strain) (Vallejo and Ferrer, 2011; Zoback, 2007). These two processes are shown in figure 4-1. Creep is defined as the gradual flow³ of a crystalline material under a deviatoric load, which results in permanent distortion (see chapter 4.2.). Because of that, such materials can even fail under constant, maintained, long-term load or strain conditions (Jackson and Hudec, 2017; Vallejo and Ferrer, 2011). Salt is a specific engineering material with a pertinent behavior, unlike other materials such as consolidated rocks or metals. Due to their ductile characteristics, salts have a limited linear stress-strain curve extending over a small stress increment. At stress levels as low as 10 to 20% of its ultimate strength salt starts deforming plastically. Its stress-strain curve is very dependent on temperature, confining pressures, salt composition, water content, impurities, prior stress history, loading rate, etc. (Barker and Meeks, 2003).

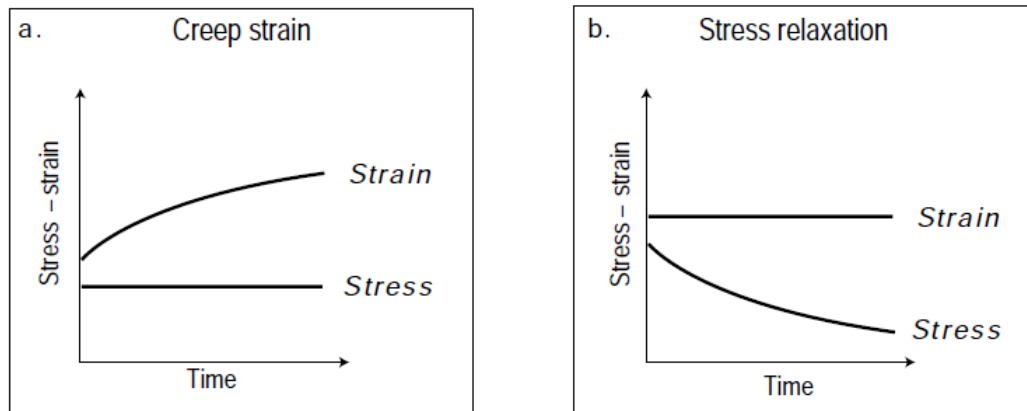


Figure 4-1. Mechanisms of (a) creep strain and (b) stress relaxation (Zoback, 2007)

4.1. Salt morphology

Usually, materials susceptible to creep exhibit brittle failure and behave similarly to consolidated rocks at room temperature and under compression. However, they lose their brittleness at rather low-stress levels under triaxial compression, while failure does not occur

³ Here, flow refers to permanent deformation without permanent loss of cohesion (Jackson and Hudec, 2017).

in shear but rather through creep (Infante and Chenevert, 1989)⁴. For example, salt poses a high fracture strength (ca. 24 MPa) at the surface conditions compared to unconsolidated sediments that are weaker at/near the surface (100-1000 m). That changes with increasing the burial depth. As siliciclastic sediments are being buried, they compact and undergo diagenesis as they lithify to sedimentary rocks. That makes them increasingly stronger than salt, which in contrast, weaken slightly as burial depth and temperature increase. The strength profile of deeply buried salt can be summarized as a linearly increasing, confining pressure-sensitive downward through the overburden, a drop to constant, near-zero strength level within the salt layer, and a resumption with abruptly increasing trend in subsalt formations (Jackson and Hudec, 2017). This is summarized in figure 4-2. So, with the qualifications of long duration, large size, and burial, rock salt is weaker than most surrounding sedimentary rocks.

Salt can be seen as virtually incompressible fluid at confining pressures relevant to salt tectonics since its density change is almost constant with increasing confining pressure (0.7% increase in density at 10 km depth relative to the density at ambient conditions) (Jackson and Hudec, 2017). As a constant-density salt layer is underlying sedimentary rocks, the density inversion phenomenon causes compacting overburden to become denser than the salt, thus creating gravitationally unstable conditions that can promote salt flow toward the surface (Fossen, 2010).

⁴ Note that there will be a depth specific to each rock at which, due to elevated confinement, brittle failure mode vanishes (so-called depth of brittle-ductile transition). In the case of salt, the transition occurs at or near the surface (Jackson and Hudec, 2017).

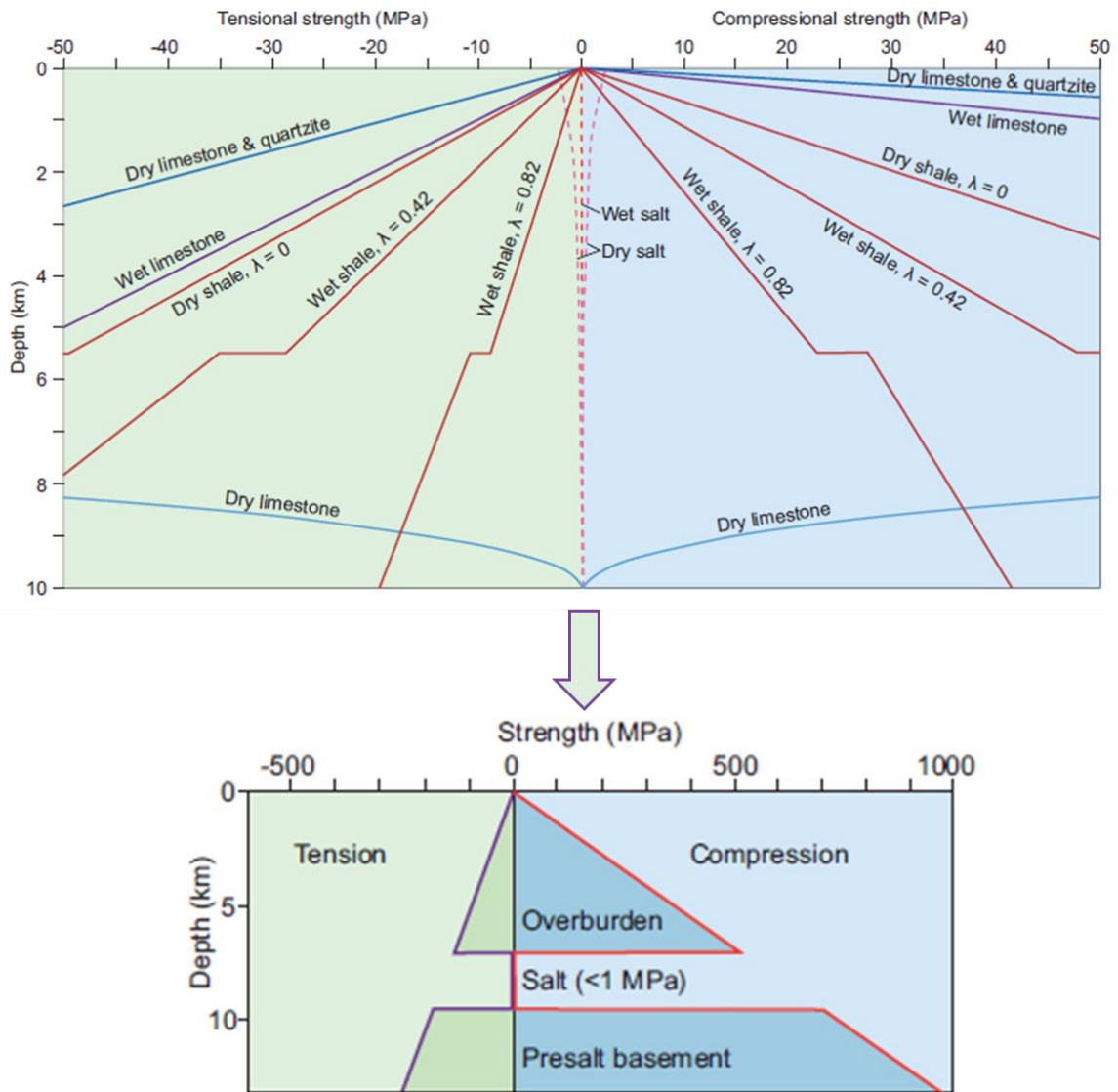


Figure 4-2. The strength profile of deeply buried salt, λ is the ratio of pore pressure to a lithostatic pressure (modified from Jackson and Hudec, 2017).

Salt volumes present in the Earth's crust take a variety of geometric shapes, from elongated structures such as salt anticlines and salt pillows to more localized structures such as salt stocks. However, most of these structures represent various stages that could lead to or result from the diapirism, i.e., forming a true diapir (Fossen, 2010). Salt diapirs can take on various forms based on the maturity of the diapirism process (figure 4-3.). For example, they may be elongated stocks displaying along a particular direction (salt walls), circular, bulbous bodies (domes), vertical plug-like shapes (salt stocks). Moreover, sometimes salt can be detached from its source, forming isolated salt bulbs (so-called teardrop diapirs). On the

other extreme, salt bodies can also flatten out and coalesce on one or several stratigraphic levels, thus forming various types of salt canopies⁵ (Fossen, 2010).

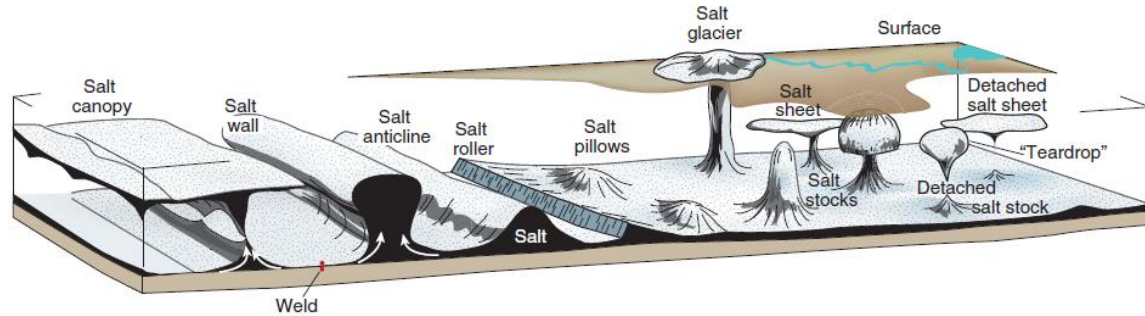


Figure 4-3. Evolution of salt structures in the subsurface (Fossen, 2010)

4.1.1. Salt diapirs

1. Full-scale diapirs and salt tongues are associated with crustal extensional regimes. Extensional regimes can be horst-graben structures (e.g., Zechstein salt in the North Sea) or open-to-the-sea passive continental margins such as the subsalt prospects in Nova Scotia, West Africa, or GoM. Although less common, diapirism can be found in strike-slip regimes as well (Dusseault et al., 2004b). The driving force for diapirism is self-reinforcing stress imbalance. The driving force arises from the overburden-caused perturbations in the source salt, and it is maintained by salt buoyancy resulting from density contrast between salt and surrounding sediments. Salt flow viscously as force imbalance is sustained by continued sedimentation, stress transmission from depth upward through the salt, and erosion removal of the overlying strata (Dusseault et al., 2004b, Nikolinakou et al., 2013a). As long as imbalance exists, salt creeps, distorts the overlying rocks, and pierces through them. Once frictional forces in surrounding rocks become sufficient to sustain the imbalanced buoyancy forces, vertical extension is halted, and salt may or may not continue to propagate laterally (Nikolinakou et al., 2015; Jackson and Hudec, 2017). Vertical propagation of rising diapir is likely to be controlled by lateral stress magnitudes. In extensional regimes with isotropic horizontal stresses, generated gravitational instabilities cause roughly circular salt domes. On the contrary, in the presence of a strongly anisotropic horizontal stress state salt structures elongate in

⁵ The Sigsbee salt canopy in GoM the largest known salt structure on Earth which comprises more than 100 salt sheets and stocks that have coalesced over the time. This structure covers more than 137,000 km² on the lower continental slope of the northern GoM and as such is one of the most interesting areas for O&G exploration worldwide (Jackson and Hudec, 2017).

a direction normal to the minimum horizontal stress. In areas of the regional contraction, most of the large-scale diapir structures had been probably initiated during extension and accordingly amplified or reworked in contraction afterward. Here existing salt diapirs represent rather weak elements that preferentially deform or squeeze under contraction (Dusseault et al., 2004b; Fossen, 2010).

4.1.2. Salt sheets

Similarly, contraction can squeeze diapirs and push them to the surface (salt glaciers) or between stratigraphic units (salt sheets) where they can extrude and overlay younger and stratigraphically higher sediments; hence they are also referred to as salt nappes. Although a variety of non-ideal salt geometries exist underground, simplification-wise a salt body with an aspect ratio larger than 5 is referred to as a salt sheet (Fossen, 2010). However, note that the existence of salt sheets is not necessarily constrained to compressional regimes. In compressional regimes surrounding rocks tend to conform to the salt shape due to the higher lateral stresses denser and much more competent rocks than found in extensional regimes (Dusseault et al., 2004b).

4.2. Salt behavior

Creep is the rock deformation caused by the dissipation of strain energy generated by the stress relief in an undisturbed salt rock mass (Wang and Samuel, 2013). Salt rocks creep when subjected to distortional or deviatoric stress inherent in the salt formations. Ergo, the creep strength of salt is the deviatoric stress required to drive salt flow. Salt creep strength is inversely proportional to the deformation rate and the temperature, i.e., the lower is the deviatoric stress needed to initiate salt creep. Figure 4-4. corroborates this premise. Moreover, wet salt (salt with traces of water (4-45 ppm)) is orders of magnitude weaker than dry salt and far weaker than the sedimentary rocks encasing it (Jackson and Hudec, 2017). Therefore, when compared with other sedimentary rocks that increase in (fracture) strength with depth, salt becomes weaker (due to an increase in temperature with depth) and thus more susceptible to flow under the same differential pressure. Moreover, as Young's modulus increases only slightly with increasing confining pressure (by 3% at a burial depth of 10 km), the stiffness of rock salt shows weak dependence on burial depth (Senseny et al., 1992).

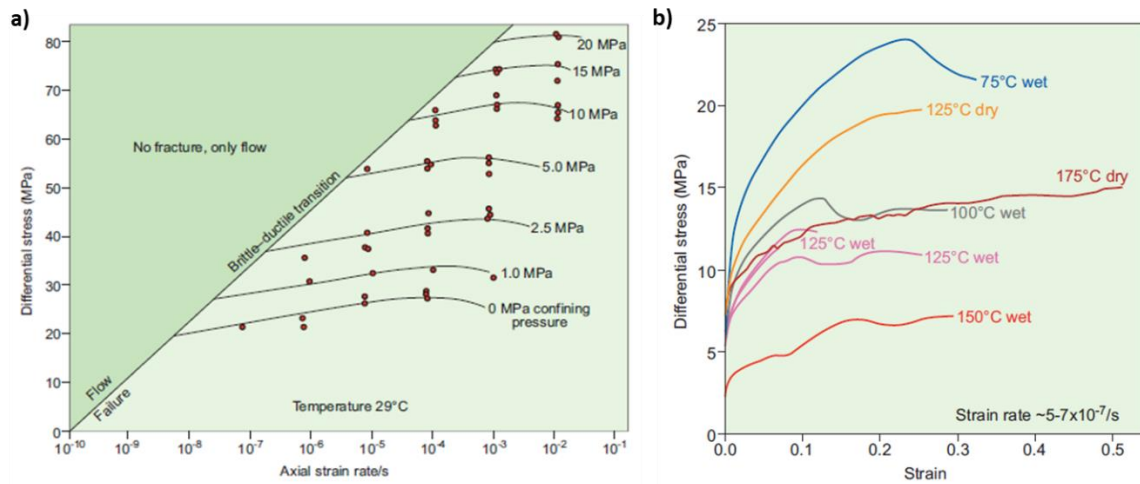


Figure 4-4. Differential stress required to initiate salt creep as a function of (a) confining pressure and strain rate and (b) temperature and salt wetness (modified from Jackson and Hudec, 2017).

More importantly, different salts pose different mobility characteristics, which directly impacts Mud Weight (MW) design. For example, anhydrite and gypsum can be seen as essentially immobile, posing negligible creep characteristics for engineering purposes (Firme et al., 2014; Jackson and Hudec, 2017). On the contrary, evaporites like carnallite and bischofite are extremely weak salts, what makes them much more mobile than halite under the same pressure-temperature conditions (figure 4-5.). Due to their unfavorable mobilities, these salts are often referred across the drilling literature as “squeezing salts” and necessitate substantially higher MW to stabilize the wellbore (Muecke, 1994; van Oort, 2004).

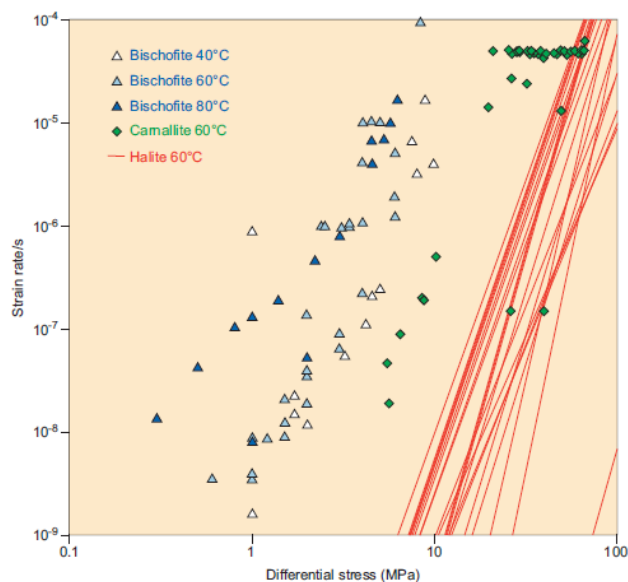


Figure 4-5. Creep rates of different salts for varying p-T conditions (Urai et al., 2008).

4.2.1. Creep micromechanisms

Under enough differential stress, rocks change in shape or volume by intracrystalline and intercrystalline processes called deformation mechanisms. As per Hudec and Jackson (2017), the three main microstructural processes in rock salt are:

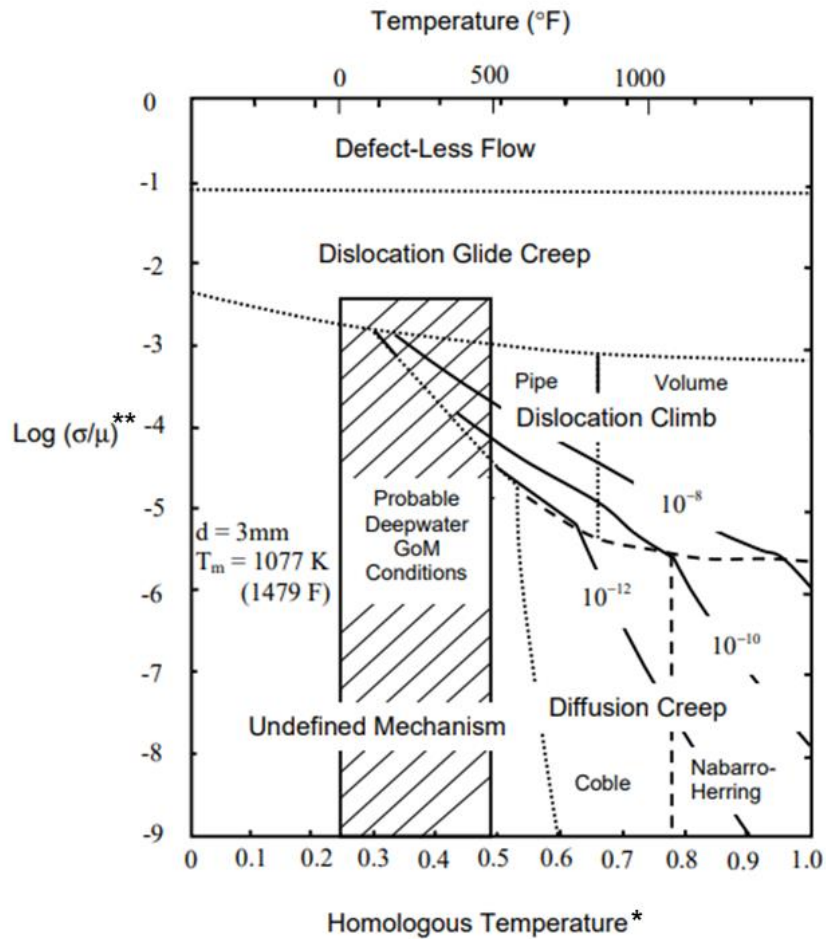
- microcracking and cataclastic flow,
- dislocation creep,
- solution-precipitation creep.

Dominant mechanisms will vastly depend on the rock properties (mineralogy, impurities, intergranular fluid, grain size, fabrics, porosity, and permeability) and external factors such as temperature, overburden, fluid pressure, differential stress, and imposed strain rate (Jackson and Hudec, 2017). At very low effective confining pressures (< few MPa) and high deviatoric stresses (> 20 MPa), inter and intragranular microcracking, grain rotation, and intergranular slip are important strain accumulating processes alongside crystal plasticity (Urai et al., 2008). However, for petroleum engineering applications where high confining pressures are encountered, the mean effective stress increases, thus causing microcracking and dilatancy to diminish. Consequently, dislocation creep (dislocation glide and dislocation climb) and solution-precipitation creep (also fluid assisted grain boundary migration; wet diffusion; fluid assisted diffusional creep or FADC) become relevant deformation mechanisms in salt. The dashed area represented in figure 4-6. shows the expected conditions encountered in Deepwater GoM. As per Fossum and Fredrich (2002) this region encompasses two distinct deformation mechanisms:

- dislocation creep (dislocation glide at conditions of very high shear stresses and dislocation climb mechanism promoted in high-temperature areas),
- undefined mechanism⁶ anticipated at somewhat lower shear stresses and temperatures.

Similar findings were provided by Dusseault et al. (2004a). Although creep micromechanisms are out of the Thesis` scope, the author finds it relevant to mention them since the choice of representative creep mechanism will determine coefficients embedded in models used for creep estimation (refer to 9.1.).

⁶ Originally unidentified in work by Munson (1979), FADC was yet identified latter as being the second driving mechanisms (Costa et al., 2010).



* a ratio of thermodynamic temperature to its melting point (T_m ; kelvin)

** differential pressure normalized by shear modulus

Figure 4-6. Deformation micromechanism map for salt in probable Deepwater GoM conditions (modified from Fossum and Fredrich, 2002)

4.2.2. Creep regimes

Creep tests of salt specimens typically show an instant elastic response followed by a three-stage permanent strain increase (Fjær et al., 2008, Costa et al., 2010; Jackson and Hudec, 2017). Figure 4-7. presents the theoretical creep curve (fig 4-7a.) and creep curve obtained through laboratory testing (figure 4-7b.).

- When the load is initially applied, immediate elastic deformation is produced, followed by primary creep or transient creep. During transient (primary) creep, internal dislocation occurs, evidenced by the rock hardening (Vallejo and Ferrer, 2011; Firme et al., 2014). As the rock hardens and the strain-time curve becomes less

steep and the strain rate declines monotonically until reaching constant value. Here, salt is extremely sensitive to imposed strain rates (Jackson and Hudec, 2017).

- Once the constant rate is achieved, the strain-time curve becomes linear as the material begins steady state creep (secondary creep) and hardening starts being balanced with recovery (Jackson and Hudec, 2017). As per Firme et al. (2014), the dislocations` density reaches the state of equilibrium where dislocation growth and accumulation become balanced. Here, creep rate will only depend on imposed stress and temperature (Jackson and Hudec, 2017). This premise is a very important assumption in many drilling-related creep models.
- Depending on the axial strain, temperature and the differential⁷ stress applied to the specimen, a final, tertiary creep occurs, characterized by acceleration of the creep strain rate resulting from the accumulated specimen damage (Fjær et al., 2008). The deformation rate accelerates with the onset of the volumetric deformation (dilatation), and the creep curve steepens. Laboratory specimens may fail or not at this stage, depending on the confining pressure (Costa et al., 2010).

In well engineering, the third stage is not as important as the casing and cement do not allow further deformations of the salt, i.e., the deformations are constrained (Wang and Samuel, 2013). Moreover, post-third creep stage failure should not occur as high confining pressures promote the healing of induced microcracks in salt, i.e., salt failure is not expected with physically reasonable MW deployed. Because the transient creep occurs soon after excavation and only lasts for a short time, transient creep is normally dissipated during drilling and cementing operations and usually vanishes on a day's scale (Wang and Samuel, 2013). Dusseault et al. (2004a) further indicated that transient creep strains are small and can be neglected for practical purposes of drilling through salt. Hence, the usual practice in practical well engineering aspects is to assess the overall strain rate of the salt formation by considering only the steady state creep.

⁷ Here it is important to distinguish between differential stress imposed in laboratory and stress encountered during drilling operations. In the laboratory, differential stress represents a stress difference between the confining and the applied axial stress, whereas in case of drilling, a differential stress results from the existing difference between borehole annular pressure and overburden pressure.

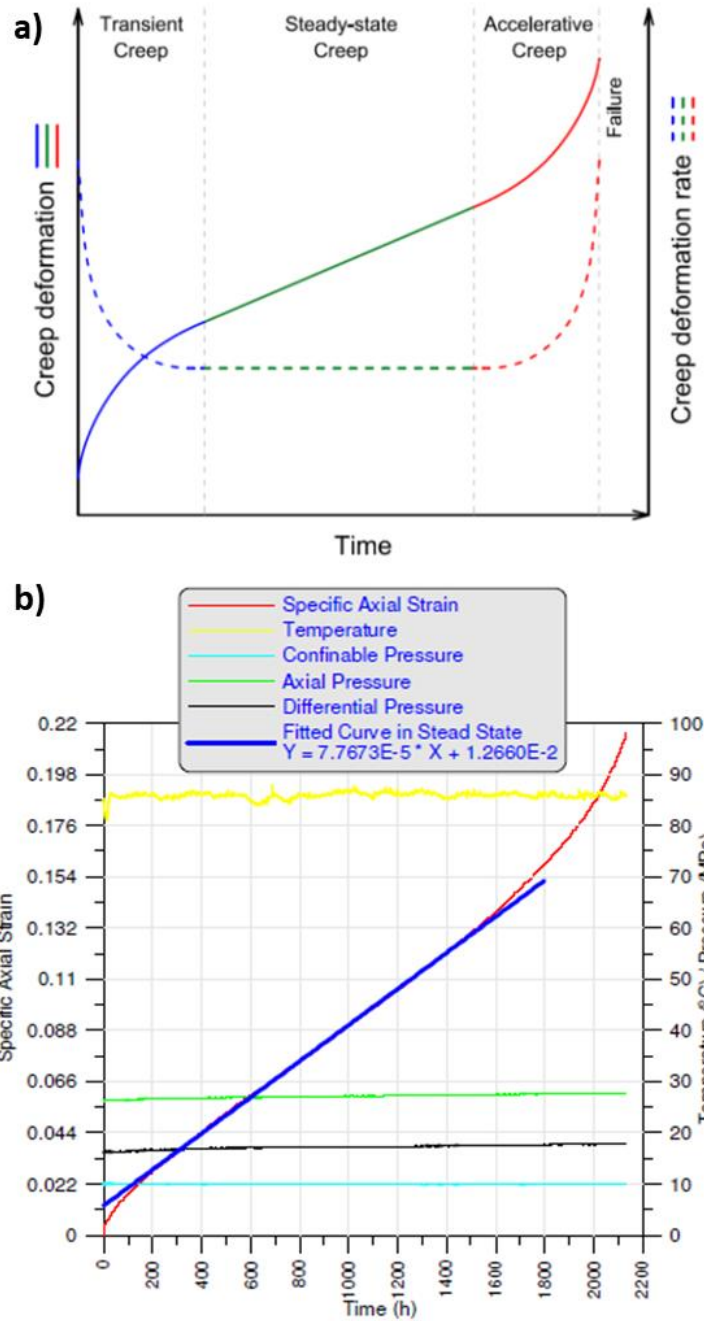


Figure 4-7. The (a) theoretical creep curve and (b) creep curve obtained through laboratory testing (Costa et al., 2010)

4.3. Modeling salt behavior

Salt behaves as a viscoelastic material (Barker and Meeks, 2003; Zoback, 2007; Fossen, 2010; Jackson and Hudec, 2017). Although salts deform differently from fluids, given the constant temperature conditions and the relaxation rate involved, the salt can be seen as viscous fluid on the geological time scale. Assuming salt as a viscous Newtonian fluid, it will strain proportionally to the change in differential stress ($\Delta\sigma$). For the conditions of a

constant temperature, a proportionality constant that correlates shear stress and shear rate is known as a dynamic viscosity (η). Therefore, a representative constitutive model for creep deformation in salt rocks is needed to predict the salt creep behavior under various operational conditions relevant for well design in salt sections. Due to the complexity of salt creep mechanisms, predicting a borehole creep closure with time requires different constitutive models depending on the mechanical behavior of salt. These models can be either empirical, rheological, or physical. Botelho (2008) apud Orozco et al. (2018) tabulated the most important constitutive creep models. To illustrate salt viscoelastic behavior to the reader, a theory behind a simple Maxwell's constitutive model will be presented. Industry applications of creep modelling are discussed further under chapter 9.1.

4.3.1. Maxwell's constitutive model

A simple constitutive model comprising spring and the dashpot (Maxwell's model) can be used to represent salt creep. Although more complex models exist (e.g., Zener or Burgers models) that can capture transient creep behavior, the Maxwell model is sufficient for this Thesis to provide a necessary understanding of a steady state salt creep in the wellbore (Dusseault et al., 2004a). Namely, when a material is subjected to constant stress, the strain response will have two components (a) an elastic component that manifests instantaneously but relaxes immediately upon stress release and (b) a viscous component that increases with time as long as the stress is applied (figure 4-8.).

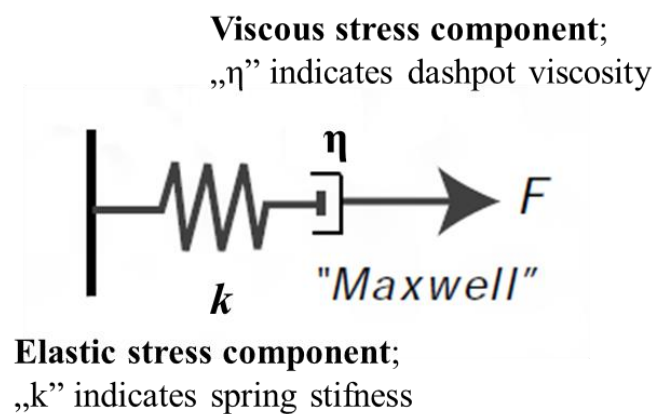


Figure 4-8. Schematic representation of Maxwell's viscoelastic model (modified from Roylance, 2001)

The elastic stress represented by the spring ($\sigma_{elastic}$) has the relationship:

$$\sigma_{elastic} = E\varepsilon \quad (4-1)$$

Whereas the viscous stress represented by the dashpot ($\sigma_{viscous}$) has the relationship:

$$\sigma_{viscous} = \eta \dot{\epsilon} \quad (4-2)$$

where E is Young`s modulus, ϵ strain, $\dot{\epsilon}$ strain rate, t time, and η is dynamic viscosity.

Finally, the model can be represented by combining two stress components as follows:

$$\frac{d\epsilon_{total}}{dt} = \dot{\epsilon}_D + \dot{\epsilon}_S = \frac{\sigma}{\eta} + \frac{1}{E} \frac{d\sigma}{dt} \quad (4-3)$$

Following important observations arise here:

- at the application of constant stress (second term vanishes), the strain will increase with time, i.e., material creeps,
- at the constant strain (zero strain rate), the stress decreases with time, i.e., material relaxes,
- the effective stiffness of the model depends on the loading rate, young modulus, and salt viscosity.

The elastic stresses imposed circumferentially around the drilled wellbore immediately begin to dissipate through viscous creep. Adhering to the linear Maxwell model, separating variables and integrating equation (4-3) under the condition of zero strain rate, we obtain an equation to approximate the decay rate of initial elastic stresses on the wellbore drilled through salt:

$$\sigma(t) = \sigma_0 \exp(-Et/\eta) \quad (4-4)$$

where σ_0 is a relaxation rate of elastic stresses (Roylance, 2001). This behavior arises as a result of the salt viscosity. Namely, the time required for the stress to relax, i.e., approaches its initial value is proportional to the salt viscosity. The effective viscosity of rock salt (i.e., halite) could be found in the range between 10^{15} and 10^{20} Pa s (Weijermars et al., 2013; Jackson and Hudec, 2017)⁸. Authors argued that elastic wellbore stresses dissipate at very slow rates at the upper limit of that range (figure 4-9.). That said, it corroborates the

⁸ In a salt diapir, viscosity ranges from 10^{17} to 10^{20} Pa s, but in fine-grained extrusive salt, viscosity can be as low as 10^{15} Pa s since the viscosity of salt increases by order of magnitude as its grain size doubles (Jackson and Hudec, 2017).

observations by Muecke (1994) and Wilson et al. (2002), who argued that halite salts are relatively slow-moving and do not pose a significant threat to well construction.

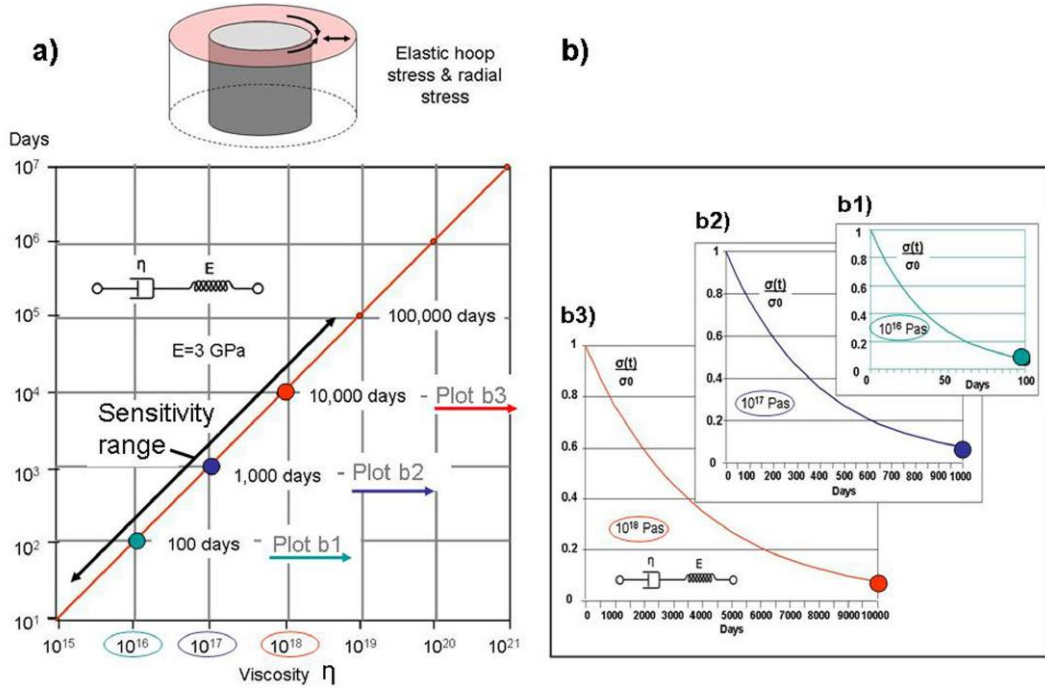


Figure 4-9. (a) Sensitivity plot of elastic stress relaxation time versus viscosity and (b) Elastic stress relaxation time for wellbore stresses as a function of salt viscosities in the range from 10^{16} to 10^{18} Pa s (Weijermars et al., 2013)

It all comes to the fact that the higher the salt mobility is (lower salt viscosity), the higher is the tendency of a borehole closure (faster wellbore diameter reduction).

5. BASIC CONCEPTS IN ROCK MECHANICS

Rock is a hard natural aggregate of mineral particles connected by strong, cohesive forces that are usually considered as a continuous system. However, its composition, characteristics, and properties of intact rocks are often highly variable. As a result, rocks are neither homogeneous nor isotropic⁹ materials (Vallejo and Ferrer, 2011). Rock's anisotropic and heterogeneous character results from its structure. On a microscopic level, rock consists of small grains of varying sizes, shapes, orientations, and mineral components with embedded discontinuity due to lamination and micro-cracking. The degree of cementing and interlocking of the grains greatly influence the spatial distribution of mechanical rock properties. In addition, rocks are affected by geological and environmental processes that, over time, led to fracturing, alteration, and weathering (Vallejo and Ferrer, 2011). As a result, rocks with properties such as strength, deformability, and in-situ stresses might exhibit different behavior if loaded in different directions (Aadnøy and Looyeh, 2011). Although most of the rock's mechanical properties show a certain dependence on the orientation of the rock grains, such dependence can pose a severe limitation to technical applications. Hence, simplification is often made in applied rock mechanics by assuming homogeneity and limited anisotropy. This allows for material properties such as Young's modulus, E , and Poisson's ratio, ν , to be viewed as scalars, i.e., implying these properties are equal in all directions within the volume of consideration. However, detailed characterization of rock behavior is outside the Thesis' scope, and the reader is referenced to the mentioned literature for a deeper insight.

5.1. Rock strength

Stresses generated by the application of forces on rocks may produce deformation and failure, depending on the strength of the rocks and on other conditions external to the rock material itself. We distinguish between (a) peak strength (tensile strength or compression strength), i.e., the maximum stress the rock can sustain for a specific, peak strain, and (b) residual strength, i.e., the lowered value of rock strength reached upon exceeding peak strength (after considerable post-peak strain). Tensile strength is not of practical significance in well construction applications and measuring it directly is often impractical. Since rocks

⁹ Homogeneity implies that uniform properties exist throughout the volume of interest, for which its properties are not functionally dependent upon position. In contrast, isotropy reflects the same material properties in any direction within the material.

are much weaker in tension than in compression, tensile strength is often approximated as being either a tenth of compressive rock strength or, more conservatively, zero (Zoback, 2007; Aadnøy and Looyeh, 2011). On the contrary, compressive strength refers to the rock's strength under compressive loading. In further text, the term “strength” will be referring to compressive strength if it is not mentioned otherwise. The strength depends on the intrinsic rock properties (cohesion and angle of friction) and external factors (confinement, the loading and unloading cycles rock has sustained, and the water content)¹⁰. Rock properties are determined through laboratory tests and correlations (Zoback, 2007). The latter can be easily found in any rock-mechanics-related textbook.

5.2. Stress

Simply, stress is defined as an operator that relates the traction (force intensity) vector $\mathbf{t}(\mathbf{n})$ to a unit-length direction vector \mathbf{n} across an infinitesimally small surface perpendicular to \mathbf{n} . In general, the traction $\mathbf{t}(\mathbf{n})$ is not collinear with the normal \mathbf{n} . Thus, the traction vector will have a normal component, $\mathbf{t}(\mathbf{n})_{\mathbf{n}}$, aligned with \mathbf{n} and a shear component, $\mathbf{t}(\mathbf{n})_{\mathbf{s}}$, lying in the plane with which \mathbf{n} is associated. Hence, to completely describe the stress state at any point within a three-dimensional (3D) body, it is necessary to identify the stress components related to surfaces oriented in three orthogonal directions. However, since the orientation of the shear traction must be identified, it will be decomposed into two shear stress components, both parallel to the plane associated with normal \mathbf{n} . A tensor has 3^x components in space, where x represents the order of the tensor. Correspondingly, nine stress components will form a second order (stress) tensor (figure 5-1.).

$$t_{(n)j} = \sigma_{ij}n_j \quad (5-1)$$

The following notation is used such that subscripts i and j may be given by numbers 1, 2, 3, which represent the x -, y - and z -axis, respectively. The first index provides information about the plane normal and the second about the component direction relative to the referenced coordinate system. A tensor (σ_{ij}) component is normal stress if $i = j$ and shear stress if $i \neq j$. Due to the symmetry of the stress tensor ($\sigma_{ij} = \sigma_{ji}$), to fully describe the state of stress at depth, rather six quantities will be required.

¹⁰ As strength cannot be represented by a single intrinsic but rather range of values and variations for specific conditions (Vallejo and Ferrer, 2011).

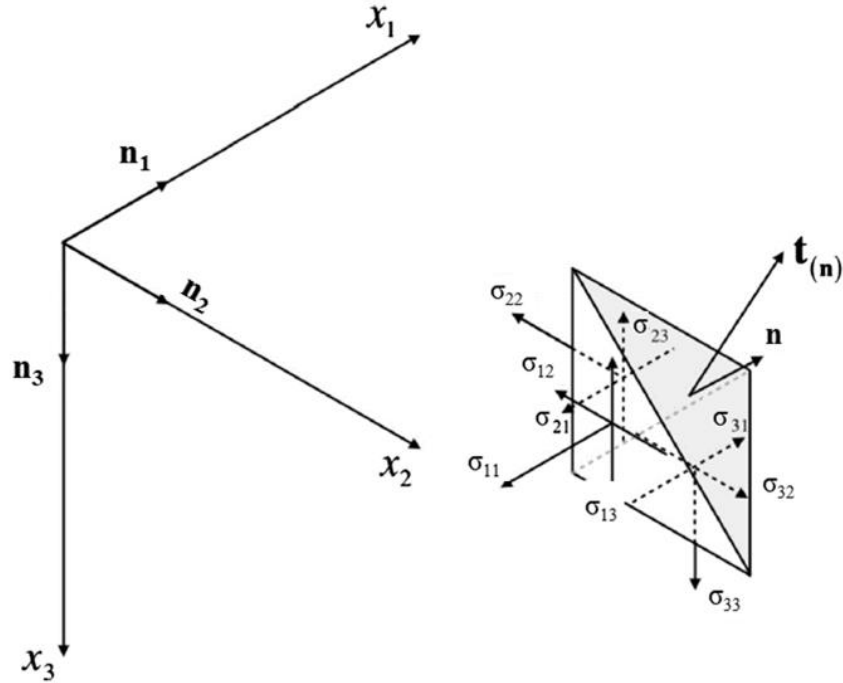


Figure 5-1. Traction vector and stress tensor components (modified from Pattillo, 2018)

In other words, six stress magnitudes or three stress magnitudes and the three angles that define the orientation of the stress coordinate system relative to a reference coordinate system (e.g. coordinate system referenced to wellbore coordinates). In matrix form tensor is given as follows:

$$\sigma_{ij} = \begin{bmatrix} \sigma_{xx} & \sigma_{xy} & \sigma_{xz} \\ \sigma_{yx} & \sigma_{yy} & \sigma_{yz} \\ \sigma_{zx} & \sigma_{zy} & \sigma_{zz} \end{bmatrix} = \begin{bmatrix} \sigma_{xx} & \tau_{xy} & \tau_{xz} \\ \tau_{xy} & \sigma_{xx} & \tau_{yz} \\ \tau_{xz} & \tau_{yz} & \sigma_{xx} \end{bmatrix} \quad (5-2)$$

5.2.1. Principal stresses

There exists a specific orientation of the 3D element, such that shear stresses vanish and the resultant stresses are only normal stresses. In other words, the plane normal vector, \mathbf{n} , will be colinear with traction vector, $\mathbf{t}(\mathbf{n})$. By closely following work by Pattillo (2018), we can write:

$$t_{(n)j} = \lambda n_j \quad (5-3)$$

Rearranging Eq. (5-3) gives:

$$t_{(n)j} - \lambda n_j = 0 \quad (5-4)$$

And by substituting Eq. (5-1) in the Eq. (5-4) we obtain:

$$(\sigma_{ij} - \lambda \delta_{ji})n_j = 0 \quad (5-5)$$

Where 0 is the vector null vector, of the same dimension as traction vector and unit normal vector, λ is scalar and δ_{ji} is Kronecker-delta symbol (a function it takes as input the pair (i, j) and returns one if they are the same and zero otherwise). Adhering to stress tensor symmetry, the Eq (5-5) can be written in the expanded form:

$$\begin{bmatrix} \sigma_{11} - \lambda & \sigma_{12} & \sigma_{13} \\ \sigma_{12} & \sigma_{22} - \lambda & \sigma_{23} \\ \sigma_{13} & \sigma_{23} & \sigma_{33} - \lambda \end{bmatrix} \begin{bmatrix} n_1 \\ n_2 \\ n_3 \end{bmatrix} = \begin{bmatrix} 0 \\ 0 \\ 0 \end{bmatrix} \quad (5-6)$$

Given that \mathbf{n} is not a null vector, equations will have nonzero solutions if and only if the determinant of $\sigma_{ij} - \lambda \delta_{ji}$ equals zero. Hence:

$$0 = \det(\sigma - \lambda I) = \begin{vmatrix} \sigma_{11} - \lambda & \tau_{12} & \tau_{13} \\ \tau_{12} & \sigma_{xx} - \lambda & \tau_{23} \\ \tau_{13} & \tau_{23} & \sigma_{xx} - \lambda \end{vmatrix} \quad (5-7)$$

By solving so-called ‘‘characteristic equation’’ of σ (Eq. (5-7)), where σ is the tensor represented by 3-by-3 matrix, the resulting solution will be a third-degree polynomial. The solution can be expressed in form of a cubic equation where coefficients having the common power are combined under single parameter I_i , as expressed by Eq. (5-8):

$$\lambda^3 - I_1 \lambda^2 - I_2 \lambda - I_3 = 0 \quad (5-8)$$

I_1 , I_2 , and I_3 (given by equations 5-9 to 5-11) are known as stress tensor invariants because their form, and values remain unchanged under coordinate transform.

$$I_1 = \text{tr} \{ \boldsymbol{\sigma} \} = \sigma_{jj} \quad (5-9)$$

$$I_2 = \frac{1}{2} [\sigma_{ij} \sigma_{ij} - (\sigma_{kk})^2] \quad (5-10)$$

$$I_3 = \det(\boldsymbol{\sigma}) = \frac{1}{6} \varepsilon_{ijk} \varepsilon_{pqr} \sigma_{ip} \sigma_{jq} \sigma_{kr} \quad (5-11)$$

Where $\text{tr} \{ \boldsymbol{\sigma} \}$ represent the trace of the stress tensor, ε_{ijk} and ε_{pqr} are the Levi-Civita¹¹ or permutation symbols. Invariants are very useful to formulate the rock constitutive models as

¹¹ A function that returns -1,0 or 1. In a case where any two subscripts are equal, the symbol automatically evaluates to 0. The symbol evaluates to 1 if the even number of permutations is required to order the indices. Finally, the symbol evaluates to -1 if an odd number of permutations is required to order the indices

they are independent of the reference system (Schlumberger, 2021). The real roots of Eq. (5-8), λ , are termed characteristic values or eigenvalues. Consequently, by solving the characteristic equation, both the principal stress magnitudes (eigenvalues) and their directions (eigenvectors) can be determined. Simply, when each λ is substituted into Eq. (5-6) the corresponding solution of \mathbf{n} yields an eigenvector (as represented in figure 5-2.). Here, the angles associated with the principal stresses ($\sigma_1 = \sigma_x$, $\sigma_2 = \sigma_y$, $\sigma_3 = \sigma_z$) are called principal angles, with each angle differing by 90° (the planes are mutually perpendicular). The principal stresses play an important role in failure theories as they represent the maximum and minimum stresses (or the maximum differential stress values). Namely, despite that most materials are strong when loaded hydrostatically, they fail much easier when subjected to a deviatoric load (Aadnøy and Looyeh, 2011). Moreover, understanding the terminology is crucial for further problematics outlined in the Thesis.

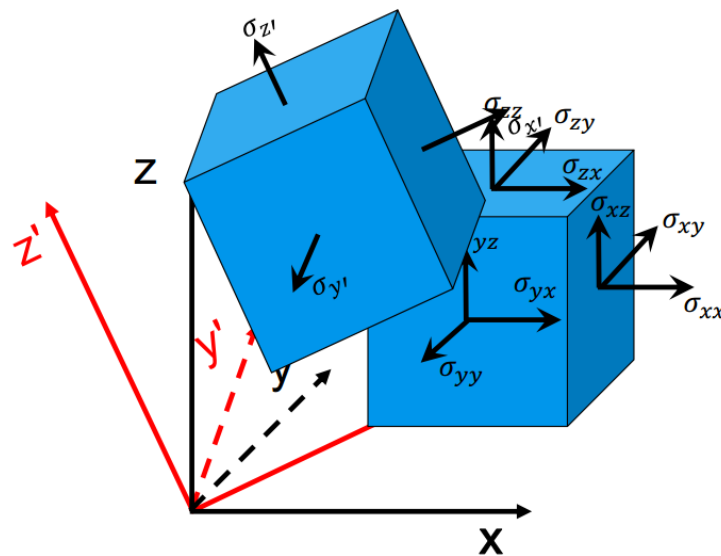


Figure 5-2. Schematic representation of principal stresses (Schlumberger, 2021)

5.2.2. Deviatoric stresses

A stress tensor can be decomposed into two components: an isotropic component and a deviatoric stress state. From figure 5-3. can be seen that the deviatoric stress reflects the shear stresses whereas mean stress reflects normal stress influence. The mean normal (hydrostatic) stress given by Eq. (5-12), only produces a volumetric strain without distorting the shape itself, viz., causing either uniform compression or extension of a matter. Note that the mean hydrostatic stress is tantamount to the first stress invariant scaled by one-third. Hence, the mean stress is independent of the coordinate transformation itself (Fjær et al., 2008).

$$\bar{\sigma} = (\sigma_{xx} + \sigma_{yy} + \sigma_{zz})/3 \quad (5-12)$$

On the other hand, deviatoric stress causes body distortions, viz., shape change at nil volume change. As given in figure 5-3, the latter is simply obtained by subtracting the average hydrostatic stress from the overall stress state:

$$\begin{bmatrix} \sigma_{xx} & \tau_{xy} & \tau_{xz} \\ \tau_{xy} & \sigma_{yy} & \tau_{yz} \\ \tau_{xz} & \tau_{yz} & \sigma_{zz} \end{bmatrix} = \begin{bmatrix} \bar{\sigma} & 0 & 0 \\ 0 & \bar{\sigma} & 0 \\ 0 & 0 & \bar{\sigma} \end{bmatrix} + \begin{bmatrix} \sigma_{xx} - \bar{\sigma} & \tau_{xy} & \tau_{xz} \\ \tau_{xy} & \sigma_{yy} - \bar{\sigma} & \tau_{yz} \\ \tau_{xz} & \tau_{yz} & \sigma_{zz} - \bar{\sigma} \end{bmatrix} \quad (5-13)$$

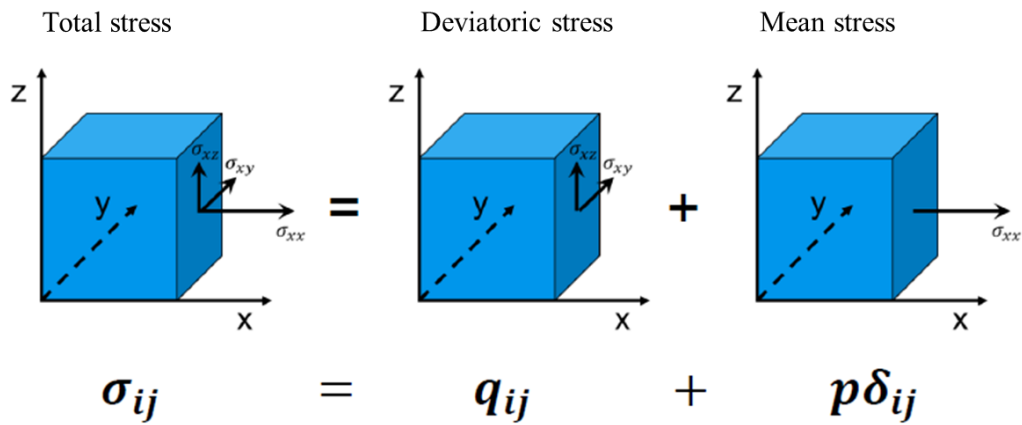


Figure 5-3. Decomposition of total stress tensor to deviatoric and isotropic component (modified from Schlumberger, 2021)

Following a procedure outlined under 5.2.1., deviatoric invariants can be obtained in the same way but using a deviatoric stress tensor q_{ij} . There are many ways of representing deviatoric stress invariants, thus the reader is referenced to the above-mentioned literature (e.g., Fjær et al., 2008).

5.2.3. Octahedral stress theory

A plane normal to the hydrostatic axis (plane spanned by points (1,1,1)) in principal stress space is also known as an octahedral plane (also a π -plane; a deviatoric plane). Correspondingly, the stresses in this plane are called the octahedral normal stress (σ_o) and the octahedral shear stress (τ_o) (Fjær et al. 2008):

$$\sigma_o = \bar{\sigma} \quad (5-14)$$

$$\tau_o = \frac{1}{3} \sqrt{(\sigma_1 - \sigma_2)^2 + (\sigma_2 - \sigma_3)^2 + (\sigma_3 - \sigma_1)^2} = \sqrt{\frac{2}{3} J_2} \quad (5-15)$$

Where J_2 is the second invariant of deviatoric stress. Alternatively, using the stress tensor components, Eq. (5-15) can be written as:

$$\tau_o = \frac{1}{3} \sqrt{(\sigma_{xx} - \sigma_{yy})^2 + (\sigma_{yy} - \sigma_{zz})^2 + (\sigma_{zz} - \sigma_{xx})^2 + 6(\tau_{xy}^2 + \tau_{yz}^2 + \tau_{xz}^2)} \quad (5-16)$$

When the stress vector associated with the normal to the octahedral plane (figure 5-4.) is generated, its components in the principal directions are the eigenvectors (principal stresses). Likewise, the normal stress makes the same angle with the direction of all three principal stresses. This stress vector has two components, one normal to the plane, whose magnitude equals the mean stress, and one tangential to the plane, with a magnitude equal to the octahedral shear stress. Further, octahedral shear stress magnitude is proportional to the magnitude of the deviatoric stress (Infante and Chenevert, 1989). Although the octahedral shear stress is smaller than the highest principal shear stress, it constitutes a single value that is influenced by all three principal stresses, making it an important factor for predicting the yielding of a stressed material (Roylance, 2001; Wolf et al., 2001).

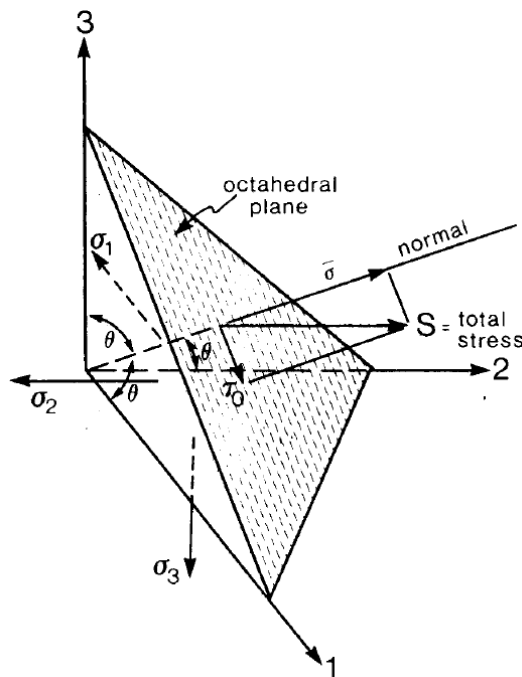


Figure 5-4. Schematic representation of octahedral stress (modified from Infante and Chenevert, 1989)

5.2.4. Von Mises equivalent stress

The yielding of the material occurs when the octahedral shear stress is equal to or exceeds a stress critical value for the onset of failure in a given material (Wolf et al., 2001). This critical value can be related to the uniaxial yield strength (σ_y) obtained from the laboratory testing where $\sigma_y = \sigma_1$ and $\sigma_2 = \sigma_3 = 0$; hence the Eq (5-15) becomes:

$$\tau_o = \frac{1}{3} \sqrt{(\sigma_y - 0)^2 + (0)^2 + (0 - \sigma_1)^2} \quad (5-17)$$

After rearranging, the octahedral stress criterion can be related to the yield strength using the following relation:

$$\tau_o = \frac{\sqrt{2}}{3} \sigma_y \quad (5-18)$$

Thus, the von Mises theory can be related to the octahedral shearing stress theory of failure follows by combining Eq. (5-17) and (5-18):

$$\sigma_y = \sqrt{\frac{1}{2} [(\sigma_1 - \sigma_2)^2 + (\sigma_2 - \sigma_3)^2 + (\sigma_3 - \sigma_1)^2]} \quad (5-19)$$

Eq. (5-19) implies that any combination of principal stresses will cause yielding if the right side of this equation exceeds the value of σ_y . Alternatively, we can express Eq. (5-19) in terms of equivalent uniaxial stress, σ_e or Von Mises equivalent (VME) stress, where σ_e is the value of uniaxial stress which produces the same level of octahedral shear stress as does the combination of existing principal stresses:

$$\sigma_e = \sigma_{VME} = \sqrt{\frac{1}{2} [(\sigma_1 - \sigma_2)^2 + (\sigma_2 - \sigma_3)^2 + (\sigma_3 - \sigma_1)^2]} \quad (5-20)$$

However, it has to be emphasized that the von Mises criterion is limited to materials having similar strength in tension and compression, thus its direct application to wellbore stability may be inadequate (Wolf et al., 2001). However, it will be seen later that the VME stress plays an important in the optimization of the wellbore placement.

5.3. Laboratory tests

Laboratory tests are run to quantify the physical and mechanical properties governing intact rock behavior. In these tests, a small axial hole is drilled along the axis of a cylindrical sample (core). The forces applied to the rock create a particular stress state. Deformation and failure of the rocks will be governed by the magnitude and direction of these stresses. Rocks fracture under conditions of differential stress, and a specific relationship between the principal stresses produces a particular state of deformation. The idea is to establish the relationship between stresses and strains recorded during loading and failure processes and its strength parameters. By recording a statistically representative number of tests, characteristic values for the rock strength parameters can be derived from the force applied to a standardized specimen at the moment of failure. A list of the most common laboratory tests and obtained parameters can be found in table 5-1. These parameters are then applied in failure criteria to identify fracture and collapse capability of rock/formation before, during, and after drilling construction (Aadnøy and Looyeh, 2011; Vallejo and Ferrer, 2011). Figure 5-5. illustrates the different states of stress applied during testing.

Table 5-1. Laboratory tests for determining rock`s strength and deformability properties (Vallejo and Ferrer, 2011)

Laboratory tests for strength and deformability		
Tests		Parameters obtained
Strength	Uniaxial compression test	Uniaxial compressive strength, σ_c
	Triaxial compression test	Cohesion (S_0), internal friction angle (φ)
	Direct tension test	Tensile strength, σ_t
	Indirect tension (Brazilian) test	Tensile strength, σ_t
Deformability	Uniaxial compression test	Static deformation moduli; E and ν
	Acoustic velocity	Dynamic deformation moduli; E_d and ν_d

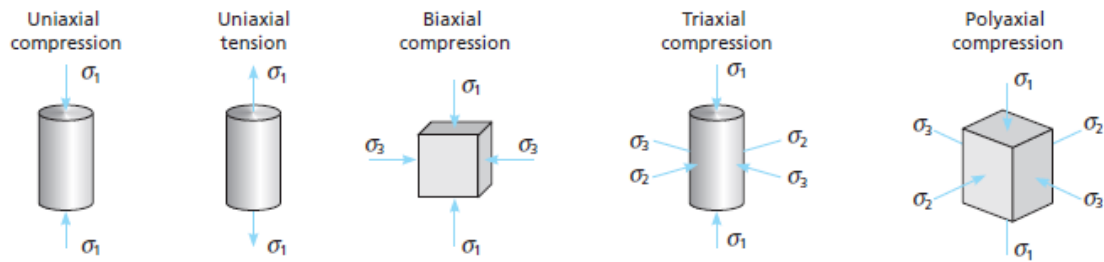


Figure 5-5. Different states of stress applied to laboratory specimens. Note: Uniaxial: $\sigma_1 \neq 0$; $\sigma_2 = \sigma_3 = 0$, Biaxial: $\sigma_1 \neq 0$; $\sigma_3 \neq 0$; $\sigma_2 = 0$, Triaxial: $\sigma_1 \neq 0$; $\sigma_2 \neq 0$; $\sigma_3 \neq 0$, Polyaxial: $\sigma_1 \neq 0$; $\sigma_2 \neq \sigma_3$ (Vallejo and Ferrer, 2011)

5.4. Failure criteria

However, the loading conditions applied in laboratory tests do not indicate rock failure in practice. Mainly because of the cost of core recovery, a sufficient number of specimens are rarely available for comprehensive laboratory testing. Thus, one could hardly capture failure modes under various loading conditions pertinent to well construction (Aadnøy and Looyeh, 2011). From a practical side, somewhat theoretically complicated failure criteria better describe rock under different stress conditions as a relatively low amount of laboratory data is required.

Failure Criteria are theoretical or empirical formulations used to link the evolution of internal stress and material strength to understand specific material failure mechanisms. Various failure theories are used to predict the conditions under which solid materials fail due to the action of external loads (both hydrostatic and deviatoric). A failure theory is expressed in the form of various failure criteria which are valid for a specific material (e.g., Rankine, Tresca, Hencky-Hubert-von Mises, Mohr-Coulomb, Griffith, Drucker-Prager, Hoek-Brown, etc.). Failure criteria represent surfaces in 3D (2D) stress or strain space that separates "failed" from the "safe" states. Here, a 3D surface is an extrapolation of the 2D yield surface along the hydrostatic axis in 3D principal stress coordinates (figure 5-6). Practically speaking, all these failure criteria identify the state of stress when conditions are such that the influence of combined loads transcend a certain threshold, consequentially causing the material to fail (Wolf et al., 2001). Most importantly, this limit is a function of the total stress state rather than on the uniaxial stress (Fjær et al., 2008). The failure can occur either in a brittle manner (fracturing) or yield (onset of plastic deform) (depending on the material itself). The Failure criteria are usually divided into peak strength criteria (e.g., Mohr-

Coulomb or Hoek-Brown) and plasticity/elasticity limit criteria (e.g., von Mises, Drucker-Prager, or Lade). Peak strength criteria describe the combination of stresses at which peak strength is exceeded and material fractures. In contrast, plasticity criteria describe the ratio between the stress components required to establish yield (Vallejo and Ferrer, 2011).

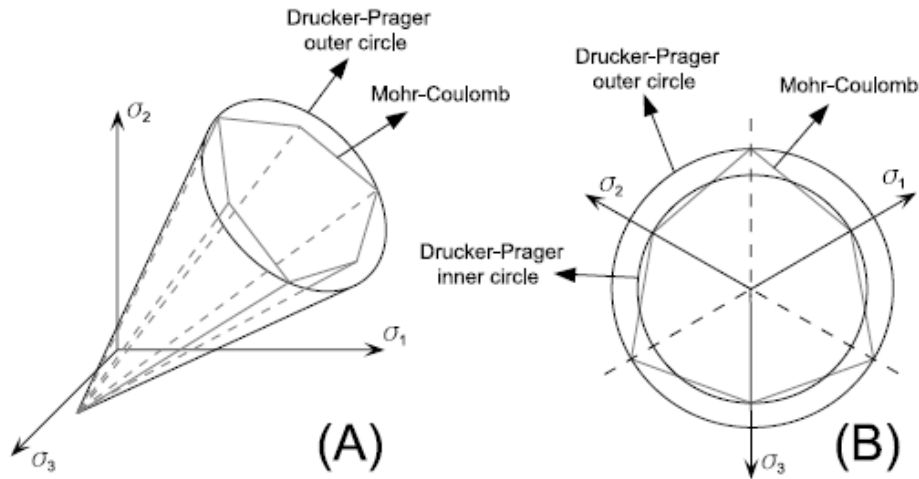


Figure 5-6. The Mohr-Coulomb and the Drucker-Prager plastic yield criteria in the (a) principal stress space and (b) π - plane (Luo et al., 2012b)

In addition, the pore pressure will also influence rock failure at depths relevant for petroleum applications. Hence, when evaluating conditions that could lead to rock failure, the term effective stress must be well understood.

5.4.1. Effective stress

The concept of effective stress is based on Terzaghi's pioneering work (1923). He observed that soil behavior (or a saturated rock) is controlled by the difference between externally applied stress and internal pore pressure P_p . Hence, effective stress in tensor (σ'_{ij}) form can be written as:

$$\sigma'_{ij} = S_{ij} - \delta_{ij} P_p \quad (5-21)$$

The Kronecker-delta symbol implies that pore pressure only influences normal stress tensor components, σ_{11} , σ_{22} , σ_{33} . Therefore, as observed in figure 5-7., the stresses acting on individual grains result from the difference between the externally applied normal stresses and the internal fluid pressure (Zoback, 2007; Schlumberger, 2021).

To match the experimental observations, Nur and Byerlee (1971) introduced the so-called Biot parameter:

$$\sigma'_{ij} = S_{ij} - \delta_{ij} \alpha P_p \quad (5-22)$$

The Biot parameter (α ; $0 \leq \alpha \leq 1$) is defined as follows:

$$\alpha = 1 - \frac{Kb}{Kg} \quad (5-23)$$

Kb is the drained bulk modulus of the rock or aggregate, and Kg is the bulk modulus of the rock's solid grains.

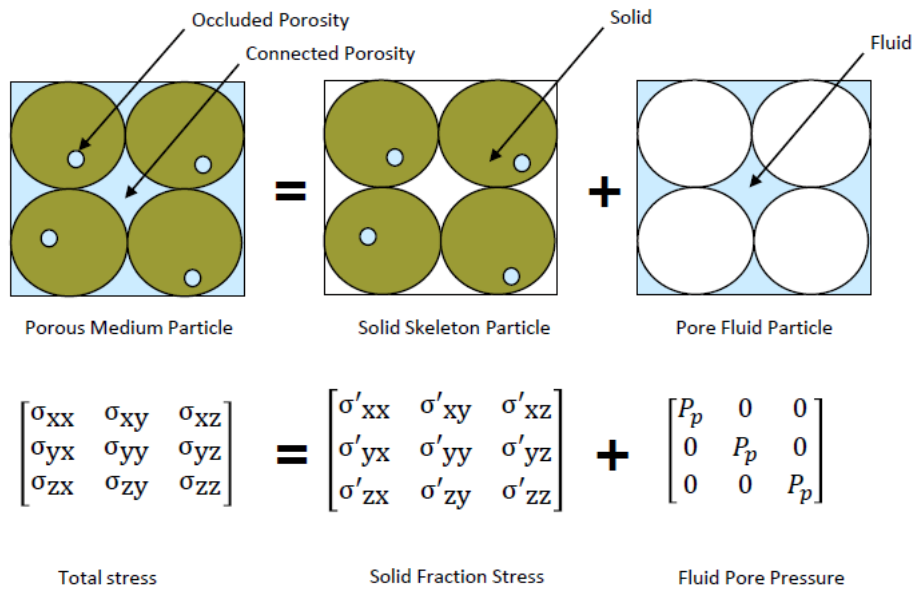


Figure 5-7. Decomposition of total stress Tensor of a porous material (Schlumberger, 2021)

For a nearly solid rock with no interconnected pores, α leans toward 0, and that pore pressure exerts virtually no influence on rock behavior. On the contrary, in highly porous, compliant, loose formation α tends to 1, and pore pressure has a maximum effect (Zoback, 2007). In most petroleum rock mechanics applications, the Biot coefficient varies between 0,8 and 1,0 (Aadnøy and Looyeh, 2011). However, the rock matrix of tight sandstones and shales may have a Biot coefficient as low as 0,5 (Espinoza, 2021).

5.4.2. Linear Mohr-Coulomb failure criterion

In simple terminology, Mohr-Coulomb (M-C) Failure Criterion is a theoretical model that describes strength as a function of cohesion (S_0) and angle of internal friction (ϕ). This criterion relates the shearing resistance to the contact forces and friction between two rock

“bodies” (Fjær et al., 2008). The friction angle represents the minimum angle of the inclined surface, which causes a superimposed block of similar material to slide (usually $25^\circ < \varphi < 45^\circ$). Cohesion represents the shear strength of the rock at zero normal stress (Aadnøy and Looyeh, 2011). Analogously, once the peak strength is exceeded and rock fails, cohesion vanishes, and residual strength is controlled only by friction, proportional to the magnitude of normal stress (Zoback, 2007). Analogously, The M-C criterion expresses the shear strength along the plane subjected to a triaxial state of stress as a linear relationship between the normal stress exerted onto the plane and shear stresses acting along the plane at the moment of failure. The latter clause is crucial as it indicates that material fails once a linear relationship (given by the Eq. (5-24)) is met:

$$\tau = S_0 + \sigma_n \mu_i \quad (5-24)$$

Where μ_i is the dimensionless coefficient of internal friction represented by the slope such that:

$$\mu_i = \tan \varphi \quad (5-25)$$

and S_0 , the intercept of a linear M-C Failure line. Since S_0 is not a physically measurable parameter, it is more convenient to express rock strength in Uniaxial Compressive Strength (UCS). Relationship between UCS and S_0 is given by equation

$$UCS = 2S_0[(\mu_i^2 + 1)^{1/2} + \mu_i] \quad (5-26)$$

5.4.3. Alternative expression for Mohr-Coulomb failure criterion

Assume a continuous homogeneous material, subjected to a constant force field over an infinitesimally small, static, square area. The state of stress acting on a plane can be described using a 2D tensor notation. Here, only x and y faces of the element are subjected to stresses, all of which are acting parallel to either the x-axis or y-axis. Normal and a shearing component of stress tensor will act on each side of 2D element to maintain equilibrium. However, the magnitude of these components depends on the plane orientation. For an arbitrarily plane, stress can be expressed in terms of the stresses acting on the x-y element by using equations of static equilibrium. From the condition of the force equilibrium, the resultant of the forces acting along the x and y-axis must be equal to zero. Likewise, the rotational equilibrium implies that the moments must also be equal to zero (thus $\tau_{xy} = \tau_{yx}$).

If conditions are satisfied, the state of in-plane stress can be represented by using only three stress components, i.e., σ_x , σ_y , and τ_{xy} . Here, certain transformation rules are required to relate normal, and shear stresses acting on the arbitrarily plane to the 2D stress tensor components (Gere and Timoshenko, 1991). By setting equilibrium conditions for plane stress conditions (as depicted in figure 5-8.) and implementing basic trigonometric identities, transformation relations are given by Eq. (5-27) and Eq. (5-28):

$$\sigma_n = \frac{1}{2}(\sigma_{xx} + \sigma_{yy}) + \frac{1}{2}(\sigma_{xx} - \sigma_{yy}) \cos 2\theta + \tau_{xy} \sin 2\theta \quad (5-27)$$

$$\tau = \frac{1}{2}(\sigma_{yy} - \sigma_{xx}) \sin 2\theta + \tau_{xy} \cos 2\theta \quad (5-28)$$

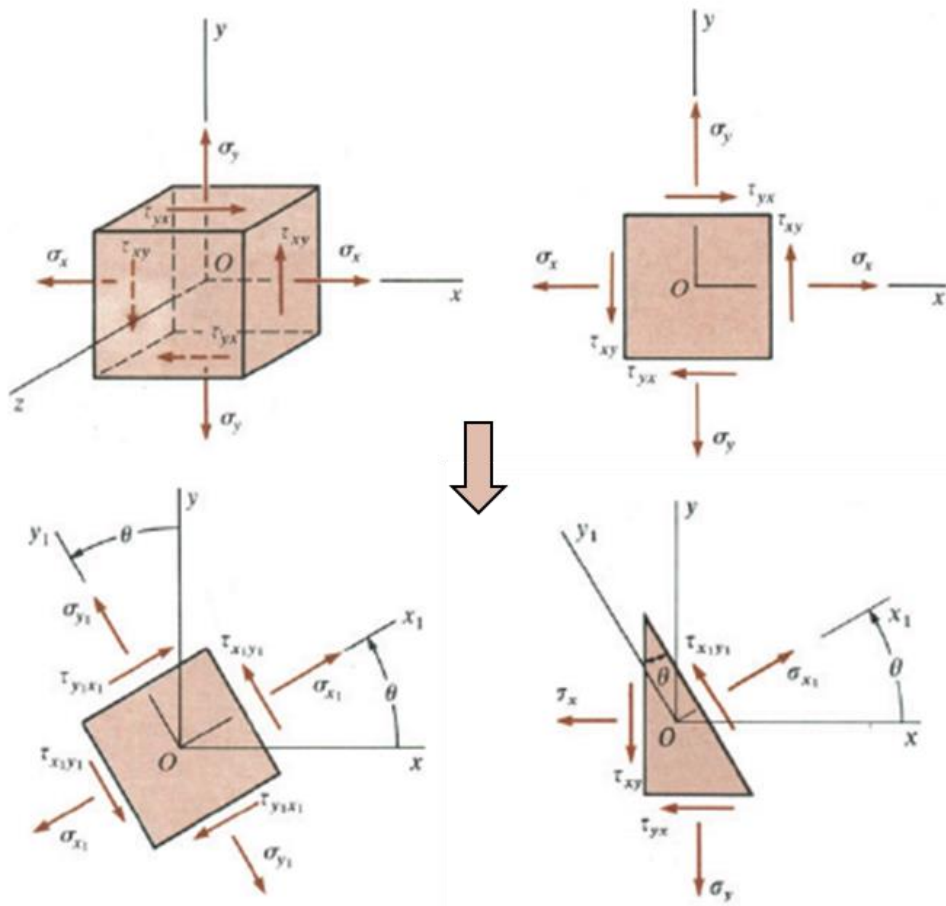


Figure 5-8. Representation of 2D Tensor components acting on the arbitrarily cut plane (modified from Gere and Timoshenko, 1991)

The equations (5-27 and 5-28)¹² represent the transformation equations for plane stress conditions and can be utilized to calculate normal, and shear stresses for any orientation of the 2D plane stress element of interest. Similarly, we can assume that plane can be oriented in such a way where shear components vanish, and only principal stress remains. Since overall stress can neither increase nor decrease, acting stress components must change in magnitude. Transformation equations can be differentiated and solved to obtain the alternate description of the state of stress acting on a plane (Gere and Timoshenko, 1991):

$$\sigma_n = \frac{1}{2}(\sigma_1 + \sigma_3) + \frac{1}{2}(\sigma_1 - \sigma_3) \cos 2\theta \quad (5-29)$$

$$\tau = \frac{1}{2}(\sigma_1 - \sigma_3) \sin 2\theta \quad (5-30)$$

Corresponding normal stresses (σ_1 and σ_3) are the principal stresses. Since the principal planes are mutually perpendicular, according to Eq. (5-30) the failure in isotropic material (rock) occurs at 45° relative to principal planes, as such orientation raises the maximum shear stress value.

Also, Eq. (5-29) and Eq. (5-30) represent an alternative expression of M-C failure criteria. If plotted in $\tau - \sigma_n$ coordinates, these equations define a circle (figure 5-9b. and 5-9c.). Such graphic representation of the stress state at a given point is called Mohr's Circle. The circle's position and diameter on the σ_n axis are defined by the magnitude of principal stresses, σ_1 , and σ_3 . The circle radius represents the maximum value of the shear stress a material can withstand. Any arbitrary state of stress comprising both τ and σ_n can be evaluated along the circle's circumference. A point along the circle represents the state of plane stress with the normal closing angle θ with the direction of the major principal stress (σ_1). Knowing only the magnitude of principal stresses permits graphical calculation of values of σ_n and τ and vice versa. While the linear M-C failure criterion is the simplest form of the M-C failure criterion, the usual practice is to conduct a series of triaxial tests under different confining pressure and fit results to a curve rather than a line¹³ (figure 5-9a-c.). Once a Mohr envelope

¹² Since the transformation equations are derived solely from equilibrium considerations, they are applicable to stresses in any material (Gere and Timoshenko, 1991). The same equations apply when transforming far-field stresses to cylindrical coordinates as well.

¹³ By conducting a series of triaxial tests, Hoek and Brown (1980) noted that a linear relationship does not seem suitable for describing the rock failure as it does not conveniently fit obtained results. In reality, the linearized M-C failure criterion slope is not constant but somewhat decreases under increasing confinement. Thus, a linearized M-C may overestimate rock strength in the domain of very low and very high normal

has been constructed based on test data, S_0 and μ_i by using regression techniques or finding a line equation when a linear criterion is used. To satisfy the M-C criterion, the stress state should not exceed the M-C envelope (Zoback, 2007; Fjær et al., 2008).

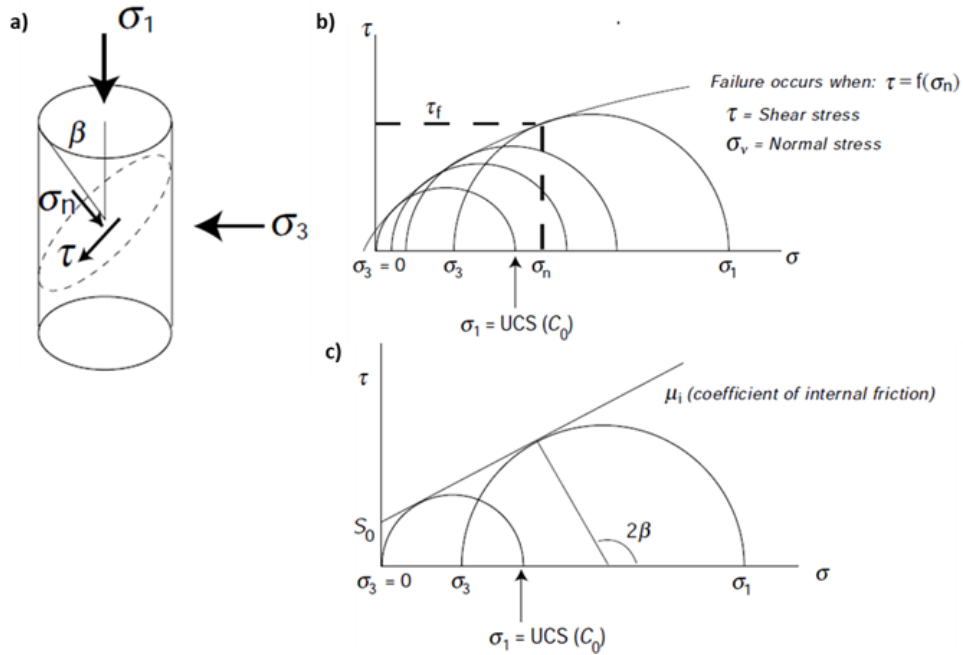


Figure 5-9. (a) Running triaxial tests on different core specimens allows (b) fitting a non-linear M-C model or (c) constructing a linearized M-C model (modified from Zoback, 2007)

Note that the angle at which rock specimen fractures (β) and the angle of internal friction ϕ embedded into a linear relationship are related to one another by the following equation:

$$\beta = 45^\circ + \frac{\phi}{2} \quad (5-31)$$

Considering a rock as a porous material and adhering to principles outlined under chapter 5.4.1., major and minor principal stresses σ_1 and σ_3 must be replaced with their effective stress counterparts. That ensures that the rock strength is a function of the effective stress rather than its absolute value. As a result, the Mohr's effective stress circle constructed from the triaxial test on a dry specimen will move leftward for a distance equal to the pore pressure's value. However, its radius will remain preserved as pore pressure counteracts all three principal stresses equally. Accordingly, Eq. (5-29) and Eq. (5-30) are rewritten to capture the effect of pore pressure:

stresses. Instead, a non-linear model is deemed more suitable for characterizing rock behavior as the mentioned drawbacks are overcome (Vallejo and Ferrer, 2011).

$$\sigma_n = \frac{1}{2}(\sigma'_1 + \sigma'_3) + \frac{1}{2}(\sigma'_1 - \sigma'_3) \cos 2\theta \quad (5-32)$$

$$\tau = \frac{1}{2}(\sigma'_1 - \sigma'_3) \sin 2\theta \quad (5-33)$$

where σ'_1 and σ'_3 are identical to $(\sigma_1 - P_p)$ and $(\sigma_3 - P_p)$, respectively.

5.4.4. Limitations of Mohr-Coulomb failure criterion

From Eq. (5-32) and Eq. (5-33) can be seen that M-C criteria, ignore the influence of intermediate principal stress (σ_2). Peška and Zoback (1995) showed that the intermediate principal stress significantly influences the borehole stability. Likewise, a considerable misfit is noticed when fitting test data of rocks whose failure is affected considerably by intermediate principal stress, such as Dolomite and Limestones (Zoback, 2007). To counter that finding and improve the estimate of rock failure, a series of more robust failure criteria were introduced over the years, such as Drucker-Prager, modified Lade, modified Wiebols-Cook, Mogi-Coulomb, etc. (see e.g., Fjær et al., 2008). However, the failure envelope size plays a more important role than its exact shape in practice. For example, Al-Ajmi and Zimmerman (2006) have shown that the Drucker-Prager criterion tends to overestimate rock strength, whereas the M-C underestimates it. However, when applied to wellbore stability problems in relatively strong rocks, it was shown that the M-C criterion yields reliable results. On the contrary, the modified Lade and modified Wiebols-Cook perform very well in weaker rocks (Zoback, 2007; Aadnøy and Looyeh, 2011).

5.5. Rock Failure

Failure occurs when the rock cannot sustain the forces applied, and the stress reaches a maximum value corresponding to the peak strength of the material. Ergo, the maximum stress state at which a rock loses its ability to support applied stress (Zoback, 2007). The direction of the failure surface will depend on both the direction of applied forces and, if present, the anisotropies in rock material (either at the microscopic level or the macroscopic level) (Vallejo and Ferrer, 2011; Espinoza, 2021). Rock yield¹⁴ and failure can happen due

¹⁴ At certain level of deformation, the rock losses its ability to sustain elastic behaviour and onset of ductile or plastic deformation is reached, i.e., Yield Point (YP). Here the linear relationship between stress and strain vanishes. Beyond this point the rock may still withstand considerable deformation before reaching its ultimate strength and total failure. The deformation increment required to reach ultimate compressive strength is dependent on rock brittleness; for brittle rocks YP and are either very close or coincide, but substantial deformation increment exist in ductile rocks.

to tensile stresses, shear stresses, compressive stresses, and a combination of all three (Zoback, 2007).

5.5.1. Compressive failure

Compressive failure can be either brittle (abrupt) or ductile (progressive) failure. The type of failure will depend on the rock's brittleness, which characterizes strain localization and energy rate release with failure. Factors affecting brittleness include, but are not limited to, the material constituting a rock, temperature, loading rate, and effective mean stress. Under compression, brittle rocks fail quickly and along well-defined shear planes¹⁵, showing well-defined peak stress on the stress-strain curve. The deformation mechanism is predominantly elastic, and once catastrophic failure occurs, material weakens and essentially loses all its strength. The failure surface created under the brittle failure conditions results from the generation and eventual coalescence of numerous fracture surfaces throughout the rock (Zoback, 2007; Vallejo and Ferrer, 2011).

On the contrary, ductile rocks fail gradually rather than abruptly. Here, deformation is predominantly plastic, and as strain is distributed during failure, such material frequently poses no well-defined peak strength. These rocks can even increase strength with increasing deformation (so-called strain-hardening rocks) (Vallejo and Ferrer, 2011; Espinoza, 2021). The peak strength is higher for rocks under confining conditions than rocks without confinement (e.g., uniaxially loaded core cylinder). The increment in peak stress will be a function of the internal frictional strength of the rock, i.e., both the cohesive rock strength and the applied normal effective compressive stress (Espinoza, 2021). As observed in figure 5-10., the rock fails along a shear plane at low confining pressures, but only partially. A well-defined plane will result from increasing confining pressure, and by increasing the confining pressure further, the rock sample will deform plastically and fail along numerous planes.

¹⁵ Although the stress state is governed by compressive loads, the raise of deviatoric stress causes the material to fail in shear rather than in compressive mode. Thus, it would be more practical to characterize compressive failure as a shear failure. However, approach to nomenclature varies across the literature. The author opted to follow the nomenclature as outlined in Zoback (2007).

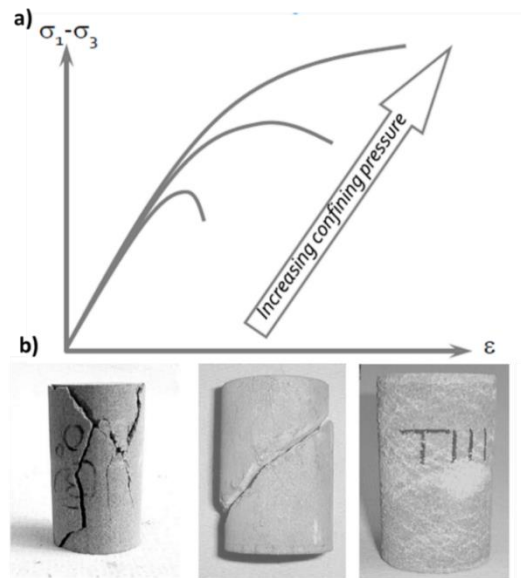


Figure 5-10. The effect of the confining pressure on the (a) compressive rock strength and (b) compressive failure modes (Schlumberger, 2021)

5.5.2. Tensile failure

Compared to the compressional strength of rock, the tensile strength of rock is relatively unimportant. The main reason is that the rock tensile strength is relatively low, often not exceeding a few MPa (Zoback, 2007). Furthermore, in rocks with pre-existing flaws, tensile strength would be expected to be near zero. More importantly, in situ stress is never tensile (Aadnøy and Looyeh, 2011). Still, tensile failure can occur around wellbores in particular stress states if the stress concentration at the wellbore wall exceeds tensile strength. Examples include drilling-induced tensile fractures and hydraulic fracturing. Unlike compressional strength, tensile strength does not seem to be dependent on effective stress, especially in low-porosity/low-permeability rocks (Zoback, 2007).

5.5.3. Shear failure

A rock loaded hydrostatically is unlikely to fail, except when highly porous rock is subjected to either extremely high mean effective stress (Volumetric failure; pore collapse) or itself is very weak (e.g., chalk) (Zoback, 2007; Aadnøy and Looyeh, 2011). However, under the deviatoric loading, rocks can either exhibit yielding under the increased mean effective stress or simply fail by reaching the state of critical shear as a result of non-hydrostatic compression. The yield of porous rock is associated with the onset of irreversible deformation, manifested as the loss of porosity and, consequently, permeability (Zoback, 2007; Espinoza, 2021). Ergo, with increasing effective stress state beyond the yield point,

inelastic deformations become an important mechanism to failure of the porous medium. Most plastic deformation occurs due to the tendency of grains to assemble (rotate and slide) in an energetically more favorable state (lower stress positions) (Sayers and Schutyens, 2007). Importantly, as shear stress promotes reassembling of grains, the value of mean confining pressure at which porous material fails decreases with increased shear stress. As a result, a state of high compression enhanced by shear can lead to grain re-orientation or crushing, resulting in denser packing with increased grain contact (Espinoza, 2021). This phenomenon is called shear-enhanced compaction, and it is utterly important for long-term field development strategies. The yielding behavior of rocks is often represented using yield surfaces of constant porosity (so-called "end caps"). These "end-caps" represent the locus of points that have reached the same volumetric plastic strain, and their exact position and shape depend on the properties of the examined rock (Zoback, 2007). However, all the rock failure modes are usually unified under a single failure envelope defined by laboratory testing (Zoback, 2007; Schlumberger, 2021). As per figure 5-11., a stable area, i.e., an area under which only elastic deformation occurs is retained within the failure envelope. Otherwise, the rock splits (tension failure) if the stress state exceeds tensile strength. Likewise, shearing will be experienced if the stress state is pushed across the linear part of the envelope (indicated by green arrows). The volumetric failure (either pore collapse or shear-enhanced compaction) occurs where the curved part of the envelope, the end cap, is exceeded (indicated by red arrows).

Usually, it is more common to represent the failure envelope in P - q space where:

$$P = \frac{1}{3} \Gamma_1 = \frac{1}{3} \text{tr}\{\sigma_{ij}\} = \frac{1}{3} (\sigma_1 + \sigma_2 + \sigma_3) \quad (5-34)$$

$$q = \sqrt{3J_2} = \sqrt{\frac{1}{2} [(\sigma_1 - \sigma_2)^2 + (\sigma_2 - \sigma_3)^2 + (\sigma_3 - \sigma_1)^2]} \quad (5-2)$$

Where σ_{ij} is the effective stress tensor as given in Figure 5-7, Γ_1 is invariant of the effective stress tensor and J_2 is the second invariant of deviatoric stress tensor¹⁶.

¹⁶ ($q_{ij} = \sigma_{ij} - P\delta_{ij}$).

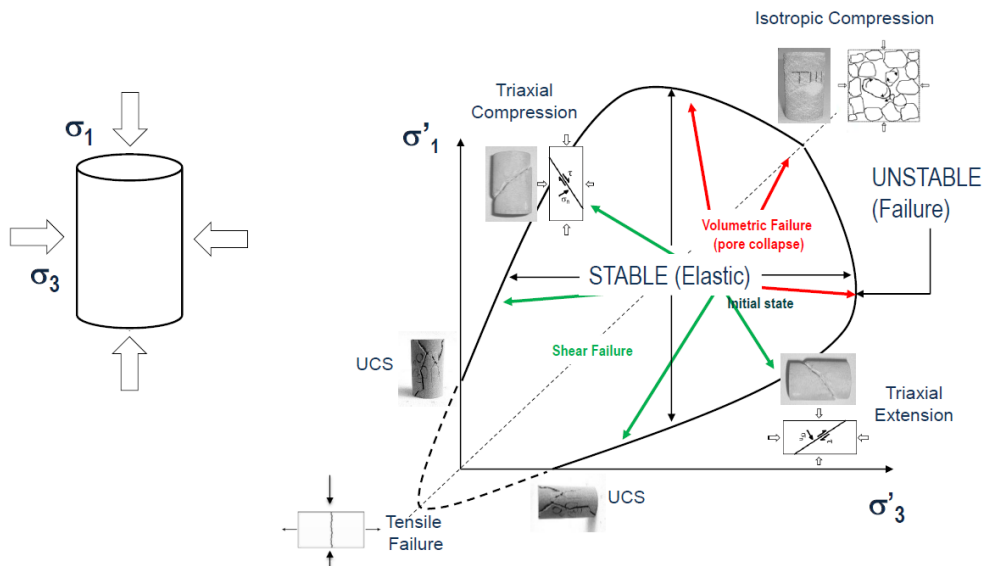


Figure 5-11. Failure envelope in principal stress space (Schlumberger, 2021)

Note that if the in-situ stress state stays within the domain bounded by the failure envelope (figure 5-12.), the formation should not undergo plastic deformation. At relatively low P and high q, rock failure typically occurs by localized shear along a plane oriented at some angle relative to the principal stress axes (e.g., as described in chapter 5.4.2.). However, at relatively high P and low q, porous rocks exhibit pore collapse initiated by breakage of cement and loss of cohesion at grain contacts. The author found this topic important as numerous authors argued on the existence of shear zones adjacent to salt bodies (Fredrich et al., 2003; Wilson and Fredrich, 2005; Lou et al., 2012a; Nikolinakou et al., 2012; Jackson and Hudec, 2017). Ergo the impact of shear on potential rock instabilities needs to be elaborated.

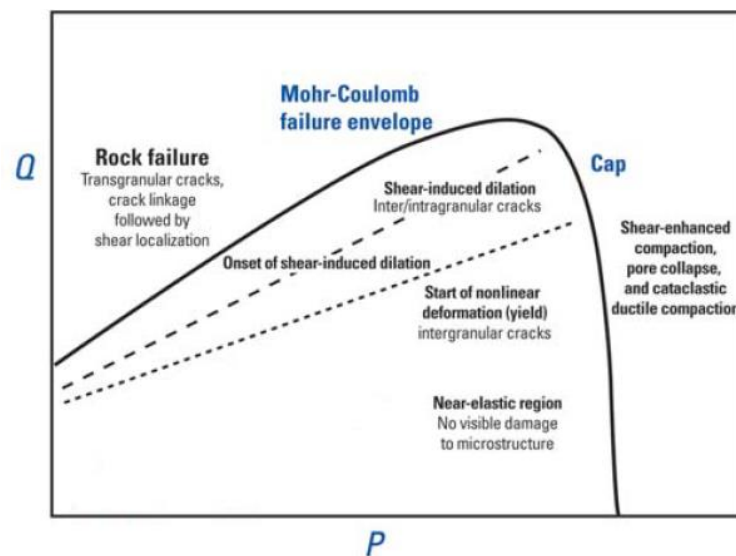


Figure 5-12. P-Q failure envelope (Sayers and Schutyens, 2007)

6. PETROLEUM ROCK MECHANICS IN THE FUNCTION OF WELLBORE STABILITY

As mentioned above, many failure criteria have been developed over the years and extensively explained across the literature (e.g., Zoback, 2007; Fjær et al., 2008). However, no single of them is applicable to characterize the failure of all the rocks. To apply the appropriate and most suitable criteria for wellbore construction associated problems, understanding and physical interpretation of those criteria must exist. In order to ensure safe drilling operations and efficient well design, several factors must be assessed during the well planning. These include (Aadnøy and Looyeh, 2011):

- in-situ stress and mechanical rock properties,
- formation FG,
- formation PP distribution,
- casing depth selection and design.

In-situ stresses and mechanical rock properties are crucial factors for wellbore design. Since engineering work modifies the state of stress to which rock is subjected on a very short timescale, it is essential to understand the a priori state of stress. That allows one to understand the redistribution of natural stresses upon a proposed activity (Vallejo and Ferrer, 2011). Ergo, no estimate of formation pore and fracture gradients and borehole failure evaluation can be conducted before assessing in situ conditions. By understanding stress state and mechanical rock properties, well planning team can:

- inspect the magnitude and orientation of the major principal stresses,
- understand the stress effects which may affect well construction,
- identify the directions and modes in which the formation rock is likely to fail,
- provide input for a wellbore stability analysis.

6.1. In-situ stress

In practical applications, because the stresses acting in the earth at depth are intensely concentrated around wellbores, it is of higher importance to correctly estimate the in-situ stresses rather than obtain exact values of rock strength and deformability (Zoback, 2007).

6.1.1. Andersonian stress classification

Rocks underground are subjected to various stresses whose magnitude and direction are determined by the sources they are generated from. The original, unperturbed state of stress to which formation is subjected is considered an in-situ stress state (often called far-field stress state) (Aadnøy and Looyeh, 2011). Global patterns of tectonic stress are meant to be the main drivers of the stress variations. The relative movement of tectonic plates is governed by convection of the mantle, resultant buoyant forces to which plates are subjected, and the ongoing erosion (Griffiths, 2009). Based on the relative movement of tectonic plates and their interaction, linear features that exist at their boundaries can be divided into convergent, divergent and strike-slip margins (figure 6-1.).

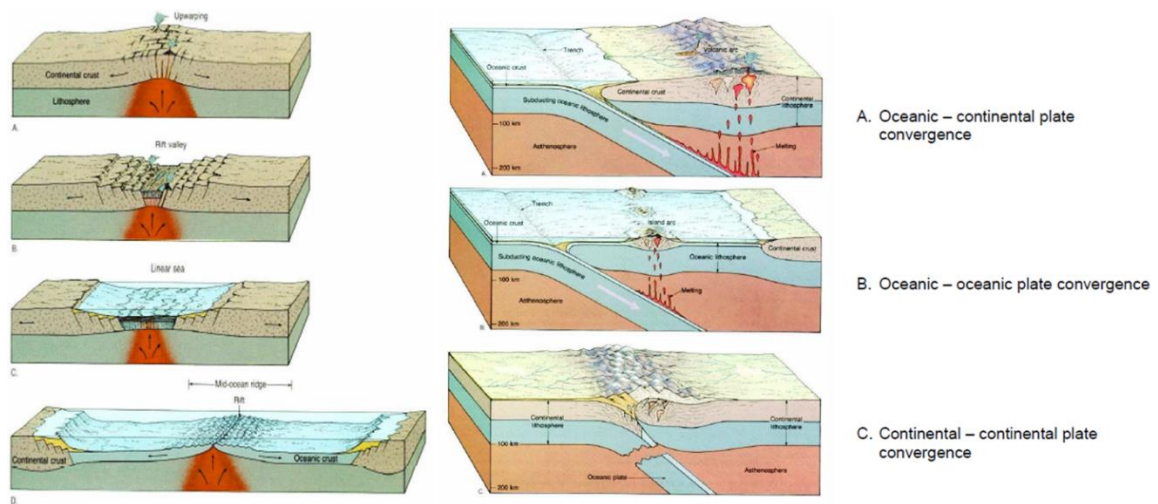


Figure 6-1. Representation of convergent (left) and divergent (right) margins (Griffths, 2009)

As discussed, three principal stresses can fully characterize the state of stress. These stresses are mutually independent, perpendicular normal stresses acting to a plane where no shear stress is applied. Given the assumption that the earth's surface acts as a free surface, one of the principal stresses is usually assumed to be vertical (S_v). Accordingly, the other two principal stresses must be horizontal (S_H and S_h ; figure 6-2.). The vertical or overburden stress exists mainly due to the weight of the overlying formations and the fluids they contain (Aadnøy and Looyeh, 2011).

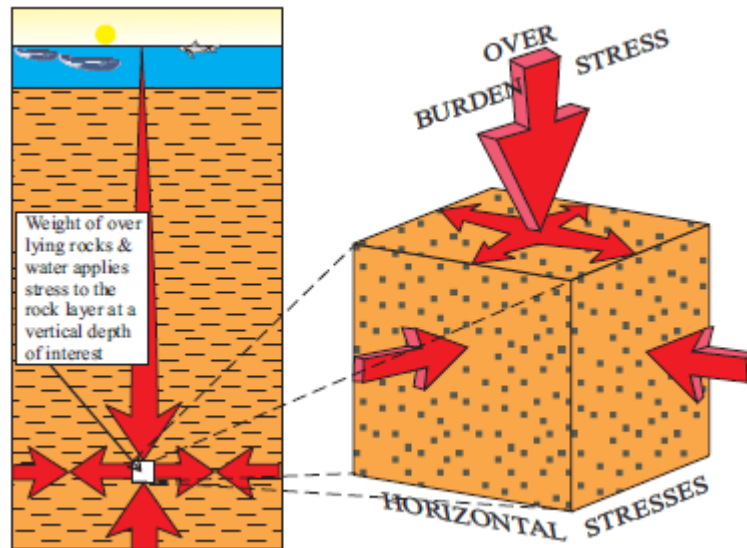


Figure 6-2. Schematic representation of in-situ stresses acting on the infinitesimal subsurface element (Amoco, 1996)

However, other sources such as salt emplacement can give substantial rise to in-situ vertical stress. In tectonically relaxed areas, the lateral movement caused by the overburden stress can be considered as the sole driver of the evolution of horizontal stresses. Namely, adjacently constrained rocks tend to spread and expand horizontally because Poisson's ratio gives rise to, virtually equal, two lateral horizontal stresses. In tectonically active areas, plate movement tends to either amplify or reduce values of horizontal stresses. While convergent plates promote horizontal compression, divergent plates decrease it (Schlumberger, 2021). Whereas overburden can be nearly precisely calculated from density logs, horizontal stresses can be only bounded using techniques that rely on specific assumptions (Zoback, 2007, Aadnøy and Looyeh, 2011). Besides tectonic activity, geologic anomalies or salt emplacement can cause variations in horizontal stresses, thus disallowing their quantification. Aadnøy and Looyeh (2011) indicated that the in-situ stress field is typically non-hydrostatic, i.e., all three principal stresses exhibit different magnitudes. Generally, stress fields in sedimentary basins can be divided into three distinct groups according to the Andersonian classification. The Schematic is given in figure 6-3.

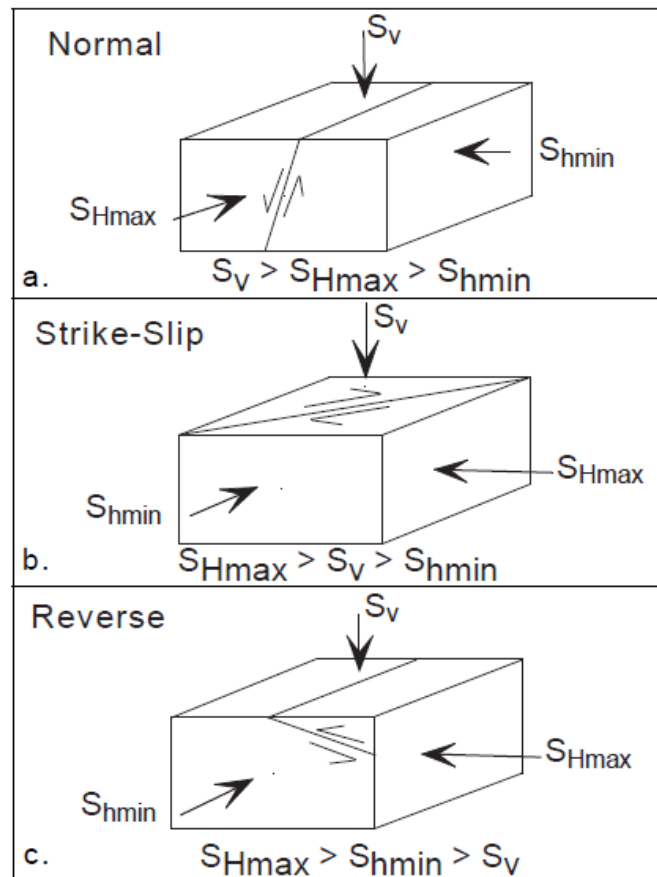


Figure 6-3. Andersonian classification of stress states (Zoback, 2007)

- Normal faulting (NF) regime occurs in tectonically passive or extensional environments such that principal stress relative magnitudes are given as follows: $S_1 = S_v > S_2 = S_H > S_3 = S_h$;
- Strike slip (SS) faulting regime occurs in "mild" tectonically compressive environments, such that principal stress relative magnitudes are given as follows: $S_1 = S_H > S_2 = S_v > S_3 = S_h$;
- Reverse faulting (RF) regime occurs in "strong" tectonically compressive environments such that principal stress relative magnitudes are given as follows: $S_1 = S_H > S_2 = S_h > S_3 = S_v$.

Figure 6-4. exemplifies the stress profile schematic assuming linear elasticity and constant Young's modulus with depth. Observe that horizontal stresses are lower than the overburden stress in a relaxed depositional geological setting. However, in strongly tectonically active stress regimes, the horizontal stresses exceed the vertical stress. In reality, a combination of these regimes often coexists, i.e., normal-strike slip and strike slip-reverse (Zoback, 2007; Espinoza, 2021).

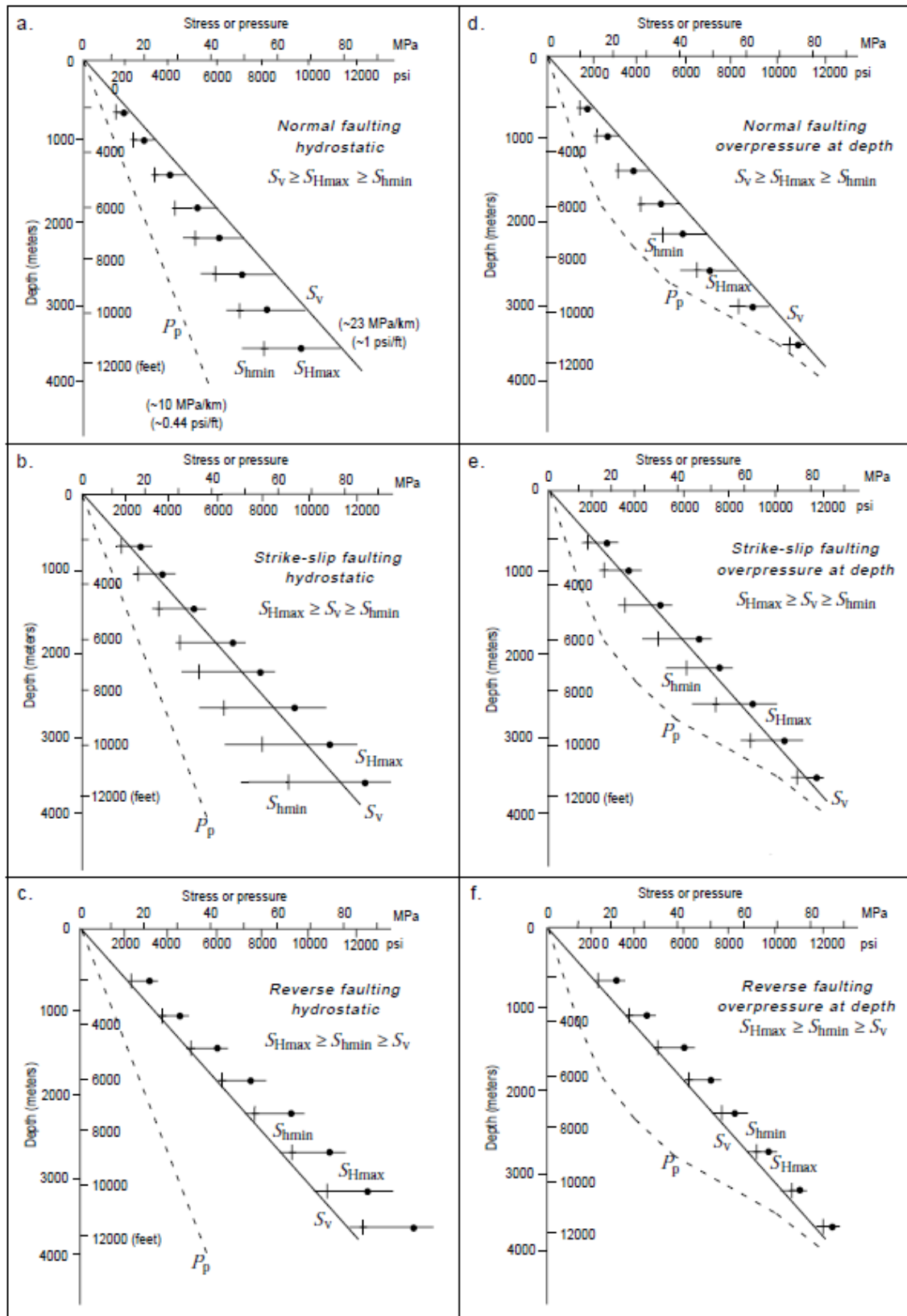


Figure 6-4. General stress-depth relation of principal stresses in different tectonic environments (Zoback, 2007)

Assuming that rock is treated as a poroelastic, Eq. (6-1) and Eq. (6-2) can be utilized to estimate values of the total horizontal stresses (Espinoza, 2021; Schlumberger, 2021):

$$S_H = \frac{\nu}{1-\nu} S_v - \frac{\nu}{1-\nu} \alpha P_p + \alpha P_p + \frac{E}{1-\nu^2} \varepsilon_{xx} + \frac{\nu E}{1-\nu^2} \varepsilon_{yy} \quad (6-1)$$

$$S_h = \frac{\nu}{1-\nu} S_v - \frac{\nu}{1-\nu} \alpha P_p + \alpha P_p + \frac{\nu E}{1-\nu^2} \varepsilon_{xx} + \frac{E}{1-\nu^2} \varepsilon_{yy} \quad (6-2)$$

Where ε_{xx} is the maximum (compressive) tectonic strain, and ε_{yy} the minimum (compressive) tectonic strain in each direction, S_v overburden stress, while ν and α represent Poisson's and Biot's coefficients, respectively. Note that the last two terms in the equations mentioned above vanish in tectonically relaxed areas, i.e., horizontal stresses are equal.

6.2. Stress concentration around a vertical wellbore

As a circular borehole is created, the formation surrounding the wellbore wall becomes subject to a stress concentration (figure 6-5.). Assuming overburden stress as principal stress, cylindrical wellbore drilled in isotropic, elastic medium, state of stress can be described using Kirsch equations (for derivation, see Fjær et al., 2008), state of stress can be represented by:

- radial stress component acting along the wellbore radius (σ_{rr}),
- hoop (tangential) stress acting around the wellbore circumference ($\sigma_{\theta\theta}$),
- axial stress acting parallel to the vertical (σ_{zz})
- additional shear stress components, which in case of vertical wellbore vanish¹⁷

¹⁷ In a vertical wellbore where its axis is aligned with one principal stress, a self-supporting wellbore wall acts the principal planes, and thus cannot sustain shear stresses (Zoback, 2007; Vallejo and Ferrer, 2011).

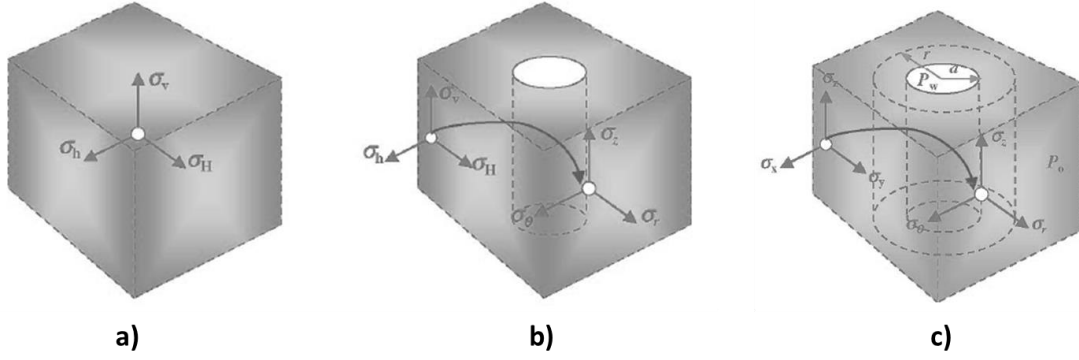


Figure 6-5. (a) Rock formation with uniform stress state, (b) rock formation with a drilled hole that perturbs in-situ stresses, and (c) distribution of stresses around a wellbore (Aadnøy and Looyeh, 2011)

The general elastic Kirsch's solution (1898) can be utilized to relate stresses acting around a cylindrical wellbore placed along a principal stress direction (assuming a perfect mud-cake):

$$\sigma_{rr} = \frac{1}{2}(\sigma_H + \sigma_h) \left(1 - \frac{R^2}{r^2}\right) + \frac{1}{2}(\sigma_H - \sigma_h) \left(1 - \frac{4R^2}{r^2} + \frac{3R^4}{r^4}\right) \cos 2\theta + \frac{\Delta PR^2}{r^2} \quad (6-3)$$

$$\sigma_{\theta\theta} = \frac{1}{2}(\sigma_H + \sigma_h) \left(1 + \frac{R^2}{r^2}\right) - \frac{1}{2}(\sigma_H - \sigma_h) \left(1 + \frac{3R^4}{r^4}\right) \cos 2\theta - \frac{\Delta PR^2}{r^2} + \sigma_{\Delta T} \quad (6-4)$$

$$\sigma_{zz} = \sigma_v - 2\nu(\sigma_H - \sigma_h) \left(\frac{R^2}{r^2}\right) \cos 2\theta + \sigma_{\Delta T} \quad (6-5)$$

$$\tau_{r\theta} = \frac{1}{2}(\sigma_H - \sigma_h) \left(1 + \frac{2R^2}{r^2} - \frac{3R^4}{r^4}\right) \sin 2\theta \quad (6-6)$$

Where $\sigma_{\theta\theta}$, σ_{rr} , σ_{zz} are tangential (hoop), radial and vertical effective stresses, respectively. $\tau_{r\theta}$ is the shear stress in a plane perpendicular to r in tangential direction θ , R is wellbore radius, r distance measured from wellbore center, θ angle between the azimuth of S_H along the wellbore and ΔP pressure differential across the wellbore wall such that:

$$\Delta P = P_w - P_p \quad (6-7)$$

Where P_w and P_p are pressure exerted on the wellbore wall by mud and the pore pressure, respectively. The term $\sigma_{\Delta T}$ represents the contribution of thermal stress caused by the difference in mud and the formation temperature such that:

$$\sigma_{\Delta T} = \left(\frac{\alpha_t E}{1 - \nu} \right) \Delta T \quad (6-8)$$

Where α_t is the linear thermal expansion coefficient and ΔT is the change in temperature such that:

$$\Delta T = T_w - T_b \quad (6-9)$$

Where T_w and T_b are mud and formation temperature, respectively. Note that $\sigma_{\Delta T} < 0$ for $\Delta T < 0$ applies and that the radial stress remains unchanged regardless of any temperature changes.

As the equations (6-3) to (6-6) are independent of Young's modulus, they can apply to any formation in which a vertical borehole is drilled. The stress concentration varies with the angular position and the distance around and from the wellbore wall, respectively. By looking at figure 6-6., it can be noted that the value of the highest hoop stress coincides with the direction of the least principal stress (compression increases hoop stress). On the contrary, the hoop stress values converge toward zero at the azimuth of maximum principal stress as a relatively significant difference between two horizontal stresses exists. Highly perturbed stresses reach their extrema at the wellbore wall. Accordingly, any borehole failure is supposed to initiate at the wellbore wall. This stress perturbation can extend up to a few wellbore diameters away from the wellbore central axis (Zoback, 2007). At the distance of approximately three wellbore radii, stresses relax back to values virtually equal to far-field stresses (Schlumberger, 2021).

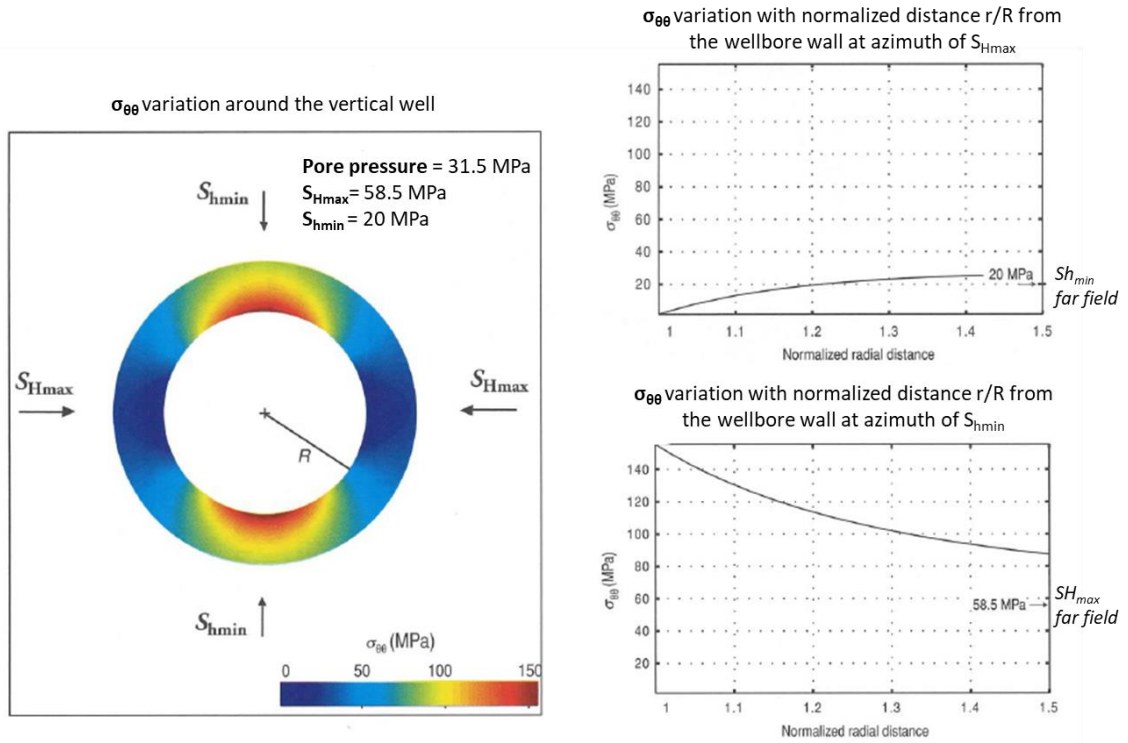


Figure 6-6. Hoop stress variation around the vertical wellbore as a function of normalized distance (modified from Zoback, 2007)

6.2.1. Wellbore stability in vertical wells

Accordingly, by setting $R = r$ and substituting, the stresses acting at the wellbore wall can be estimated through the following equations:

$$\sigma'_{rr} = \Delta P \quad (6-10)$$

$$\sigma'_{\theta\theta} = (\sigma'_H + \sigma'_h) - 2(\sigma'_H - \sigma'_h)\cos 2\theta - \Delta P + \sigma_{\Delta T} \quad (6-11)$$

$$\sigma'_{zz} = \sigma'_v - 2\nu(\sigma'_H - \sigma'_h)\cos 2\theta + \sigma_{\Delta T} \quad (6-12)$$

$$\tau_{r\theta} = 0 \quad (6-13)$$

Where maxima occur at 0° and 180° , thus the point of maximum hoop stress ($\sigma'_{\theta\theta max}$) is given by:

$$\sigma'_{\theta\theta max} = 3\sigma'_H - \sigma'_h - \Delta P + \sigma_{\Delta T} \quad (6-14)$$

And minima occur at 90° and 270° ; thus, the point of minimum hoop stress ($\sigma'_{\theta\theta min}$) is given by:

$$\sigma'_{\theta\theta min} = 3\sigma'_h - \sigma'_H - \Delta P + \sigma_{\Delta T} \quad (6-15)$$

This is schematically presented in figure 6-7.

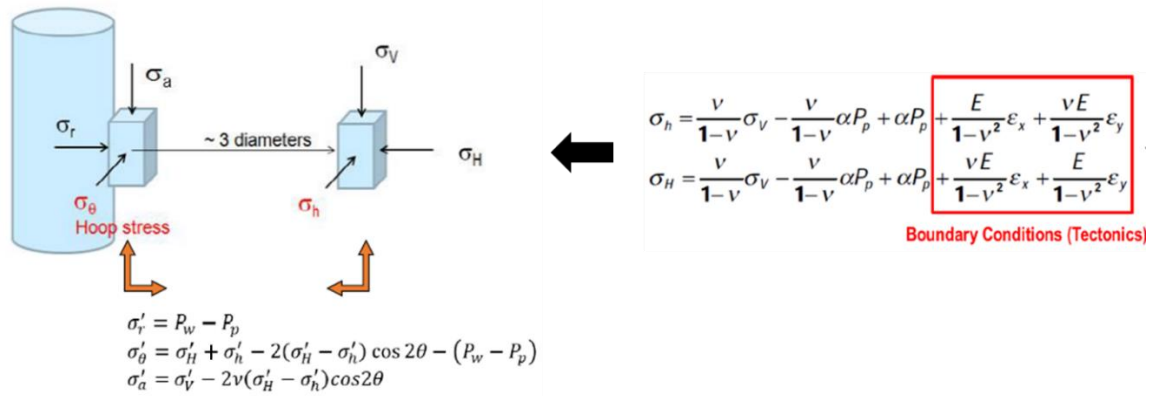


Figure 6-7. Schematic representation of stress concentration at the wellbore wall (modified from Schlumberger, 2021)

The difference between the minimum and maximum hoop stress corresponds to the amplitude of hoop stress variation around the wellbore, which represents itself in a sinusoidal manner (figure 6-8):

$$A\sigma_{\theta\theta} = \sigma'_{\theta\theta max} - \sigma'_{\theta\theta min} = 4(S_H - S_h) \quad (6-16)$$

Where $A\sigma_{\theta\theta}$ is simply amplitude of the hoop stress oscillation around the borehole wall. Having the excavated portion of underground, i.e., wellbore, exposed to the pressure of drilling fluids, the stress concentration around wellbores can lead to instability at the wellbore wall. Consequently, wellbore rock can fail in either compression or tension. Once the formation's compressive strength is exceeded, stress-induced breakouts develop. From figure 6-8., once the rock's compressive strength is exceeded (assuming peak-strength M-C failure criterion), the rock on the wellbore wall is expected to fail 180° apart (stress values in a yellow-colored domain). On the contrary, exceeding tensile strength gives rise to the creation of drilling-induced tensile wall fractures (Zoback, 2007; Aadnøy and Looyeh, 2011). Zones of very low hoop stress coincide with an azimuth of S_H , which will tend to push the stress state around the wellbore into tension. Given the very low rock's σ_T , even a small tensile stress increment can cause tensile failure (as discussed previously, a reasonable assumption is to set tensile strength to zero).

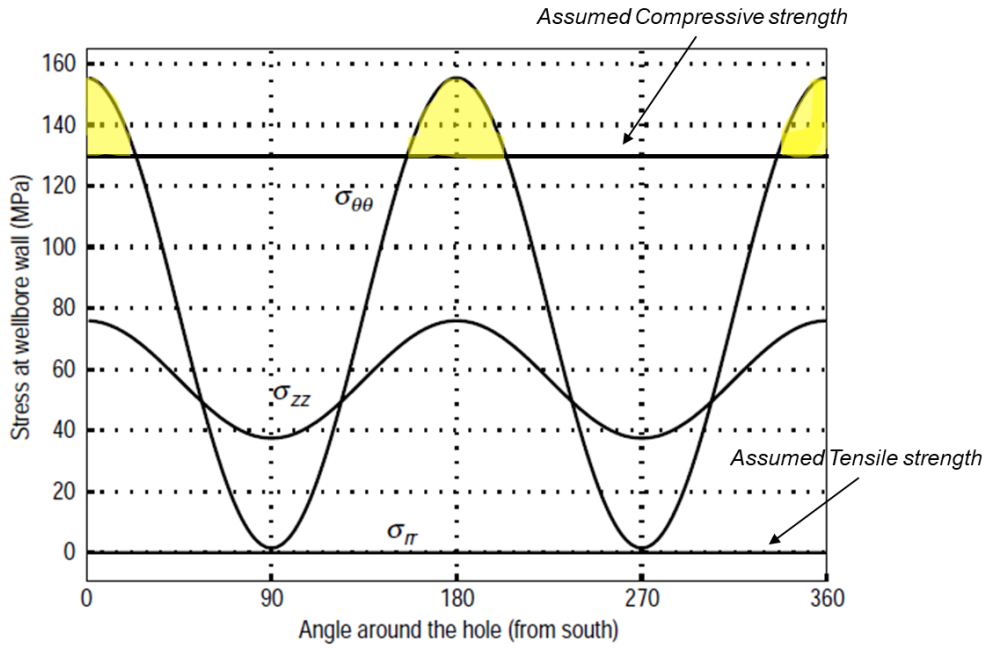


Figure 6-8. Schematic representation of stress bounds at the wellbore wall (modified from Zoback, 2007).

In tectonically relaxed areas, Eq. (6-2) enables approximation of the fracture gradient's lower bound, i.e., the pressure required to open a tensile fracture. Simply, such pressure will be equal or greater than the minimum horizontal total stress S_h (Espinoza, 2021). Assuming nil tectonic strains and $\alpha = 1$, Eq. (6.2) becomes:

$$S_h = \frac{\nu}{1 - \nu} S_v + \frac{1 - 2\nu}{1 - \nu} P_p \quad (6-17)$$

As the gradient is the derivative with respect to depth, its value can be obtained by dividing the equation with the depth interval of interest and gradient values characteristic to region of interest can be plugged-in accordingly.

Eq. (6-10) and (6-11) illustrate that mud overbalance increases radial stress while decreasing the hoop stress around all the positions along the wellbore circumference. Ergo, increasing the MW helps stabilize the wellbore. However, if imposed overbalance is too high, the stress of the state can develop such that the wellbore fails in tension. That implies that allowable limits exist within which MW must be contained (figure 6-9.).

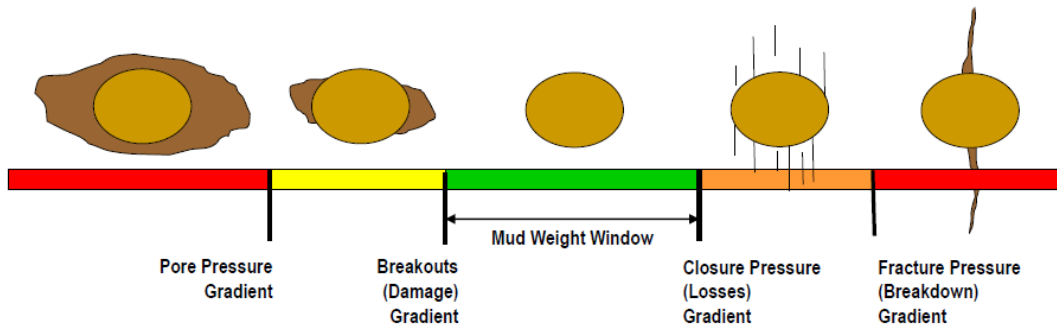


Figure 6-9. The allowable MW window (Schlumberger, 2021)

The schematic in figure 6-10. summarizes the “fast-forward” procedure for determining MW bounds in the vertical wellbore. In addition, temperature induced stresses will lead to shrinkage and stress relaxation, viz., a reduction of compression stresses. On the contrary, wellbore heating will cause the hoop stress to increase, and thus promote shear failure.

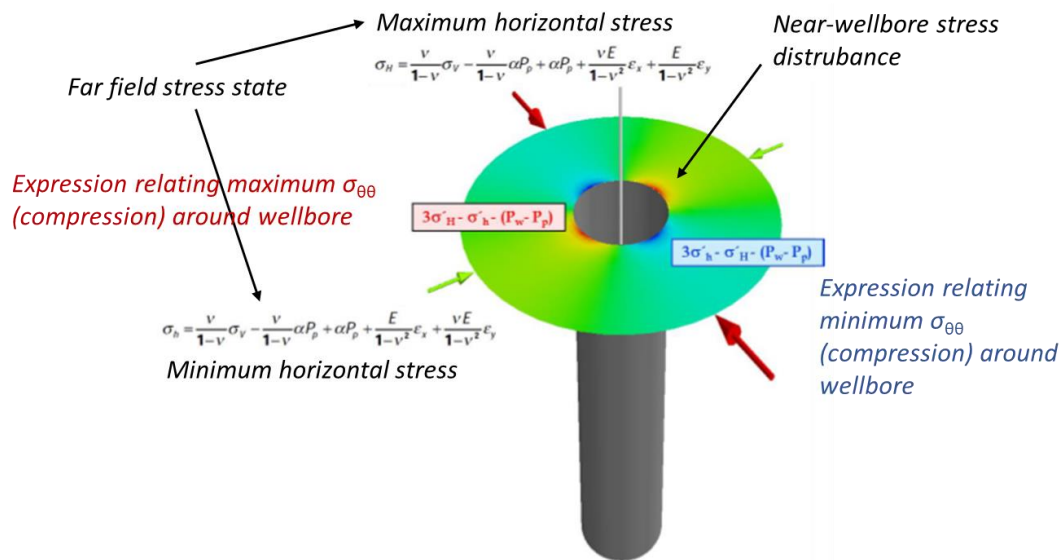


Figure 6-10. Workflow for defining an MW window in a vertical wellbore (modified from Schlumberger, 2021)

A special care must be taken to include thermal stresses in stability analysis of Deepwater wells as large temperature differences exist between circulating mud and bottomhole formation (especially important in High Temperature wells). During routine round-trip operations, shallow sections may exhibit substantial heating whereas deeper section will be cooled correspondingly. Such hoop stress variations are analogous to swab and surge pressures discussed later (Amoco, 1996; figure 6-11.).

Variations in Hoop Stress in a High Temperature Well

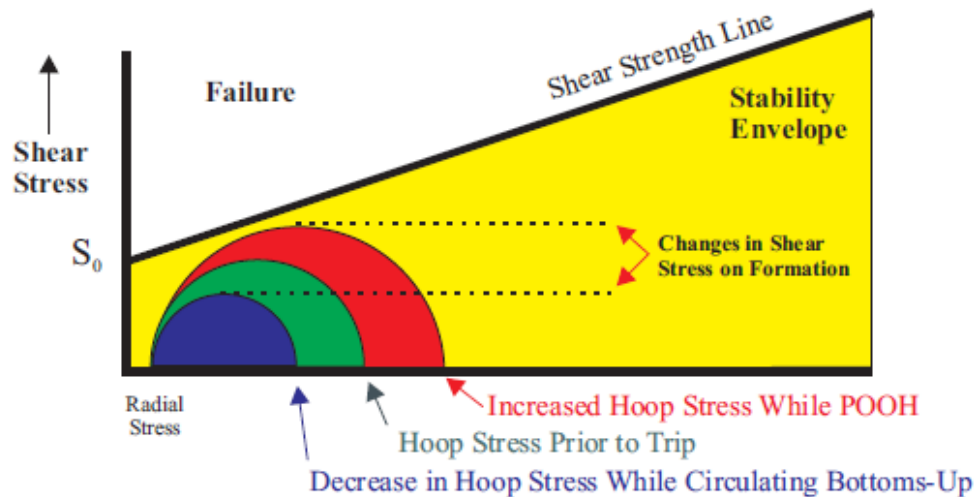


Figure 6-11. The thermal effects on the hoop stress variation (Amoco, 1996)

6.3. Stress concentration around a deviated wellbore

However, as stress is a tensor, Kirsch solutions expressed with equations (6-3) to (6-15) are no longer valid when the wellbore has deviated. Accordingly, expressions mentioned within the figure 6-10 are no longer valid to estimate the maximum, and minimum hoop stress at the wellbore wall and consequently cannot be used in constructing the MW window. As per tensor definition¹⁸, certain transformations must be applied to characterize the stress state around a deviated wellbore, i.e., under the transformation of the coordinate system to which the wellbore is referenced. Ergo, the components of a second-order tensor will change under a change of coordinate system. Furthermore, breakout and tensile fracture patterns and directions substantially vary in deviated holes from what would occur in vertical wellbores (Peška and Zoback, 1995). Once a well has deviated, the principal stresses acting in the vicinity of the wellbore wall will usually not be aligned parallel to the wellbore axis. Peška and Zoback (1995) presented a methodology that could be utilized to determine the magnitude and orientation of the stress tensor in deviated wells. Entire workflow can be found in work presented by authors, but in essence, methodology implies applying the set of transformations between different coordinate systems (see figure 6-12.), i.e., Tensor basis as follows:

¹⁸ Tensor is an abstract quantity that obeys certain coordinate transformation laws (Pattillo, 2018).

1. Defining the principal stress tensor S_{ij} and a cartesian coordinate system (X, Y, Z) referenced to principal planes to describe far-field stress state using only three principal stresses (Eq. 6-18):

$$S_{ij} = \begin{bmatrix} S_1 & 0 & 0 \\ 0 & S_2 & 0 \\ 0 & 0 & S_3 \end{bmatrix} \quad (6-18)$$

2. Tensors such as stress are often defined as mathematical entities whose components transform according to the rule (Eq. 6-19):

$$T_{new} = Q^T T Q \quad (6-19)$$

Where Q is arbitrary transformation matrix whose components contain the instruction for the change of tensor basis, Q^T its transpose and T tensor subjected to change of basis.

3. Hence, one can identify the rectangular global coordinate system (x_1, x_2, x_3) referenced to geographic coordinates. Two axes are aligned with the geographic north and east, respectively, and the third one is positioned looking vertically down. Transform principal stress field from step 1 to the newly identified global coordinate system using the following Eq. (6-20):

$$S_{kl} = R^T_{ki} S_{ij} R_{jl} \quad (6-20)$$

Where R_{jl} is transformation matrix and R^T_{ki} its transpose such that:

$$R_{jl} = \dots \begin{bmatrix} \cos \alpha \cos \beta & \sin \alpha \cos \beta & -\sin \beta \\ \cos \alpha \sin \beta \sin \gamma - \sin \alpha \cos \gamma & \sin \alpha \sin \beta \sin \gamma + \cos \alpha \cos \gamma & \cos \beta \sin \gamma \\ \cos \alpha \sin \beta \sin \gamma + \sin \alpha \cos \gamma & \sin \alpha \sin \beta \sin \gamma - \cos \alpha \cos \gamma & \cos \alpha \cos \gamma \end{bmatrix} \quad (6-21)$$

Where α, β, γ represent three Eulerian angles defining the orientation of three principal stress with respect to the geographic coordinate system.

4. Identify a third rectangular coordinate system (x_{b1}, x_{b2}, x_{b3}) of interest such that x_{b1} and x_{b3} are aligned with the wellbore radius and wellbore centreline, respectively, and x_{b2} is such that unit vectors along the three coordinate axes satisfy vector product, i.e., that x_{b3} is perpendicular to both axes x_{b1} and x_{b2} . Once the principal stresses are transformed to the global geographic rectangular coordinate system (S_{kl}), state of stress can be

transformed to the rectangular coordinate system aligned to the wellbore applying the following transformations outlined by Eq. (6-22):

$$S_{Ms} = R_{Mk} S_{kl} R_{ls}^T \quad (6-22)$$

Where R_{ls}^T is transformation matrix and R_{Mk} its transpose such that:

$$R_{Mk} = \begin{bmatrix} -\cos \delta \cos \phi & -\sin \delta \cos \phi & \sin \phi \\ \sin \delta & -\cos \delta & 0 \\ \cos \delta \sin \phi & \sin \delta \sin \phi & \cos \phi \end{bmatrix} \quad (6-23)$$

δ, ϕ represent wellbore azimuth and inclination, respectively.

5. Once the far-field stress state is re-expressed in terms of a rectangular coordinate system aligned with the local tangent to non-vertical wellbore trajectory, given the wellbore axial symmetry¹⁹, effective stress around an arbitrarily placed well σ_{Ms} such that:

$$\sigma'_{Ms} = S_{Ms} - \delta_{Ms} P_p \quad (6-24)$$

can be expressed in terms of radial, hoop, axial, and shear stresses using the following formulas given by Eq. (6-25) to Eq. (6-29):

$$\sigma'_{rr} = -P_w + \alpha P_p \quad (6-25)$$

$$\sigma'_{\theta\theta} = \sigma_{11} + \sigma_{22} - 2(\sigma_{11} - \sigma_{22}) \cos 2\theta - 4\sigma_{12} \sin 2\theta + P_m + \alpha P_p \quad (6-26)$$

$$\sigma'_{zz} = \sigma_{33} - 2\nu(\sigma_{11} - \sigma_{22}) \cos 2\theta - 4\nu\sigma_{12} \sin 2\theta + \alpha P_p \quad (6-27)$$

$$\tau_{\theta z} = 2(\sigma_{23} \cos \theta - \sigma_{13} \sin \theta) \quad (6-28)$$

$$\tau_{r\theta} = \tau_{zr} = 0 \quad (6-29)$$

¹⁹ When the geometry and loading are symmetric about the wellbore axis (z_b), the assumption of axisymmetric geometry implies $\partial/\partial\theta = 0$, along with $\sigma_{r\theta} = \sigma_{\theta r} = \sigma_{\theta z} = \sigma_{z\theta} = 0$ in a cylindrical coordinate system as displayed in figure 6-12a.

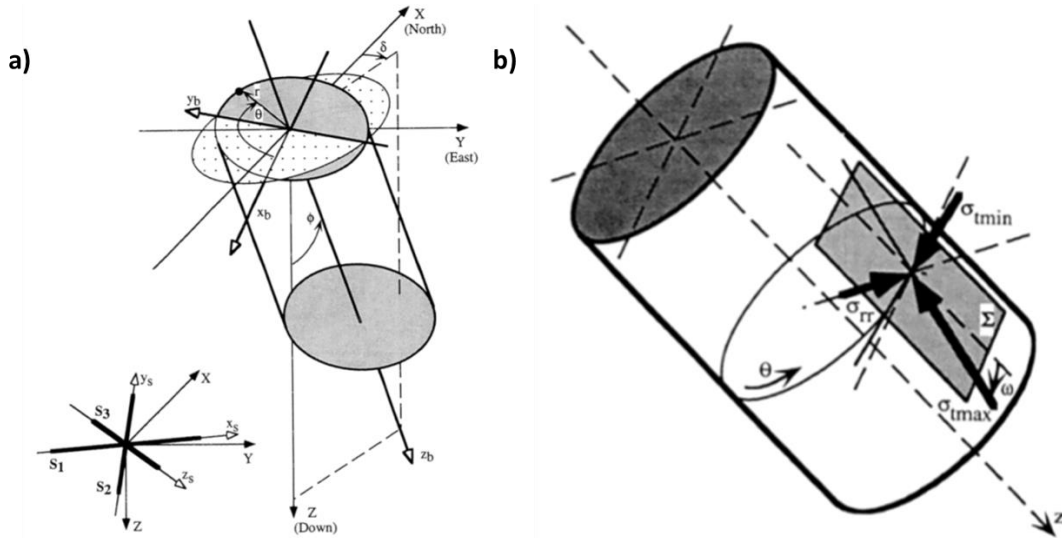


Figure 6-12. (a) The orientation of arbitrarily deviated wellbore relative to the principal stresses and (b) effective stresses obtained upon the transformation (modified from Peška and Zoback, 1995)

Figure 6-12a. represents coordinate systems of interest. Note that the borehole coordinate systems in rectangular (x_b, y_b, z_b) and cylindrical coordinates (r, ϕ, z_b) . The relation between the far-field (S_1, S_2, S_3) stress coordinate system (x_s, y_s, z_s) and the rectangular geographic coordinate system (X, Y, Z) is displayed bottom left. The azimuth δ and inclination ϕ referenced to rectangular geographic coordinates describe arbitrarily placed trajectory. Finally, maximum (σ'_{tmax}) , and minimum (σ'_{tmin}) effective stresses acting in the plane tangential to the wellbore are given by Eq. (6-30 to 6-32)²⁰:

$$\sigma'_{tmax} = \frac{1}{2} \left(\sigma'_{\theta\theta} + \sigma'_{zz} + \sqrt{(\sigma'_{zz} - \sigma'_{\theta\theta})^2 + 4\tau_{\theta z}} \right) \quad (6-30)$$

$$\sigma'_{tmin} = \frac{1}{2} \left(\sigma'_{\theta\theta} + \sigma'_{zz} - \sqrt{(\sigma'_{zz} - \sigma'_{\theta\theta})^2 + 4\tau_{\theta z}} \right) \quad (6-31)$$

$$\sigma'_{rr} = -P_w + \alpha P_p \quad (6-32)$$

²⁰ Using abovementioned equation, principal stresses (S_1, S_2, S_3) are transformed to σ'_{tmax} , σ'_{tmin} and σ_{rr} acting at the wellbore wall at a point oriented at angle θ measured from the low side of the hole. Note that σ_{tmax} and σ_{tmin} act in a plane tangential to the borehole whereas, σ_{rr} acts perpendicular to that plane. From the schematic can be seen that the maximum tangential stress, σ_{tmax} , does not coincide with the borehole axis as it was case for a vertical wellbore (figure 6-12b.).

6.3.1. Wellbore stability in deviated wells

Since radial principal stress is always perpendicular to the borehole wall, the two tangential stresses σ'_{tmin} and σ'_{tmax} act in a plane tangential to the borehole wall and are deviated by angles ω , $\omega + 90^\circ$ respectively, from the axis parallel to the wellbore centreline (Peška and Zoback, 1995). Equation (6-25) to (6-28) reduce to the simple Kirsch equations if one of the principal stresses coincides with the wellbore centreline. The maximum and minimum values of the principal stresses around the borehole define the azimuths θ_c and θ_t at which compressive or tensile failure could occur if the rock strength is exceeded (figure 6-13a.). Note that minimum effective principal (σ_{tmin}) is a function of angle θ . If MW exists such that there is an angle for which hoop stress reduces to a level where it falls under the tensile strength, fracture is initiated at the borehole wall (Ito et al., 2001). Ergo, deviated borehole fails in tension when stress is such that:

$$\sigma'_{tmin} \leq \sigma_{T0} \quad (6.33)$$

Where σ_{T0} is the rock tensile strength (convention is such that compression is positive whereas the tension is negative). Expressing Eq. (6-31) in terms of hoop stress allows it to be manipulated and inserted into Kirsch's solution and solved afterward for the wellbore pressure at which fracture is initiated at the wall of the deviated wellbore (Aadnøy and Looyeh, 2011). Opposite to wellbores whose trajectory is aligned with one of the principal stresses (e.g., vertical well and horizontal wells drilled in the direction of principal stress), in deviated wellbores where principal stress direction differs from the borehole axis, thus giving rise to shear stresses, drilling-induced tensile fractures occur in echelon, zigzag, pattern (Zoback, 2007; Aadnøy and Looyeh, 2011). Here, the angle ω defines the initial inclination of the fracture trace at the wellbore wall with respect to the wellbore centreline. Fracture propagation in deviated wells has been investigated by several authors (Aadnøy, 1990; Brudy and Zoback; 1993; Ito et al., 2001).

Mastin (1988) indicated that the stresses around the borehole wall are repeated periodically. However, they are not necessarily repeated in a sinusoidal manner, as was the case with the vertical wellbore. Moreover, there may be cases in which the hoop stress has more than one extremum in the range of $0 < \theta < \pi$ (figure 6-13b). Simply, in an arbitrarily oriented trajectory with respect to the in-situ principal stresses, the point of the wellbore failure (breakout occurrence) depends not only on the principal stresses' magnitude and orientation but the orientation of the wellbore trajectory with respect to the stress field too (Zoback, 2007).

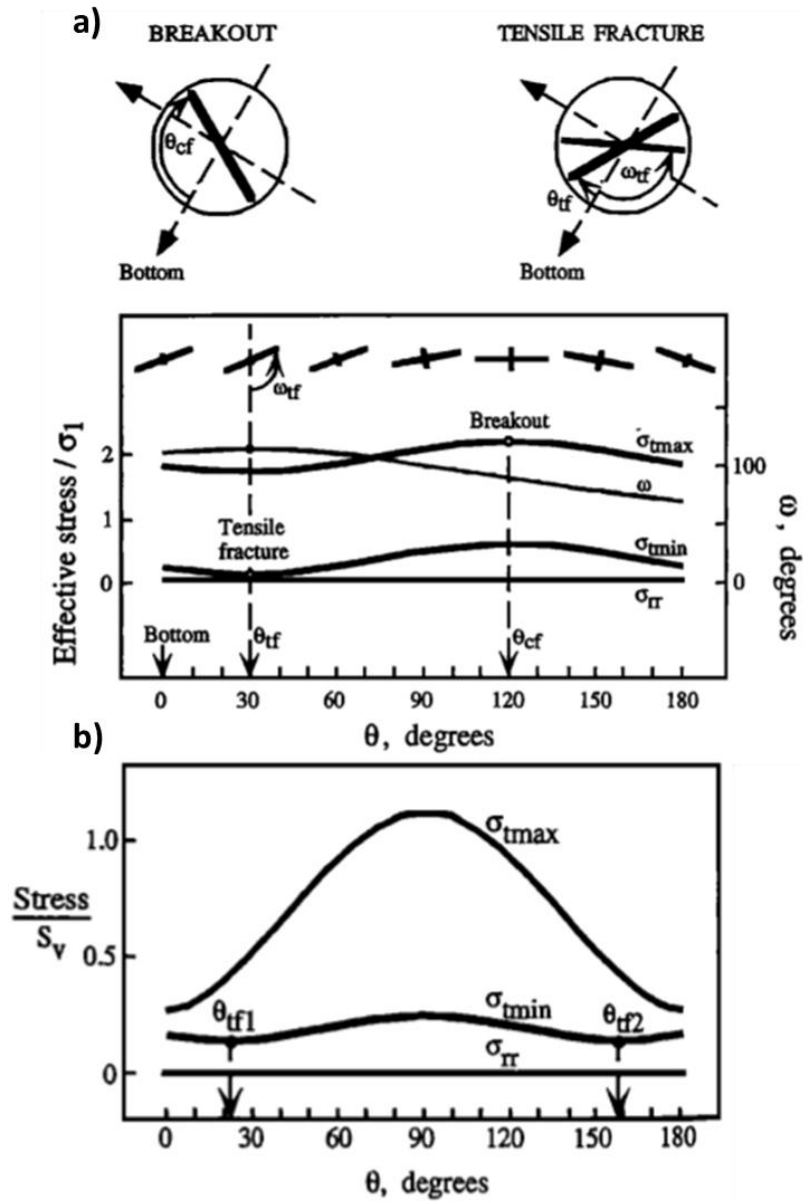


Figure 6-13. Breakout and tensile fracture creation in deviated wells (modified from Peška and Zoback, 1995)

For trajectories aligned with one of the principal stresses, one can manipulate expressions given in figure 6-7. relatively straightforwardly to constrain MW so that it does not hamper wellbore stability. Contrary to solving for critical fracture pressure in inclined and turned trajectories, it is not possible to obtain closed-form expressions that will bound necessary well pressure at which wellbore fails in shear. As Fjær et al. (2008) indicated, one shall resort to iterative methods to find a range of permissible MWs. By following the workflow by Pattillo (2018), the explanation is summarized within figure 6-14. for the reader's convenience.

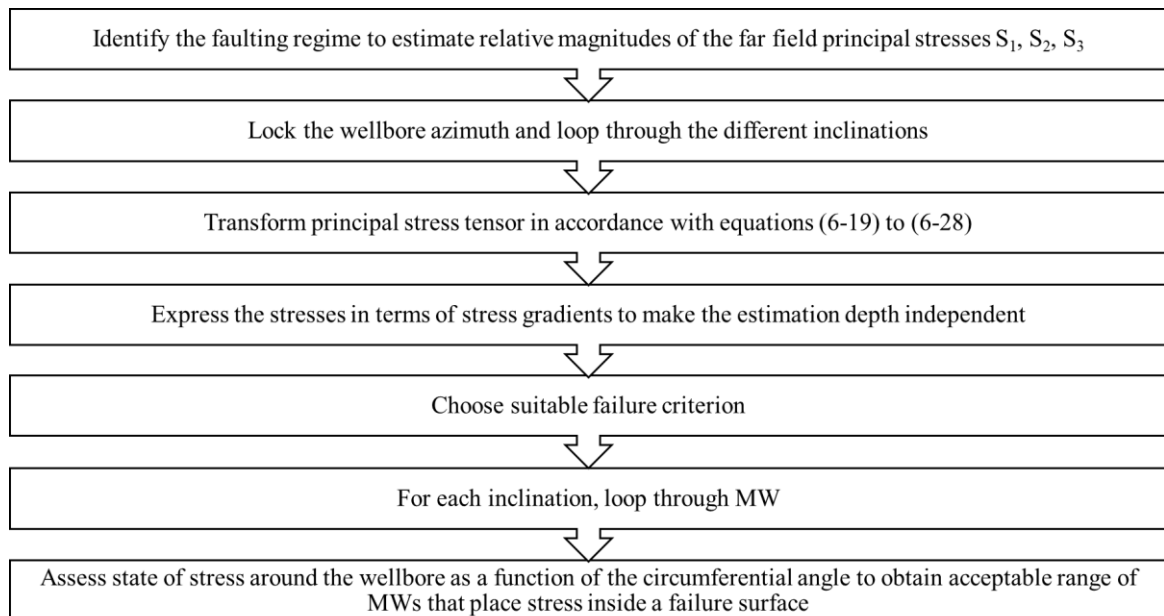


Figure 6-14. Wellbore stability workflow to assess shear failure gradient

6.4. General considerations for wellbore stability

A convenient way to evaluate the stability of wells at any orientation is to use a lower hemisphere diagram (Schmidt plot) as illustrated in figure 6-15. Arbitrarily oriented trajectories are shown as a function of their inclination and azimuth. Concentric circles present inclination such that a vertical wellbore is situated in the plot center, whereas horizontal wells lie at the periphery. The wellbore azimuth is expressed by the angle measured clockwise from the north. Plots can be used in conjunction with heat maps to represent the tendency of borehole failure as a function of parameters such as in-situ rock strength, differential pressure, MW, etc. (Peška and Zoback, 1995). Zoback (2007) indicated that such a concept provides an effective means to assess well drillability as a function of MW.

The effect of borehole deviation on the breakout orientations is dependent on the tectonic regimes (Mastin, 1988). It is accepted that the wellbore instability is promoted by stresses magnitude and increasing stress disequilibrium that is controlled by the difference between the vertical stress and horizontal stresses. As such, it is dependent on the relative magnitude of applied far-field stresses at a given depth, i.e., the local stress regime (Schlumberger, 2021). At a given depth, stress magnitudes are the most compressive RF regime while the least compressive in extensional (normal faulting) regimes. Therefore, higher rock strengths are required to prevent compressive (shear) failure in RF regimes than in NF regimes. Ergo, for a given value of rock strength, wellbores are considered least stable in RF regimes and

the most stable in NF regimes (Peška and Zoback, 1995). Since hoop stress is governing factor for a compressive failure, compressive regimes will necessitate higher MWs.

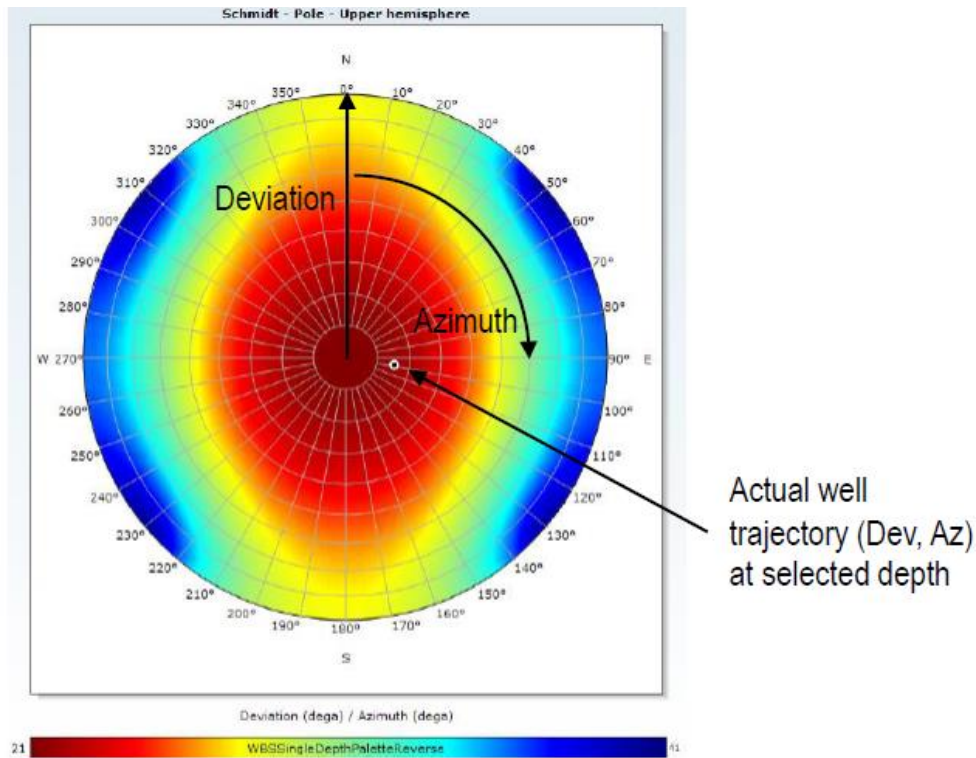


Figure 6-15. Schematic representation of a lower hemisphere diagram aka Schmidt plot (Schlumberger, 2021)

It is important to emphasize that no universal rule of thumb defines the relative stability of deviated wells with respect to the principal stress directions. However, figure 6-16. enables understanding based on analogy inferred from the case of horizontal wells. The trajectory of a horizontal well drilled in NF environment parallel to S_H causes the greatest principal stress disequilibrium as S_v , pushing down, acts against the minimum principal stress, S_h , pushing a well path horizontally. Consequently, a trajectory designed at such azimuth results in the maximum possible stress concentration at the wellbore wall. On the contrary, horizontal wells drilled parallel to S_h exhibit smaller disequilibrium as S_H , whose relative magnitude exceeds S_h , now counteracts vertical suppression caused by $S_v = S_1$; hence resulting in a lesser stress concentration on the wellbore wall. This analogy applies to horizontal wells drilled in SS and RF environments. As the well deviation increases, the well section gets progressively subjected to in-plane vertical stress (S_v) compression while reducing the contribution of horizontal stresses. This contribution will depend on azimuth and is highly specific to stability conditions in different stress regimes (Schlumberger, 2021). From the study by Peška and Zoback (1995), a rather general rule is that the most stable orientation of

the borehole is always in a plane perpendicular to the intermediate principal stress S_2 , and it rotates within this plane from the azimuth of S_1 towards the S_3 direction as S_2 approaches in magnitude to S_1 (Peška and Zoback, 1995). A detailed study about the tendency and occurrence of wellbore instability for varying parameters is given by mentioned study and will not be discussed further. However, the presented concept is vital for understanding the stress orientations in complex stress fields near salt bodies and corresponding effects on wellbore stability.

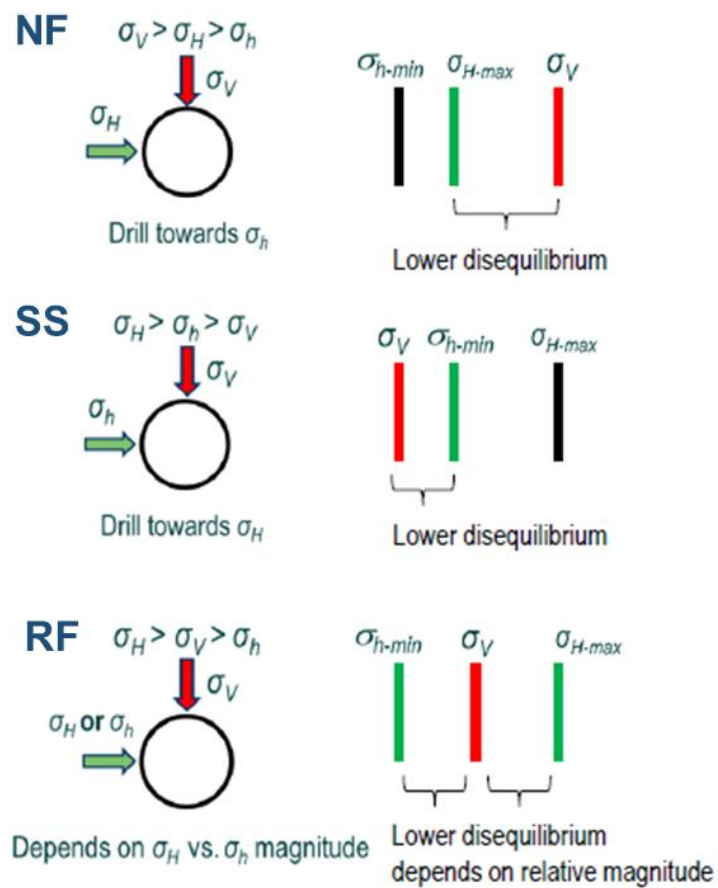


Figure 6-16. The effect of well's azimuth on the wellbore stability (modified from Schlumberger, 2021).

7. PORE PRESSURE AND FRACTURE GRADIENT IN DEEPWATER SALT ENVIRONMENT

Once a Deepwater drilling project is approved, pressure and wellbore stability shall be conducted before starting the well design. Since the sediments around a salt dome are usually massively disturbed, the challenges associated with abnormal and uncertain formation pressures are expected both in the overburden and the reservoir section. Hence, this study aims to provide a comprehensive regional pressure analysis that would later be used to estimate the pore pressure and fracture gradient (PPFG) spatial distribution and ensure safe well placement (Aird, 2019). As per Zhang (2011), pressure analyses include three distinct aspects:

1. pre-drill pressure prediction - prediction made by using the seismic interval velocity data in the planned well location or geological, well logging and drilling data from the offset wells;
2. pore pressure prediction while drilling - relies on data from logging while drilling (LWD), measurement while drilling (MWD), drilling parameters, and mud logging services;
3. post-well pressure analysis - analyze pore pressures in the drilled wells using all available data. The built pore pressure model is later used for pre-drill pore pressure predictions in future wells.

While drilling for the wildcat wells in frontier basins, operators lack data for proper correlation during the planning phase. Scarce or absent drilling data leave companies nothing but to rely on the 3D seismic pre-drill analysis. Analyzing can be run using commercial software by processing the available petrophysical data and 2D/3D seismic velocity data. The prospect wellsite is then examined for spatial pore pressure distribution and wellbore stability, including shear wellbore failure, rock tensile strength, and predicted break-out angles. (Vallejo et al., 2012b; Webb et al. 2016). Rigorous 3D seismic pressure prediction is an essential tool in planning Deepwater wild cat wells; however, if un-calibrated, seismic pressure prediction in this scenario will carry a high degree of uncertainty and potential inaccuracy to pre-drill PPFG predictions (Brown et al., 2015). Namely, overestimating the pressure gradients may substantially elevate well construction costs in terms of additional casing strings determined by the basis of design and unnecessarily designed high MWs. On the contrary, under-estimated pressure gradients will increase the risk of influxes and wellbore instability. Even in the case of rigorous pre-drill pressure analysis, uncertainty

coupled in PPFG analysis often requires a detailed and comprehensive monitoring program to be implemented so that real-time corrections to the pre-drill model can be made (Li et al., 2019). Several case studies bring examples (Marland et al., 2007; Mathur et al., 2010; Schlumberger, 2014; Brown et al., 2015, Zhang and Yin, 2017). A common finding suggests that no single pressure methodology often yields a definite pressure gradient estimate in real-time, thus necessitating a combination of different measurement techniques. Therefore, by determining the PPFG conditions in real-time, data can be used onsite to decide the casing points and optimize hole stability. If these advantages are successfully utilized, a larger hole size can be attained eventually, resulting in enhanced well deliverability and reduced costs.

On the other hand, the planning process can be augmented by identifying relevant offset wells and gathering data of interest accordingly by having the available data repository in place. Offset wells data screening is done by examining real-time data, reports, and planning documents. Normally pressure data of interest include direct and indirect measurements (figure 7-1.), with the former being more reliable and preferred. That facilitates overall understanding of pressure regimes and corresponding causes of their generation and pressure magnitudes and distributions pertinent to the Deepwater environment to be drilled (Aird, 2019).

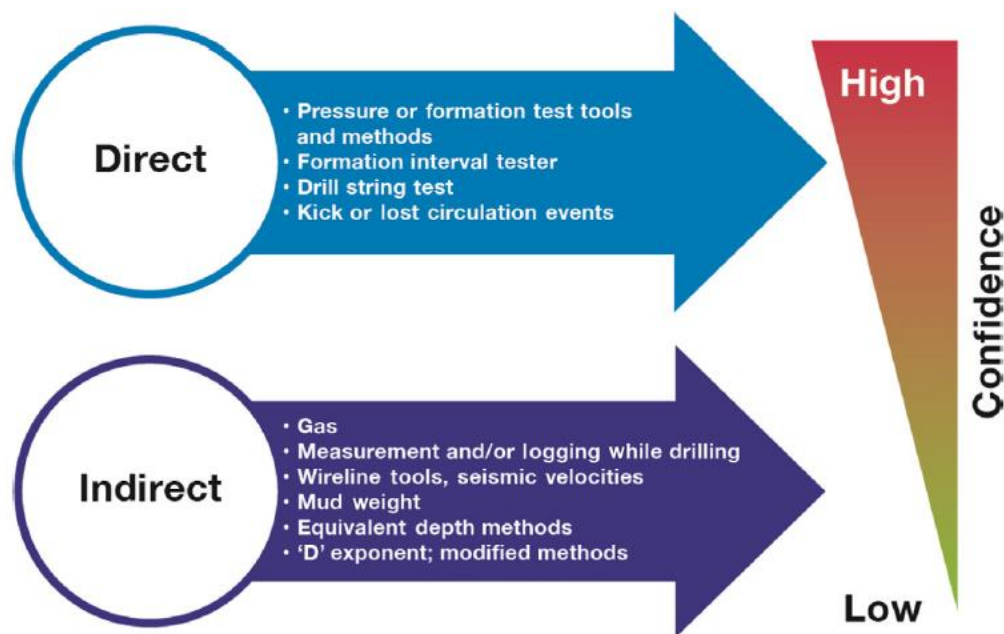
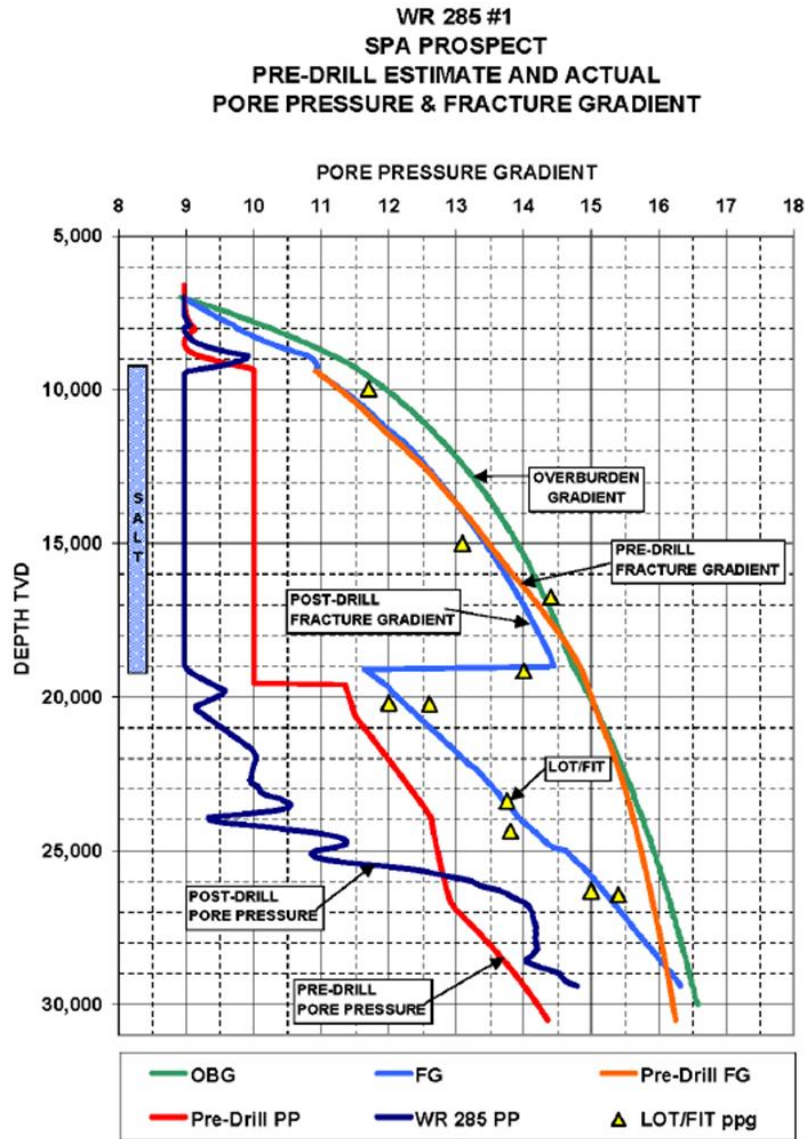


Figure 7-1. Data to estimate PPFG trends expressed in confidence ranking. “Equivalent depth” in this case refers to relative comparison of data (Aird, 2019).

Post-well pressure analysis shall be conducted prior to spud-in if offset data is available. Available drilling data, wellbore instability events²¹, and pore pressure records (both indirect and direct) can be used to calibrate lower drilling margin (SF or PP). Similarly, extended LOT (XLOT) and ballooning episodes can be utilized to calibrate the upper (FG) drilling margin (Vallejo et al., 2012; Marland et al., 2007). Example is given in figure 7-2.



Ft to m conversion: x 0,3048

Ppg to kg/m³ conversion: x 120; pressure gradients expressed in EMW

Figure 7-2. PPFG plot including both pre-drill and post-drill MW window (Rohleder et al., 2003)

²¹ A pore pressure serves as a key input to wellbore stability analysis. The higher pore pressure gets, the heavier MW is required to prevent a wellbore shear failure. Therefore, wellbore breakout can help to bound pore pressures encountered in shale sequences (Zoback, 2010; Zhang and Yin, 2017).

7.1. Pore-pressure regimes in Deepwater

In Deepwater, pressure profiles are normally pressured from the seabed aka mudline to a vertical depth where an abnormal or subnormal pressure mechanism would exist (Aird, 2019). Point of gradient change indicates a change in depositional setting or the presence of mechanical and chemical processes that alter the in-situ pressure state. As seen from the figure 7-3, pore pressures vary from hydrostatic pressure to severely overpressure (as per Zhang et al. (2011), variations are in the range of 48% to 95% of the overburden stress). Many overpressure mechanisms exist in Deepwater and are well explained across the literature (e.g., Mouchet and Mitchell, 1989; Zoback, 2007; Aird, 2019). However, this Thesis will be limited to mechanisms of overpressure generation around evaporates and their implications in well design. As per Aird (2019), the Deepwater pressure profiles can usually be divided into conventional pressure profiles (1-3 in figure 7-3.) and complex pressure profiles (4-6 in figure 7-3.), with the latter being the more challenging and costly in terms of well design.

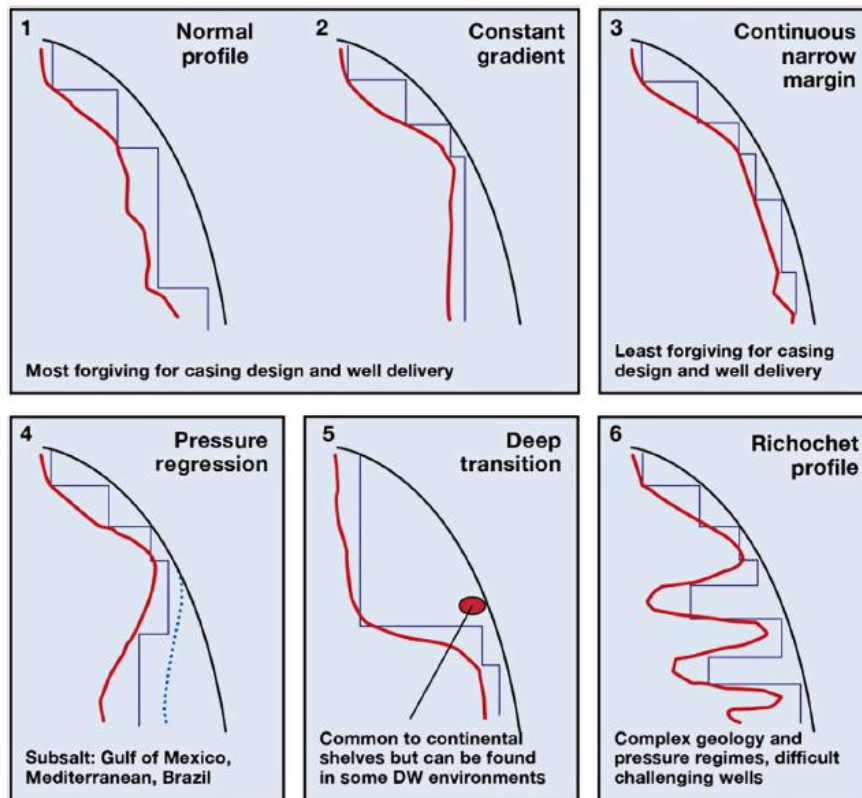


Figure 7-3. Generalized pore pressure profiles in Deepwater (Aird, 2019)

Abnormal pressure is very frequent in the sites of rapid sedimentation offshore: recent deltaic formations, passive continental margins, and the accretionary wedges (Mouchet and

Mitchell, 1989). Examples include the Deepwater continental margins (DCM) such as GoM, Norway, Africa, India, SE Asia, Caspian, etc., all being operating are with a strong presence of massive salt structures. Principle elements of a typical DCM include continental shelf, continental slope, continental rise, and abyssal plain (Aird, 2019). The sedimentation rate²² will govern the rate at which overburden load is applied to the compacting sediments. Moreover, unfavorable hydraulic conductivity, as seen in fine clay material, will further aggravate fluid expulsion and promote the creation of abnormal pressure. Hydraulic conductivity will mainly be determined by the amount and extent of the deposited material (Mouchet and Mitchell, 1989). Figure 7-4. shows sedimentary depositional rates across a continental margin in a prograding deltaic system. As can be seen, the continental shelf is generally characterized by massive amounts of laterally extensive sands, causing very high conductivity. On the contrary, the sedimentation process at the slope yields fewer amounts of sand with a limited extent, thus resulting in low hydraulic conductivity. Similar goes to continental rise, but rather moderate hydraulic conductivity develops compared to the slope as a result of wider aerial extent (Aird, 2019).

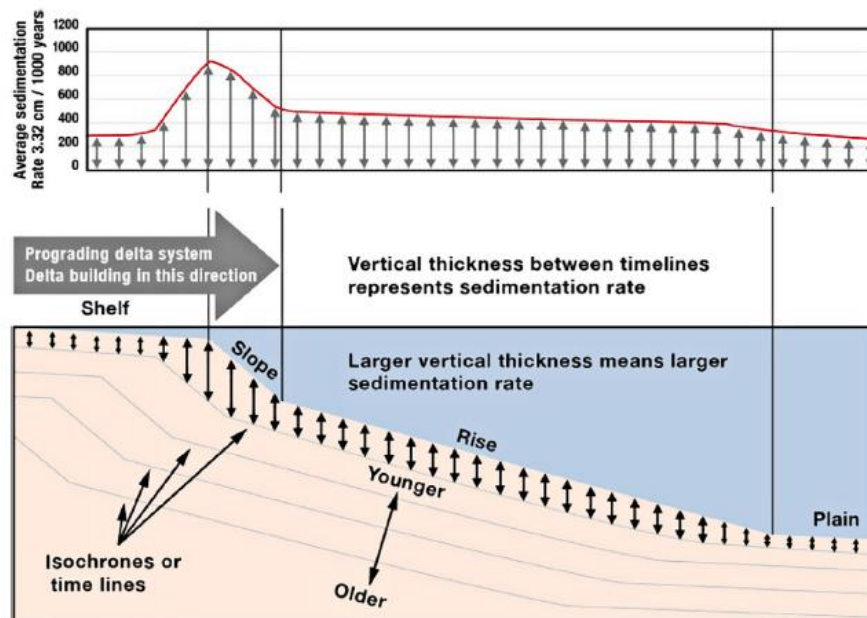


Figure 7-4. Sedimentation rate at the DCM in the deltaic environment (Aird, 2019)

Accordingly, the combination of overburden, sedimentation rate, and hydraulic conductivity will depend on the water depth. Since the spud location determines water depth, the well

²² Likewise, should high sedimentation rates exist, an increased risk associated with shallow hazards exists, but this is not of primary interest to author.

planning team should understand the resulting pore-pressure variances existing below the mudline (BML). For example, coupled with relatively low sedimentation rates, high hydraulic conductivity will promote long, normally pressured sections BML, as is usually the case on the shelf. On the contrary, in regions of high sedimentation rate, such as adjacent to the slope break, the top of abnormal pressure (ToAP) will generally be seen much higher in the sediment section. Pore pressure changes in the function of water depth are shown in figure 7-5., followed by table 7-1. containing further explanation. A fact of particular interest in the Deepwater environment is that the water depth will have a pronounced effect on the encountered fracture pressure at the casing shoe. In offshore applications, the overburden stress is the sum of the hydrostatic pressure of the water column above the mudline, and the bulk weight of the rock formation overlying the depth of interest. As the water depth increases, the depth BML reduces overburden pressure at a depth of interest and consequentially reduces FG which is highly influenced by the overburden itself (Aadnøy, 1998). However, any increase of pressure conditions from hydrostatic will be followed by the increase of the fracture pressure as a result of poroelastic effects (see chapter 6.1.1.).

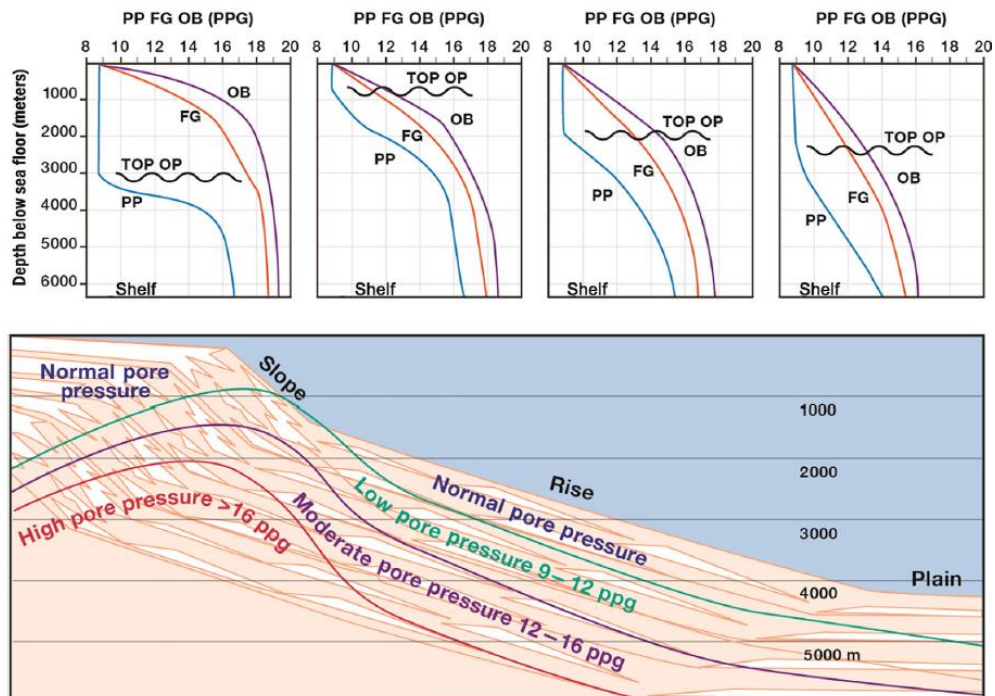


Figure 7-5. Effect of the water depth on pore pressure gradient (Aird, 2019)

Table 7-1. summarizes general pore pressure distribution trends in Deepwater, including typical Top of Abnormal Pressure (ToAP), pressure transition trends, and MW window width (Aird, 2019).

Table 7-1. General PPFG trends across the continental margin

The Deepwater continental shelf	Continental slope	Continental rise	Abyssal plains
very high hydraulic conductivity and long normally pressured intervals	rapid sedimentation rate and low hydraulic conductivity promoting shallow ToAP	somewhat lower sedimentation rates and slightly higher hydraulic conductivity than encountered at the continental slope	long (near-) normally pressured sections resulting from very low sedimentation rates and moderate hydraulic conductivity
ToAP encountered from 2134 to 3048 m (7000 - 10000 ft) BML with equivalent MWs (EMWs) in range of 1917 to 2157 kg/m ³ (16-18 ppg)	ToAP ²³ as shallow as 305 m (1000 ft) BML, approaching EMWs in range of 1917 to 2157 kg/m ³ (16-18 ppg) in deep sections	ToAP ranging from 610 to 3048 m (2000 - 10000 ft) BML with EMWs in range of 1678 to 2157 kg/m ³ (14-18 ppg)	ToAP ranging from 1524 to 3048 m (5000 - 10000 ft) BML with EMWs in range of 1438 to 1678 kg/m ³ (12-14 ppg)
sharp transition to AP at a rate of 240 to 600 kg/m ³ (2-5 ppg) per 304,8 m (1000 ft)	modest transition to AP at a rate of 120 to 240 kg/m ³ (1-2 ppg) per 304,8 m (1000 ft)	slow transition to AP at a rate of 60 to 120 kg/m ³ (0,5-1 ppg) per 304,8 m (1000 ft)	slow transition to AP at a rate of 60 to 120 kg/m ³ (0,5-1 ppg) per 304,8 m (1000 ft)
relatively large MW window, spanning from 599 up to 959 kg/m ³ (5-8 ppg) with rapidly narrowing to the span values in range as low as 240 to 360 kg/m ³ (2-3 ppg) in AP zones	reduced overburden, when coupled with shallow ToAP results in a very narrow MW window, generally in a span of 120 to 480 kg/m ³ (1-4 ppg)	MW window span gradually increases with depth at first, reaching maximum at ToAP (a span in the range of 360-599 kg/m ³ (3-5 ppg)), and decreases at slower rate afterward to a span of ca. 120-360 kg/m ³ (1-3 ppg)	extreme water depths can result in the lowest overburdens, causing narrow MW window to traverse the entire section with a span in range of 120-360 kg/m ³ (1-3 ppg)

²³ Study carried out by Li et al. (2011) on pressure data from more than 100 exploration wells in GoM indicates that at depths of ca. 600 m BML pore pressure is found to be hydrostatic as hydraulic communication with the sea floor exist. Further, a zone of moderate overpressure develops at depths of approximately 600 to 1200 m BML, whereas at depths below 1200 m BML, zones of hard overpressure start developing.

7.2. Salt effects on the pore pressure:

Based on the results of numerical simulations and observations from subsalt prospects in GoM O'Brien et al. (1993) demonstrated that the salt lying sheets have a significant impact on the overpressure profile of subsalt wells. During evaporite deposition, the sealing efficiency of evaporite sediments acts as a barrier to the vertical expulsion of fluids from underlying sediments. Undercompaction is likely to occur in the presence of interlayered or underlying argillaceous series where lateral hydraulic conductivity is insufficient to permit adequate drainage. In such an environment, the overburden effect will continue increasing, and eventually, abnormal pressure will be generated (Mouchet and Mitchell, 1989). The thickness of the evaporite zone will vary widely due to erosion, salt flow, and gouging caused by thrust faulting occurring after the deposition (Jackson and Hudec, 2017).

The exact degree of overpressure and its build-up rate is influenced by the dip of the salt base, the three-dimensional permeability profile in the formations surrounding and underlying the salt, salt depth, the catchment volume underlying the salt, burial history, etc. However, a significant increase in pore pressure always occurs through a laterally extensive salt sheet, leading to pressure gradients in the subsalt formations more than 20,36 MPa/km (0,9 psi/ft). Likewise, the salt emplacement affects the compaction status, causing normal compaction trend changes across the thick salt bodies (Marland et al., 2007). Below the salt, overpressure development was shown to be accompanied by an increase in porosity (approx. 3 to 5% for GoM) relative to the regional trend far from the salt. On the other hand, overpressure in the section overlying the salt will be correspondingly reduced due to a reduced supply of fluids from beneath the salt. These two effects, when combined, result in a large pressure difference across the salt body (O'Brien et al., 1993). Lesser overpressures may be encountered in wells penetrating locations near the edge of the salt sheet as here. This is because the salt sheet may only partially block the outflow of the fluid (figure 7-6.). However, where allochthonous salt is connected to its source, the increased sedimentation will increase the salt stress and thus promote the horizontal loading of the adjacent rocks. If adjacent rocks are characterized by small hydraulic conductivity, overpressure generation will be promoted (Nikolinakou et al., 2015).

Furthermore, beyond its lateral extent, the salt sheet has little impact on the pore pressure profile itself. In GoM, overpressures lower in magnitude have been encountered in locations underneath the salt where the sand is present, compared to areas with shaly sequences. This is because sand provides a high permeability path to a fluid flow around the edge of the salt,

thereby relieving the excess pore pressure below the salt. The effectiveness of this mechanism will depend on whether the sand is a regional carrier bed or an isolated unit. In the case of the former, a relieving pathway may be oriented in such a way to promote charging of formations laterally adjacent to the salt, causing an increase of pore pressure at sheet flanks.

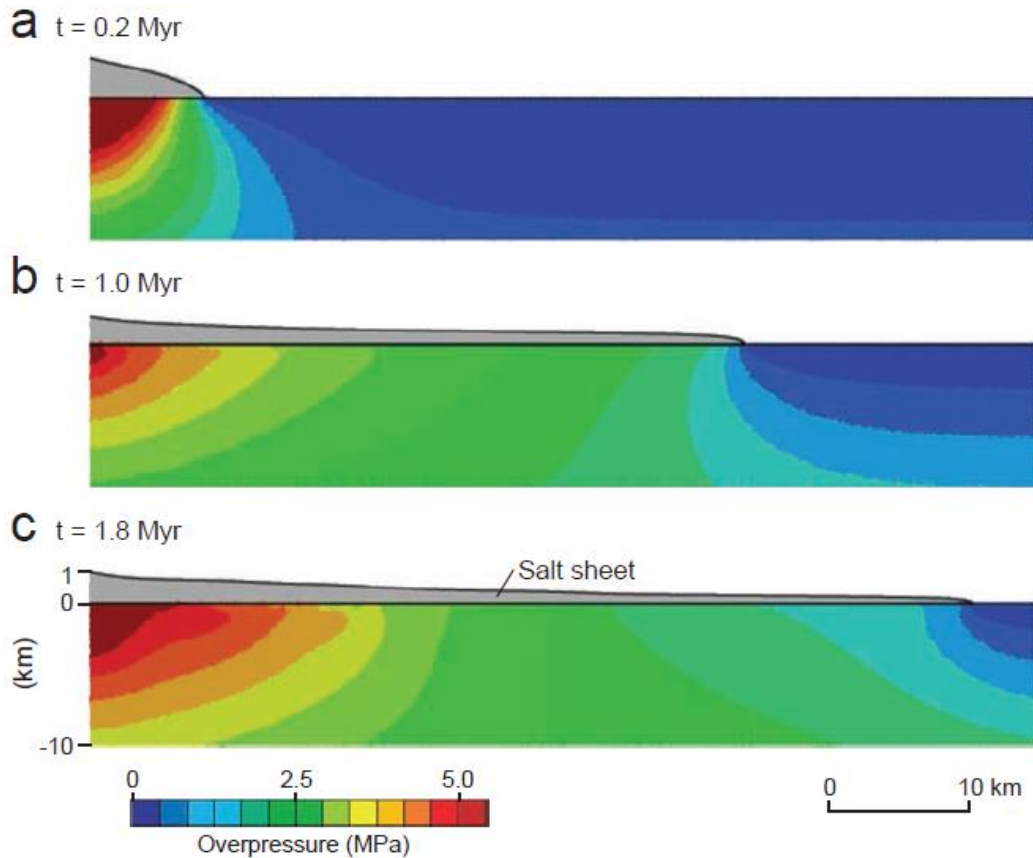


Figure 7-6. Simulation of salt sheet emplacement and overpressure generation in the undrained environment (Luo et al., 2012b)

Li et al. (2011) correlated the overpressure with the stress anisotropy (indicated by a ratio of minimum horizontal stress to vertical stress). Adhering to the bilateral constraint assumption, any increase in pore pressure will result in a partial rise in horizontal stresses, as suggested by a trend in figure 7-7a. However, the study finds that the stress anisotropy in the GoM is low compared with overpressure increase with depth. The authors argued that the highest overpressure correlates with isotropic and/or nearly isotropic stress conditions, implying pronounced effects of salt-driven pressure perturbations on PP (figure 7-7b.). Adachi et al. (2012) argued that overpressures exceeding EMW of 15 ppg (1800 kg/m^3) are likely to be

encountered at depths larger than 9144 m (30,000 ft) BML and even amplified by smectite-illite transformation (Adachi et al., 2012).

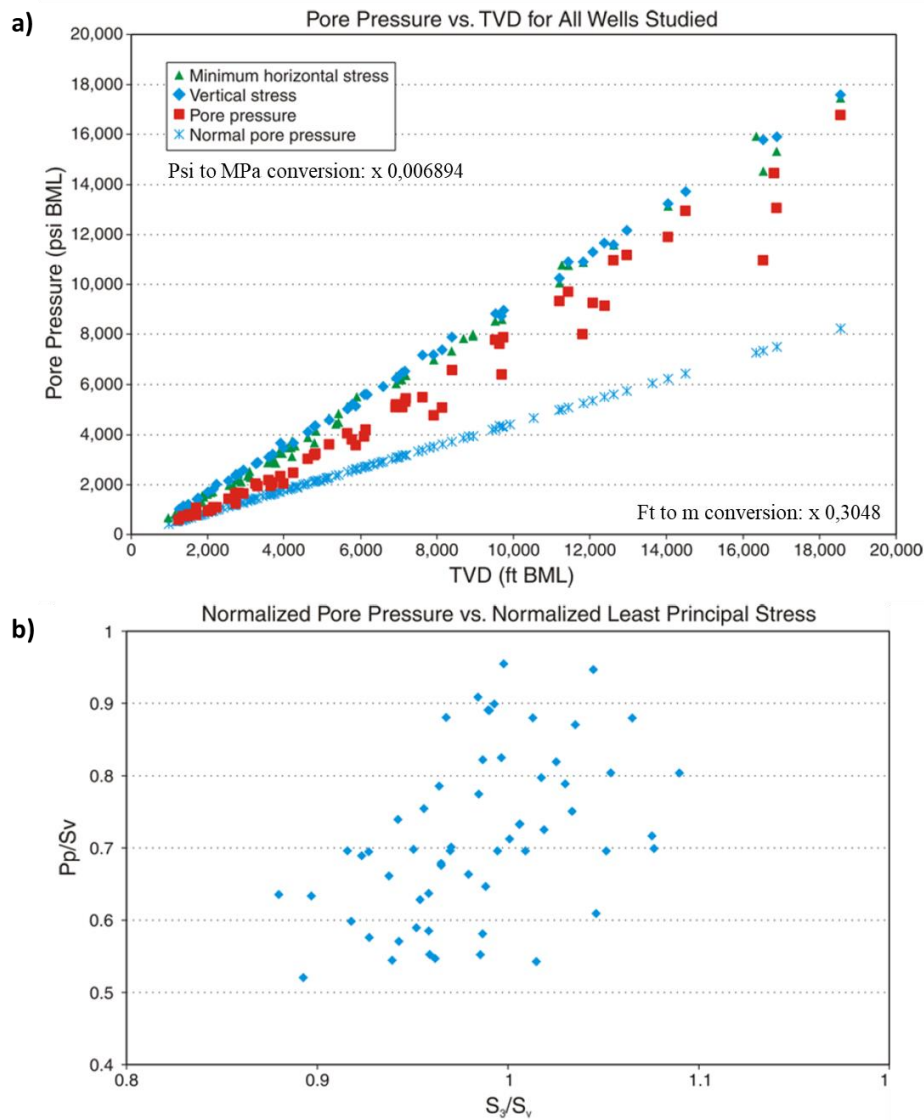


Figure 7-7. Scatter plot of pore pressure data from GoM represented as (a) pressure trend with depth BML and (b) normalized pore pressure versus normalized minimum principal stress (modified from Li et al., 2011)

Nikolinakou et al. (2012) studied the effects of salt relaxation on pore pressure generation. In a case where fluid drainage is permitted, no overpressure is predicted. As viscoelastic salt relaxes and pushes against adjacent sediments, a large area near the salt will yield plastically. However, if pore pressure dissipation is restricted, the loading caused by lateral salt expansion causes fluid overpressures (see figure 7-8.). Many authors argued that narrow MW windows encountered below the salt (O'Brien et al., 1993; Barker and Meeks, 2003; Moyer et al., 2012) could result from minimum principal stress convergence toward the pore

pressure. On the contrary, where the undrained system is loaded by salt perturbation, the development of underpressure is promoted in areas that exhibit stress relaxation, i.e., both above and below the salt. However, stress-relaxed underpressures are rare phenomena in Deepwater drilling due to the low salt permeability and lack of dewatering pathways below extensive salt bodies (Nikolinakou et al., 2012).

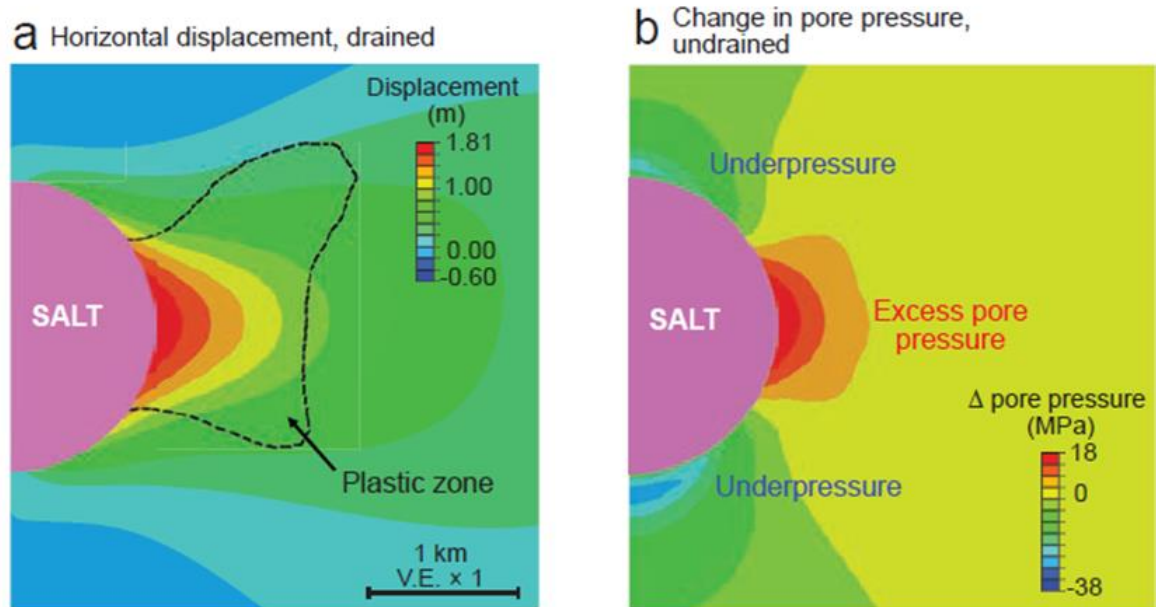


Figure 7-8. Simulation of salt relaxation against elastoplastic sediments; (a) horizontal displacement around the salt body in drained conditions and (b) stress-induced pressure change around the salt body (modified from Nikolinakou et al., 2012)

7.3. Salt stringers

Vugs of high porosity and high permeability may exist within the salt. Very problematic vugs are so-called stringers (also floaters or floating blocks). Stringers are layers or fragments embedded in salt, mainly consisting of rock minerals other than halite (e.g., anhydrite, carbonate) and pose different mechanical and flow properties than the salt (Zijp et al., 2017). These interbedded sequences may separate salt in the range of a few to a few hundred feet (Sheffield et al., 1983). Stringers can accommodate significant volumes of fluid or gas trapped by low permeability dolomite or anhydrite (van Oort, 2004). The inclusions may be abnormally or sub-normally pressured, depending on the mechanism that formed it and the lithology of the inclusion (Israel et al., 2008). Generally, overpressure mechanisms in stringers are associated with the following (Mouchet and Mitchell, 1989; Zijp et al., 2017):

- Dewatering of gypsum during transformation to anhydrite in stringers filled with brine,
- Hydrocarbon generation in the stringers that had migrated to the oil or gas maturation window during their burial history,
- H₂S generation due to bacterial or thermochemical sulfate reduction associated with breakdown or maturation of organic matter.

Most of these processes can generate significant overpressures if the stringers are hydrologically disconnected (sealed off) from their surroundings by impermeable salt. This tends to happen during the salt burial as the movement of salt may result in intense deformation of the anhydrite, dolomite, and claystone formations (figure 7-9.). Consequentially, this will cause fragments of these formations to become encapsulated by impermeable salt (Jackson and Hudec, 2017; Zijp et al., 2017). In addition to drilling mechanics-related problems (documented over Whitson and McFadyen, 2001; Marland et al., 2007; Israel et al., 2008; Mathur et al., 2010; Chatar et al., 2010; Moyer et al., 2012; Chowdhury et al., 2012), the uncertainty in pore pressure within the inclusion rises questions around estimated pre-drill MW window, often requiring onsite modifications to the MW and casing program. Compartmentalized pore-pressures will lead to charging or depletion of formations, causing influxes or LC and the possibility of differential sticking (in significantly permeable formations). In a case where inclusions within the salt section are critically stressed, any cumulative stress applied by drilling fluid will cause pre-existing fractures to dilate and induce severe losses. Encountering repeated loss zones while drilling the interbedded salt section puts an upper bound on MWs. Where high creep rates are encountered, setting an upper bound on MW will adversely affect the creep rate (Brown et al., 2015). In other words, drilling into either can force operators to balance between overestimating the MW and potentially inducing LC or underestimating and dealing with a WCI (Chatar et al., 2010). Kicks of intensity approaching overburden have been documented offshore Netherlands and in GoM (van Oort, 2004; Zijp et al., 2017). Such inconvenience may have repercussions on the well design. It can necessitate pushing planned casing shoes at shallower depths or deploying contingency strings to tackle expected kicks adequately.

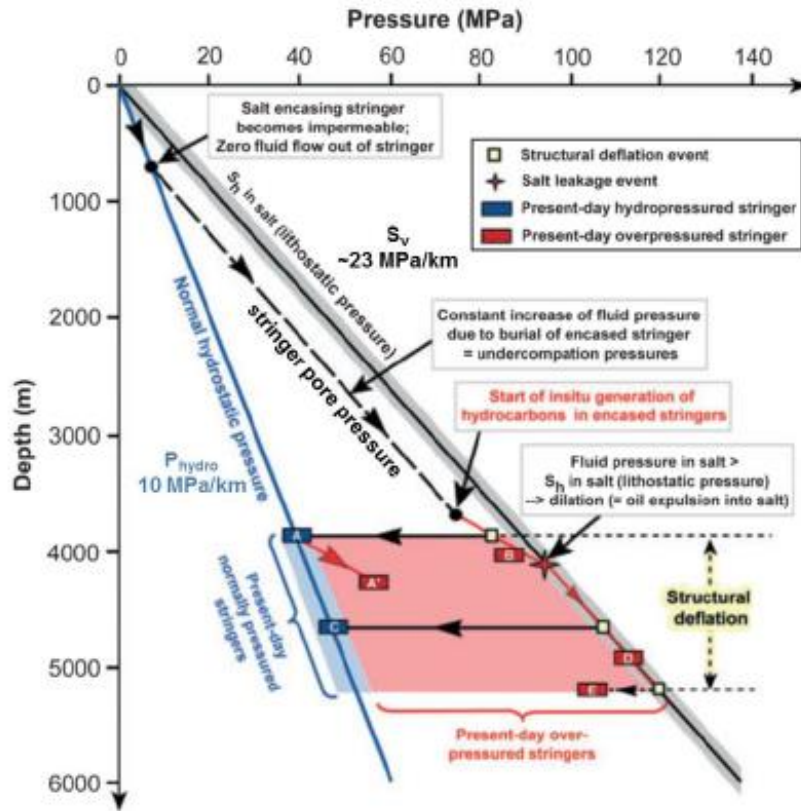


Figure 7-9. Evolution of abnormally pressured stringers (Zijp et al., 2017)

8. WELLBORE STABILITY IN DEEPWATER SUBSALT

The wellbore stability is substantially affected by in situ stresses conditions. The presence of a salt body can significantly perturb the in-situ stress conditions and, as a result, influence the stability of the wellbores drilled through or around it (Bradley, 1978; Fredrich et al., 2003; Wilson and Fredrich, 2005; Nikolinakou et al., 2012). Where highly stressed formations are drilled, wellbore instability will occur if the wellbore lacks adequate pressure support from the drilling fluid and a significant pressure difference exists across the wellbore wall. Likewise, the greater the mean in situ stress and greater the in-situ stress difference (S_1-S_3), the more prominent the problem of wellbore instability will be (Bradley, 1978; Pašić et al., 2007; Luo et al., 2012a). Drilling wells in Deepwater subsalt environments is expensive and technically challenging, and the cost of drilling these wells easily exceeds 50 million dollars (Sanz and Dasari, 2010). If excessive, wellbore instability can induce substantial costs to well construction due to the occurrence of drilling problems such as BHA pack-off, mechanical sticking, LC, side-tracking. In addition, for wellbores failing in shear, the existence of significant enlargement aggravates cementing operation, affects hydraulic requirements, and causes problems during logging operations (York et al., 2009; Aregbe, 2017). As per York et al. (2009), wellbore instability accounted for approx. 12.6% of total well construction time and 41% non-productive time (NPT) excluding Wait on Weather (WoW) in 38 evaluated Deepwater Subsalt wells in GoM. In extreme cases, complete borehole failure may occur, thus only incurring costs to the operator rather than creating the value out of the planned well. Hence, designing a stable wellbore requires a specific MW and modification to the well architecture with aim of preventing or limiting breakouts to an acceptable breakout width.

It follows that incorporating geomechanical aspects in Deepwater well design offers mean of achieving substantial savings through, but not limited to:

- reduced drilling cost,
- reduced exploration risk,
- improved drilling safety and reliability,
- reducing the probability of casing failure in shear and/or collapse,
- reducing or eliminating instability-caused NPT drivers,
- allowing feasibility evaluation of novel well construction techniques such as Managed Pressure Drilling (MPD) or Drilling with Casing (DwC).

8.1. Estimating in-situ conditions around salts

In the passive sedimentary basins, vertical stress is governed by the weight of the overburden material, and the horizontal stress equals some fraction of the vertical stress. In such environments, assuming uniaxial deformation, porosity and effective vertical stress can be correlated, thus allowing pore pressure prediction if the vertical stress and porosity are known. However, such an approach breaks down around salt bodies stresses within salt tend to relax toward an isotropic state of stress ($S_v = S_H = S_h$) where no deviatoric stresses can exist. As salt relaxes towards an isotropic state (figure 8-1a.), it behaves as a viscous fluid over long periods, thus loading the adjacent sediments (figure 8-1b.) that can, on the contrary, sustain deviatoric stresses through frictional resistance (Dusseault et al., 2004b; Lou et al., 2012a; Nikolinakou et al., 2012; Nikolinakou et al., 2013b). Note that the salt has minimal deviatoric stresses upon relaxation but the stress field around the salt has changed.

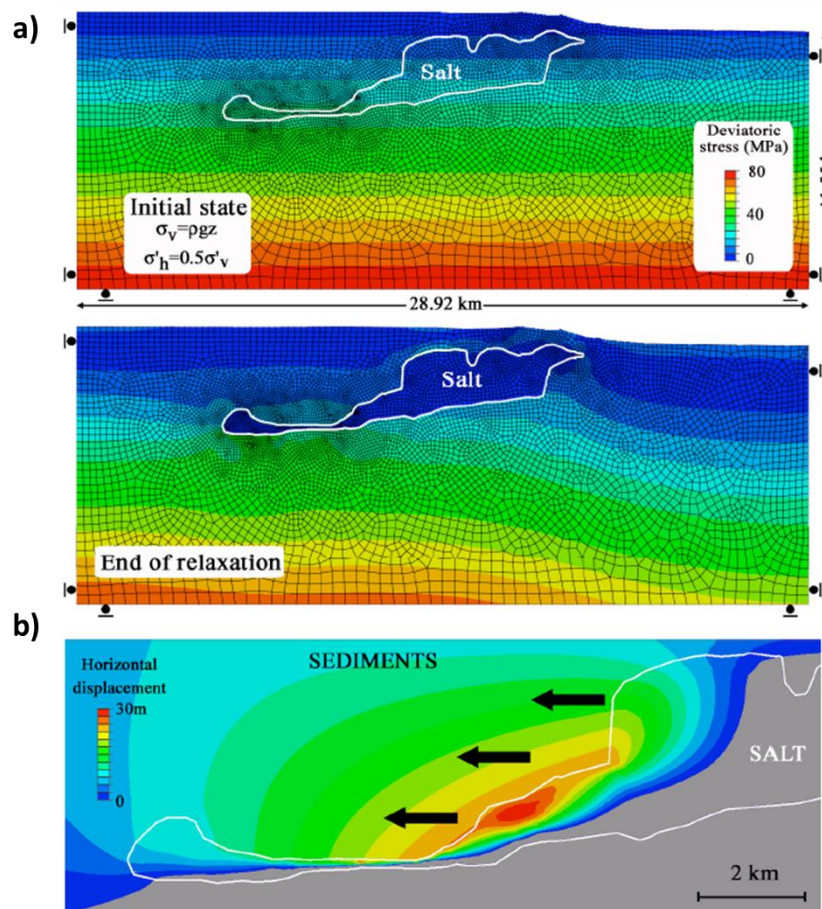


Figure 8-1. Plane-strain numerical model of a Mad Dog cross section with the representation of (a) deviatoric stress at the time of salt emplacement and after the relaxation (ca. after 0,4 million years) and (b) salt outward horizontal displacements loading the wall rocks (modified from Nikolinakou et al., 2013b)

In order to satisfy stress equilibrium within the salt body and maintain continuity with the surrounding formations, flowing salt causes a highly complex and anomalous stress state to exist near the interface. Apart from perturbing relative magnitudes of tectonic stresses, salt tends to rotate them away from initial conditions so that principal stresses are perpendicular and parallel to the interface. As a result, stress rotations at the rock/salt interfaces will be controlled by the shape of the salt body (Fossum and Fredrich, 2002; Fredrich et al., 2003; Zoback, 2007; Sanz and Dasari, 2010; Nikolinakou et al., 2013a). Figure 8-2. indicates that the presence of the salt is expected to significantly deflect stress trajectories away from horizontal and vertical as the salt interface supports no shear stress (Zoback, 2007; Nikolinakou et al., 2012).

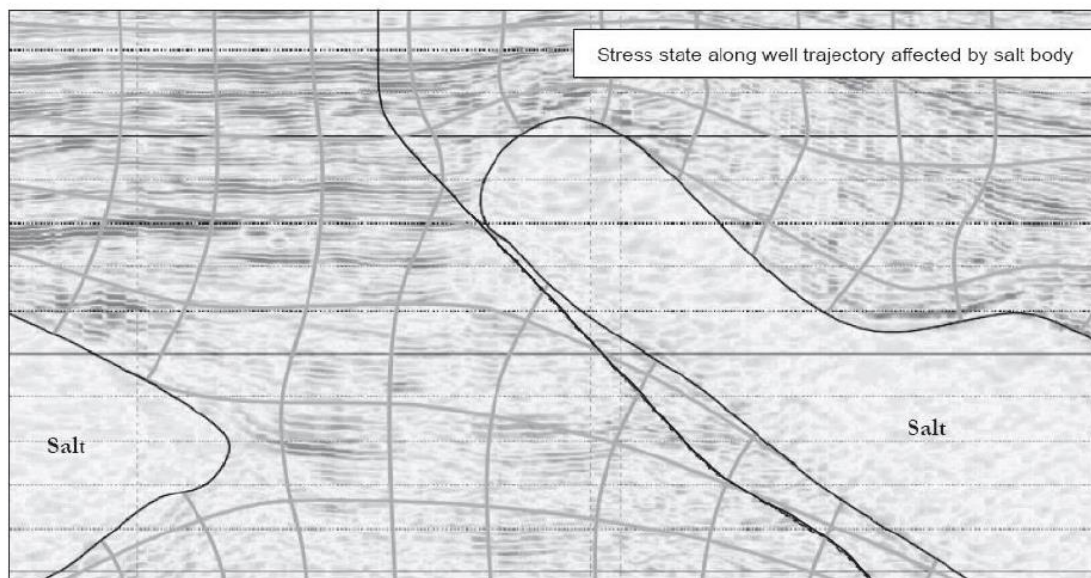


Figure 8-2. Seismic lines in the vicinity of two other salt bodies in the Gulf of Mexico (Zoback, 2007)

For all these reasons, minimizing the risks of drilling through and/or near salt bodies requires the ability to predict the pore pressure and the orientation and magnitude of the stresses around the salt. Since the vertical stress above, through, and below the salt body is perturbed from the far-field value and different from the weight of the overlying material, conventional density logs are not representative for estimation of vertical stress around salt bodies. Moreover, salt emplacement causes pore pressure changes in adjacent sediments, which cannot be accounted through the relationship between porosity and effective vertical stress. As stress changes in the vicinity of salt, the structures affect permissible PPFG window, and therefore wellbore stability (Bradley, 1978). Understanding stress fields and rock fabric

around salt structures facilitates well design around salt, whereas economic benefits are more likely to be realized as uncertainty is minimized and problems can be anticipated and managed proactively (Sanz and Dasari, 2010; Dusseault et al., 2004b). Ergo, the only way to determine the stress perturbations around the salt bodies is to solve the complete set of equilibrium, compatibility, and constitutive equations with the appropriate initial and boundary conditions using a numerical solution technique such as FEA (Fredrich et al., 2003). In such complex geologic environments, numerical models enable accurate estimation of the in-situ conditions by linking stresses to deformations resulting from the salt shape, the variability of the rock properties, and pore pressure around it (Adachi et al., 2012; Nikolinakou et al., 2013b).

8.1.1. Literature review on numerical modeling of salt-induced stress perturbations

Fredrich et al. (2003) investigated the magnitude and character of stress perturbations adjacent to idealized axisymmetric salt bodies applying linear elasticity formulations. The analyses revealed that shear stresses around salt bodies may be highly amplified, horizontal and vertical stresses significantly perturbed from far-field values, principal stresses rotated and modified while the horizontal stress anisotropy may arise.

Sanz and Dasari (2010) investigated the relaxation effects of different salt configurations to surrounding elasto-plastic²⁴ sediments. An important finding of the latter study was the effect of the salt connectivity to its source. The stress perturbations and associated plastic deformation can be substantially increased when allochthonous salt is attached to its source. For disconnected salts, vertical stress near the salt-sediment interface is increased relative to far-field value regardless of density contrast between salt and surrounding sediments. In this case, the stress field is controlled by the initial stress condition and body geometry. On the contrary, for connected salt bodies, vertical stress adjacent to the salt will be affected by the density contrast. When salt density is lower than the density of surrounding sediments, salt counteracts overburden stress, thus reducing vertical stress from its far-field values. On the other hand, for shallow buried salt bodies (<1500 m BML), salt will usually be denser than

²⁴ As per Luo et al. (2012b), deviatoric stresses in surrounding sediments are highest when sediments are assumed to be elastic, whereas plastic yielding in elastoplastic models limits the deviatoric stresses that the rocks can support and make calculated stress perturbations smaller. Nikolinakou et al. (2012) added that elastic models overestimate stress changes and underestimate displacements, creating the illusion of a stiffer material response to salt loading.

surrounding sediments, and vertical stress is enhanced relative to its far-field values, i.e., the system's response is similar to disconnected bodies.

Nikolinakou et al. (2012) incorporated a poromechanical formulation to treat plastic deformation around salt in more detail. A valuable amendment to previous work was the poro-elastoplastic treatment of adjacent sediments that enabled authors to capture plasticity effects on the evolution of stresses and overpressure. The authors separately studied sediment loading under drained (sediment loading is followed by pressure dissipation that enables preservation of hydrostatic conditions) and undrained conditions (trapped fluids are loaded together with sediments, thus elevating in-situ pore pressure). Authors have shown that stress changes around salt bodies induce pore-pressure perturbations that may extend kilometres away from the salt. These pressure perturbations may require a substantial time to dissipate if they occur within the low-permeability wall rocks. In areas where the salt flow is still active (e.g., GoM), such perturbations may still be present nowadays, thus posing challenges to well construction. Namely, since the difference between the minimum principal stress and the pore pressure decreases with pore pressure dissipation, understanding the in-situ pore pressure and stress conditions becomes important for estimating the drilling margins.

Importantly, all studies indicated that the geometry of the salt body significantly influences the qualitative character of the stress perturbations. While it is believed that spheroidal or bulbous salt bodies induce more significant stress perturbations than salt sheets, thin horizontal-lying salt sheets are not expected to cause significant stress perturbations in surrounding sediments regardless of their lateral extent. Namely, substantial stress perturbations are only apparent for significantly thick salt sheet (> 1524 m or 5000 ft). Apart from comparing approaches to geomechanical modeling around salt bodies, Luo et al. (2012b) studied the effects of non-idealized salt geometries on stress perturbations. The authors presented the finite-element model (figure 8-3.) that simulates an irregular sheet of viscoelastic salt relaxing against elastoplastic sediments. Displacement vectors show that convex portions of the salt tend to expand laterally into concave parts, eventually enforcing compressive stress in concave parts (e.g., type of behavior seen in salt diapirs expanding against adjacent minibasins). As VME stress tends to concentrate in areas where the salt is convex (i.e., where the salt bulges outward, such as areas below convex-down allochthonous salt), FG in convex portions is lower, and narrow MW windows are encountered. Conversely, areas where the salt is concave (i.e., where the salt curves inward, such as supra-

salt mini basins or sub-salt concave-down embayments) exhibit wider MW windows due to the relatively large FG (Adachi et al., 2012; Luo et al., 2012a).

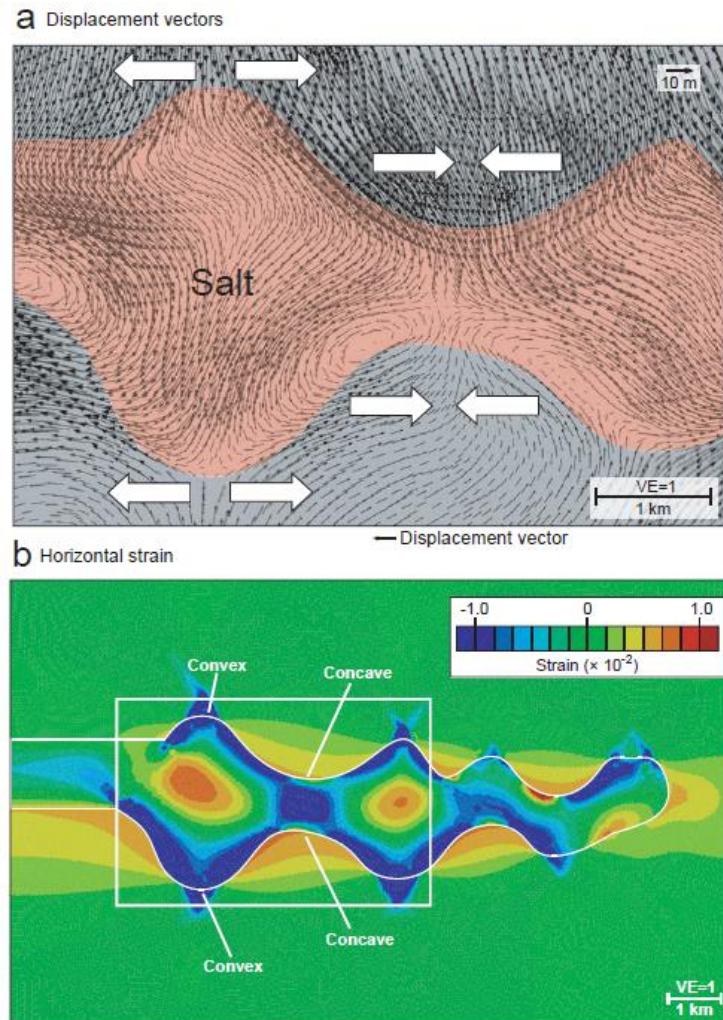


Figure 8-3. Representation of (a) displacement vectors around moving salt sheet and (b) horizontal strains resulting from these displacements (compressive strains have positive value) (Luo et al., 2012b)

8.1.2. General trends in stress disturbances around salt bodies

Given that drilling window uncertainties depend on salt position (proximity to the mudline, its thickness, attachment to a mother salt), salt morphology²⁵, and tectonic setting, it is hard

²⁵ Importantly, as the geometry of a salt body can substantially differ from the idealized, the salt aspect ratio provides clues about the stress characteristics in and around the salt. Namely, as the width to height ratio decreases and approaches a more spheroidal geometry, the characteristics of the stress perturbations evolve towards the behavior seen with the spherical models. For example, for an aspect ratio of 1:1, the isotropic stress within the salt body falls between the far-field values of the vertical and horizontal stresses. On the contrary, with an aspect ratio larger than 4:1, the isotropic stress within the salt body approaches the far-field vertical stress. Note the analogy with salt diapirs, viz, salt sheets.

to provide definite guidelines for well planning around salt bodies (Sanz and Dasari, 2010; Adachi et al., 2012). However, the relative magnitudes of stress perturbations for two idealized geometries are summarized below following the work of Fredrich et al. (2003), Dusseault et al. (2004b), Sanz and Dasari (2010), Nikolinakou et al. (2012), Nikolinakou et al. (2015), and Jackson and Hudec (2017).

8.1.3. *Stress perturbations around spherical salt bodies*

- in NF regime salt relaxation towards isotropic state causes vertical stress in the salt to reduce. In contrast, the horizontal stress in the salt increases to match the vertical stress in the salt.
- to satisfy the stress continuity across the salt-sediment interface, vertical and horizontal stress perturbation must extend into the surrounding non-salt formation. As a result, the vertical stress is decreased both above and below the connected spherical salt body.
- the horizontal stress is elevated adjacent to the lateral edge of the salt sphere but reduced immediately above and below the salt sphere. As the horizontal stress perturbations above and below the salt sphere are more spatially restricted than the vertical stress perturbations, the ratio of horizontal to vertical stress is not constant but varies around the salt body.
- under the undrained conditions, the stress increases pore pressure, locally shifting the pore pressures gradient to higher values than in areas under relaxation.
- the significantly elevated shear stresses may arise in sediments adjacent to salt bodies to satisfy the stress field equilibrium around the salt body. These levels can be sufficient to induce shear failure of adjacent material.
- even in the existence of isotropic far-field horizontal stress state, the stress changes within and surrounding the salt body can result in horizontal stress differences next to the salt body with reported anisotropy between the minimum and maximum horizontal stresses reaching up to 35%.
- as the salt body relaxes towards the isotropic state, the VME stress within the salt body converges to zero. However, the region surrounding the salt body exhibits substantial VME stress perturbation. VME stress will be reduced above and below the salt sphere but highly elevated in the laterally adjacent sediments.

- although the maximum perturbations occur adjacent to the salt body, the salt-induced pressure and stress perturbations vanish at a certain distance from the salt body. Hence, the drilling margins will be significantly altered away from a salt body (see figure 8-4a.).

8.1.4. *Stress perturbations around salt sheets*

- generally, the predicted stress perturbations caused by emplacement of the salt sheet are smaller than the stress perturbations caused by salt spheres of similar dimensions.
- regardless of the salt sheet thickness, the vertical stress within the salt body is not perturbed from lithostatic conditions as salt sheets tend to maintain the vertical stress within the salt unchanged from the corresponding far-field values. Consequently, the salt pressure is increased to catch up with the far-field vertical stress, and the overburden load is transferred through the salt rather than around it.
- vertical stress is increased from the far-field values, i.e., lithostatic condition, in the region adjacent to the edge of the salt sheet.
- horizontal stresses increase within the salt sheet relative to the far-field but reduce both above and below the salt sheet.
- the emplacement of the allochthonous salt sheet causes a decrease in the stress ratio immediately below the sheet.
- VME stress is elevated from the far-field value above and below the salt sheet. However, smaller stress perturbations are encountered than around spherical bodies, given the rather smaller stress fluctuations when compared to the salt sphere. Here, the zones of elevated VME stress result from a reduction in horizontal stress compared to their vertical counterpart.
- significant horizontal stress difference exists in the region immediately adjacent to the lateral edge of the salt sheet. Horizontal stress anisotropy is proportional to the salt sheet thickness. On the contrary, horizontal stress anisotropy is inversely proportional to the horizontal to vertical stress ratio. Consequently, amplification of VME is proportional to salt sheet thickness and stress anisotropy (see figure 8-4b.).

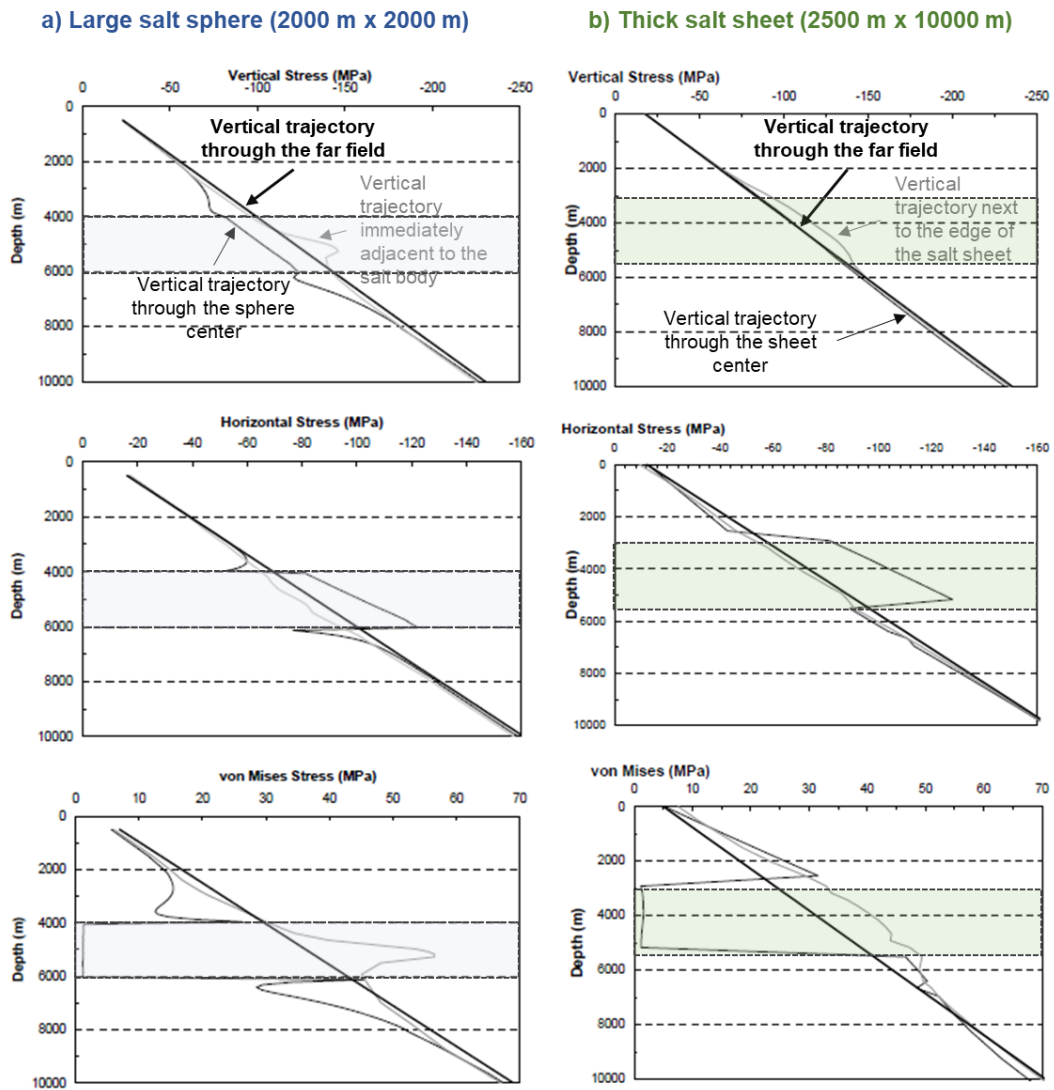


Figure 8-4. Generalized stress gradient character for different positioned well trajectories around (a) large spherical salt body and (b) thick salt sheet (modified from Fredrich et al., 2003)

8.2. Drilling hazards around salt bodies

Apart from the salt-induced stress perturbations, some specific configurations pertinent to the salt environment may give rise to increased drilling risks and thus impact well design around salt bodies. These are summarized in figure 8-5. Collectively, these include pore-pressure variations, salt creep, rubble and shear zones, salt inclusions, tar zones, and associated features.

8.2.1. Area of tectonic instability

Most importantly, the area of tectonic instability refers to induced faulting around rising diapirs. A locally perturbed stress field by the outward expansion of a rising diapir implies

that a gradient of stresses toward the far-field must exist. In formations adjacent to the flanks of the salt diapir, the in-situ hoop stress around the salt diapir may be significantly lowered relative to far-field values. While the radial horizontal stress increases toward the salt (see the schematic “d” in figure 8-5.), the horizontal hoop stress decreases as the outward expansion of the diapir stretch the wall rocks circumferentially. As a result, for some distance away from the dome maximum horizontal stress becomes radial ($S_H = \sigma_1 = \sigma_{rr}$) and the vertical stress becomes intermediate principal stress ($S_v = \sigma_2$). The minimum horizontal stress in this region remains minor principal stress oriented tangentially ($S_h = \sigma_3 = \sigma_{\theta\theta}$). Since the tangential stress is lowered, the difference between primary (radial) and least (hoop) principal stresses increase, thus creating hole instability and aggravating well construction (Bradley, 1978; Seymour et al., 1993; Wilson and Fredrich, 2005; Nikolinakou et al., 2013a).

Moreover, the source to which diapirs are connected is usually pressurized by the weight of the overburden column. These pressures are transmitted up the diapir, where they contribute to the already elevated horizontal stress by pushing out against adjacent sediments and enhancing their deformation. As a result of substantial radially outward deformations that occur off the crest of a domal structure, stress perturbation can potentially revert stress state such that $S_H = \sigma_1$, $S_h = \sigma_2$, and $S_v = \sigma_3$ (Jackson and Hudec, 2017; Sanz and Dasari, 2010; Nikolinakou et al., 2013a). Although rare, stress regimes associated with reverse faulting conditions were found near salt domes in the GoM (Saleh et al., 2013) and in the North Sea (Seymour et al., 1993; Dusseault et al., 2004b). Not only restricted to rising diapirs, but tectonic instability around salt bodies also includes extensional activity above structural highs (lowering horizontal stress) and compression above structural lows (increasing minimum horizontal stress). As shown at schematic “a” in figure 8-5., such occurrences can give rise to a local stress regime different from that acting on a basin-wide scale (Wilson and Fredrich, 2005).

8.2.2. Rubble (brecciated) zones

The “rubble or brecciated zone” comprises older and competent sediments that have been disturbed by salt movement and/or fault creation around salt bodies. Associated shearing motion results in a complex network of intersecting fractures and other planar weaknesses (usually below the salt), which poses a significant risk of LC (refer to schematics “c” and “d” in figure 8-5.). Moreover, due to existing fractures, sediments pose little or no intrinsic strength. As a result, an elevated risk of wellbore instability exists. When the encountered formations are permeable, any attempt to stabilize the wellbore by increasing MW in the

rubble zone can promote mud penetration into the cracks within the rock fragments and thus further destabilize the borehole, often leading to massive wellbore collapse. Although circulation losses are the most common and expensive issues encountered within the subsalt rubble zone, occurrence of WCI is also more likely due to narrow drilling windows. In addition, weak formations below the salt can aggravate cement placement, as a substantial risk of LC exists in these zones. When compared to the sheared zones adjacent to salt bodies, sediments in rubble zone are less affected by salt-induced stresses and are usually not deformed to a pore collapse state arising from high pore pressures (see 8.2.10.) (van Oort, 2004; Wilson and Fredrich, 2005; Saleh et al., 2013).

8.2.3. Salt welds with trapped pressure

The salt welds (also called salt wings) can hide very high trapped pore pressure under the existence of structural highs or restricted dewatering pathways around the edge of salt. Salt welds represent the evacuated remnants of pre-existing autochthonous or allochthonous salt bodies that comprise zones of mechanically contrasted strata that used to be separated by cut-in salt. Salt welds are essential parts of hydrocarbon migration pathways, as they either provide leakage pathways into overlying traps or constitute a trap seal (see the schematic “d” in figure 8-5.). Welds are unlikely to pose drilling difficulties. However, PP differentials across welds remain a major concern in well design (Wilson and Fredrich, 2005; Jackson and Hudec, 2017).

8.2.4. Tar bands

The primary problem occurring when encountering tar (refer to schematic “b” and “c” in figure 8-5.) is associated with borehole closure and well construction-related problems (vibrations, running of tubulars, inefficient cementation, etc.). This problem is not extensively present in subsalt/presalt environment, but its occurrences have been documented across the literature (Rohleder et al., 2003; Romo et al., 2007; Han et al., 2008; Han et al. 2010).

8.2.5. Major subsalt pressure regression

See chapter 7.2. for more details. Here, ECD management in a narrow drilling window becomes of utmost importance. In such situations, casing design strategy can be tailored to address hardly drillable intervals below the salt body.

8.2.6. *Overturned beds*

Due to significant lateral movement, complex near-salt sediment deformation can occur beneath salt sheets and salt overhangs. Bedding rotation can occur due to the withdrawal of underlying salt. In contrast, imposed strains on adjacent wall rocks caused by raising diapirs can cause sediments adjacent to salt to steepen or even overturn (upturn; schematic “d” in figure 8-5.). Additionally, the latter may be highly faulted, fractured, and sheared. Rotated or overturned and faulted sediments can cause stress rotation due to bedding anisotropy. In these instances, circulation losses, wellbore instability, and rubble zones can be expected, thus necessitating custom-tailored salt exiting strategies (Wilson and Fredrich, 2005; Jackson and Hudec, 2017). Salt emplacement will modify the depositional pattern, resulting in the thinning of beds and changes in dipping angle approaching the salt sheet (van Oort, 2004). Wellbore instability problems may become quite severe if weak bedding planes intersect a wellbore at unfavorable angles. The fractures, as in shales, may provide a pathway for mud or fluid invasion that can lead to time-dependent strength degradation, softening, and ultimately to hole collapse (Amoco, 1996; Pašić et al., 2007). This problem will be dependent on the “angle of attack” (AoA) chosen to drill the anisotropic formation, as some angles will be more favorable, i.e., yield a higher effective rock strength²⁶, than others (van Oort, 2004; Fekete et al., 2014).

AoA is defined as the angle between the wellbore and the bedding plane, it’s normally taken as acute angle. For the AoA of 0° the wellbore will be drilled parallel to the bedding plane, whereas the AoA of 90° corresponds to the wellbore drilled perpendicular to bedding. If trajectory cannot be designed to prevent that plane of weakness is exposed, wellbore failure will not be controlled only by the borehole orientation relative to in-situ stress conditions but also the borehole orientation relative to the bedding plane (Fakete et al., 2014). The weak bedding failure could aggravate wellbore stability and consequently impact further well construction and lifelong integrity through problems related to excessive borehole

²⁶ Sedimentary rocks have a strength, which is direction dependent. For example, rocks such as shales or laminated sandstones can be broken along the bedding plane relatively easily while they are much stronger across the bedding plane (Plane of Weakness concept). It follows that the rock shear strength clearly exhibits anisotropic character (Aadnøy and Looyeh, 2011). The importance of strength anisotropy depends on relative weakness of bedding and the bedding plane orientation with respect to the applied stress. Consequently, the rock strength can be defined in terms of intact rock strength (failure is not controlled by presence of weak planes; usually at high and low angles relative to bedding plane) and the strength of weak planes (when the weak planes govern the rock failure; usually in a specific range of angles relative to the bedding) (Zoback, 2007).

breakouts/cavings. Typically, any AoA between 10° and 30° is considered unfavorable as very high MW may be required to prevent failure along weak plane (Aadnøy and Looyeh, 2011). Since MW-s required to stabilize wellbore in such case are highly dependent on stress state, plane of weakness dip and the borehole orientation, it is hard to provide any definite guidelines regarding trajectory optimization and the problem should be seen as a case sensitive. A good example is brought by the case study in Pompano field (Wilson et al., 2003) where the risk of exiting into subsalt environment at the angle near-parallel to weak-bedding planes necessitated well planning team to increase EMW for approximately 120 kg/m³ (1 ppg).

8.2.7. Salt idiosyncrasies

Special considerations need to be given to problematic features encountered within the salt interval. These include creeping at low effective stress, squeezing salts, and overpressure in salt inclusions. These problems are presented in schematic “b” in figure 8-5. but they are discussed separately under the chapters 9. and 7.3., respectively.

8.2.8. Overpressured fluids trapped against salt

Trapped sediments on salt seams can be overpressured and highly plasticized. As a result, pore pressures on salt seams may be elevated when the shortening of adjacent rocks occurs under undrained conditions. Similarly, deeper pore pressures can migrate the upturned sediments upward, thus forming zones of high PP next to salt, which halts further migration (see schematic “d” in figure 8-5.). As already mentioned, elevated pore pressures can play key roles in creating shear zones (Wilson and Fredrich, 2005; Nikolinakou et al., 2012; Jackson and Hudec, 2017).

8.2.9. Fractured carapace zones

Carapace sections are typically brittle fractured formations laying immediately above the salt. These older, brittle sediments may be carried upwards by the rising salt body and thus are better cemented than other suprasalt, less compacted lithologies. These, initially deeper buried, formations may transport paleo pressures to the lower stratigraphic areas, where if depressurized, they can be become progressively fractured and result in circulation losses (see schematic “a” in figure 8-5.). Additionally, lateral displacement by the salt can create extensional zones in the overlying sediments, decreasing horizontal stresses and promoting circulation losses. Other than by fracturing, if the rate of salt rise exceeds the pressure

dissipation rate, these rafted sediments will fail to dewater and accordingly retain transported overpressures (Wilson and Fredrich, 2005; Jackson and Hudec, 2017).

Moreover, as salt diapir rises, its movement forms complex fracture and fault networks adjacent to diapirs along which migration pathways may form. At the same time, the presence of fractured carapace sediments enables fluid vertical migration. Experiences from the North Sea (Seymour et al., 1993; Dusseault et al., 2004b) demonstrated that gas clouds might be encountered in supra dome regions where fault-sealed, gas-charged, sand bodies exist which may act as a pressure source. Low S_h and intensely deformed and fractured rocks (mostly shales) promote gas migration upward, increasing the risk of well control incidents during the well construction. When coupled with decreased FG, these risks can necessitate additional casing string to be installed on-fly and impose limits on ROP.

8.2.10. Salt shear zone

Sheared zone, or, interchangeably used, salt gouge zone, is a term for the zones that may be created in situ if the imposed effective stresses arising from salt emplacement or fluid migration exceed a threshold that adjacent rocks can withstand (see schematics “b” and “c” in figure 8-5.). The high PP associated with rapid depositional rates, typically common in Deepwater environments, result in under-compaction of the sediments with corresponding low formation strength. Ergo, overpressured zones of high plasticity are typical risks associated with such zones. Attributed to high shearing forces, the sediments can be at or near the “pore collapse” state. Even when shearing forces are insignificant, elevated PP anticipated adjacent to salt and below the base of salt lowers the minimum effective stress and thus weakens surrounding sediments, resulting in very narrow PPF windows (Saleh et al., 2013). In areas where the smectite-illite transformation is encountered, diagenesis effects cause clay shrinkage, which if large, can lead to reduction of S_3 . Due to high shale’s cohesion, the shales can fail in tension if in-situ PP is near to S_3 values and thus cause intensely fractured quartz-illite shales to exist (Dusseault et al., 2004b). Similarly, the salt body's presence can significantly perturb the near-salt stresses and induce horizontal stress anisotropy, consequently amplifying VME stress sufficiently to cause in situ rock failure. Numerous studies (Whitson and McFadyen, 2003; Barker and Meeks, 2003; Saleh et al., 2013) reported that MWs approaching (93 to 95%) FG had been required for hole stabilization (Wilson et al., 2003; Wilson and Fredrich, 2005; Saleh et al., 2013; Jackson and Hudec, 2017).

Another problem pertinent to gouge zones is adverse behaviour of encountered shales. Namely, the low geothermal gradients common to Deepwater hampers the progressive transformation of smectite to illite at the depths where smectite-illite transformation²⁷ would usually be common onshore. Shales with a high proportion of smectite are characterized by high sorption (swelling) capacity which tend to promote plastic, gumbo-like behavior. In such instances, a substantial plastic deformation may occur at the wellbore wall and thus impose elevated risk of BHA sticking. Likewise, if not addressed, chemical effects will promote sticking of cuttings onto the bit wetted by the drilling fluid due to swelling tendencies of hydrophilic clay particles. In addition to stuck pipe incidents, if the drilling team fails to react promptly (or proactively), anticipated bit balling when exiting salt in the gouge zone comprising gumbo shales may trigger various downhole problems; reduced ROP, increased trip time due to swabbing and presence of tight holes, high torque and drag (T&D), stuck pipe due to swelling of clay minerals, LC occurrences caused by formation of the mud rings and hole pack-off, blocked nozzle(s), etc. (Ledgerwood and Salisbury, 1991). On the contrary, where brittle, sloughing shales are encountered (characterized by relatively high overall illite content in clay component), the sloughing nature of shales becomes a primary concern as excessive cavings can result in hole pack-off, stuck pipe, or issues related to excessive hole enlargement (O` Brien and Chenevert, 1973). However, problematics related to chemical instability of shales is usually addressed through proper mud formulation or inhibition, and BHA modifications, and as such pose minor effect on well architecture design relative to mechanical instability concerns.

²⁷ Under considerable depths and high temperatures, clay diagenesis occurs and smectite gradually transforms to illite. Apart from implications to wellbore stability, this transformation is followed by expulsion of previously adsorbed water, where it can contribute to AP creation. However, this phenomenon is believed to be a rather secondary cause whose effects could help explain more steeply PP gradients than encountered in AP zones generated solely by undercompaction (Mouchet and Mitchell, 1989).

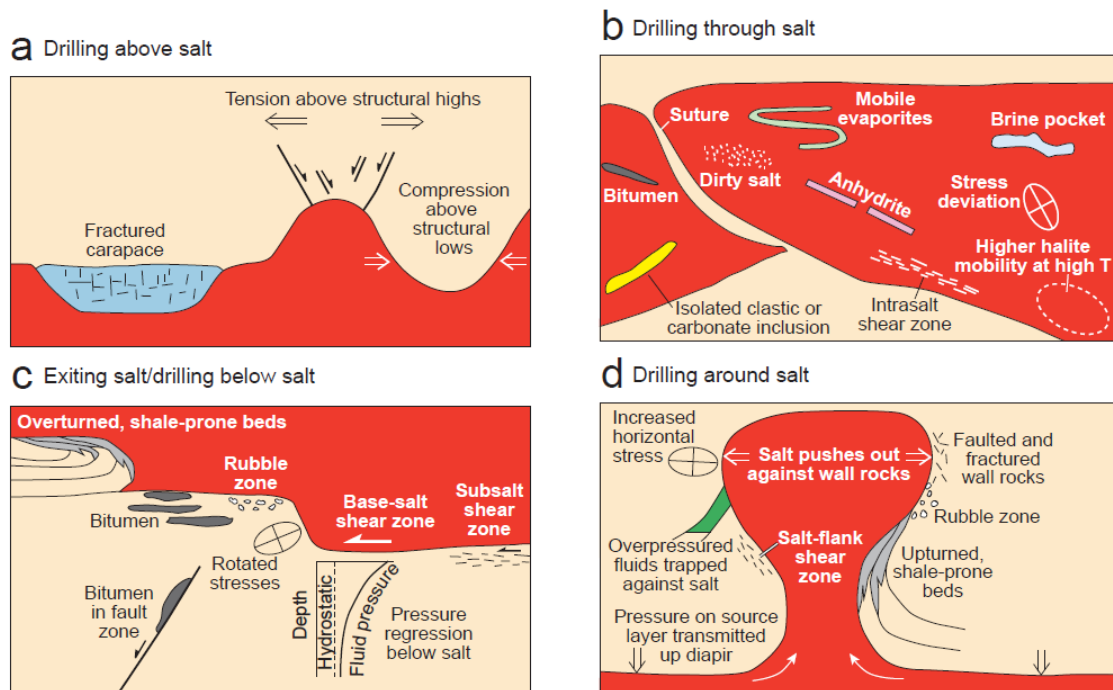


Figure 8-5. Summary of geomechanical instabilities around and within salt bodies (Jackson and Hudec, 2017)

8.3. Salt implications to wellpath optimization in Deepwater salt environment

A high uncertainty coupled with often scarce data and challenges present in the Deepwater salt environment will necessitate pushing wellbore sections towards the drilling margins limit while simultaneously optimizing hole diameter to allow several sizes of intermediate casing highlight. That highlights the need for flexible well designs that allow implementation of unconventional borehole and casing sizes such that any unanticipated drilling hazards and wellbore problems can be addressed (Marland et al., 2007). Mud densities must be carefully managed to overcome pore-pressure and salt creep but sufficiently low to prevent wellbore tensile failure and avoid corresponding losses. Need for safer and efficient well design and delivery offshore necessitate an in-depth understanding of geomechanical properties, stress regimes, downhole pressures, and wellbore hazards (Schlumberger, 2014). Despite immense experience gained and advances in offshore salt well design over the last 20-30 years, it should be emphasized that practices developed and proven in one subsalt basin might not necessarily apply in another subsalt field (Alfayyadh et al., 2020). Wellbore trajectory planning plays an important role in the development and optimization during the field lifecycle. Underestimation during the planning phase could result in elevated well construction costs due to purchasing excessive casing strings or, in extreme cases, lead to decisions not to drill the well if cost and risk assessment characterized well as unfeasible.

The wellbore placement may influence the amount of hydrocarbons contacted and the ease at which a well meets its long-term objectives. With the encroachment of new drilling techniques and improved accuracy during the drilling process, the ability to deliver various types and shapes of wells has increased demand for understanding stability problems specific to wellbore trajectory planning (Griffiths, 2009; Himmelberg and Eckert, 2013; Aird, 2019).

8.3.1. Salt entry and exit selection strategy

A typical drillability indicator is a difference between S_3 and PP (figure 8-6b.). However, the MW window is a function not only of the pore pressure and fracture gradient, but also of the potential for shear failure. Therefore, the real drilling window is a function of the relative orientation between the wellbore, the local stresses, and the rock properties (especially the UCS, friction angle, and tensile strength). The VME stress can be used as another indicator to evaluate drillability or casing design schemes during the planning phase (Fredrich et al., 2003; Schlumberger, 2014). Under the constant mean stress, shear strength decreases with the increase in horizontal stress anisotropy, viz., the disparity between S_2 and S_3 , which is seen as the increase of VME stress. Combined, these two indicators can be used to estimate preferred locations of salt entry and exit (Schlumberger, 2014). For example, referring to figure 8-6b., guided by logic to traverse the salt section as quickly as possible and minimize adverse creep implications to well design (see Chowdhury et al., 2016), a tempting entry to a salt body would be near the well “A”. However, given the amplified VME stress (figure 8-6a.), virtually nil drilling window exists (figure 8-6b.) and such a trajectory adjacent to the salt body does not seem feasible.

Fredrich et al. (2003) exemplified the importance of considering both stress perturbations and principal stress rotation around the salt body in well design. Figure 8-7. represents polar plots of minimum MW necessary for wellbore stability for three distinct scenarios:

- A) Unperturbed stress state,
- B) Perturbed stress state where no rotation of principal stresses occurs and,
- C) Perturbed state of stress and stress rotation adjacent to the spherical salt body.

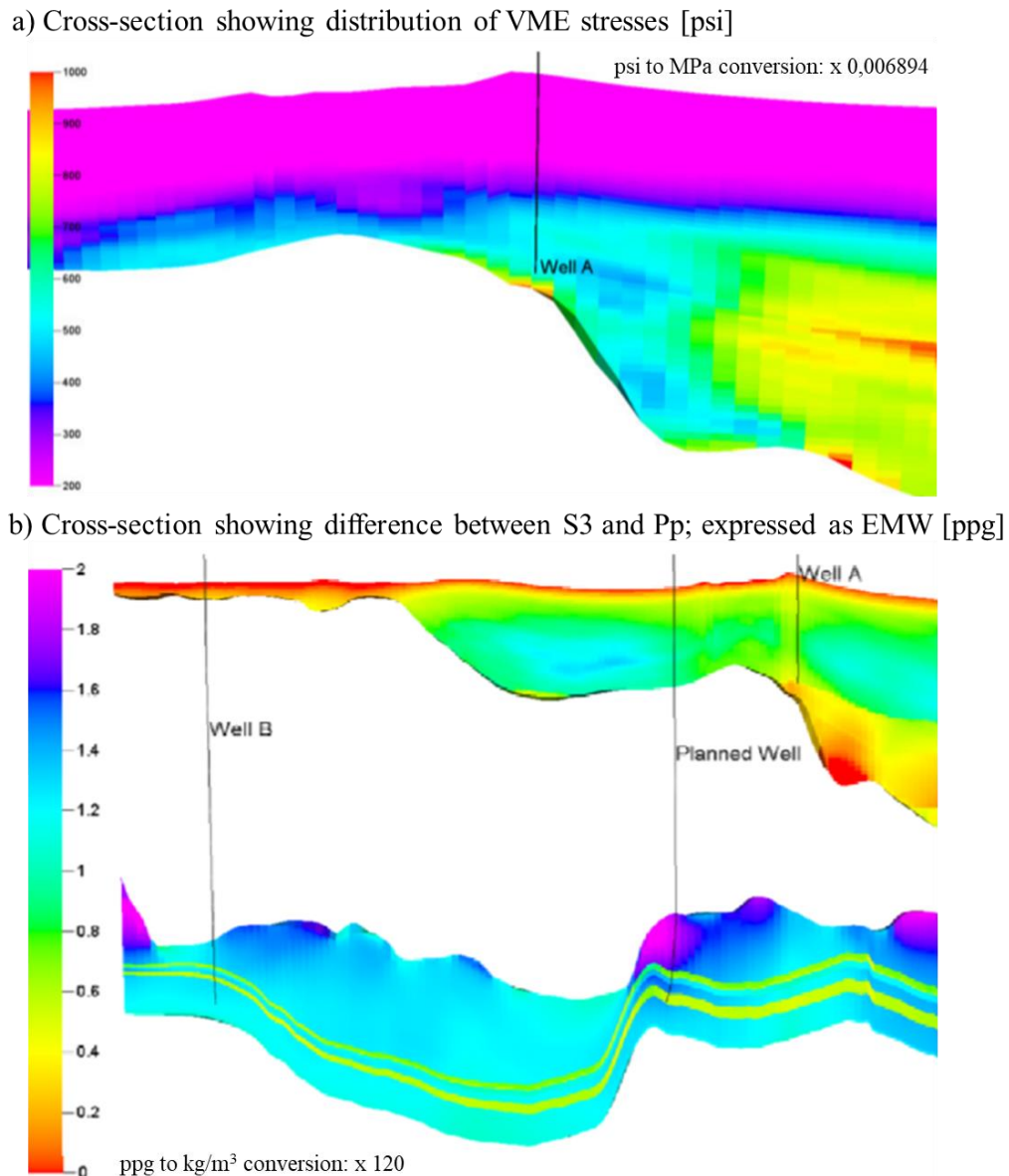


Figure 8-6. Typical indicators used to evaluate potential salt entry and exit (Schlumberger, 2014)

By observing mentioned cases (B) and (C), one can note that vertical wells drilled adjacent to the spherical salt body is stabilized under all three cases. However, in cases (B) and (C), drillability is substantially decreased even though smaller MW-s are needed to stabilize near-vertical wells than in case (A). Moreover, the direction of the planned wellbore will also have a pronounced effect on the range of permissible mud weights. The reason for that is the decrease of FG at the point of interest (Bradley, 1978; Fredrich et al., 2003). It follows that only well trajectories up to 30° inclination deviated away from salt are possible in practice. Similar was indicated by Wilson and Fredrich (2005), who showed that the imposed stress

rotations below salt have a modest impact on required MW, yet its effects on the drill-out direction are significant (see figure 8-7.).

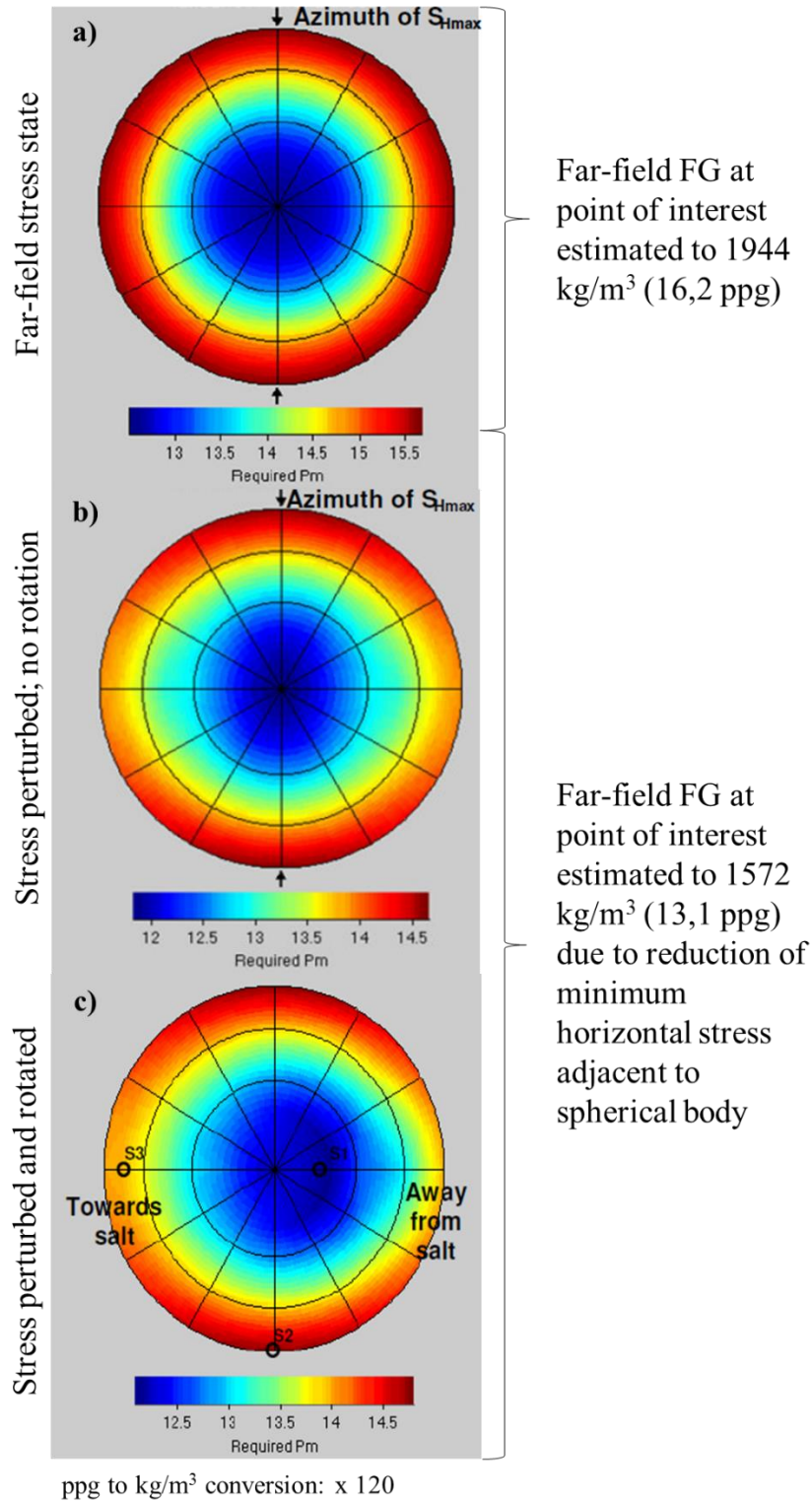


Figure 8-7. Wellbore shear limit expressed in EMW for (a) unperturbed stress state (b) perturbed stress state where no rotation of principal stresses occurs and (c) perturbed state

of stress and corresponding stress rotation adjacent to the spherical salt body (modified from Fredrich et al., 2003)

8.3.2. Wellbore stability implications to well architecture in Deepwater salt environment

In most cases, MW window and corresponding wellbore trajectory planning are based upon assuming the Andersonian state of stress where one principal stress is assumed vertical. Such assumption allows utilization of a rather simple 1D method that enables inferring horizontal stress from overburden stress and logging data along the wellbore (Zoback, 2007). In most simple terms, Poisson's ratio can be derived from compressional and longitudinal wave slowness, and minimum horizontal stress can be related through effective stress ratio, K :

$$K = \frac{\nu}{\nu - 1} = \frac{\sigma'_h}{\sigma'_v} \quad (8-1)$$

By knowing PP (e.g., from seismic) and overburden stress (easily obtained from Density logs), the above-mentioned equation can be rearranged to estimate σ'_h :

$$\sigma'_h = K(S_v - P_p) \quad (8-2)$$

Numerous methods for estimating the effective stress ratio have been proposed over the years, based on normal faulting theory, theory of elasticity, or empirical correlations (see Zoback, 2007). In O&G applications, the K value typically ranges from 0,3 to 0,5 for hard, elastic rocks, whereas, in the case of softer, plastic sediments, the K value may approach 0,8 or even 1,0 (Barker and Meeks, 2003). The stress ratio can be seen as an indicator of shear stresses and risk of circulation loss. Ratio values close to 1,0 indicate that the stress state is nearly isostatic and shear stresses are small. On the contrary, low K values indicate that the minimum principal stress is much lower than the overburden value. Due to low minimum principal stress, the risk of LC occurrence increases while large differential stress promotes borehole instability (Nikolinakou et al., 2015).

For this Thesis, it is sufficient to understand that in most cases, minimum horizontal stress will represent a certain fraction of overburden, allowing to put an upper margin on the MW easily. Furthermore, once the FG is calibrated (as outlined in chapter 7.), the upper drilling margin can be constructed with sufficient certainty for further drilling activity. On the other hand, a lower margin will be constructed as later outlined later (see section 10.1.). While such a concept works well in most cases, even in simple Deepwater environments (Aird, 2019), it cannot capture the effect of complex geologic conditions such as present in heavily

faulted areas or, as in our case, salt structures (Himmelberg and Eckert, 2012; Shen et al., 2014; Nikolinakou et al., 2013b). Here, K values vary around the salt body, and it is directly dependent upon the geometry and value of the stress components (Shen, 2012; Nikolinakou et al., 2013b). Since wellbore stability depends on well geometry relative to the 3D state of stress, rapidly changing stress tensor caused by salt-induced perturbations can cause significant changes in stress magnitudes acting on a wellbore wall even for small trajectory deviations or turns. The overall stability of a wellbore trajectory cannot be studied continuously using a single polar plot, as its validity becomes restricted over a limited depth range when stresses are perturbed (Himmelberg and Eckert, 2013; Fredrich et al., 2003). Likewise, equivalent depth methods (extrapolation of formation intrinsic properties, pressures, and stress gradients from the existing offset wells along with geological markers) can result in erroneous assumptions leading to costly failures in well design around salt bodies (Nagy et al., 2013). Here, 3D mechanical earth models (MEM) can be utilized to predict potential safe drilling conditions for well location since it relates the influence of the 3D geostructure to stress patterns around salt bodies (Shen, 2012). The MEM is defined as a mathematical representation of rock properties, pore pressure, and in-situ stress as a function of the depth for a particular interval (Adachi et al., 2012; Schlumberger, 2014). These models consist of 3D, discretized, geometrical mesh. Under the assumption of the continuum, a set of equilibrium constitutive equations is solved in discrete points located in cell nodes by imposing appropriate loads and boundary conditions. The approximate solution of deformation and stress between the designated points is then propagated using shape functions defined for each cell node. Eventually, stress and strain tensor components can be found for each model grid cell (Schlumberger, 2021; Vita, 2021). Schematic representation of building a 3D model is shown in figure 8-8. For a detailed explanation of the 3D modeling technique around salt see, e.g., Luo et al. (2012a).

The output of such models can provide a quick and visual way of representing drillability conditions in suprasalt and subsalt regions. The common industrial practice became to enhance conventional trajectory design in the complex geological environment using a 3D MEM (Adachi et al., 2012; Himmelberg and Eckert, 2013; Schlumberger, 2014; Shen et al., 2014). In essence, all the approaches, seemingly different, suggest extracting the stress tensor components from a 3D MEM and applying them to analytical stability analysis workflow as discussed under chapter 8. Accordingly, wellbore stresses can be assessed as a function of the well path and the trajectory examined for tensile and shear failure.

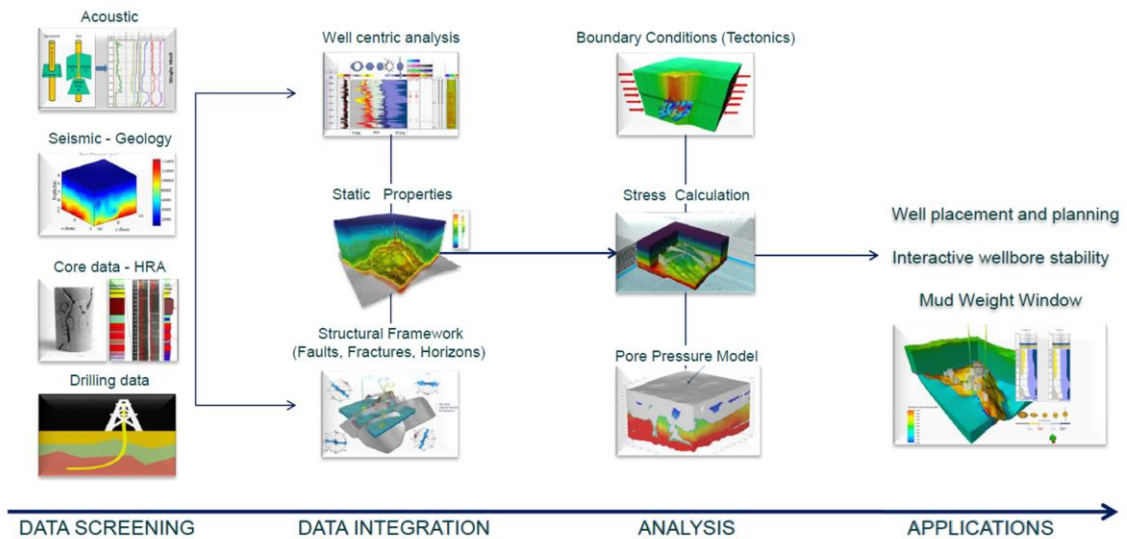


Figure 8-8. Summary of procedure for creating 3D MEM and its applications (Schlumberger, 2021)

Work by Adachi et al. (2012) presented a well planning tool that allows assessment of MW window for arbitrarily chosen trajectory and corresponding MW window sensitivity analysis to the change of wellbore inclination and azimuth. Relevant mechanical and rock properties are extracted from the 3D MEM along the nodes situated on the wellbore trajectory and used in critical MW calculation. Figure 8-9. shows that only trajectory 1 (bright red) and 2 (blue) yield drillable MW windows. In the case of trajectories 3 (purple) and 4 (dark red), the shear failure limit practically touches the upper MW window margin. Authors indicated that the tool facilitates wellbore stability assessment as quick analysis of different wellbore placement alternatives can be done without recalculating mechanical, stress, and pressure properties already available from large MEM.

Himmelberg and Eckert (2013) went a step further and proposed a methodology (Appendix-1) for trajectory optimization and demonstrated its applicability in a subsalt environment. First, a virtual well path is constructed based on the polar plot at the target location (figure 8-10a.) (determines optimum drilling azimuth and inclination angle) and surface location, which can be either fixed or flexible. If the prior is the case (e.g., subsea template), the well lateral distance will determine the type of trajectory (“build and hold” or “S-shape”). The safe Kick-off Point (KOP) depth will be found by examining polar plots constructed in discrete points along the vertical BML, with the KOP defined by a polar plot of the highest drillability.

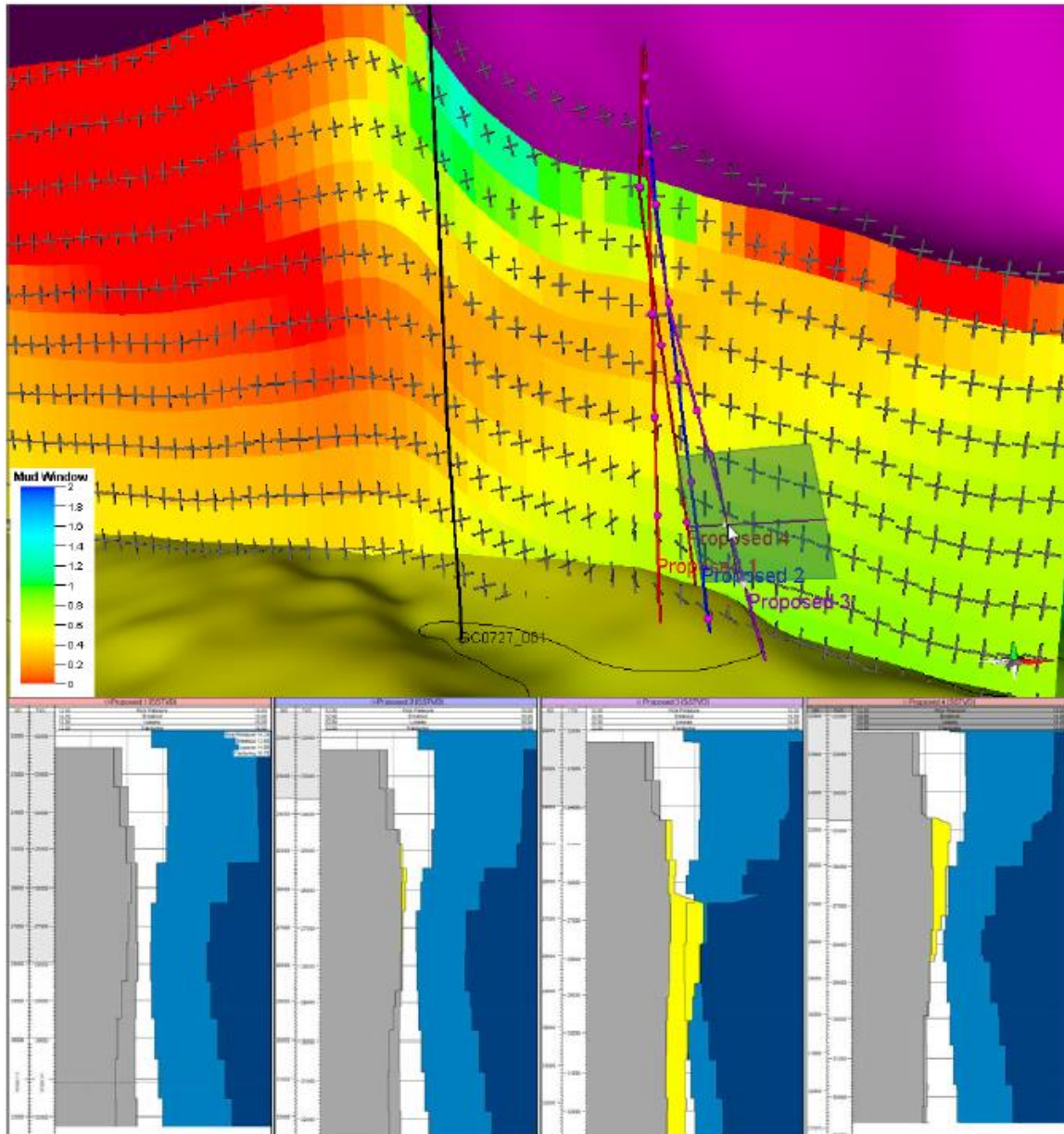


Figure 8-9. A MW window evaluated for different well architectures using Fast Wellbore Stability engine; yellow - shear limit; gray - pore pressure; bright blue - minimum horizontal stress; dark blue - tensile failure limit (Adachi et al., 2012)

Once the KOP is identified, the distance between KOP and drilling target is discretized, and drillability is evaluated along the horizontal departure. Optimal inclinations at the hold and drop sections will be determined in a way that the conditions identified at the target entry are met (figure 8-10b.). In the case that the surface location is flexible, the “build and hold” trajectory is usually preferred. Continuous MW window is eventually constructed using the Nearest Neighbour algorithm which maps stress tensor components and rock properties onto a proposed virtual path from a 3D MEM (figure 8-10c.). Figure 8-10. summarizes the procedure. The authors indicated that a wellpath with the most favorable drilling conditions

is expected by following the proposed methodology. As a result, the least number of casing strings should be deployed.

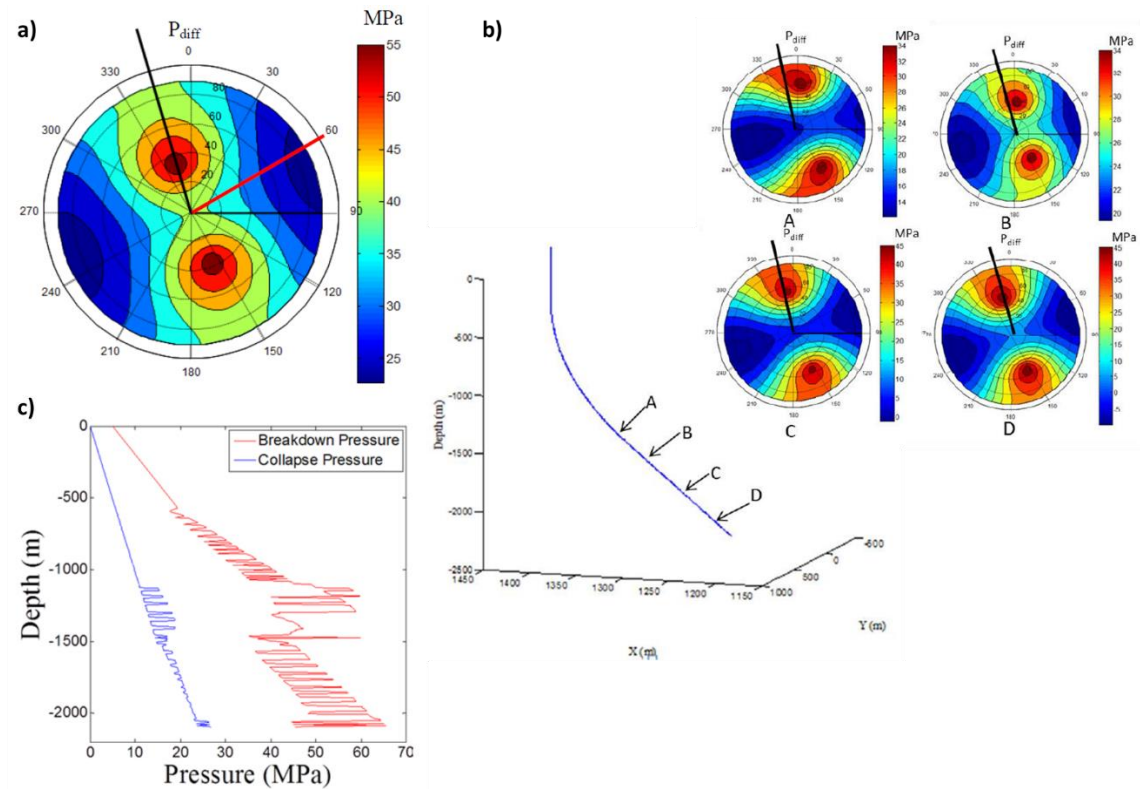


Figure 8-10. Trajectory optimization workflow (modified from Himmelberg and Eckert, 2013)

8.3.3. Well trajectory design challenges in offshore salt play

Apart from defining trajectory with the largest drillability, geomechanical hazards around salt may have a significant impact on the well design. Furthermore, the situation is far more complicated in reality as a perfect salt body rarely exists, and a wide array of unfavorable pressure conditions and potential geomechanically unstable zones can be encountered around salt. Even though the well path may be modified to address a certain problem or avoid a specific hazard, opting for such a trajectory may be counter-intuitive considering other factors affecting overall well design. Optimizing wellbore trajectories with the aim to deliver safe operating windows becomes of utmost importance in sub/pre-salt wells, particularly in zones when entering and drilling abnormally pressured transition zone or specific intervals with narrow drilling margins (Aird, 2019). Thus, the optimum wellpath will not necessarily be identified as the most attractive MW window but also needs to consider rather local phenomena:

- shallow hazards above salt (Dusseault et al., 2004a, b; Israel et al., 2008),
- salt creep severity and salt exposure time (van Oort, 2004; Poiate et al., 2006; Zhang et al., 2008; Jackson and Hudec, 2017; Orozco et al., 2018),
- inclusions (van Oort, 2004; Chatar et al., 2010; Zijp et al., 2017; Gerritsen, 2018),
- wellbore stability below salt sections and impact of stress rotation (Fredrich et al., 2003; Wilson et al., 2003; Wilson and Fredrich, 2005; Israel et al., 2008; Saleh et al., 2013),
- PP uncertainty below salt (Whitson and McFadyen, 2001; van Oort, 2004; Wilson et al., 2003; Wilson and Fredrich, 2005; Marland et al., 2007; Moyer et al., 2012),
- salt exit angle relative to subsalt sediments` bedding angle (under preferred AoA) (Fredrich et al., 2003; Wilson and Fredrich, 2005; van Oort, 2004; Israel et al., 2008; Saleh et al., 2013).

When drilling around domes, salt-flank settings are not normally as challenging as subsalt because drilling in salt flanks does not usually involve an abrupt transition from the relatively predictable to the wildly variable and unknown environment. However, special attention must be paid to drilling hazards, including but not limited to strongly deformed sediments, high pore pressures, shear zones near the edge of salt (Dusseault et al., 2004, b; Wilson and Fredrich, 2005). Here, especially tempting to avoid are the shear (drag) zones. In addition to rotated principal stresses, the borehole will additionally be subject to shear stress, thus complicating an already difficult situation. Encountering either an active shear zone adjacent to the salt or critically stressed fault could shear off a wellbore or cause casing collapse during the well lifecycle (Dusseault et al., 2001; Dusseault et al., 2004b). Therefore, many operators prefer to drill through gently dipping base-salt contacts or deviate the trajectory such that the wellbore emerges normal to the salt-sediment interface. Salt exit is the most dangerous moment when drilling thick salt bodies in any drilling program (Jackson and Hudec, 2017). The hazards associated with drilling through the base of salt were mentioned previously. However, the impact of specific risks may be high to an extent where it requires a particular salt exit target²⁸ as:

- the interpretation of seismic data below the salt is less reliable for determining pore-pressure and geological structures,

²⁸ This operation is so critical that it became a usual practice for operators in GoM Deepwater to develop company-specific salt exit procedures (see Israel et al., 2008).

- the existence of the rubble zone,
- uncertainty in the principal stress state below the salt exists as stresses are disturbed, rotated, and the fracture pressure reduced,
- fracturing and faulting are also common, and these features can cause pore pressure compartmentalization. In significantly permeable formations, compartmentalized pore-pressures will lead to charging or depletion of formations, causing influxes or LC and the possibility of differential sticking.

Israel et al. (2008) summarized the main factors that can impact trajectory design in Deepwater drilling:

1. Due to their enormous potential to reduce cost, cluster wells are preferred solutions for many operators and can add significant value to the field development in these areas. Although they are designed to deviate at shallower depths to achieve the step-out required to hit reservoir targets, drilling from the same slot does reduce the number of additional drilling centers to be deployed.
2. Limiting the inclination angle (usually below 40°) by putting the KOP into shallower depth will ease and shorten the time needed for subsequent completion and workover operations. However, a special attention should be put when designing KOP in Deepwater. Namely, shallow KOP will facilitate building and maintaining wellbore angle in suprasalt regions. While the shallower KOP might help to enter the salt at preferred angle or maintain designed architecture within the salt body, such approach may negatively affect T&D. On the contrary, deeper KOP helps reduce T&D forces in latter sections as the hangdown weight at the KOP is reduced. Besides, other things to consider when designing KOP include completion requirements, hole cleaning, logging requirements, casing wear, and drilling tool limitations, to name a few (Israel et al., 2008; Chatar et al., 2010). Hence, one shall find a balance between hitting the target, torque and drag, and other things when designing for KOP in Deepwater.
3. With wells exceeding 6000 m TVD, inclination limitations imposed to the wireline operations and interventions are dropping down to 35-40° different from the shallow waters, where angles of 50-60° are still considered safe.
4. By developing a field with installed Floating Production Storage and Offloading (FPSO) unit, having a lot of subsurface slots, nudging the wellbore may be required to maintain the anticollision separation needs.

5. The presence of shallow hazards may significantly impact the spud site itself. In turn, this will require appropriate modifications to the well trajectory so that the reservoir can be penetrated at the optimal target.
6. Directional drilling in salt may also be desired to ensure exit in a salt body with a dipping base at a deeper TVD due to increased drilling margin later along the proposed trajectory. That ensures that the added instability and associated issues that can arise from the rotation of stresses at higher dipping salt bases can be avoided.
7. Directional drilling will often be required to avoid troublesome zones identified at the salt exit, such as tar zones and/or rubble zones.
8. Due to much uncertainty arising when drilling through salt inclusions, a well planning team should deviate the trajectory in salt rather than traverse inclusion.

Likewise, the type of well to be drilled (e.g., exploration, appraisal, development, etc.) will also govern the well architecture. A better reservoir description by appraising the field through highly deviated and horizontal wells. These well types are capable of greater production rates and improved recovery factors compared to vertical wells (Seymour et al., 1993). Even though early exploration wells were drilled as vertical, operators have realized that a deviated trajectory usually results in the saving of one casing or liner string, with reduced risk of well construction. However, such a decision must be underpinned by the cost comparison of the additional time spent drilling versus the potential cost of an event and associated risk (e.g., risk of sidetracking or setting the casing shoe prematurely) (Cromb et al., 2000; Dusseault et al., 2004b).

9. CREEP IMPLICATIONS TO WELLBORE STABILITY

The creep is considered a wellbore stability issue that is highly mud sensitive. If not addressed properly during the well planning, creep-related instabilities can incur a significant NPT and endanger the well economics (Orozco et al., 2018). On the contrary, the wellbore wall stability of the salt is slightly MW sensitive, and the geomechanics-stability problems are rather related to areas outside the salt body (Whitson and McFadyen, 2001). In terms of well-design, creep will directly impact the selection of MW-s, casing seat selection and design of strings exposed to mobile salt (Wilson et al., 2002; van Oort, 2004; Zhang et al., 2008; Wang and Samuel, 2013). Creep-related issues associated with well-construction are well documented across the literature; excessive off-bottom torque, vibrations, pack-offs, mechanically stuck pipe, casing running blockage, well deviation issues, and poor cementing job (Barker et al., 1994; van Oort, 2004; Israel et al., 2008; Omojuwa et al., 2011; Castagnoli et al., 2016; Alfayyadh et al., 2020). The higher the salt thickness is encountered, the more the overall drilling performance will be affected (Omojuwa et al., 2010). However, as thinner layers tend to relax more quickly than the massive salt bodies, they can be more problematic for particular drilling operations. Wilson et al. (2002) indicated that borehole closures of up to 2.54 cm/hour were recorded when traversing thin layers in GoM. However, this Thesis will be limited to creep implications in trajectory optimization and well design.

9.1. Industry models for creep estimation

Appropriate creep modeling is of utmost importance when trying to proactively address operational issues that can result from excessive salt encroachment. The key to modeling creep behavior is to choose a representative constitutive model for creep in salt formations. Two most notable models are presented below.

9.1.1. The Munson and Dawson “Sandia” model

The Munson and Dawson “Sandia” model (1979; 1982) (Multi-mechanism Deformation Model; MD model) is probably, up to now, the most sophisticated model in O&G industry which simulates transient and steady state salt creep. This model resulted from a large-scale research and testing program for a radioactive waste depository in New Mexico. It is based on the superposition of three micromechanical creep mechanisms (glide and climb dislocating motions and FADC mechanism) in steady state, quantitatively estimated by a power law and hyperbolic sine expressions. By adjusting the steady state creep rate using a transient function that comprises evolutionary hardening variable and fitting parameters, the

transient creep can be modeled using the mentioned model. Due to the complexity of the model, the reader is referenced to the original work by Munson and Dawson (1979; 1982).

9.1.2. Double Mechanism creep law

Another widely accepted model is Double Mechanism Creep Law, also called the DM model. The constitutive equation was developed by Costa et al. (2005) as a simplification of the model developed by Munson and Dawson. Several studies (Poiate et al., 2006; Costa et al., 2010; Firme et al., 2014) indicated that this model presents good results in terms of creep rate. Although the inability to capture the transient creep causes a lag in the results when calculating absolute displacements, this shall not invalidate the results for long-term analyses.

$$\dot{\epsilon} = \dot{\epsilon}_0 \times \left(\frac{\sigma_e}{\sigma'_0} \right)^n e^{\left(\frac{Q}{RT_0} - \frac{Q}{RT} \right)} \quad (9-1)$$

Where $\dot{\epsilon}$ is resultant steady state creep, $\dot{\epsilon}_0$, T_0 and σ'_0 are the reference strain rate, temperature and effective stress at the experimental point where the transition of the governing mechanism happens, σ_e is equivalent stress (as defined in section 5.2.4.), Q is Activation energy, R is Universal gas constant, T is the rock temperature, t is time and n is the stress coefficient.

In both models, the temperature and stress difference (underbalance between the mud pressure and the overburden stress) are the main factors governing the overall creep deformation (Dusseault et al., 2004a; Costa et al., 2010). Firme et al. (2014) carried out a creep analysis along the interval of wellbore located in a presalt Campos Basin to compare the performance of constitutive creep models. The authors indicated that both DM and MD models yielded adequate results when compared against laboratory tests and caliper logs, with the latter being more accurate.

9.1.3. Creep modeling applications

Factors to populate the relevant model will depend on the stress level of the engineering problem and the timescale over which the problem is examined. As such, factors need to be fitted to the model chosen and validated accordingly, what is achieved in one of the following ways (Dusseault et al., 2004a; Costa et al., 2010; Firme et al., 2014; Orozco et al. 2018):

- A) Fitting constitutive models with laboratory data

Constitutive creep models for real strain/time curves are fitted with experimental creep data from compression tests. Wagner *et al.* (1982) apud Orozco et al. (2018) explained that creep closure in salt can be very sensitive to the rheologic constitutive model chosen to model experimental data. Moreover, a very complex mechanical behavior and long-lasting nature of laboratory creep tests aggravate validating Constitutive models with laboratory data.

B) Numerical simulations

The purpose of numerical simulations is to validate constitutive models for salt rocks through a comparison of laboratory triaxial creep tests and numerical simulation outputs.

C) Caliper logs and numerical simulations

Creep models can be arranged to assess borehole closure as a function of MW in use and, consequently, compared with caliper logs and numerical simulations (Costa *et al.*, 2010). That is especially useful for drilling purposes as it facilitates MW planning through matching the creep predictions based on rheologic constitutive models with offset wells data.

Upon fitting the creep parameters, one can with certainty model the well closure as a function of MW and/or time during drilling through thick salt deposits. Consequentially, these results will then be used to define technically feasible MW span, as well as contingencies during the well planning phase (Costa et al., 2010; Pinto et al., 2019). Besides, the examined creep law should be calibrated with drilling data such as tight holes, abnormal increases in average torque or drag, high levels of torsional vibration, etc. to reduce prediction uncertainty (Orozco et al., 2018).

9.2. Creep relation to octahedral stress

On a timescale relevant to well construction (10^0 - 10^3 hr), salt can be seen as an elastoplastic solid. Therefore, its deformation and flow can be associated with deviatoric stress. The magnitude of the deviatoric stress determines the character of the flow of the rock salt around the borehole (Infante and Chenevert, 1989; Weijermars et al., 2013). The process of creating the wellbore through a salt section may create instabilities that subject the near-wellbore area to plastic flow of salt, which is different from creep, but together with creep is considered as the main driver of wellbore closure. It has been already discussed that the salt flows when

exposed to deviatoric loading. Further, the magnitude of the deviatoric stress is proportional to the octahedral stress whose value determines the character of the flow of the rock salt around the borehole (Infante and Chenevert, 1989; Carcione et al., 2006).

Prior to drilling, salt formations can be in a near- or at equilibrium stress state. When the salt body is fully relaxed, the salt's stress state is isotropic, and VME stress within the salt is zero (Luo et al., 2012a; Nikolinakou et al., 2013b). However, drilling through salt destabilizes the in-situ conditions, consequently triggering a time-dependent borehole stability issue driven by differential stress. Due to the nature of salt, the risk of borehole contraction presents the major concern in well construction challenges. Thus, to address this problem properly, the creep and the plastic flow must be understood together with their associated differences.

Infante and Chenevert (1989) demonstrated that salt exhibits three distinct behaviors:

- If the octahedral stress (τ_o) is lower in magnitude than τ_{oe} , the material will behave elastically, recovering all the strains upon stress removal. However, the salt follows a viscoelastic stress-strain relation under the constant applied stress. There is a gradual but rather inappreciable²⁹ creep;
- Above τ_{oe} , both flow and limited plastic deformations occur. Since the material behaves as partly plastic and partly elastic, the total displacement is caused by a partially recoverable, elastic part and a partially unrecoverable, plastic part (Infante and Chenevert, 1989). Here, the creep rate rises to a constant, steady state (secondary) creep which depends only on stress and temperature (Fossum and Fredrich, 2002; Carcione et al., 2006);
- If the magnitude of octahedral stress exceeds τ_{op} , failure is likely to occur or the material will flow plastically, behaving like a very viscous fluid until it fails. Again, this depends on the level of mean compressive stress. At low mean stress, this breakage will result in a brittle fracture, but appreciable deformation before rupture may be substantial or even indefinite at the higher mean stress.

The temperature significantly influences this process. Namely, the higher the temperature, the more pronounced the plastic behavior and the lower the numerical values of the quantities

²⁹ This type of creep is present at all levels of octahedral stress but becomes important yet when τ_o exceeds the elastic octahedral stress. Carcione et al. (2006) assumed that below this level creep is considered as transient.

τ_{oe} and τ_{op} (Infante and Chenevert, 1989). The octahedral limits are represented in figure 9-1.

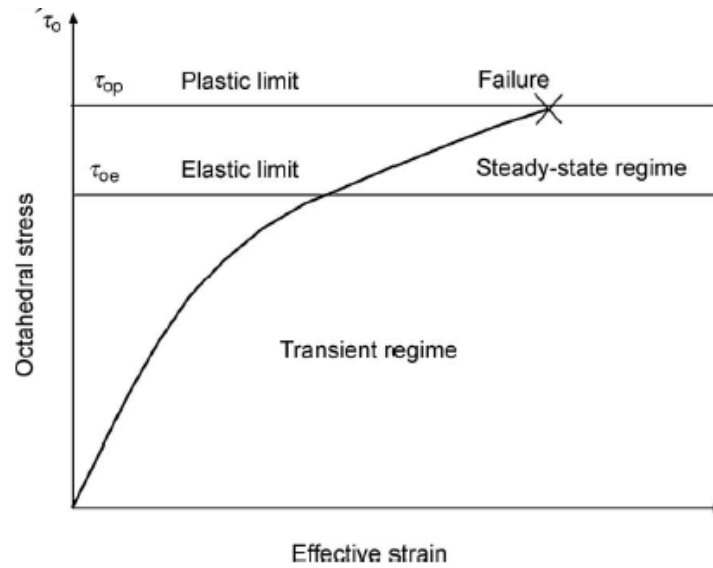


Figure 9-1. The creep rate as a function of octahedral stress displayed together with threshold limits (Infante and Chenevert, 1989)

Infante and Chenevert (1989) investigated the magnitude of the stresses in the vicinity of wellbore values caused by drilling in salt formations. Authors have shown that for the isotropic medium, the maximum value of octahedral stress (τ_{omax}) at the wellbore wall occurs when:

$$\tau_{omax} = 0.817|\sigma_v - P_w| \quad (9-2)$$

Hence, the MW must be formulated such that the absolute value of octahedral stress does not exceed the value of τ_{oe} . The equation can be written in terms of MW required to maintain τ_o below τ_{oe} :

$$\sigma_v - \frac{\tau_{oe}}{0.817} \leq P_w \leq \sigma_v + \frac{\tau_{oe}}{0.817} \quad (9-3)$$

Note that very high MWs are required to keep the borehole in an elastic condition. Otherwise, the plastic flow into the wellbore will occur which manifests as a borehole reduction. On the other extreme, the excessive MW can lead to hole enlargement or even LC (if insufficient FG is encountered within the salt or at the salt exit). As an amendment to work by Infante and Chenevert (1989), Carcione et al. (2006) provided equations to limit the choice of optimum MW to avoid borehole closure in salt sections considering both isotropic (relaxed salt body) and anisotropic stress state (unrelaxed salt body):

$$P_1 \leq -P_w \leq P_2 \quad (9-4)$$

Where P1 and P2 limits are given by Eq. (9-5) and Eq. (9-6) provided below:

$$P_1 = \frac{3\sigma_H - \sigma_h}{2} - \frac{1}{6} \sqrt{54\tau_{oe}^2 - 3(3\sigma_H - \sigma_h)^2 - 12\sigma_{zz}^2 + 12(3\sigma_H - \sigma_h)\sigma_{zz}} \quad (9-5)$$

$$P_2 = \frac{3\sigma_H - \sigma_h}{2} + \frac{1}{6} \sqrt{54\tau_{oe}^2 - 3(3\sigma_H - \sigma_h)^2 - 12\sigma_{zz}^2 + 12(3\sigma_H - \sigma_h)\sigma_{zz}} \quad (9-6)$$

Under the assumption of realistic GoM conditions, authors argued that if a relaxed salt body is drilled (isotropic stress state), no complications should arise in maintaining the borehole below the elastic octahedral threshold as the MWs smaller than overburden gradient suffice. However, in a situation where horizontal stress anisotropy exists (unrelaxed, flowing salt), the required MW to maintain the borehole below the elastic octahedral threshold might exceed the overburden stress gradient (see figure 9-2.). Also, the time-dependent change of borehole geometry could differ along the drilled section.

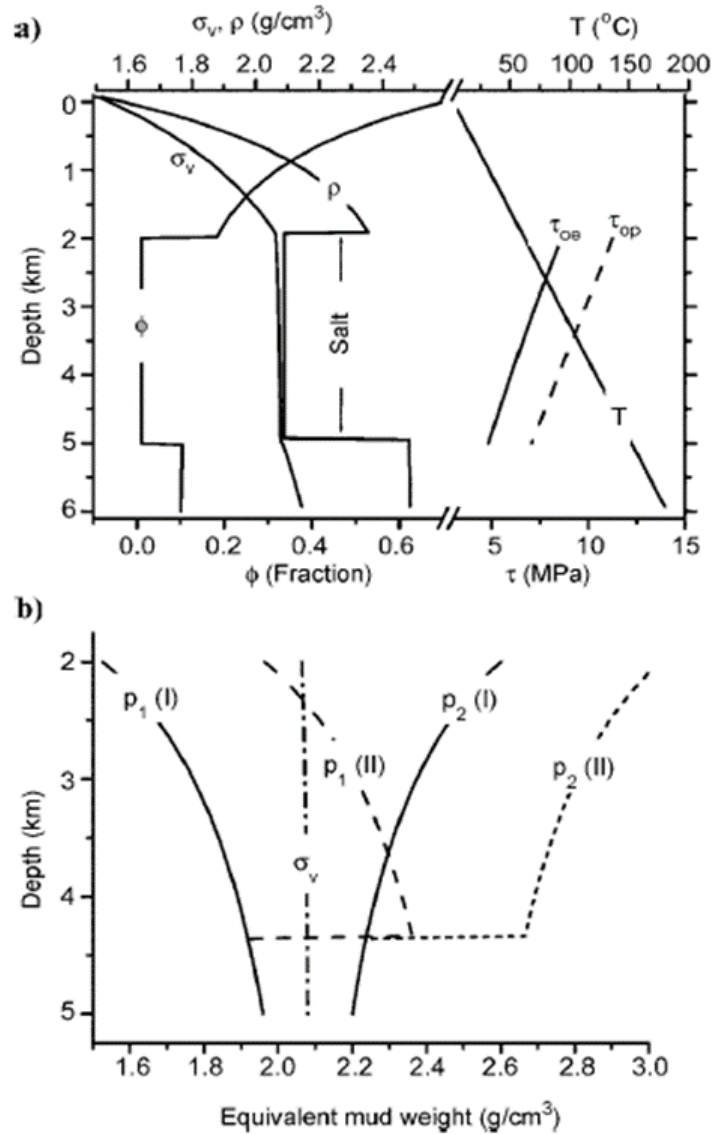


Figure 9-2. Representation of (a) realistic GoM model containing a buried salt layer with appropriate porosity and density trends, and (b) the corresponding mud pressure P_1 and P_2 expressed as an EMW as expressed by Eq. (9.5) and (9.6) for (I) isotropic stress state and (II) anisotropic stress state ($\sigma_h = S_h = 0.8 \sigma_H$; $\sigma_H = S_H = 1.1 \sigma_v$; $\sigma_v = S_v$) (Carcione et al., 2006)

9.3. Creep-caused borehole closure

As per Infante and Chenevert (1989), the rule of thumb solution when drilling in salt would be to traverse the salt section with the MW equal to the overburden gradient. However, fluctuating fracture pressures within salt sections (inclusions) or below the salt may limit the range of permissible MWs to retain stresses at the wellbore wall in the elastic domain. If the deployed MW is too low, imposed stress difference on the wellbore wall may be high enough to shift octahedral shear stress to the plastic region where a substantial risk of wellbore failure exists. Moreover, high MW may increase the risk of the stuck pipe due to differential

sticking in case interbedded permeable zones are encountered and, as such, must be limited. Since the complete plastic deformation and the wellbore collapse in salt sections are unlikely³⁰, the trade-off can be made in casing seat selection at the cost of real-time diameter reduction. Sometimes, this can be the only way to reduce fluctuating fracture pressure above and/or beneath the salt body without deploying a contingency string before reaching the planned casing shoe. However, one must understand that plastic stresses in the wellbore vicinity will result in the plastic flow, which increases the risk of possible borehole shrinkage and the sticking of the bit and drill collars. To counter that, strategies such as underreaming or controlled leaching will be required but at the cost of increased non-drilling time (Infante and Chenevert, 1989; Castagnoli et al., 2016). The schematics presented in figure 9-3. display the implications of thick salt on the well construction.

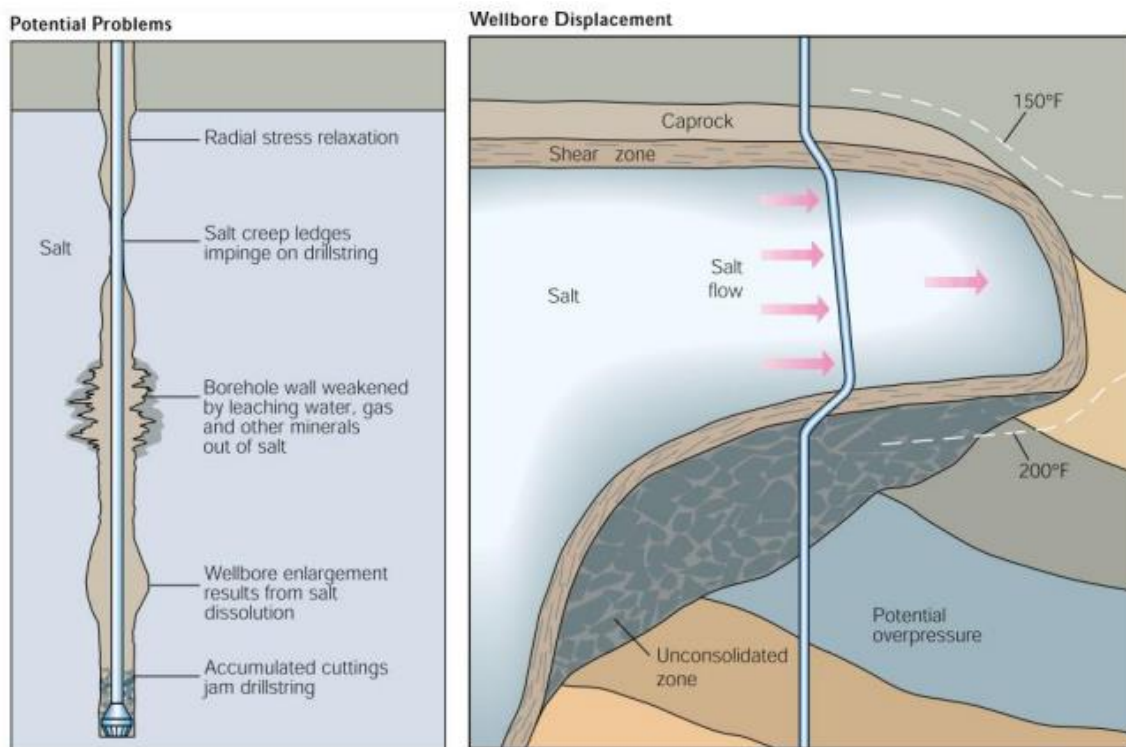


Figure 9-3. Typical well-construction problems encountered in thick salt sections (Farmer et al., 1996 apud Wang and Samuel, 2013)

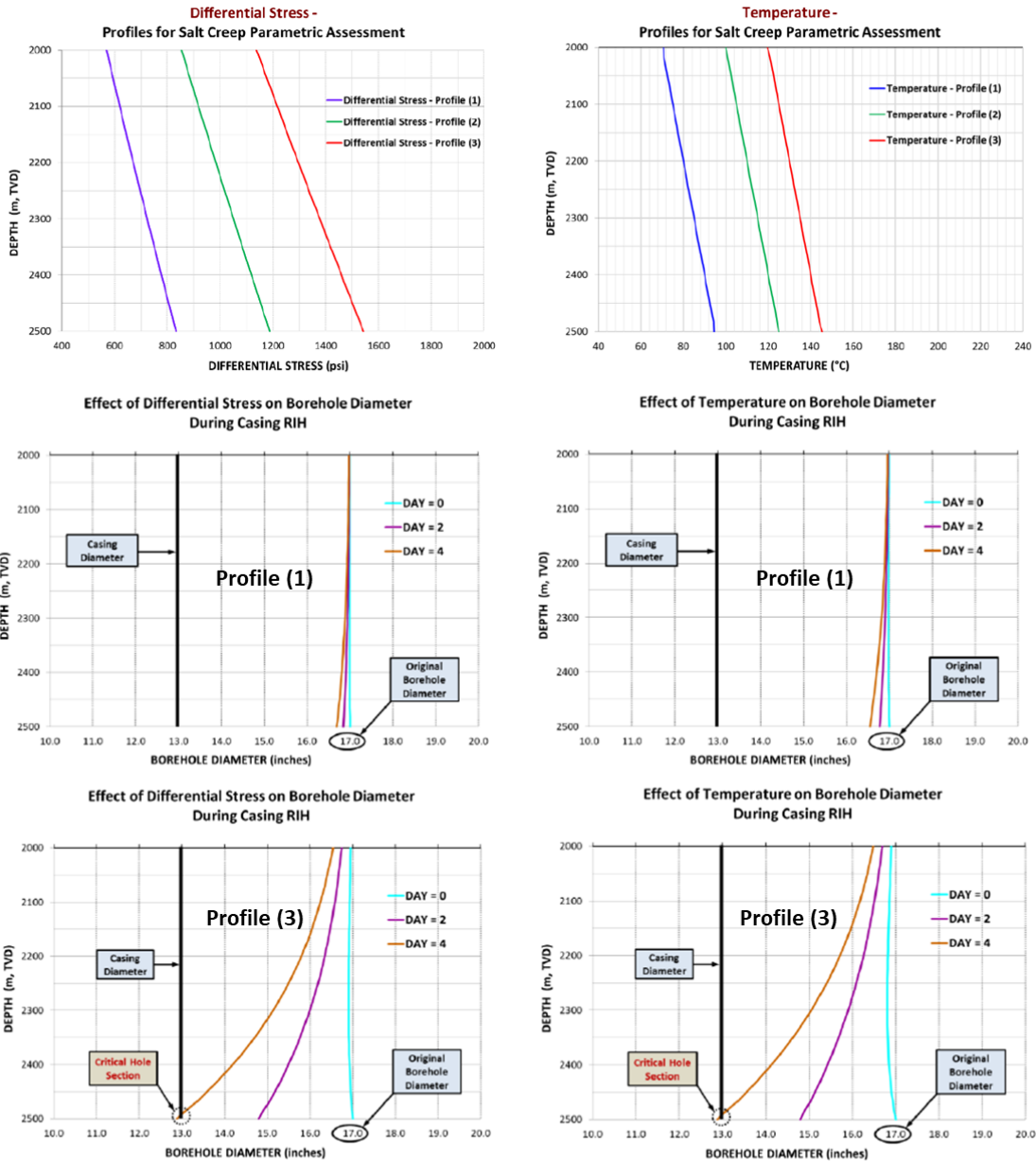
A lot of research has been done so far in search of analytical (Bogobowicz et al., 1991; Barker et al., 1994; Carcione et al., 2006; Liu et al., 2011) and numerical models (Munson

³⁰ Namely at the distance of 2-3 borehole diameters, stress bridging takes place and plastic stresses vanish making the hole collapse impossible (Carcione et al., 2006)

and Dawson, 1979; Costa et al., 2005; Mackay et al., 2008; Weijermars et al., 2014) to predict the salt-governed borehole closure. When drilling through a salt formation, the well design team should evaluate potential risks associated with creeping issues to identify adequate creep prevention strategies. As discussed previously, salt creep modeling can help identify zones of elevated creep rate. In turn, this will allow a well construction team to act proactively and thus minimize the additional incurred NPT. Common industry practice is to use pre-established MWs inferred from the usage of the abovementioned models. However, if the salt creeping is underestimated or wrongly predicted, the resulting reduction of ROP and associated NPT can cause the well construction costs to skyrocket above economic limits. Here the parametric analysis can help address creep salt uncertainty during the planning stage, especially in the exploration phase, where little or nil data are available. The effect of different salt formations, MWs, temperature, and/or open-hole exposure time profiles can be evaluated to assess borehole closure for varying parameters. Orozco et al. (2018) argued that different factors bring uncertainty salt closure projections during the planning operations:

- differential stress across the wellbore wall,
- limited or faulty laboratory creep test data,
- salt sequences within the along-trajectory stratigraphic column (primarily thicknesses of salt layers expected to be encountered),
- the uncertainty in salt composition (impurities, granulation, water content, etc.),
- delays in drilling operations such as WoW or logistics issues may significantly increase the open-hole exposure time and thus adversely affect the borehole closure rate,
- exact temperature profile.

The authors presented a sensitivity analysis for different effects affecting salt creep, among which differential stress and temperature showed the greatest influence on borehole closure (figure 9-4.).



psi to MPa conversion: x 0.006894
in to m conversion: x 0.0254

Figure 9-4. Sensitivity analysis of differential stress (left) and temperature (right) effects on creep closure for the given set of parameters (modified from Orozco et al., 2018)

In Zhang et al.'s (2008) study, diameter reductions were assessed for different time steps using Barker's s model steady state creep. That allowed the drilling team to make prudent decisions on when the hole reaming may be needed to maintain a sufficient clearance for subsequent casing and cement jobs. Likewise, sensitivity analysis helped the drilling team to assess lower and upper estimates of MW needed to control salt creep. The left track of figure 9-5. shows a comparison between the calculated creep after 10 days and actual caliper

readings after the 0,3747 m (14 3/4") hole was drilled. The right track shows the recorded ECD value and the originally designed MW window.

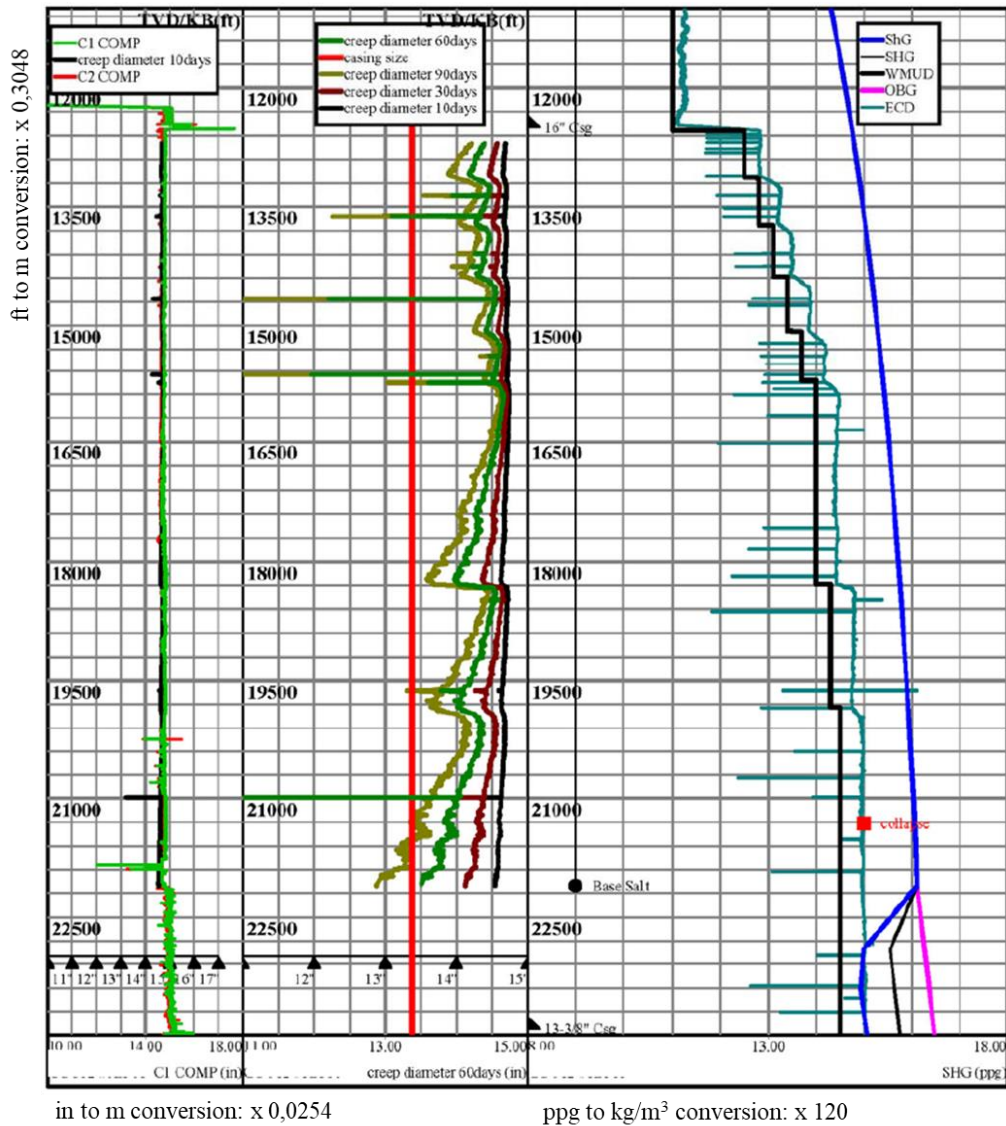


Figure 9-5. Projections on borehole closure of a well in GoM are shown for 10, 30, 60, and 90 days upon drilling activity(Zhang et al., 2008)

Since not all the salts behave identically and have the same impact on wellbore stability, a detailed characterization of rock salt behavior utilizing laboratory experiments arises as a prerequisite to the borehole stability evaluation (Carcione et al., 2006). Especially problematic here are dirty salts found offshore Brazil, such as tachyhydrite. Tachyhydrite is a type of salt formation that is very weak compared to halite, and as such, it can creep at rates higher than halite in magnitude or two for the same state of temperature and stress (Costa et al., 2010). Tachyhydrite, can creep and close around a tubular very rapidly, even during drilling and cementing operations, but it has a negligible long-term impact (Wang

and Samuel, 2013). Similar is observed with the chloride and sulphate salts, such as bischofite, carnallite, kieserite, and sylvite, whose viscosities are lower, making those salts more mobile (Wilson et al., 2002; Jackson and Hudec, 2017). Figure 9-6. shows the creep rate of different salt types (under equal p-T conditions) as a function of MW.

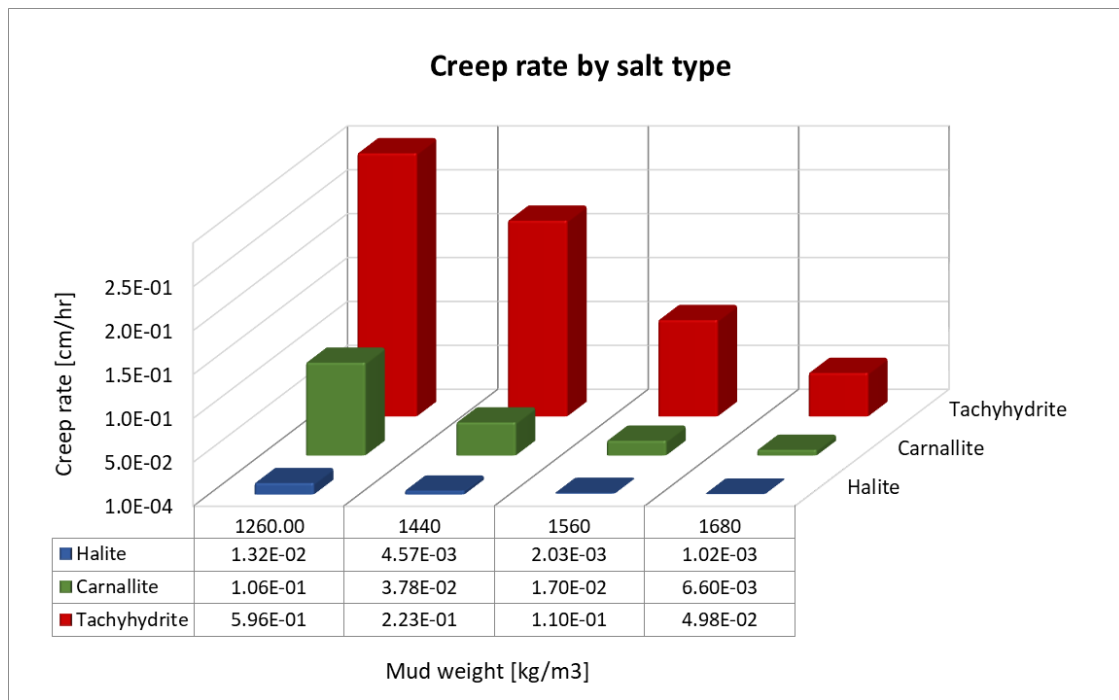


Figure 9-6. Creep rate of different salts as a function of MW (reproduced with data from Costa et al., 2010)

9.4. Overburden and temperature effects on creep

As shown previously, the closure rate of salt increases with increasing differential pressure between the salt stress and the mud-weight hydrostatic pressure and temperature. At the shallow depths, differential pressures and temperatures are small, thus the creep rate will be slight. However, at greater depths, higher differential pressures and higher absolute temperatures³¹ can significantly increase the creep rate (Barker, 1994). Several studies demonstrated that the wellbore closure patterns might change downward along the wellbore due to differing creep rates (Carcione et al., 2006; Weijermars et al., 2014; Firme et al., 2014).

³¹ The creep rate is strongly influenced by temperature as well. For example, if the differential stress between wellbore hydrostatic pressure and salt internal stress maintains the same level in the entire salt section, then the creep rate at the bottom of the hole would be expected to be one-hundred times faster caused by temperature effects alone (Dusseault et al., 2004a).

9.4.1. Overburden implications to salt creep

Most importantly, spheroidal bodies are expected to perturb vertical (overburden) stress in overlying sediments. The vertical stress within the salt is reduced so that the isotropic state can be reached. However, in the case of salt sheets, the vertical stress within the salt body is not perturbed from lithostatic conditions as salt sheets tend to maintain the vertical stress within the salt unchanged from the corresponding far-field values. Therefore, as the overburden weight is transferred through the salt, the vertical stress obtained from density logs is expected to be accurate (except in regions laterally adjacent to the sheet edge where the vertical stress is disturbed) (Fredrich et al., 2003; Sanz and Dasari, 2010). Furthermore, let's consider the latter case; as already mentioned, salt bulk density does not increase with burial depth as most clastic sediments generally do. Ergo, as the salt body is penetrated, the bulk density trend starts decreasing from the top of the salt to its base. Correspondingly, the overburden gradient will be reduced relative to the overburden obtained for a fully sedimentary clastic basin, where no salt body is present. Figure 9-7. compares the salt body's influence on the overburden gradient (OBG) obtained relative to a fully sedimentary clastic basin (case A). Note that local overburden gradient (within salt) may increase (B-C), remain constant (D), or even undergo regression and reduce (E-F), depending on the burial depth of the salt sheet. Similarly, the influence of the salt body on the overall OBG decreases with the depth of burial.

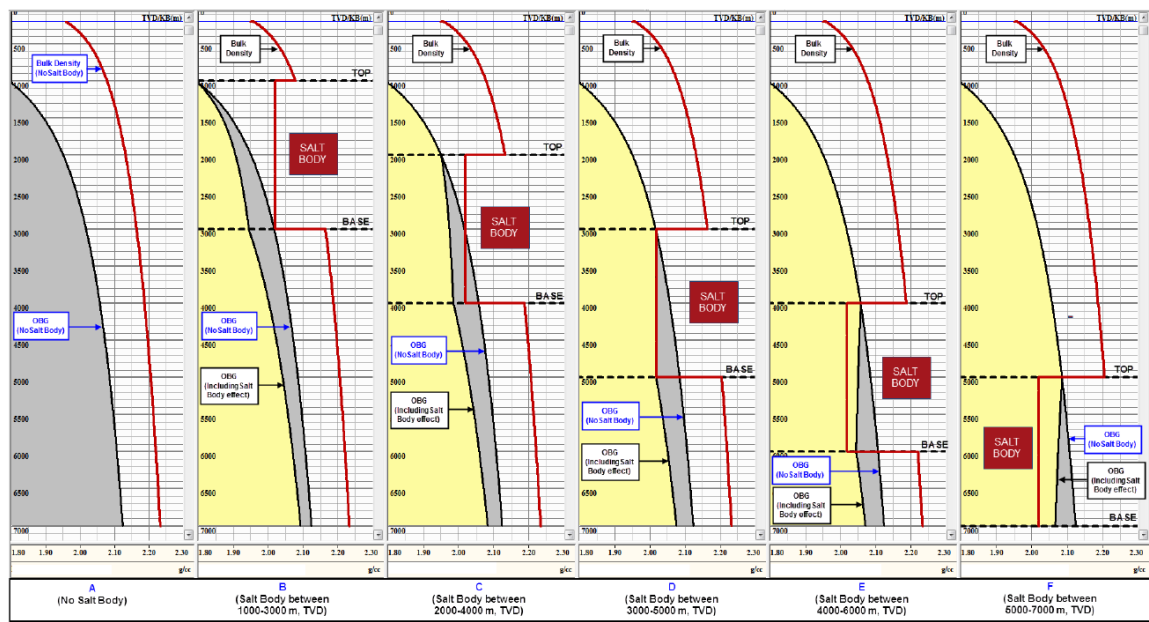


Figure 9-7. The effect of salt burial depth on the overburden gradient through salt (Orozco et al., 2018)

As MW required to suppress creep in salt is usually expressed as a percentage of OBG, the repercussions of salt depth on OBG should be discussed (Orozco et al., 2018; Pinto et al., 2019). Figure 9-8. describes the effect of salt body depth on the differential stress and MW/OBG ratio. Assuming that the previous casing is set at the top of salt and that the section is drilled using a single MW, equivalent to 0,9 OBG encountered at the top of the salt, note the following:

- deeper the salt body, the larger is the pressure difference between MW and salt pressure, i.e., the differential pressure across the wellbore,
- with the constant MW deployed, MW/OBG ratio drastically reduces in the salt section with a shallow depth of burial,
- with the constant MW deployed, the differential pressure rate of change reduces with increasing depth of burial.

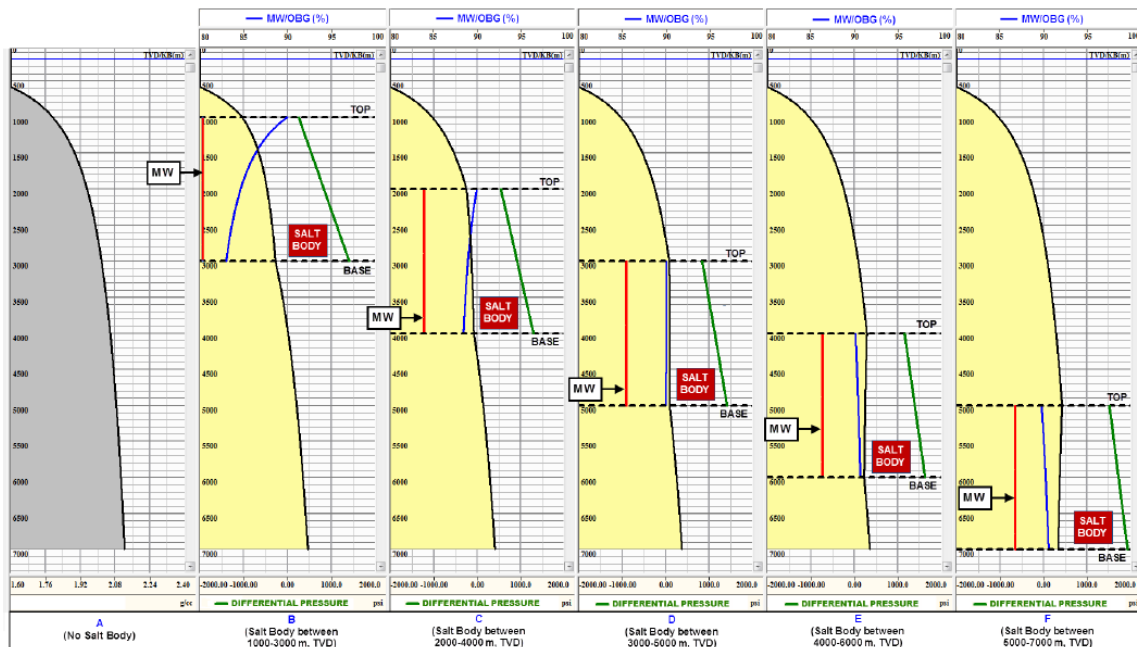


Figure 9-8. Effect of salt burial depth on MW/OBG ratio through salt (Orozco et al., 2018)

This effect on pressure differential will significantly impact the closure rate of the respective section, even without considering temperature-related effects. An important observation for well planning arises here; deeper the salt body (generally salt sheet) is buried, higher OBG and temperature will require higher MW to equilibrate the in-situ stresses in the salt formation, which again, may not be physically possible in all situations (Orzoco et al., 2018). Similar observations were presented by Costa et al. (2010). Note how the MW required for stabilization in figure 9-9. varies with depth and temperature.

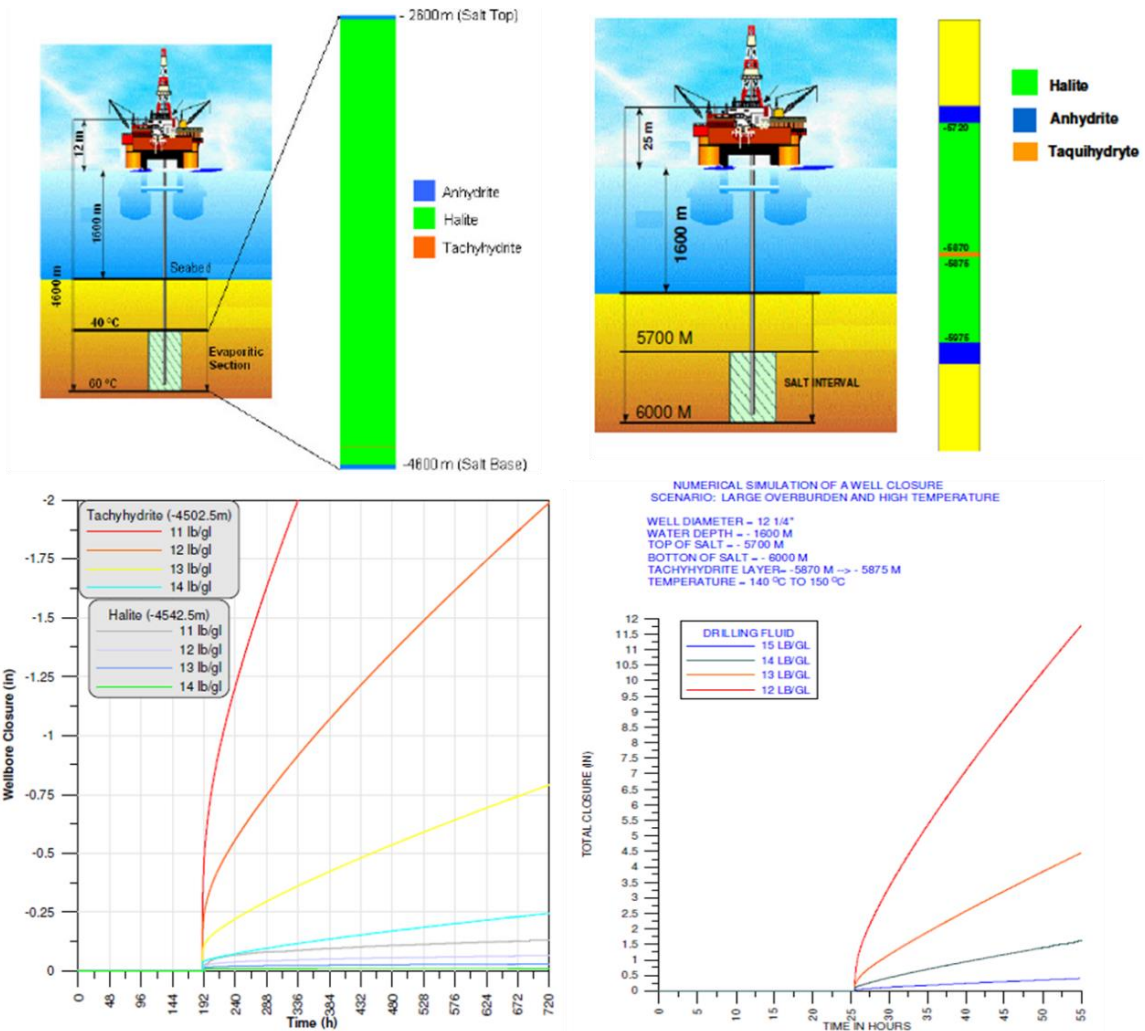


Figure 9-9. MW (12 ppg; 1440 kg/m³) needed to retain Tachyhydrite layer below 5,08 cm (2 in) closure over the period of +500 hours for case a) 4502,5m TVD; ca. 60 °C and b) 5872,5m TVD; ca. 145 °C (modified from Costa et al., 2010)

9.4.2. Temperature implications to salt creep

Additionally, salt's high thermal conductivity will provide a high-conductivity path for heat flow in the sub-surface compared to other sediments. As a result, the overlying formations will be heated, while the underlying formations will be cooled. This effect has been observed in the vicinity of salt domes and is also expected to influence the temperature distribution around the sheets (Fredrich and Fossum, 2002; Dusseault et al., 2004a, b; van Oort, 2004). Such thermal anomalies may complicate wellbore stability in formations immediately above the salt, imposing higher thermal stresses while aggravating LC problems in formations immediately below salt due to reduction imposed by lower thermal stresses. Namely, the cooling effect below the salt body will increase the tensile stresses at the wellbore wall, thus increasing the likelihood of tensile-induced failure. On the contrary, elevated thermal

stresses above the salt body will incur additional compressive stress and thus increase the risk for the creation of wellbore breakouts. Similarly, problems with increased temperature in the upper portions of salt may also aggravate the problem of hole enlargement due to increased solubility.

The profile will also depend on where the well will penetrate the salt. The temperature profile is commonly estimated by propagating the thermal gradient from offset wells. However, the uncertainty propagates proportionally to offset wells and the geological correlation. The alternative methodology to determine the temperature profile is obtained through numerical modeling. The prior is preferred when the areal measurements are neither available nor the shape of the salt is known (figure 9-10.; Castagnoli et al., 2016).

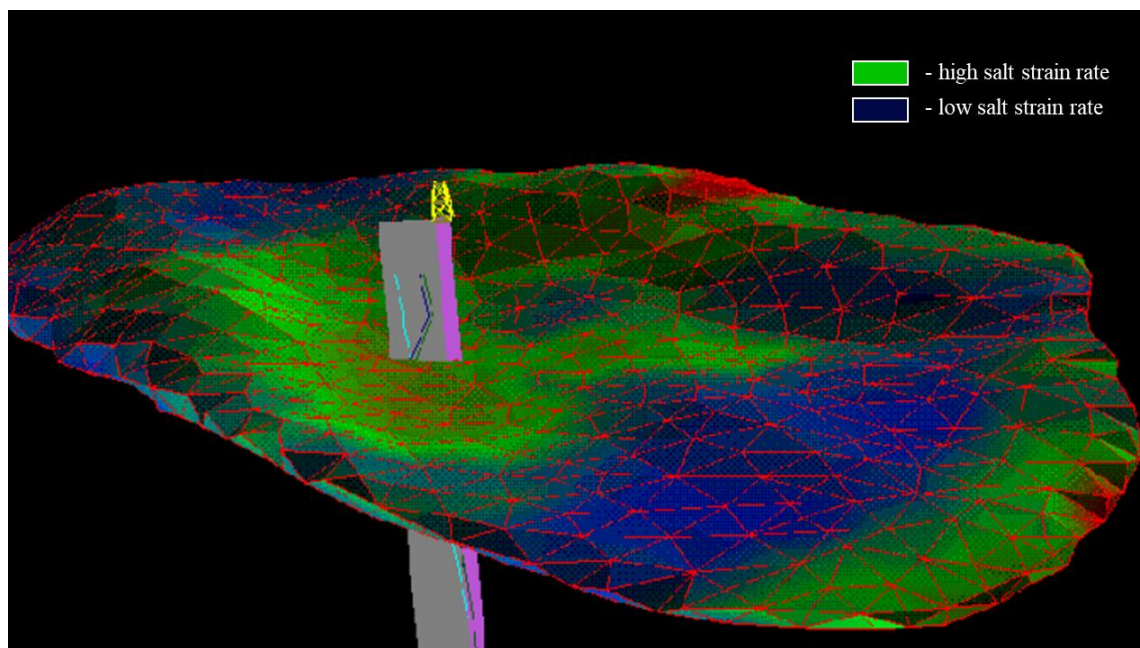


Figure 9-10. The strain rate of the GoM salt sheet predicted from FEA (modified from van Oort, 2004)

Another important effect to consider in the design of development wells is the production-induced heating of the salt (Fossum and Fredrich, 2002). In Deepwater, producing temperatures typically vary from 80 °C to 150 °C, depending on the depth of the producing interval. That may be a particular issue in Spar-type or subsea template developments where the near-vertical wells are relatively closely spaced (typically at the radial spacing of 30 ft to 80 ft; 9,14 m to 24,38 m). Given the low temperatures below the mudline, the shallow wellbore parts and reservoir temperature difference can exceed 120 °C. Figure 9-11. displays the spatial distribution of temperature for a producing wellbore at two different depths BML.

As a result of lasting production, the salt formations adjacent to producing wells will heat up to match the temperature of the producing fluid. This production-induced heating will exacerbate the creep rates in shallow sections and, as such, needs to be considered in the well planning. In addition to the change of steady state creep, the thermal loads will also impose transient strains caused by thermal stress perturbations. Whenever a stress change happens, a salt mass will respond by straining at a rate different from the steady state creep. Change in straining rate will depend on whether the stress change results in salt loading or unloading. For Deepwater applications, transient creep associated with stress changes induced by heating or cooling will contribute to overall creep magnitudes. In turn, this may adversely affect wellbore stability during well construction or long-term wellbore integrity (Fossum and Fredrich, 2002).

In addition, danger from Annular Pressure Build-up (APB)³² failure may exist if adequate measures are not proactively incorporated into the design (Wilson et al., 2002). Here, the reader is prompted to scrutinize Pattillo et al.'s (2006) case study that discusses the reasons behind APB-induced casing failure during drilling in Deepwater GoM.

³² ABP results from a closed fluid-filled annulus, which if heated will have to accommodate for temperature induced pressure change. Namely, the temperature increase due to the heat flux across the casing wall(s) will tend to increase the volume of a fluid compartmentalized by casing. The closed annulus is a consequence of either deliberately put TOC above the previous casing shoe or unanticipated closure of annulus in the vicinity of previous shoe due to solid settling or wellbore instability. Hence, due to inability to expand and accommodate the volume change, compressibility of annulus fluid results in increase of fluid pressure. Contrary to the onshore and shallow water wells where annulus venting is done via surface wellhead valves, the configuration of subsea wellheads is such that Annuli other than “A” are inaccessible. This translates to inability to monitor and promptly release any pressure build-up. Given the fact that Deepwater wells are usually brought to significantly higher production rates than wells encountered onshore, large temperature differences between the mudline and the reservoir (over 100 °C) elevate the risk of casing burst or collapse at the weak point, what can result in additional cost and temporarily production loss (Aird, 2019; Pattilo, 2018).

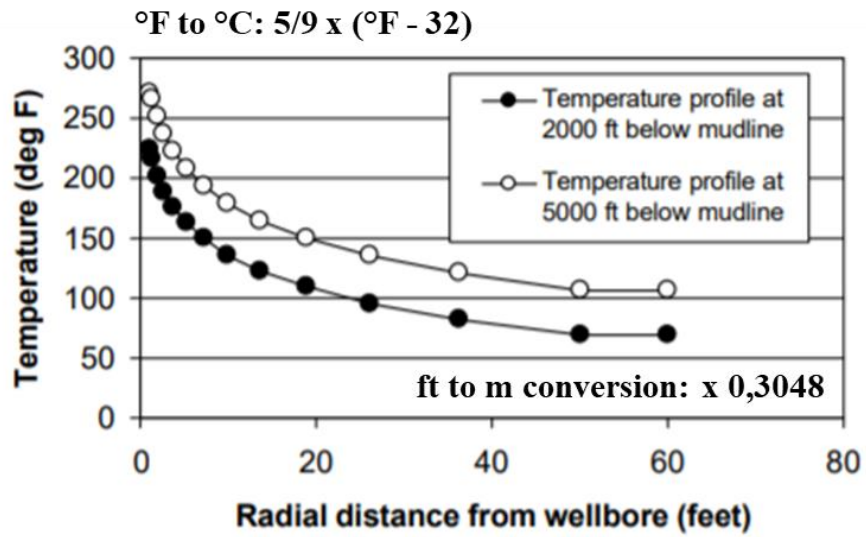


Figure 9-11. Temperature Profiles as a function of time and radial distance from the wellbore (Wilson et al., 2002)

10. CASING SEAT SELECTION IN DEEPWATER SALT ENVIRONMENT

10.1. Mud weight window design

The setting casing strings along the wellbore is a prerequisite to maintaining a stable wellbore throughout well construction (Pattillo, 2018). As discussed previously, the drilling fluid ensures that the adequate support is applied to the wellbore wall, but rock deficiencies limit the length of section upon which fluid pressure is exerted. As a result, mud density suitable at a depth of interest may hamper well integrity elsewhere along the well trajectory. Therefore, it is necessary to deploy a set of tubular strings whose length is determined to allow the most efficient and effective well construction, i.e., at least cost and time burden. In essence, casing shoe selection is governed by drilling window constraints using either a bottom-up or a top-down approach³³. Mud window constraints denote the range of acceptable drilling fluid densities that enables meeting well construction goals in the safest way and with the least risk. The bottom and upper margin will be defined as limits that satisfy all imposed constraints from the spud location to the wellbore bottom. Based on the extensive literature review (Amoco, 1996; Krištafor, 2009; Aadnøy 2010; Pattillo, 2018; Aird, 2019), constraints pertinent to the design of MW window in the offshore salt environment will be discussed below.

10.1.1. Base pressure constraints

These constraints present the minimum constraint for the wellbore fluid density in terms of:

- PP gradient;
- FG.

Exceeding PPFG constraints will result in either fluid influx (if the permeability of the exposed formation is sufficient) or tensile failure and, consequently, loss of wellbore structural confinement.

10.1.2. Uncertainty-related constraints

These constraints are superimposed on base pressure constraints to account for error coupled with the estimation of base pressure constraints. That is addressed through either probabilistic modeling (e.g., using Monte Carlo simulations (e.g., Moos et al., 2003; Wilson

33 As per Pattillo (2018), neither the “bottom-up” nor the “top-down” philosophy has an indisputable advantage. Although, both methods often result in the same number of casing seats, more commonly, the “top-down” philosophy is preferred as it is believed that additional flexibility in casing design can be obtained as such philosophy promotes deeper casing seats.

and Fredrich, 2005) or, less sophisticated, applying design factors to base constraints and simply narrowing the acceptable range of MWs by specific value.

10.1.3. Wellbore pressure shocks

During the well planning, simulations are done to estimate pressure increments above and below hydrostatic level caused by relative movement of the wellbore fluid. These combine all transient and dynamic pressure components that exist during drilling, circulating, pump start-up, shutdown, and noncirculating conditions. Simply contributions to static conditions can be divided into friction-induced circulating pressures and all other pressure effects (AOPE) which include solids loading effects, swab and surge pressure effects, pump start-up effects, heave effects. The motion of the fluid column resulting from heave effects and/or RIH and POOH operations, if not accounted for, can push pressures across the imposed margins. The PPFG curves are often shifted for a value (a design factor) that accounts for both uncertainty and formation pressure shock effects, typically 120 kg/m³ (1 ppg) for exploration wells, and 60 kg/m³ (0,5 ppg) for development wells. Despite that all these effects are being treated using a single safety factor, margins are not necessarily equal (figure 10-1.). Instead, AOPE are functions of vertical depth and highly dependent upon operation-related factors including but not limited to ROP, annular clearance, fluid rheology, pipe geometry, and movement speed, and as such should be engineered with scrutiny.

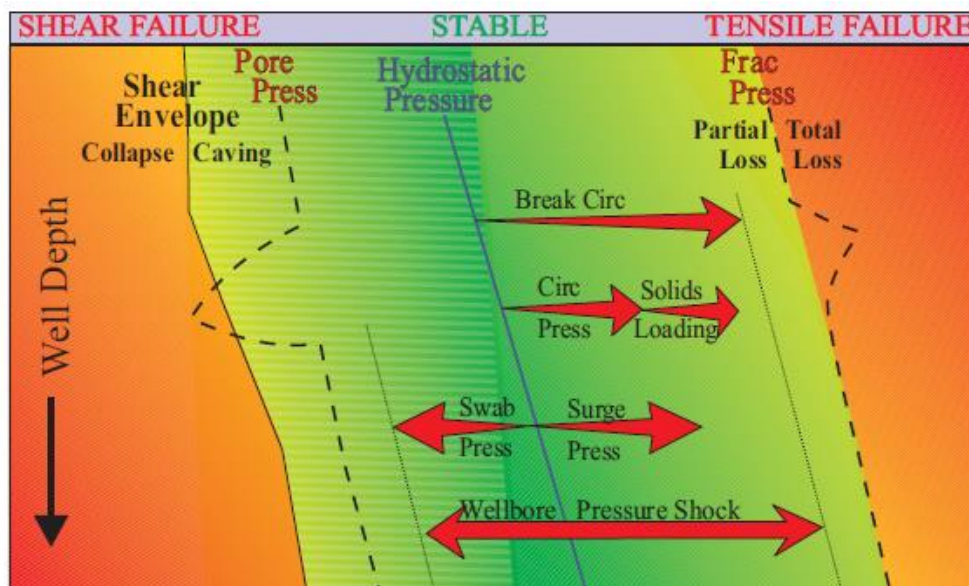


Figure 10-1. Wellbore shock constraints on allowable wellbore pressure (Amoco, 1996)

10.1.4. Differential sticking

This is a location-sensitive phenomenon pertinent to permeable formations. With the pressure overbalance across the permeable formations, drilling mud will be driven into formation. Solids and cuttings suspended in mud will pile up at the wellbore wall while the liquid phase will filter across the wellbore. Delivered material will continue to be embedded into the filter cake as long as its permeability allows continuous mud filtration. Nonetheless, the presence of a filter cake reduces wellbore diameter and introduces the potential for differential sticking, particularly if a tubular string is maintained static for prolonged periods. The differential sticking limit is expressed as a pressure difference between the local wellbore and pore pressures, usually 13,8 MPa to 27,6 MPa (2000 to 4000 psi³⁴). Note that the base pressure constraints are pressure gradients, whereas the differential sticking limit is a specific pressure value. Thus, the adjustment to account for differential sticking will therefore vary with TVD. This constraint seldom traverses the whole MW window (Pattillo, 2018).

10.1.5. Wellbore stability constraints

This constraint closely follows up problematics explained under the chapter 6. In areas where wellbore stability is not of particular interest, the minimum MW is usually taken to be the PP. However, in cases where wellbore stability is considered, the lower bound of the MW window becomes either the minimum MW required to prevent wellbore failure (also shear failure line; SF) or suppress fluid influx. In both cases, the upper bound of the MW window is the MW at which LC occurs due to hydraulic fracturing of the formation (Zoback, 2007). Not necessarily every well that fails in shear is unstable well. Applying the so-called Depth of Damage (DoD) approach, one can limit a certain breakout width as tolerable, thus allowing a wider margin for drilling operations (Schlumberger, 2021)³⁵. This limit is often drawn where the wellbore collapses such that excessive breakouts cause spalling of material from the wellbore wall in a volume that cannot be circulated out by mud circulation (figure

³⁴ Different values may apply depending on whether normally pressured or abnormally pressured zones are encountered. Krištafor (2009) argued that permissible differential pressure values are typically in range of 14-16 MPa for normally pressured zones and within range of 21-23 MPa in case overpressured zones are encountered.

³⁵ Utilizing numerical methods, one computes the stresses away from the wellbore wall ($r > R$) rather than at the wall. Consequently, shear failure pressure is set as the pressure that keeps all points at a specified distance r around the wellbore in the elastic range, thus tolerating certain breakout width ($r = \text{DoD} \times R$). In such a way, a lower MW is permitted, opposed to more conservative approach where MW is limited to a gradient that at which breakouts are initiated.

10-2.). As mentioned above, as a wellbore enlarges due to the excessive wall failure, the annular velocity of drilling mud decreases, thus reducing the mud ability to transport the cuttings and debris out of the well. The combined effect of these adverse factors can cause the cuttings and failed rock to stick to the bottom hole assembly, causing pack-off. In the vertical wells, the rule of thumb implies that effective design is limited by the maximum breakout width of ca. 90°. Breakout widths above 90° will correspond to failure of more than half of a wellbore’s circumference, potentially causing inadequate arch support. As the stress concentration around a well does not change with an increase in borehole diameter, insufficient arch support could be exacerbated to a level where failure occurs around the whole circumference, i.e., washout causing severe stability-related problems. Due to the high costs involved in constructing a Deepwater well and risks associated in the exploration and appraisal phase, shear failure (breakout) pressure is considered the minimum pressure that keeps all points around the wellbore in the elastic range. This directly translates into a more conservative approach when specifying MW and casing programs. The same applies to wells deviated above 40° and horizontal wells since they are generally more prone to failure and more difficult to clean (Zoback, 2007; Pattillo, 2018).

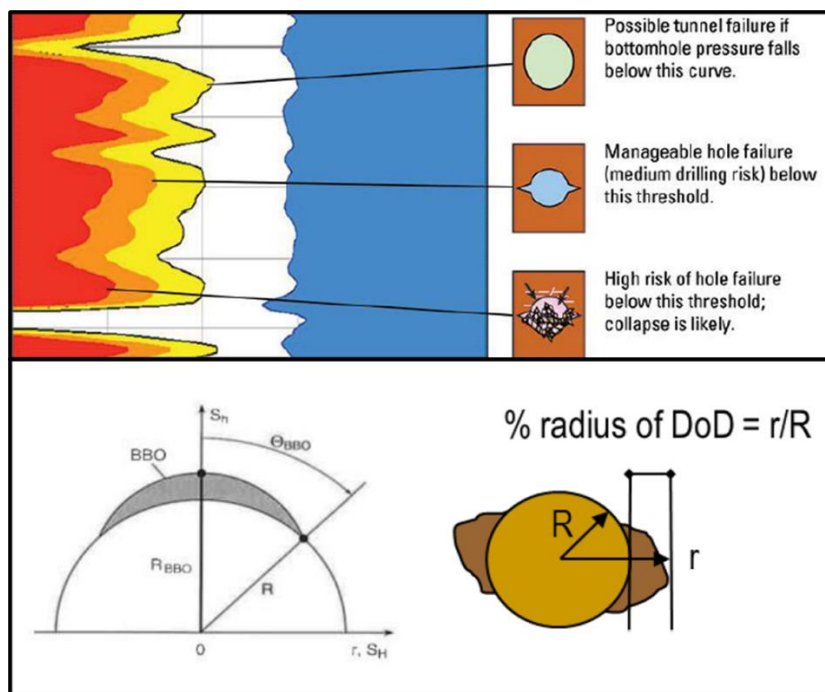


Figure 10-2. Incorporating tolerance to breakout width into MW window construction (Schlumberger, 2021)

10.1.6. Riser margin

Riser margin (RM) is an adjustment to the lower bound of acceptable drilling fluid density to account for the possibility of a loss of riser integrity during offshore drilling. Assuming the failure of the drilling riser, a loss of pressure integrity in the vicinity of the mudline is inevitable if not prevented by operating the BOP stack. With the drilling mud in the well, the portion of the drilling fluid column above the seafloor is now replaced by a column of air and seawater. Consequently, retained fluid column will exert a lower hydrostatic pressure, thus introducing the possibility that the local wellbore pressure may fall below the local pore pressure at the target depth. The RM calculation (as presented by Aadnøy 2010) ensures that the drilling fluid density is such that a positive pressure differential between the wellbore and adjacent pore pressure is maintained in the case of the abovementioned scenario (as depicted in figure 10-3.). Generally, RM applies to intermediate water depths. In shallow waters, the correction is minor. For Deepwater, imposed constraints can be so large that they provide no physical meaning, and the concept is rather neglected. Normally, operating companies and drilling contractors rely on emergency disconnection procedures, so the RM is seldomly used in constructing MW window.

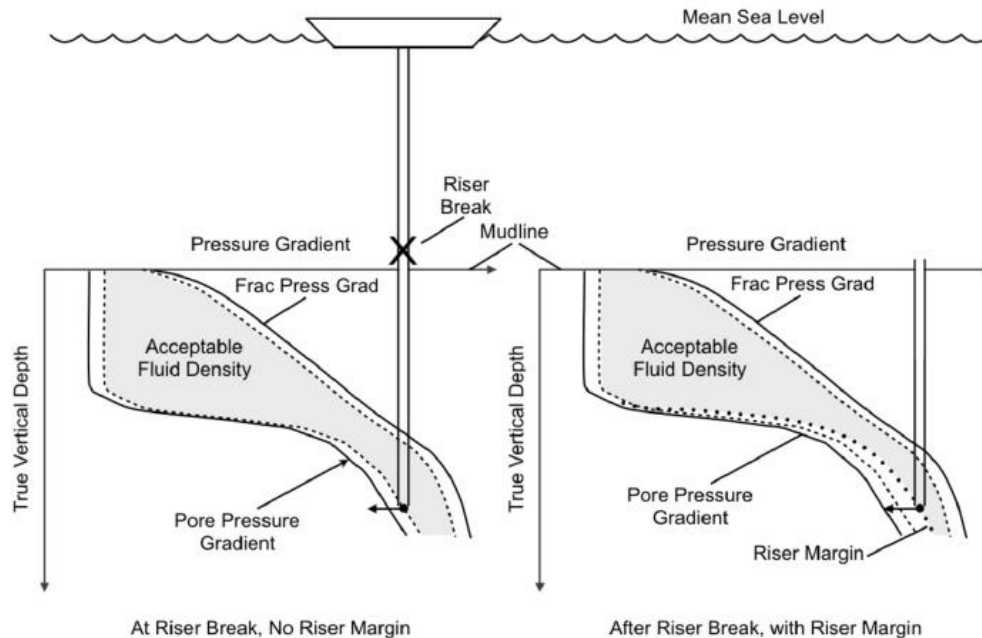


Figure 10-3. Adjustment of acceptable MW range for RM (Pattillo, 2018)

10.1.7. Constraints caused by salt creep

This constraint is typically difficult to express using general analytical solutions. Therefore, it is either embedded into conventional workflows as custom-tailored constraints or put as amendment to the initial design. Usually, operators define salt creep operational window (SCOW) and superimpose it onto conventional MW window. The upper limit is retained as explained, whereas the lower limit will depend on salt properties and acceptable borehole closure rate, which needs to be assessed using appropriate creep modeling (usually expressed as a fraction of overburden gradient that permits the safe and efficient advance of drilling operations, see Pinto et al., 2019). The impact of the creeping salts on the well design was discussed in chapter 9.

10.1.8. Regulatory requirements

Local regulatory bodies might specify the setting depths of shallow conductor and/or surface casing strings. These requirements do not constitute the MW window but are usually treated as predetermined, fixed casing seats from which other calculations begin.

10.1.9. Kick tolerance

Having selected the casing seats based on the constraints mentioned above, one has to assess the kick volume (in the worst-case scenario gas) referenced at the downhole conditions that can be safely circulated out of a wellbore. Ergo, gas volume for which no point in the open hole will fail in tension. The gas influx³⁶, driven by the density difference between the influx and that of the drilling fluid, will travel to the surface while increasing the pressure in the open hole section (at least until the previous casing shoe is reached and after which pressure remains constant). The failure can theoretically occur everywhere along the open hole section but is usually assumed at the previous casing shoe since an exact measure of the formation strength exists there (LOT). Practically, kick tolerance (KT) is an evaluation of the structural capacity of the current open hole environment. If calculated KT is small, the current casing plan could be altered as the open hole below the current casing seat may be incompetent to contain possibly anticipated kicks. Typically, an operator's drilling policy

³⁶ The influx might occur at positive kick intensity or at near-zero kick intensity, as in case of swab pressure increment associated with POOH. The kick tolerance is selected upon selecting the smaller value of a critical kick size evaluated at two scenario (a) critical kick size at the bit when exiting previous casing shoe and (b) critical kick size experienced during drilling ahead in which gas volume expanded and eventually reached the open hole weak point (for calculation refer to any well control manual).

will specify increasing levels of drilling management approval for decreasing values of an open hole section's KT.

The example of an MW window in Deepwater subsalt is shown in figure 10-4. Note the convergence of PPFG margins below the salt interval.

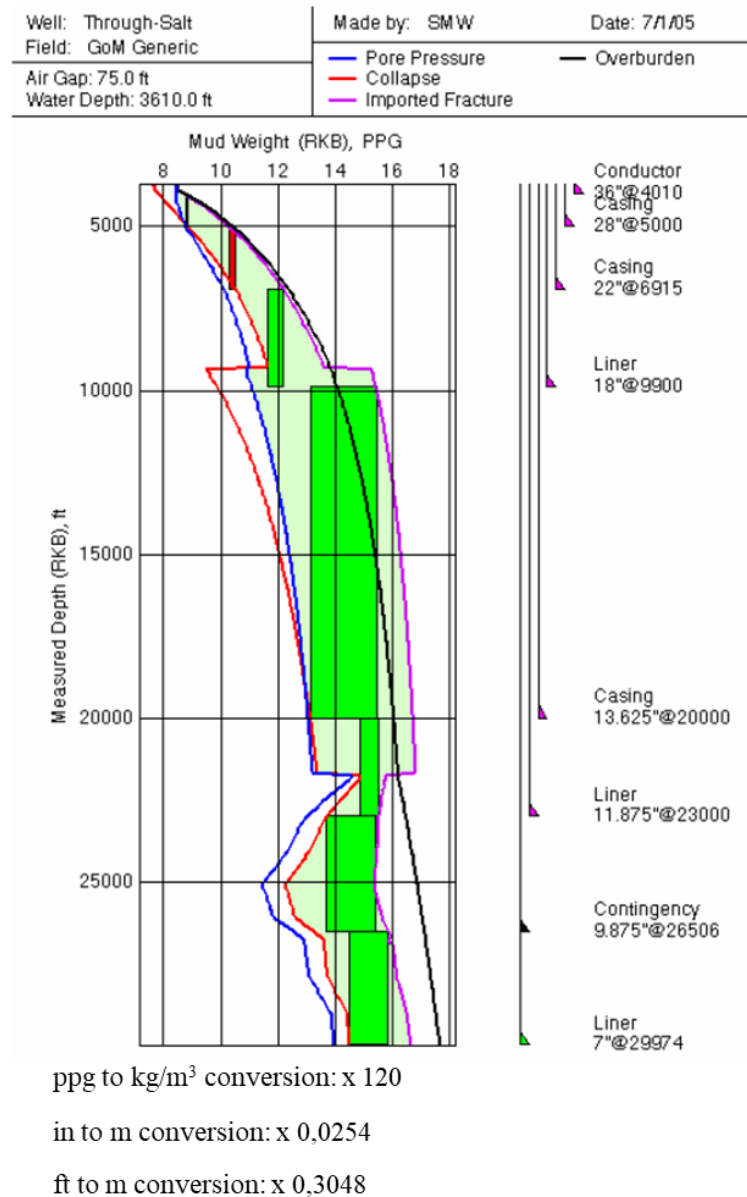


Figure 10-4. Example of MW window design in Deepwater GoM (Wilson and Fredrich, 2005)

10.2. Deepwater casing sizing

Sizing of wellbore tubulars starts with the production casing that will accommodate tubing sufficient to ensure the most-economic well deliverability. By working outward, a typical

sizing will then determine the appropriate hole size to contain the production casing under the assumption that adequate annular clearance for cement placement exists between the production casing and wellbore wall. This hole diameter will be adjusted slightly to correspond to a standard bit size. Afterward, the search for a diameter of the adjacent casing continues. The casing, however, must pose reasonable wall thicknesses so that casing can accommodate the bit necessary to drill the wellbore section for the production casing. The above steps are then repeated for each successive new casing size, proceeding from the inner tubular, outward (Pattillo, 2018). A schematic of typical Deepwater casing selection chart is given in figure 10-5.

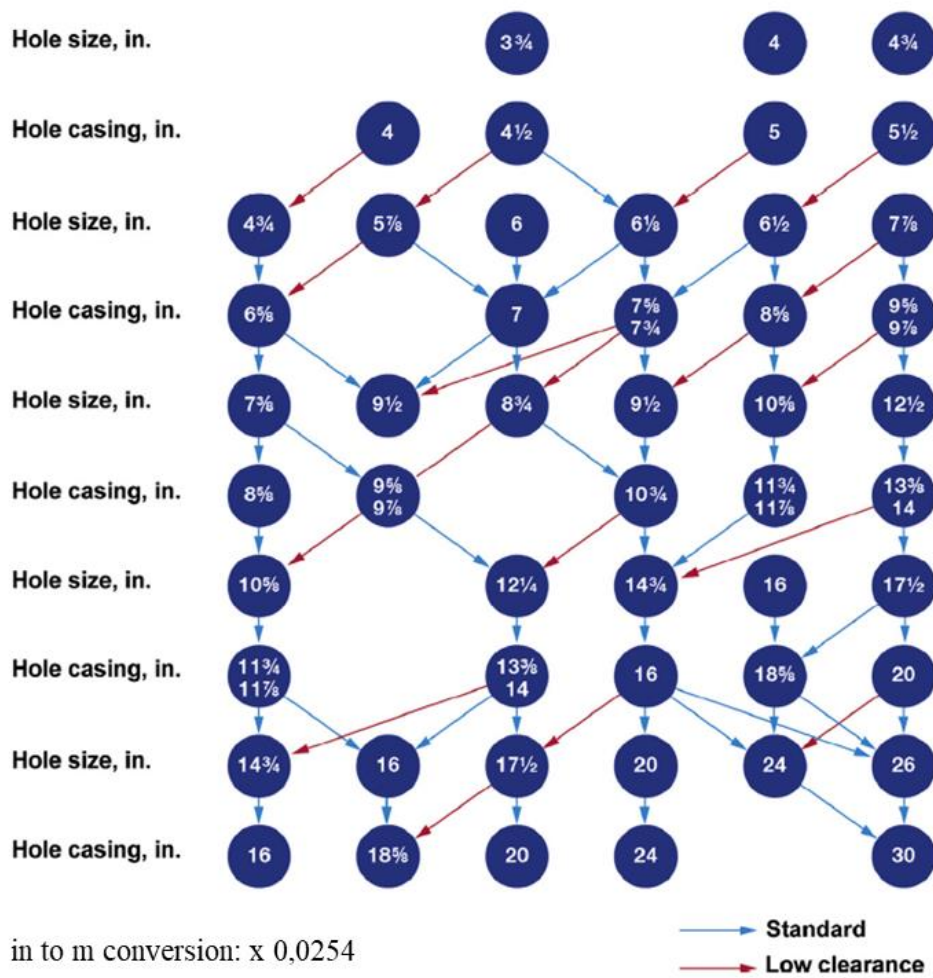


Figure 10-5. Chart for typical Deepwater casing selection (Aird, 2019)

For the reader's convenience definition of different casing strings valid for the Deepwater environment is repeated below (adopted from Aird, 2019):

- Conductor - the first string jetted or drilled and cemented up to the mudline (also foundation pipe; marine conductor). The purpose of conductor casing is to ensure

sufficient bearing surface once the BOP stack lands such that the structure is able to withstand all the axial, lateral, rotational and pressure loads imposed throughout the well life. Additionally, its purpose is to protect shallow sediments from washing out, prevent instability of tophole section and avoid shallow gas breach to the sea floor (Aird, 2019). It is usual practice to weld the Low-pressure wellhead housing (LPWHH) on the conductor casing, a housing that will host High-pressure wellhead housing (HPWHH) and the surface casing (see figure 10-6). The design of these strings is very case-specific (see e.g., API RP 2A-WSD).

- Surface - string whose depth and design provide wellbore integrity and pressure isolation needed for subsequent drilling activity. It represents the last string set before running the subsea BOP stack. In deviated wells, the casing can isolate build sections to prevent formation instability or key seating resulting during steering the well. It is typically cemented in place over the whole length, between the welded LPWHH and HPWHH sealed with special seal assembly. It is the last casing with visible cement returns to the seafloor.
- Intermediate - string whose depth and design are determined in a way to isolate problematic well sections (unstable wellbore sections, LC zones, AP zones, etc.). The top of cement is placed to isolate any pressured, permeable, and/or hydrocarbon zones. In Deepwater, often multiple intermediate strings are required. Some strings can be understood as production strings if a liner is run beneath them.
- Production - string used to isolate production zones and contain formation pressures in the event of a tubing leak. Its design must also account for all operational activities over the well lifecycle (bullheading, injection, or stimulation pressures if required).
- Liner - string that does not extend back to the subsea wellhead but instead is hung inside the lap of another casing. Liners are used to improve safe operating windows when drilling deeper sections. They also permit the use of larger tubing above the liner top and do not present a tension limitation for a rig. Liners can be intermediate or production strings and are typically cemented over their whole length.

Generally, standard clearance casing designs in Deepwater environment can be found in low-to medium-risked normal pressured regimes with fewer strings required to meet the total depth objectives (figure 10-7a.). Hence, standard wellbore sizes and casing connections are usually sufficient, with little wellbore enlargement needs. However, in the case of a subsalt Deepwater well, very often, specific casing-design considerations in salt will necessitate

higher casing grades and/or thick-walled casings³⁷ (Appendix-2) to counter creeping loads. At the same time, the annular clearances are usually designed to be larger than in the sections below the salt to delay the impingement of the salt on the casing. It follows that subsalt/presalt well needs to accommodate multiple casing strings or liners under rather unconventional clearances (figure 10-7b.) (Chatar et al., 2010; Aird, 2019). Another constraint imposed to tubular sizing offshore is the unfavorable PFG for Deepwater locations that may require more than five casing strings to accommodate the narrow range of acceptable drilling fluid density. Furthermore, Deepwater wells are further restricted in the number of casing strings because of:

- a relatively large final hole size (ca. 215.95 mm; 8,5”) needed to accommodate high production or injection volumes and large subsurface safety valves (SSSV) (ca. 228.6 mm; 9”).
- a current maximum 476.25 mm (18,75”) diameter bore on the HPWHH

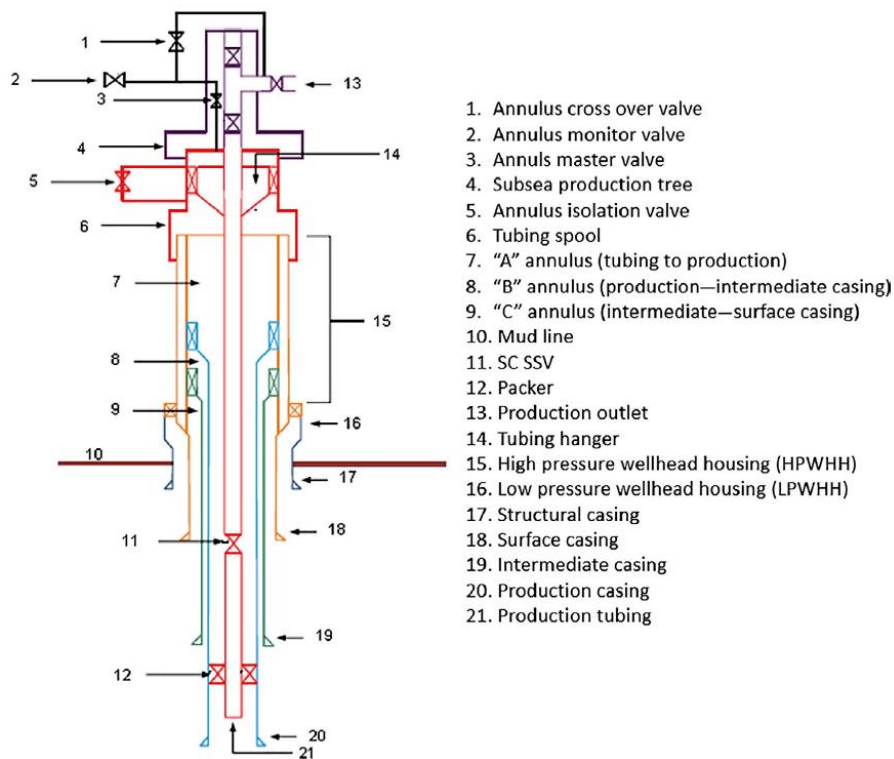


Figure 10-6. Typical Deepwater production well with a dry tree configuration (Aird, 2019)

³⁷ Casing wear in Deepwater wells is another problem to prioritize the thicker-walled casing, as thicker steel rim allows for casing to be run across areas of high dogleg severity (DLS) with a greater allowance for casing wear. Note that the issue of casing wear needs to be addressed specifically when traversing mobile salt sections as internal wear will reduce casing performance properties, including internal yield pressure and external collapse resistance (van Oort, 2004; Lin et al., 2020).

With all these implications combined, a well-design will be pushed to maximum drilling limits to accommodate the sufficient strings needed to reach the target depth. That often necessitates casing shoes to be pushed as deep as possible. In addition to the already cramped casing plan, a well-planning team needs to consider contingency strings for the base-case design to account for PPFG uncertainties, unanticipated hole problems, potential sidetracking, and the loss of geological correlation (Seymour et al., 1993; Whitson and McFadyen, 2001; Aird, 2019).

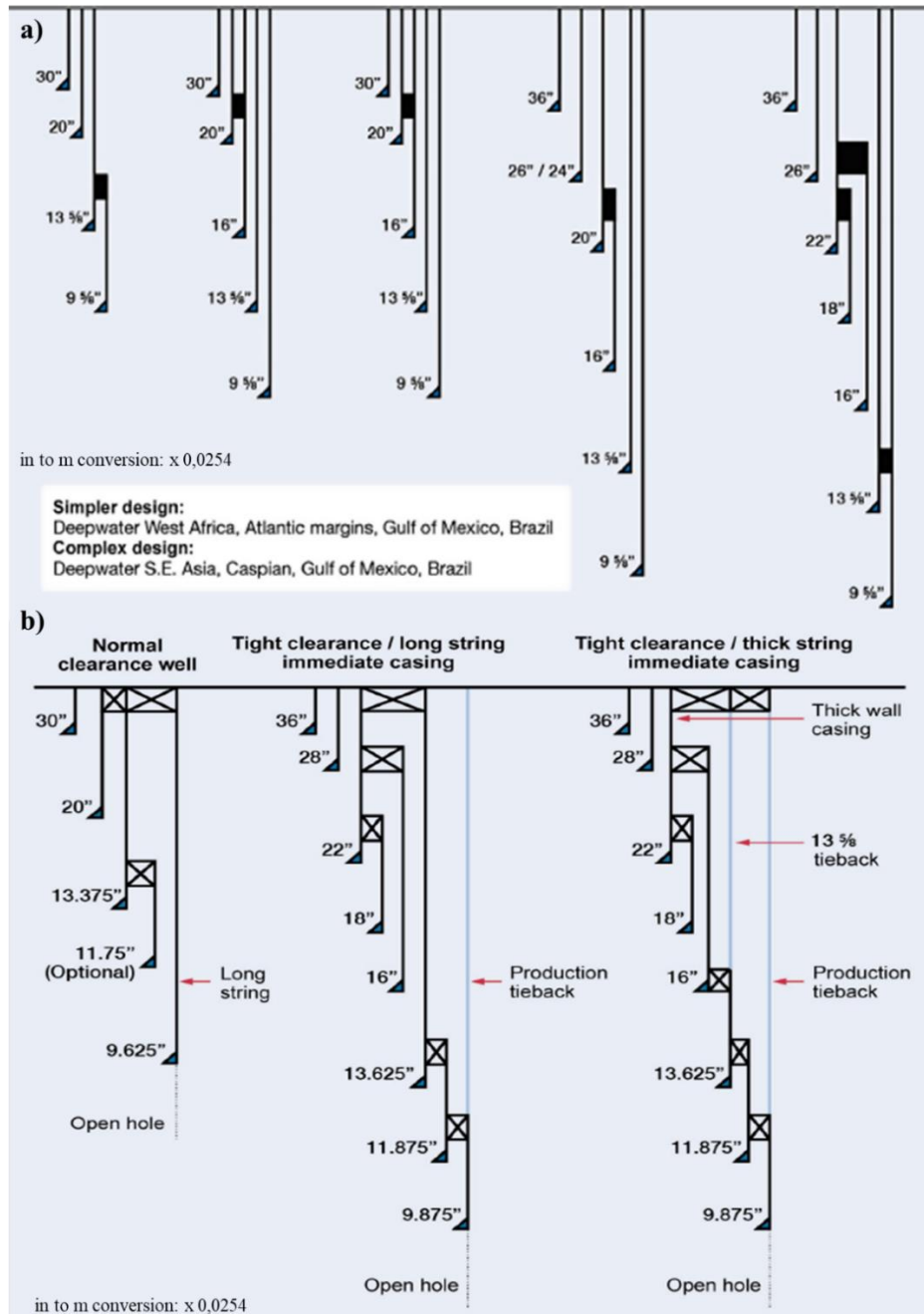


Figure 10-7. Common casing designs for the Deepwater wells; (a) normal and (b) tight clearance (Aird, 2019)

10.3. Dubiousness in Deepwater casing shoe selection in subsalt and presalt

Although pushing casing seats can be attractive in terms of economics, special care should be taken to adjust the casing seating depth adjacent to salt entry and exit. This will often require human intervention in shifting selected seat-depth to address specific problems pertinent to offshore salt well construction. Usually, the casing is manually set at the top of salt since high FG within the salt (for the given depth) allow longer hole sections between casing strings and insulation from typical well control problems associated with permeable formations (Whitson and McFadyen, 2001; Wilson et al., 2002; Barker and Meeks, 2003; Rohleder et al., 2003). In addition, such design permits higher MW in the upper salt sections that could be required to keep borehole closure under the allowable limit. However, such an approach comes at a certain price. Dusseault et al. (2004a, b) reported that if fractured shales are encountered, their time-dependent geochemical sensitivity³⁸, and the state of rock fracturing, it is desirable to drill this interval as fast as possible. In regions above salt domes containing gas clouds, high ROP in fractured shales cannot be sustained due to severe mud gas cutting. Correspondingly, ROP should be minimized and casing set prior to reaching the top of salt to prevent stability problems caused by sloughing shales. Likewise, encountering overpressurized carapace formations at the top of the salt could necessitate deploying casing string before entering salt when combined with a reduced FG above convex salt (Jackson and Hudec, 2017).

When a casing string is set into the top of a salt interval, the presence of the salt will affect the design of the casing. Since the fracture pressure in salt is higher than a comparable nonsalt formation, the casing must be designed to safely handle the pressures resulting from well control incidents encountered in the salt or below the salt (Barker and Meeks, 2003). Another disadvantage of placing the shoe of the surface/intermediate casing within the salt is that it complicates side-tracking due to hole deviation and related directional control problems in the salt (in case the side-track is required because of problems in salt and subsalt zone) (Whitson and McFadyen, 2001; Israel et al., 2008). Likewise, one needs to understand that in such a case the casing shoe will be directly exposed to salt creep, which, if substantial, may close around the casing even before cementation takes place and hamper its integrity (Wilson et al., 2002; van Oort, 2004). This is highly dependent upon the salt

³⁸ In reactive shales drilled with water-based muds, there is usually a time lag (e.g., several days because of pressure diffusion and thermal processes) before the chemical instability onset (Amoco, 1996)

type encountered, thermal anomalies at the salt top, and MW permitted by overlying sections. A similar question arises in cases where (whatever the reason) contingency has already been deployed in suprasalt, and the drilling team may consider pushing casing shoe deeper in the salt than it has been pre-planned. Especially problematic are the exploration wells since much uncertainty exists around the geomechanics properties around salt, salt characteristics, MW, all of which directly impact casing programs.

From a purely drilling and cost perspective, the optimum salt exit would be at the length of the salt interval where the FG at the top of the salt is close to the FG in the formations underlying the salt. However, this is rarely the case as reservoir targets are usually pre-determined. Again, the risk of exiting into a rubble zone exists, which can easily lead to severe circulation losses if exposed to the MW used within the salt section to contain salt creep (Barker and Meeks, 2003; Saleh et al., 2013). When opting for setting casing below the salt, one needs to understand of potentially existing low FG. In turn, this may prevent cementing the annulus between the casing and salt to the designed depth. Namely, depending on the next casing string's setting depth, the casing shoe's FG may be insufficient to hold even a column of foamed cement. Even in cases where such casing can be cemented, there might happen that additional contingency string (or liner tieback) will be required before reaching the target depth due to the unfavorable width of the MW window (Wilson et al., 2002). This will directly affect the final diameter of the production casing and tubing consequentially. Thus, due to uncertainty coupled in MW window below the salt, the casing should be seated as close to the base of the salt as possible.

11. CONCLUSION

Over the decades of the exploration for hydrocarbons offshore, the reservoirs in salt plays have proved to be lucrative targets. Deepwater hydrocarbon-bearing formations underlying salt massive salt bodies have been established as commercial reserves in areas such as offshore Brazil, Gulf of Mexico (GoM), North Sea, western Africa coast, and many more. While from the exploration point of view, the properties of salt make it appealing structures for hydrocarbon accumulation, its specific material properties add significant complexity to value creation. Although massive salt bodies have been successfully drilled over the last few decades, narrow economic margins and more-than-ever volatile market calls for rationalizing the field development expenses. Proactively addressing well construction challenges during the well planning and design phase has vast potential to decrease cost per well and thus reduce overall development expenses. As the degree of encountered instabilities around salt may be high to an extent where they drastically influence the well design and consequently elevate well delivery costs, wellbore stability was shown to be one of the major drivers for the optimization of well economics. To corroborate the Thesis` hypothesis, an in-depth analysis of multiple problems related to well design in the offshore salt environment was provided.

This Thesis demonstrated that the first step toward optimization of well economics is an accurate characterization of in-situ conditions around salt bodies. Although the character of in-situ stress perturbations is highly dependent upon the salt body geometry, it enables operators to quantify drilling margins and seek for well placement sweet spots. Moreover, a standalone approach to wellpath and architecture design breaks down around salt bodies. Namely, the adverse salt deformation caused by the raise of deviatoric stresses during well construction, unfavorable stress perturbations and geomechanical hazards found around salt bodies can result in unusually high mud weights whose deployment may be limited by the presence of weak points along trajectory. In turn, this will require numerous casing strings to meet well objectives. The operational risks are further increased due to areas of poor drillability and substantially amplified impact of Lost circulation and Well Control Incidents in Deepwater. On the other hand, development schemes and target requirements may give rise to trajectory-specific drilling problems such as Torque and Drag, drilling vibrations, poor deviation control, all of which are, again, exacerbated by increased water depths. In addition, the salt-flowing character and subsequent impingement may incur specific casing-design considerations and/or necessitate higher casing grades and wall thicknesses.

To find the most optimum well design, all the specific risks peculiar to the offshore salt environment must be well understood and evaluated. By seeing a well placement as a multidimensional problem, a wellpath can be leveraged to overcome all the above-mentioned problems. Going beyond the single cost-reduction dimension, a holistic approach enables operators to capture additional value from the well construction while improving returns, decreasing risks, and enhancing operational safety in offshore salt plays.

12. REFERENCES

1. AADNØY, B., 1990. In-situ stress directions from borehole fracture traces. [https://doi.org/10.1016/0920-4105\(90\)90022-U](https://doi.org/10.1016/0920-4105(90)90022-U)
2. AADNØY, B., LOOYEH, R., 2011. *Petroleum Rock Mechanics - Drilling Operations and Well Design*. 1st ed. Gulf Professional Publishing, Oxford
3. AADNØY, B.S., 1998. Geomechanical Analysis for Deep-Water Drilling. Presented at the IADC/SPE Drilling Conference, OnePetro. <https://doi.org/10.2118/39339-MS>
4. AADNØY, B.S., 2010. *Modern Well Design: Second Edition*. CRC Press.
5. ADACHI, J.I., NAGY, Z.R., SAYERS, C.M., SMITH, M.F., BECKER, D.F., 2012. Drilling Adjacent to Salt Bodies: Definition of Mud Weight Window and Pore Pressure Using Numerical Models and Fast Well Planning. Presented at the SPE Annual Technical Conference and Exhibition, OnePetro. <https://doi.org/10.2118/159739-MS>
6. AIRD, P., 2019. *Deepwater Drilling - Well Planning, Design, Engineering, Operations, and Technology Application*. 1st ed. Gulf Professional Publishing, Oxford
7. AL-AJMI, A., ZIMMERMAN, R., 2006. A New 3D Stability Model for the Design of Non-Vertical Wellbores. Presented at the Golden Rocks 2006, The 41st U.S. Symposium on Rock Mechanics (USRMS), OnePetro.
8. ALFAYYADH, J., AL MOQBIL, A., TAHER, A., 2020. Revisiting Subsalt Exploration Drilling Challenges. Presented at the International Petroleum Technology Conference, OnePetro. <https://doi.org/10.2523/IPTC-19849-Abstract>
9. AMOCO., 1996. *Wellbore stability Drilling Handbook*. Internal material, Amoco Production Company
10. ARBOUILLE, D., ANDRUS, V., PIPERI, T., XU, T. 2013. Sub-Salt and Pre-Salt Plays - How Much Are Left To Be Discovered?. Presented at AAPG International Conference and Exhibition, Cartagena, Colombia, September 8-11, 2013. https://www.searchanddiscovery.com/documents/2013/10545arbouille/ndx_arbouille.pdf
11. AREGBE, A.G., 2017. Wellbore Stability Problems in Deepwater Gas Wells. *World Journal of Engineering and Technology* 5, 626-647. <https://doi.org/10.4236/wjet.2017.54053>

12. BARKER, J.W., FELAND, K.W., TSAO, Y.H., 1994. Drilling Long Salt Sections Along the U.S. Gulf Coast. *SPE Drilling & Completion* 9, 185–188. <https://doi.org/10.2118/24605-PA>
13. BARKER, J.W., MEEKS, W.R., 2003. Estimating Fracture Gradient in Gulf of Mexico Deepwater, Shallow, Massive Salt Sections. Presented at the SPE Annual Technical Conference and Exhibition, OnePetro. <https://doi.org/10.2118/84552-MS>
14. BEASLEY, C. J., FIDUK, J., BIZE, E., BOYD, A., FRYDMAN, M., ZERILI, A., DRIBUS, J., MOREIRA, J., PINTO, A., 2010. Brazil's Presalt Play. *Oilfield Review* 22, 28-37.
15. BOGOBOWICZ, A., ROTHENBURG, L., DUSSEAULT, M.B., 1991. Solutions for Non-Newtonian Flow Into Elliptical Openings. *Journal of Applied Mechanics* 58, 820-824. <https://doi.org/10.1115/1.2897268>
16. BOTELHO, F.V., 2008. Numerical Analysis of Mechanical Behavior of the Salt in Oil Wells. Master's Thesis – Department of Civil Engineering, Pontifical Catholic University of Rio de Janeiro.
17. BRADLEY, W.B., 1978. Bore Hole Failure Near Salt Domes. Presented at the SPE Annual Fall Technical Conference and Exhibition, OnePetro. <https://doi.org/10.2118/7503-MS>
18. BROWN, J.P., FOX, A., SLIZ, K., HANBAL, I., PLANCHART, C., DAVIES, G., BRADFORD, C., MCCROSSAN, J., MCFARLANE, M., 2015. Pre-Drill and Real-Time Pore Pressure Prediction: Lessons from a Sub-Salt, Deep Water Wildcat Well, Red Sea, KSA. Presented at the SPE Middle East Oil & Gas Show and Conference, OnePetro. <https://doi.org/10.2118/172743-MS>
19. BRUDY, M., ZOBACK, M.D. 1993. Compressive and tensile failure of boreholes arbitrarily-inclined to principal stress axes: Application to the KTB boreholes, Germany. *International Journal of Rock Mechanics and Mining Sciences & Geomechanics*, 30, 1035-1038. [https://doi.org/10.1016/0148-9062\(93\)90068-O](https://doi.org/10.1016/0148-9062(93)90068-O)
20. CARCIONE, J.M., HELLE, H.B., GANGI, A.F., 2006. Theory of borehole stability when drilling through salt formations. *GEOPHYSICS* 71, 31-47. <https://doi.org/10.1190/1.2195447>
21. CASTAGNOLI, J.P., MONTESINOS, C., MUÑOZ, D., 2016. Drilling Geomechanics Salt Creep Monitoring: How to Optimize Mud Weight in Real Time and Get a Safe Time Window While Drilling, Tripping, Running and Cementing Casing in Salt Formations; <https://www.semanticscholar.org/paper/Drilling->

- [Geomechanics-Salt-Creep-Monitoring%3A-How-to-Castagnoli-Montesinos/6231a602d44ef6e8ed13e7040e4dabb4a34bf35e](#) (accessed 12.03.21).
22. CHATAR, C., ISRAEL, R., CANTRELL, A., 2010. Drilling Deep in Deep Water: What It Takes to Drill Past 30,000 ft. Presented at the IADC/SPE Drilling Conference and Exhibition, OnePetro. <https://doi.org/10.2118/128190-MS>
 23. CHEATHAM, J.B., JR., MCEVER, J.W., 1964. Behavior of Casing Subjected to Salt Loading. *Journal of Petroleum Technology* 16, 1069-1075. <https://doi.org/10.2118/828-PA>
 24. CHOWDHURY, A.R., CALLAIS, R., ROTHE, M., ANDERSON, M., KOONS, B., BATHGATE, G., 2016. Mitigating Salt and Sub-Salt Drilling Challenges Using Hybrid Bit Technology in Deepwater, Gulf of Mexico. Presented at the SPE Deepwater Drilling and Completions Conference, OnePetro. <https://doi.org/10.2118/180342-MS>
 25. COSTA, A.M., POIATE E., FALCÃO, J.L., COELHO, L.F.M., 2005. Triaxial Creep Tests in Salt Applied in Drilling Through Thick Salt Layers in Campos Basin-Brazil. Presented at the SPE/IADC Drilling Conference, OnePetro. <https://doi.org/10.2118/92629-MS>
 26. COSTA, A.M., POIATE, E., AMARAL, C.S., GONCALVES, C.J.C., FALCAO, J.L., PEREIRA, A., 2010. Geomechanics Applied to the Well Design Through Salt Layers In Brazil:A History of Success. Presented at the 44th U.S. Rock Mechanics Symposium and 5th U.S.-Canada Rock Mechanics Symposium, OnePetro.
 27. CROMB, J.R., PRATTEN, C.G., LONG, M., WALTERS, R.A., 2000. Deepwater Subsalt Development: Directional Drilling Challenges and Solutions. Presented at the IADC/SPE Drilling Conference, OnePetro. <https://doi.org/10.2118/59197-MS>
 28. DRIBUS, J. R., JACKSON, M. P. A., KAPOOR, J., SMITH, M. F., 2008. The prize beneath the salt: *Oilfield Review*, Autumn, 4-17.
 29. DUSSEAULT, M., BRUNO, M., BARRERA, J., 2001. Casing Shear: Causes, Cases, Cures. *SPE Drilling & Completion - SPE DRILL COMPLETION* 16, 98-107. <https://doi.org/10.2118/72060-PA>
 30. DUSSEAULT, M., MAURY, V., SANFILIPPO, F., SANTARELLI, F., 2004a. Drilling Through Salt: Constitutive Behavior and Drilling Strategies. Presented at the Gulf Rocks 2004, the 6th North America Rock Mechanics Symposium (NARMS), OnePetro.

31. DUSSEAULT, M.B., MAURY, V., SANFILIPPO, F., SANTARELLI, F.J., 2004b. Drilling Around Salt: Risks, Stresses, And Uncertainties. Presented at the Gulf Rocks 2004, the 6th North America Rock Mechanics Symposium (NARMS), OnePetro.
32. ESPINOZA, D.N., 2021. Introduction to Energy Geomechanics. Course handout. <https://dnicolasespinoza.github.io/> (accessed 05.05.21).
33. FARMER, P., MILLER, D., PIEPRZAK, A., RUTLEDGE, J., WOODS, R. 1996. Exploring the Subsalt. *Oilfield Review* 8, 50-64. https://www.slb.com/~media/Files/resources/oilfield_review/ors96/spr96/ors96_salt_p50_64.pdf
34. FEKETE, P., DOSUNMU, A., ANYANWU, C., ODAGME, S.B., EVELYN, E., 2014. Wellbore Stability Management in Weak Bedding Planes and Angle of Attack in Well Planing. Presented at the SPE Nigeria Annual International Conference and Exhibition, OnePetro. <https://doi.org/10.2118/172361-MS>
35. FIRME, P. A. L.P., COSTA, A.M., POIATE, E., CARRION, M.A., ROEHL, D., 2015. Casing Integrity of a Typical pre-salt Wellbore under Local Salt Dissolution Conditions. Presented at the 13th ISRM International Congress of Rock Mechanics, OnePetro.
36. FIRME, P. A. L.P., QUEVEDO, R.J., ROEHL, D., 2017. Modeling of Key Lifespan Stages of a Pre-Salt Wellbore. Presented at the 51st U.S. Rock Mechanics/Geomechanics Symposium, OnePetro.
37. FIRME, P. A. L.P., ROEHL, D.M., ROMANEL, C., POIATE, E., COSTA, A.M., 2014. Creep Constitutive Modeling Applied to the Stability of Pre-Salt Wellbores Through Salt Layers. Presented at the 48th U.S. Rock Mechanics/Geomechanics Symposium, OnePetro.
38. FJÆR, E., HOLT, R.M., HORSRUD, P., RAAEN, A.M., RISNES, R., 2008. *Petroleum Related Rock Mechanics 2nd Edition*. Elsevier B.V., Oxford
39. FOSSEN, H., 2010. *Salt tectonics*, in: *Structural Geology*. Cambridge University Press, Cambridge. 371-394. <https://doi.org/10.1017/CBO9780511777806.021>
40. FOSSUM, A., FREDRICH, J., 2002. Salt Mechanics Primer for Near-Salt and SubSalt Deepwater Gulf of Mexico Field Developments. <https://doi.org/10.2172/801384>
41. FREDRICH, J.T., COBLENTZ, D., FOSSUM, A.F., THORNE, B.J., 2003. Stress Perturbations Adjacent to Salt Bodies in the Deepwater Gulf of Mexico. Presented

- at the SPE Annual Technical Conference and Exhibition, OnePetro. <https://doi.org/10.2118/84554-MS>
42. GERE, J.M., TIMOSHENKO, S.P., 1991. *Mechanics of Materials, 3rd SI Edition*. Chapman & Hall, London
 43. GERRITSEN, P., 2018. Floaters in the Zechstein: (un)predictable & (un)safe to drill. TNO Expert Meeting: “Stringers in Salt - a drilling hazard”. <https://www.nlog.nl/sites/default/files/04%20engie%20-%20salt%20stringers.pdf> (accessed 15.10.21).
 44. GRIFFITHS, R., 2009. *Well Placement Fundamentals*. Schlumberger
 45. HALBOUTY, M. T., 1979. *Salt Domes: Gulf Region, United States and Mexico*. Gulf Publishing Co., Houston
 46. HAN, G., HUNTER, K.C., OSMOND, J., RESSLER, J.F., ZAMBONINI, M.J., 2008. Drilling Through Bitumen in Gulf of Mexico: The Shallower vs the Deeper. Presented at the Offshore Technology Conference, OnePetro. <https://doi.org/10.4043/19307-MS>
 47. HAN, G., OSMOND, J., ZAMBONINI, M., 2010. A USD 100 Million “Rock”: Bitumen in the Deepwater Gulf of Mexico. *SPE Drilling & Completion* 25, 290-299. <https://doi.org/10.2118/138228-PA>
 48. HIMMERLBERG, N., ECKERT, A., 2013. Wellbore Trajectory Planning for Complex Stress States. Presented at the 47th U.S. Rock Mechanics/Geomechanics Symposium, OnePetro.
 49. HOEK, E. AND BROWN, E. T., 1980. Empirical strength criterion for rock masses. *Journal of Geotechnical Engineering* 106, 1013-1035.
 50. INFANTE, E.F., CHENEVERT, M.E., 1989. Stability of Boreholes Drilled Through Salt Formations Displaying Plastic Behavior. *SPE Drilling Engineering* 4, 57-65. <https://doi.org/10.2118/15513-PA>
 51. ISRAEL, R.R., D’AMBROSIO, P., LEAVITT, A.D., SHAUGHNESSY, J.M., SANCLEMENTE, J.F., 2008. Challenges of Directional Drilling Through Salt in Deepwater Gulf of Mexico. Presented at the IADC/SPE Drilling Conference, OnePetro. <https://doi.org/10.2118/112669-MS>
 52. ITO, T., ZOBACK, M.D., PESKA, P., 2001. Utilization of Mud Weights in Excess of the Least Principal Stress to Stabilize Wellbores: Theory and Practical Examples. *SPE Drilling & Completion* 16, 221-229. <https://doi.org/10.2118/57007-PA>

53. JACKSON, M.P.A., HUDEC, M.R., 2017. *Salt Tectonics: Principles and Practice*. Cambridge University Press, Cambridge. <https://doi.org/10.1017/9781139003988>
54. KHALAF, F., 1985. Increasing Casing Collapse Resistance Against Salt-Induced Loads. Presented at the Middle East Oil Technical Conference and Exhibition, OnePetro. <https://doi.org/10.2118/13712-MS>
55. KHASAWNEH, R., TAN, F., PAUL, S. 2021. APPEC Lack of investment, more demand to drive oil price volatility -industry execs. <https://www.reuters.com/business/energy/appec-lack-investment-more-demand-drive-oil-price-volatility-industry-execs-2021-09-28/> (Accessed: 09.12.2021)
56. KRIŠTAFOR, Z., 2009. Projektiranje zacjevljenja. Course handout. Rudarsko-Geološko-Naftni Fakultet Sveučilišta u Zagrebu, Zagreb.
57. LEDGERWOOD, L.W., SALISBURY, D.P., 1991. Bit Balling and Wellbore Instability of Downhole Shales. Presented at the SPE Annual Technical Conference and Exhibition, OnePetro. <https://doi.org/10.2118/22578-MS>
58. LI, G., ALLISON, D., BAI, M., 2011. Anomalous Pore Pressure and its Relation with In-Situ Stress Regime in Deepwater Play. Presented at the SPE Annual Technical Conference and Exhibition, OnePetro. <https://doi.org/10.2118/145686-MS>
59. LI, S., RICCI, L., MCKAY, D., MITCHELL, P., CRUZ, E., 2019. Optimized Pore Pressure and Fracture Gradient Prediction for a Highly Deviated Subsalt Well in a Depleted Reservoir. Presented at the 53rd U.S. Rock Mechanics/Geomechanics Symposium, OnePetro.
60. LIN, B., COE, D., HARRIS, R., THOMAS, T., 2020. On Some Factors Affecting Casing Collapse Resistance under External Pressure. Presented at the SPE Annual Technical Conference and Exhibition, OnePetro. <https://doi.org/10.2118/201352-MS>
61. LIU, X., BIRCHWOOD, R., HOOYMAN, P.J., 2011. A New Analytical Solution for Wellbore Creep In Soft Sediments And Salt. Presented at the 45th U.S. Rock Mechanics / Geomechanics Symposium, OnePetro.
62. LUO, G., NIKOLINAKOU, M., FLEMINGS, P., HUDEC, M., 2012a. Near-salt stress and wellbore stability: A finite-element study and its application. Presented at the 46th US Rock Mechanics / Geomechanics Symposium 2012.

63. LUO, G., NIKOLINAKOU, M.A., FLEMINGS, P.B., HUDEC, M.R., 2012b. Geomechanical modeling of stresses adjacent to salt bodies: Part 1—Uncoupled models. *AAPG Bulletin* 96, 43-64. <https://doi.org/10.1306/04111110144>
64. MACKAY, F., INOUE, N., FONTOURA, S., BOTELHO, F., 2008. Geomechanical Effects of a 3D Vertical Salt Well Drilling by FEA. 42nd U.S. Rock Mechanics - 2nd U.S.-Canada Rock Mechanics Symposium.
65. MAEHS, J., RENNE, S., LOGAN, B., DIAZ, N., 2010. Proven Methods and Techniques to Reduce Torque and Drag in the PrePlanning and Drilling Execution of Oil and Gas Wells. Presented at the IADC/SPE Drilling Conference and Exhibition, OnePetro. <https://doi.org/10.2118/128329-MS>
66. MARLAND, C., NICHOLAS, S., COX, W., FLANNERY, C., THISTLE, B., 2007. Pressure Prediction and Drilling Challenges in a Deepwater Subsalt Well from Offshore Nova Scotia, Canada. *SPE Drilling & Completion* 22, 227-236. <https://doi.org/10.2118/98279-PA>
67. MASTIN, L.G. 1988. Effect of borehole deviation on breakout orientations. *Journal of Geophysical Research* 93, 9187-9195. <https://doi.org/10.1029/JB093IB08P09187>
68. MATHUR, R., SEILER, N., SRINIVASAN, A., PARDO, N.O., 2010. Opportunities and Challenges of Deepwater Subsalt Drilling. Presented at the IADC/SPE Drilling Conference and Exhibition, OnePetro. <https://doi.org/10.2118/127687-MS>
69. MCMONIGLE, J., THOMSON, A., VAN AGT, C., FITZ, R., WEBSTER, J., 2020. Oil and Gas Investment in the New Risk Environment. <https://www.bcg.com/publications/2020/oil-and-gas-investment-during-the-covid-era> (Accessed: 03.12.2021)
70. MEIER, T., BACKERS, T., DRESEN, G., GIPPER, P., 2015. Stress, Temperature, and Pore Pressure Perturbations Around a Salt Dome. Presented at the ISRM Regional Symposium - EUROCK 2015, OnePetro.
71. MELLO, U., KARNER, G., ANDERSON, R., 1995. Role of salt in restraining the maturation of subsalt source rocks. *Marine and Petroleum Geology* 12, 697-716. [https://doi.org/10.1016/0264-8172\(95\)93596-V](https://doi.org/10.1016/0264-8172(95)93596-V)
72. MOOS, D., PESKA, P., FINKBEINER, T., ZOBACK, M., 2003. Comprehensive wellbore stability analysis utilizing Quantitative Risk Assessment. *Journal of Petroleum Science and Engineering, Borehole Stability* 38, 97-109. [https://doi.org/10.1016/S0920-4105\(03\)00024-X](https://doi.org/10.1016/S0920-4105(03)00024-X)

73. MOUCHET, J., MITCHELL, A. 1989. *Abnormal pressures while drilling*. 1st ed. Boussens: Elf Aquitaine.
74. MOYER, M.C., LEWIS, S.B., COTTON, M.T., PEROYEA, L.M., 2012. Challenges Associated with Drilling a Deepwater, Subsalt Exploration Well in the Gulf of Mexico: Hadrian Prospect. Presented at the SPE Deepwater Drilling and Completions Conference, OnePetro. <https://doi.org/10.2118/154928-MS>
75. MUECKE, N.B., 1994. Heated Mud Systems: A Solution to Squeezing-Salt Problems. *SPE Drilling & Completion* 9, 276-280. <https://doi.org/10.2118/25762-PA>
76. MUNSON, D.E., AND DAWSON, P.R., 1979, Constitutive Model for the Low-Temperature Creep of Salt (With Application to WIPP). Technical Report SAND79-1853. Sandia National Laboratories, Albuquerque, New Mexico.
77. MUNSON, D.E., DAWSON, P.R., 1982. A Workhardening/Recovery Model Of Transient Creep Of Salt During Stress Loading And Unloading. Presented at The 23rd U.S Symposium on Rock Mechanics (USRMS), OnePetro.
78. NAGY, Z.R., LEE, D.W., SAYERS, C.M., ZAPATA, T.R., SILVESTRO, J.L., 2013. Iterative 3D Geomechanical Modeling to Determine Distribution and Impact of Stresses in Deepwater Gulf of Mexico Subsalt and Near-Salt Environments. Presented at the 47th U.S. Rock Mechanics/Geomechanics Symposium, OnePetro.
79. NESTER, J., JENKINS, D., SIMON, R., 1955. Resistances to failure of oil-well casing subjected to non-uniform transverse loading, *API Drilling and Production Practice*, 374-378.
80. NIKOLINAKOU, M., FLEMINGS, P., HUDEC, M., 2013a. Modeling stress evolution around a rising salt diapir. *Marine and Petroleum Geology* 51. <https://doi.org/10.1016/j.marpetgeo.2013.11.021>
81. NIKOLINAKOU, M.A., HEIDARI, M., HUDEC, M.R., FLEMINGS, P.B., 2015. Stress Changes Associated with the Evolution of a Salt Diapir into a Salt Sheet. Presented at the 49th U.S. Rock Mechanics/Geomechanics Symposium, OnePetro.
82. NIKOLINAKOU, M.A., LUO, G., HUDEC, M.R., FLEMINGS, P.B., 2012. Geomechanical modeling of stresses adjacent to salt bodies: Part 2— Poroelastoplasticity and coupled overpressures. *AAPG Bulletin* 96, 65-85. <https://doi.org/10.1306/04111110143>

83. NIKOLINAKOU, M.A., MERRELL, M.P., LUO, G., FLEMINGS, P.B., HUDEC, M.R., 2013b. Geomechanical Modeling of the Mad Dog Salt, Gulf of Mexico. Presented at the 47th U.S. Rock Mechanics/Geomechanics Symposium, OnePetro.
84. NUR, A., BYERLEE, J.D., 1971. An exact effective stress law for elastic deformation of rock with fluids. *Journal of Geophysical Research* 76, 6414-6419. <https://doi.org/10.1029/JB076i026p06414>
85. O'BRIEN, D.E., CHENEVERT, M.E., 1973. Stabilizing Sensitive Shales with Inhibited, Potassium-Based Drilling Fluids. *Journal of Petroleum Technology* 25, 1089–1100. <https://doi.org/10.2118/4232-PA>
86. O'BRIEN, J.J., LERCHE, I., YU, Z., 1993. Buildup Of Overpressure Beneath Offshore Salt Sheets:Case Histories And Models. Presented at the Offshore Technology Conference, OnePetro. <https://doi.org/10.4043/7087-MS>
87. OMOJUWA, E., OKOYE, E., OUSSENI, A., ODUNUGA, A., OSISANYA, S., AHMED, R., 2010. Understanding the Influence of Rock Stresses on Wellbore Inclination in Salt Formations: A Well Planning Approach. Presented at the Nigeria Annual International Conference and Exhibition, OnePetro. <https://doi.org/10.2118/136981-MS>
88. OMOJUWA, E.O., OSISANYA, S.O., AHMED, R., 2011. Properties of Salt Formations Essential for Modeling Instabilities While Drilling. Presented at the Nigeria Annual International Conference and Exhibition, OnePetro. <https://doi.org/10.2118/150801-MS>
89. OROZCO, S.O., PINO, J., PAREDES, M.A., VÁSQUEZ, J.L., XAVIER, A., 2018. Managing Creep Closure in Salt Uncertainty While Drilling. Presented at the 52nd U.S. Rock Mechanics/Geomechanics Symposium, OnePetro.
90. PARDO, C.A., JARAMILLO, J.M., PEARSE, J., 2016. Modelling of temperature distribution around salt diapirs: Application to hydrocarbons assessment. Bachelor Thesis.
91. PAŠIĆ, B., GAURINA MEĐIMUREC, N., MATANOVIĆ, D. 2007. Wellbore Instability: Causes And Consequences, *Rudarsko-geološko-naftni zbornik* 19(1), 87-98. Retrieved from: <https://hrcak.srce.hr/19296> (Access date: 12.12.2021.)
92. PATTILLO, P.D., 2018. *Elements of Oil and Gas Well Tubular Design*. 1st ed. Gulf Professional Publishing, Oxford

93. PATTILLO, P.D., COCALES, B.W., MOREY, S.C., 2006. Analysis of an Annular Pressure Buildup Failure During Drill Ahead. *SPE Drilling & Completion* 21, 242-247. <https://doi.org/10.2118/89775-PA>
94. PATTILLO, P.D., LAST, N.C., ASBILL, W.T., 2003. Effect of Nonuniform Loading on Conventional Casing Collapse Resistance. Presented at the SPE/IADC Drilling Conference, OnePetro. <https://doi.org/10.2118/79871-MS>
95. PEŠKA, P., ZOBACK, M.D., 1995. Compressive and tensile failure of inclined well bores and determination of in situ stress and rock strength. *Journal of Geophysical Research: Solid Earth* 100, 12791-12811. <https://doi.org/10.1029/95JB00319>
96. PINTO, C.N., LIMA, A.P., KNABE, S.P., 2019. MSE-Index: A New Concept of Energy Management to Control Salt Creep and Optimize Drilling Operations in Extensive Salt Intervals. Presented at the Offshore Technology Conference Brasil, OnePetro. <https://doi.org/10.4043/29795-MS>
97. POIATE, E., MAIA, A., FALCAO, J.L., 2006. Well Design for Drilling Through Thick Evaporite Layers. Presented at the IADC/SPE Drilling Conference, OnePetro. <https://doi.org/10.2118/99161-MS>
98. PRATSCH, J.-C., 1995. Gulf Coast Sub-Salt Play Exploration Strategies. Presented at the Offshore Technology Conference, OnePetro. <https://doi.org/10.4043/7636-MS>
99. ROHLEDER, S.A., SANDERS, W.W., WILLIAMSON, R.N., FAUL, G.L., DOOLEY, L.B., 2003. Challenges of Drilling an Ultra-Deep Well in Deepwater - Spa Prospect. Presented at the SPE/IADC Drilling Conference, OnePetro. <https://doi.org/10.2118/79810-MS>
100. ROMO, L.A., SHAUGHNESSY, J.M., LISLE, E.T., 2007. Challenges Associated With Subsalt Tar in the Mad Dog Field. Presented at the SPE Annual Technical Conference and Exhibition, OnePetro. <https://doi.org/10.2118/110493-MS>
101. ROYLANCE, D., 2001. Engineering Viscoelasticity. Mechanics of Materials. Course handout. Massachusetts Institute of Technology. <https://web.mit.edu/course/3/3.11/www/modules/>
102. SALEH, S., WILLIAMS, K.E., RIZVI, A., 2013. Rubble Zone Below Salt: Identification and Best Drilling Practices. Presented at the SPE Annual Technical Conference and Exhibition, OnePetro. <https://doi.org/10.2118/166115-MS>
103. SANZ, P.F., DASARI, G.R., 2010. Controls On In-situ Stresses Around Salt Bodies. Presented at the 44th U.S. Rock Mechanics Symposium and 5th U.S.-Canada Rock Mechanics Symposium, OnePetro.

104. SAYERS, C.M., SCHUTJENS, P., 2007. An introduction to reservoir geomechanics. *The Leading Edge*; 26 (5): 597-601. <https://doi.org/10.1190/1.2737100>
105. SCHLUMBERGER, 2014. Managing geological risk in deepwater drilling. Insights, Schlumberger, retrieved from <https://www.slb.com/-/media/files/seismic/industry-article/insights-journal-managing-geological-risk-deepwater-drilling.ashx>
106. SCHLUMBERGER, 2021. Fundamentals of Petroleum Geomechanics. NExT training course handout.
107. SENSENY, P.E., HANSEN, F.D., RUSSELL, J.E., CARTER, N.L., & HANDIN, J.W. 1992. Mechanical behaviour of rock salt: Phenomenology and micromechanisms. *International Journal of Rock Mechanics and Mining Sciences & Geomechanics* 29, 363-378. [https://doi.org/10.1016/0148-9062\(92\)90513-Y](https://doi.org/10.1016/0148-9062(92)90513-Y)
108. SEYMOUR, K.P., RAE, G., PEDEN, J.M., ORMSTON, K., 1993. Drilling Close to Salt Diapirs in the North Sea. Presented at the SPE Offshore Europe, OnePetro. <https://doi.org/10.2118/26693-MS>
109. SHEFFIELD, J.S., COLLINS, K.B., HACKNEY, R.M., 1983. Salt Drilling in the Rocky Mountains. Presented at the IADC/SPE Drilling Conference, OnePetro. <https://doi.org/10.2118/11374-MS>
110. SHEN, X., 2012. Case Studies on Stress Pattern Around Salt Bodies In Deep Water Formations. Presented at the 46th U.S. Rock Mechanics/Geomechanics Symposium, OnePetro.
111. SHEN, X., BAI, M., SMITH, R., 2010. Numerical Analysis on Subsalt Wellbore Stability in the Vioska-Knoll Deepwaters of the Northern Region of the Gulf of Mexico. Presented at the International Oil and Gas Conference and Exhibition in China, OnePetro. <https://doi.org/10.2118/130635-MS>
112. SHEN, X., WILLIAMS, K., STANDIFIRD, W., 2014. Enhanced 1D Prediction of the Mud Weight Window for a Subsalt Well, Deepwater GOM. Presented at the SPE Deepwater Drilling and Completions Conference, OnePetro. <https://doi.org/10.2118/170272-MS>
113. TERZAGHI, K., 1923. *Theoretical Soil Mechanics*, 11-14. John Wiley, New York,
114. TIXIER, M. P., ALGER, R. P., 1970. Log Evaluation of Nonmetallic Mineral Deposits. *GEOPHYSICS* 35: 124 <https://doi.org/10.1190/1.1440070>

115. URAI, J.L., SCHLEDER, Z., SPIERS, C.J., KUKLA, P.A., 2008. Flow and Transport Properties of Salt Rocks. Dynamics of Complex Intracontinental Basins: The Central European Basin System. Springer, 277-290.
116. VALLEJO V.G., SOLIS E., OLIVARES, A., AGUILERA L.E., TORRES M.E., GONZALEZ, L.F., 2012. Drilling a Deep-Water Well in a Subsalt Structure in Mexico. Presented at Deep Offshore Technology Conference, Schlumberger.
117. VALLEJO, L.G., FERRER, M., 2011. *Geological Engineering*. CRC Press, Boca Raton, 109 - 222
118. VAN OORT, E., 2004. Best Practices for Drilling, Casing and Cementing of Wells Through Salt. Technical Progress Report, Global Hole Stability Team (Ghost)
119. VITA, P., 2021. Computational Continuum Mechanics. Course handout. Montanuniversitaet Leoben.
120. WAGNER, R.A., MELLEGGARD, K.D., SENSENY, P.E., 1982. Influence of Creep Law Form on Predicted Deformations in Salt. Paper ARMA-82-684 presented at the 23rd U.S Symposium on Rock Mechanics (USRMS), Berkeley, California, 25–27 August.
121. WANG, H.Y., SAMUEL, R., 2013. Geomechanical Modeling of Wellbore Stability in Salt Formations. Presented at the SPE Annual Technical Conference and Exhibition, OnePetro. <https://doi.org/10.2118/166144-MS>
122. WARREN, J., 2006. *Evaporites: Sediments, resources, and hydrocarbons*, 1035. Berlin, Springer.
123. WEATHERL, M.H., 2010. GOM Deepwater Field Development Challenges at Green Canyon 468 Pony. Presented at the SPE Deepwater Drilling and Completions Conference, OnePetro. <https://doi.org/10.2118/137220-MS>
124. WEBB, J., ROZE, E., JARRET, C., LE ROUX, S., MEJIA, C., 2016. Drilling Engineering and Formation Evaluation: An Integrated Approach to Improve Real Time Drilling Optimization. Presented at the SPE Western Regional Meeting, OnePetro. <https://doi.org/10.2118/180400-MS>
125. WEIJERMARS, R., JACKSON, M.P.A., VAN HARMELEN, A., 2014. Closure of open wellbores in creeping salt sheets. *Geophysical Journal International* 196, 279-290. <https://doi.org/10.1093/gji/ggt346>
126. WHITSON, C.D., MCFADYEN, M.K., 2001. Lessons Learned in the Planning and Drilling of Deep, Subsalt Wells in the Deepwater Gulf of Mexico. Presented at the

- SPE Annual Technical Conference and Exhibition, OnePetro. <https://doi.org/10.2118/71363-MS>
127. WILLSON, S.M., EDWARDS, S., HEPPARD, P.D., LI, X., COLTRIN, G., CHESTER, D.K., HARRISON, H.L., COCALES, B.W., 2003. Wellbore Stability Challenges in the Deep Water, Gulf of Mexico: Case History Examples from the Pompano Field. Presented at the SPE Annual Technical Conference and Exhibition, OnePetro. <https://doi.org/10.2118/84266-MS>
 128. WILLSON, S.M., FOSSUM, A.F., FREDRICH, J.T., 2002. Assessment of Salt Loading on Well Casings. Presented at the IADC/SPE Drilling Conference, OnePetro. <https://doi.org/10.2118/74562-MS>
 129. WILLSON, S.M., FREDRICH, J.T., 2005. Geomechanics Considerations for Through- and Near-Salt Well Design. Presented at the SPE Annual Technical Conference and Exhibition, OnePetro. <https://doi.org/10.2118/95621-MS>
 130. WOLF, L., KAZIMI, M.S., TODREAS, N.E., 2001. Introduction to Structural Mechanics. Course handout. Massachusetts Institute of Technology.
 131. YANOSEK, K., ROGERS, M., 2018. *Unlocking future growth for Deepwater in the Gulf of Mexico*. McKinsey&Company
 132. YORK, P.L., PRICHARD, D.M., DODSON, J.K., DODSON, T., ROSENBERG, S.M., GALA, D., UTAMA, B., 2009. Eliminating Non-Productive Time Associated with Drilling through Trouble Zones. Presented at the Offshore Technology Conference, OnePetro. <https://doi.org/10.4043/20220-MS>
 133. ZHANG, G., QU, H., CHEN, G., ZHAO, C., ZHANG, F., YANG, H., ZHAO, Z., MA, M., 2019. Giant discoveries of oil and gas fields in global deepwaters in the past 40 years and the prospect of exploration. *Journal of Natural Gas Geoscience* 4, 1-28. <https://doi.org/10.1016/j.jnggs.2019.03.002>
 134. ZHANG, J., 2011. Pore pressure prediction from well logs: Methods, modifications, and new approaches. *Earth-Science Reviews* 108, 50-63. <https://doi.org/10.1016/j.earscirev.2011.06.001>
 135. ZHANG, J., STANDIFIRD, W.B., LENAMOND, C., 2008. Casing Ultradeep, Ultralong Salt Sections in Deep Water: A Case Study for Failure Diagnosis and Risk Mitigation in Record-Depth Well. Presented at the SPE Annual Technical Conference and Exhibition, OnePetro. <https://doi.org/10.2118/114273-MS>
 136. ZHANG, J., YIN, S., 2017. Real-Time Pore Pressure Detection: Indicators and Improved Methods. *Geofluids* 2017. <https://doi.org/10.1155/2017/3179617>

137. ZIJP, M.H., HUIJGEN, M.A., WILPSHAAR, M., BOUROULLEC, R., TER HEEGE J.H., 2018. *Stringers in Salt as a Drilling Risk*. TNO report, Utrecht
138. ZOBACK, M.D., 2007. *Reservoir Geomechanics*. Cambridge University Press, Cambridge.

13. APPENDICES

13.1. Appendix - 1

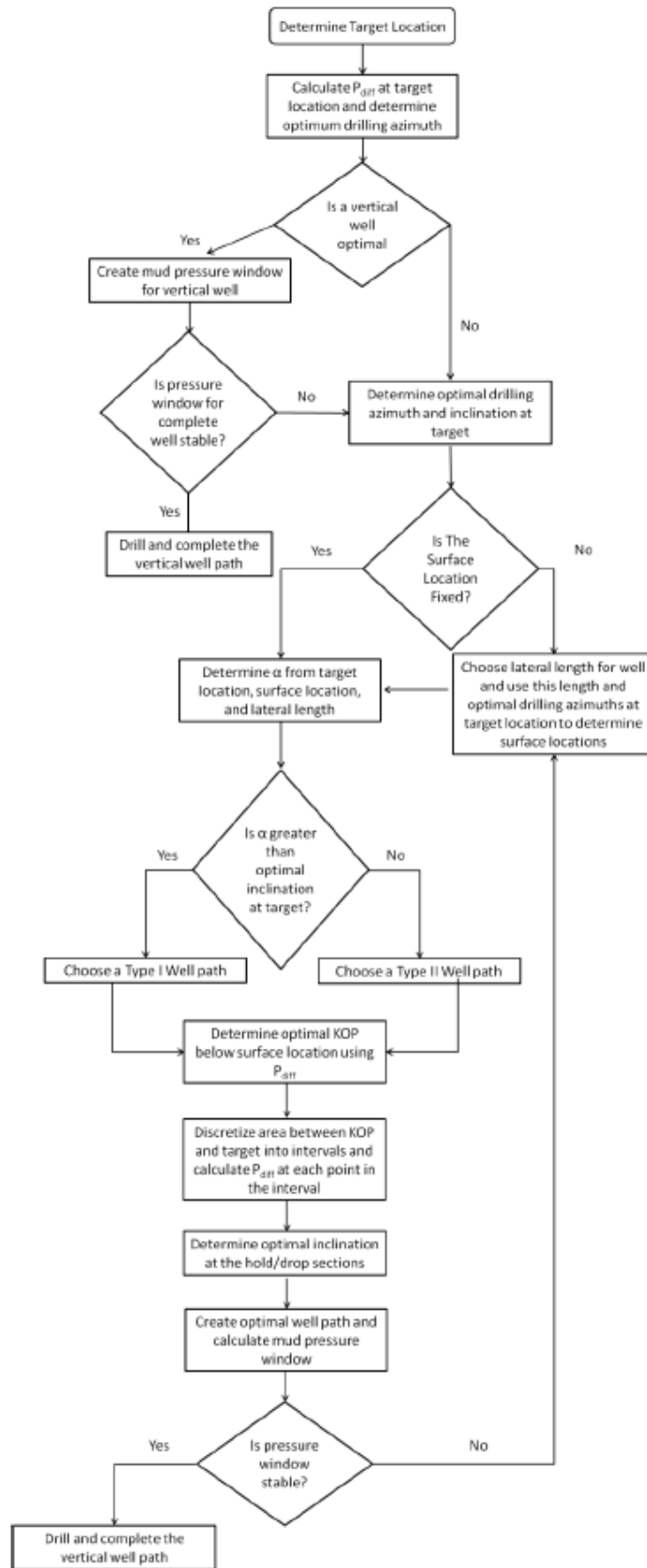


Figure 13-1. Wellbore trajectory optimization workflow (Himmelberg and Eckert, 2013)

13.2. Appendix - 2

As salt creeps into the wellbore, it will eventually contact the casing and stress the casing wall, eventually leading to collapse if the salt-induced stress exceeds the casing strength. However, once salt section is cased and drilling continues, relatively high MW will usually be required to cope with mobile tendency of salt. Even though this will reduce differential pressure across the installed casing during construction of subsequent wellbore sections, MW at the salt exit will be constrained by FG of the open hole in subsalt section. Moreover, salt loading needs to be evaluated across the whole well life cycle, not only construction. Any such unforeseen failure that may induce significant NPT or cause loss of information and/or hydrocarbon production that could significantly impact project economics. Therefore, assuring the longevity of well casings drilled through salt is a major requirement in the casing design for these sub-salt developments (Wilson et al., 2002). Typically, salt will load casing in one of the modes given in figure 13-2. (Wilson et al., 2002; Zhang et al., 2008; Wang and Samuel, 2013):

1. circumferentially (when the salt flow has completely encompassed the casing);
 - a. uniformly as in case of in-gouge hole
 - b. non-uniformly when the hole is oval
2. partially;
 - a. over a limited arc (localized loading exerted by creeping salt against incompletely covered cement sheath; both uniformly and non-uniformly)
 - b. in extreme cases point-loaded it (at the time the salt initially impinges on the eccentrically placed casing)

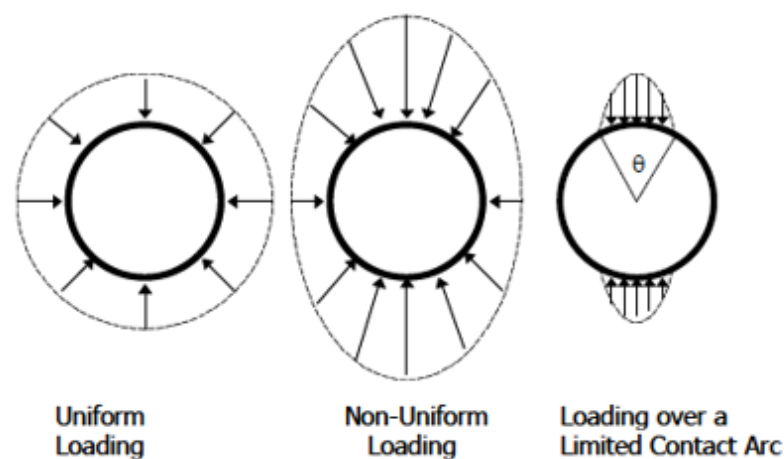


Figure 13-2. Possible salt-casing contacts (Wilson et al., 2002)

It is important to note that conventional collapse design procedures are inadequate to capture nonuniform and partial loading. Instead, a tubular collapse design shall be conducted in a way to combat the nonuniform loading. If salt loading occurs slowly, adjustments to conventional tubular design practice may be minimal since the cross-sectional ovalization can only occur at the same rate as the formation movement. However, according to Pattillo et al. (2003) such an approach neglects the fact that ovalization of the cross section due to non-uniform loading can also lower initial collapse resistance against conventional loads.

Perhaps the most severe form of nonuniform loading—point loading where the casing or tubing cross-section is loaded by opposing line loads rather than opposing distributed loads—occurs when one tubular is loaded externally by another, collapsing tubular. This often causes a cascade of collapse failures that may not be arrested until the production tubing is damaged (Pattillo, 2018). However, with the loading rate being sufficiently slow, as in case of pure halite salts found around GoM, years of useable service may exist before the drift of the casing becomes so small that will impinge on inner tubulars. The loss of collapse resistance caused by ovalization of the casing cross section from non-uniform formation loading when coupled with loss of collapse backup pressure can result in unforeseen casing collapse anytime during the well lifecycle. According to Khalaf (1985), non-uniform loading may reduce the collapse resistance of casing by an order of magnitude and is amplified by (1) DLS, (2) creep rate, (3) presence of hard rock embedded in the salt, (4) pipe geometry, (5) pipe stiffness, (6) imposed tension. Eventually, pipe may fail under anticipated uniform-loading conditions regardless of adequate design. According to models proposed to characterize the resistance of casing to non-uniform loading by Nester et al. (1955) and Cheatham and McEver (1964), it can be observed that the magnitude of yield load is proportional to $\left(\frac{t}{D}\right)^2$. This is perhaps the most important principle to apply in designing for nonuniform formation loading. One could say that is more prudent to “spend the money on steel, not on the grade of casing”. The main reason is that the resistance to point loading is proportional to the square of the wall thickness (or inversely proportional to the square of the D/t ratio), whereas it increases only linearly with steel yield strength. In other words, doubling the pipe nominal yield strength doubles the cross-section’s resistance to nonuniform loading, whereas doubling the pipe t/D ratio (usually by doubling the wall thickness) quadruples the cross-section’s resistance (van Oort, 2004, Pattillo, 2018). Similarly, Nester and al. (1955) pointed out that effect of internal pressure on nonuniform

load resistance is rather minor, only circa 10% of pressure collapse rating for tubulars with small D/t ratio, and even less for tubulars having larger D/t ratio.

Apart from deploying regular API casing grades as given from standardized casing design procedures, alternative casing solutions may be required depending on the rate of salt creep encountered:

- High collapse resistant casing (HCRC),
- Heavy-walled casing (HWC),
- Concentric casing strings.

Table 12.1 summarizes advantages and disadvantages of above-mentioned solutions (after Khalaf 1985; van Oort, 2004; Chatar et al., 2010; Pattilo, 2018).

Designing casing for non-uniform loads is much more involved as the resistance of casing to non-uniform loading is significantly lower, with reduction of collapse strength typically within 70-95% than for uniform loading. It is hardly possible to design casing for extreme non-uniform loading conditions since an unrealistic wall thickness would be required to counter non-uniform loads. Furthermore, the likelihood for non-uniform increases with creep rate, i.e., the faster the salt movement, the higher the chances of hole washouts, and consequently higher the chances of a poor cement job which increase the magnitude of non-uniform loading van Oort, 2004). Hence, the selection of a particular casing solution should be linked to the creeping rate (figure 13-3.). Advantages and drawbacks of different casing configurations are mentioned in table 13.1.

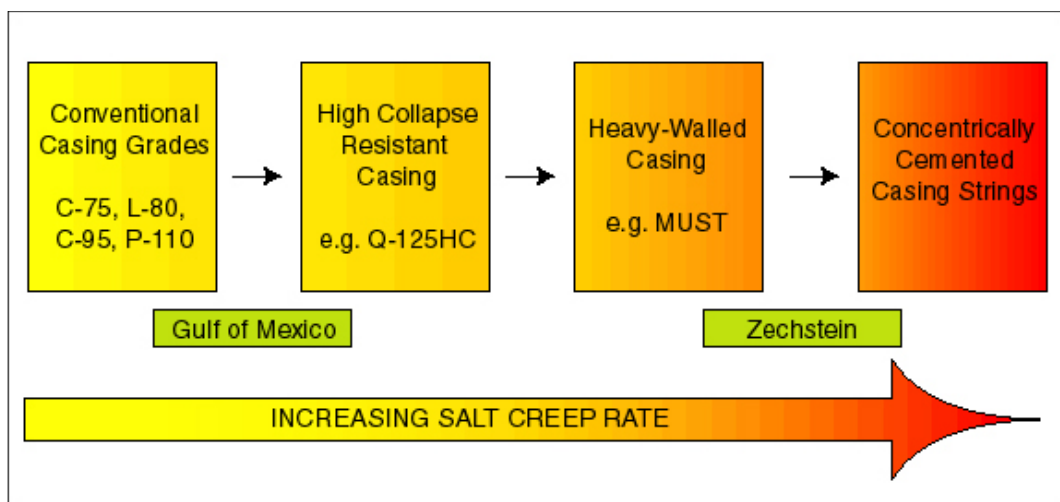


Figure 13-3. Proposed tubular solutions for varying creep rates (van Oort, 2004)

Table 13-1. Advantages and drawbacks of different casing configurations to combat creep loading

Alternative	Advantages	Disadvantages
High-Collapse Resistant Casing (HCRC) - high yield strength treated steels	<ul style="list-style-type: none"> • increased toughness and ductility • improved collapse resistance with minimum deviation from operational procedures 	<ul style="list-style-type: none"> • high steel grades (e.g., V-150) are highly brittle and less resistant to impact loads and corrosion • difficult to machine • difficult to mill for remedial operations and/or sidetracking purposes
Heavy-walled casing (HWC) - increased wall thickness, e.g., MUST	<ul style="list-style-type: none"> • improved resistance to point loading (~t/d) when compared to HCRC • customized manufacturing does not compromise standard bit selection/require underreaming • capable of withstanding high collapse gradient and non-uniform loading • higher allowable wear 	<ul style="list-style-type: none"> • non-standard sizes require specially ordered subs, centralizers, floating equipment, etc • may request modification to completion programme • cannot address most extreme non-uniform loading scenarios • lower DLS limits due to elevated stiffness • torque and drag considerations • require elevated TVD/hoisting capacity • increased lead time and cost per meter
Concentric casing strings - multiple-string coverage	<ul style="list-style-type: none"> • highest collapse resistance (up to 100% than solitary strings) • extremely effective from point-loading • less sensitive to variations in the quality of cement and borehole ovality. • opposite to single string, combination of a uniform load (cemented mid-annulus) and non-uniform salt loading increases the resistance of dual(triple) string to non-uniform loading 	<ul style="list-style-type: none"> • requires radical changes to casing and cementing programmes • loss of casing drift and wellbore size • complicate well delivery (e.g., perforation, cement bond logging) • increased total running/cementing time leading to prolonged well delivery • unsuitable for extremely fast creeping rates • most expensive • absence of cement may deem solution ineffective

STATUTORY DECLARATION

I declare in lieu of oath, that I wrote this Thesis and performed the associated research myself, using only literature cited in this volume.



BORNA LEŠ



KLASA: 602-01/22-01/24
URBROJ: 251-70-12-22-2
U Zagrebu, 15.02.2022.

Borna Leš, student

RJEŠENJE O ODOBRENJU TEME

Na temelju vašeg zahtjeva primljenog pod KLASOM 602-01/22-01/24, URBROJ: 251-70-12-22-1 od 07.02.2022. priopćujemo vam temu diplomskog rada koja glasi:

GEOMECHANICAL ASPECTS OF DEEPWATER WELL PLANNING AROUND SALT STRUCTURES

Za mentora ovog diplomskog rada imenuje se u smislu Pravilnika o izradi i obrani diplomskog rada Izv.prof.dr.sc. Borivoje Pašić nastavnik Rudarsko-geološko-naftnog-fakulteta Sveučilišta u Zagrebu i komentora Dr.sc. Petar Mijić.

Mentor:

(potpis)

Izv.prof.dr.sc. Borivoje Pašić

(titula, ime i prezime)

Komentor:

(potpis)

Dr.sc. Petar Mijić

(titula, ime i prezime)

Predsjednik povjerenstva za
završne i diplomske ispite:

(potpis)

Izv.prof.dr.sc. Luka Perković

(titula, ime i prezime)

Prodekan za nastavu i studente:

(potpis)

Izv.prof.dr.sc. Borivoje
Pašić

(titula, ime i prezime)